Investigations of Triplet-Pair States in π-Conjugated Singlet Fission Materials

Thesis by: Daniel Polak

Supervised by Dr. Jenny Clark

A thesis submitted in partial fulfilment of the requirements for the degree of Doctor of Philosophy

The University of Sheffield

Faculty of Science

Department of Physics and Astronomy

July 2019

I would like to dedicate this to my family, your love and support got me through my PhD and life in general.

Declaration:

The work within this thesis was completed by the author, unless explicitly stated in the text where the work involves collaboration. Throughout, we use the first person plural for readability. This work has never been submitted for the awarding of a degree at any other institution and is within the 80,000 word limit.

Daniel William Polak

Publications:

Daniel Polak, Rahul Jayaprakash, Anastasia Leventis, Kealan J Fallon, Harriet Coulthard, Anthony J Petty, John Anthony, Hugo Bronstein, David G Lidzey, Jenny Clark, Andrew J Musser. **2019**. Manipulating matter with strong coupling: harvesting triplet excitons in organic exciton microcavities, Chemical Science, 11, 343.

Daniel Polak, Iain Andrews, Enrico Salvadori, Andrew J Musser, Martin J Heeney, Jenny Clark. Conjugation Length Dependence of Intramolecular Singlet Fission in a Series of Thienylene-Vinylene Oligomers. - In Submission

Daniel Polak, Andrew J Musser, George A Sutherland, Alexander Auty, Federico Branchi, Jack Chidgey, Giulio Cerullo, Neil C Hunter, Jenny Clark. **2019**. Characterisation of Singlet Fission in Protein-Bound Carotenoid Aggregates: Revealing the Triplet Contributions to the $2A_g^-$ State. – Under review (PCCP) [Available on arXiv: 1901.04900]

George A Sutherland, **Daniel Polak**, Dirk B Auman, Andrew J Musser, Andrew Hitchcock, P. Leslie Dutton, Jenny Clark, Neil C Hunter. **2019**. Singlet Fission in carotenoids housed within a sterically-controlled, thermostable protein matrix. - In Submission (J. Am. Chem. Soc.).

Daniel Polak, George A Sutherland, Alexander Auty, Jack Chidgey, Neil C Hunter, Jenny Clark. **2019**. Singlet fission in Puff Q proteins, A study of naturally occurring spheroidenone aggregates. – In Preparation

Daniel Polak, George A Sutherland, Andrew Musser, Alexander Auty, Federico Branchi, Giulio Cerullo, Neil C Hunter, Jenny Clark. **2019**. Singlet fission in a protein bound, non-covalently linked tetracene dimer. – In Preparation

Acknowledgements:

First, I would like to thank my academic supervisor Dr. Jenny Clark. Throughout the last 4 years the time given to training and supporting me has meant the world. The hours of explaining concepts, working on my communication and encouragement to think big has kept me on the right path throughout. Before I began this journey, I did not feel I was capable of the things I have achieved, thank you for helping me find out I was.

I would also like to thank everyone past and present in the Clark group at the University of Sheffield who shared the last 4 years of lab highs and lows. Particularly, I would like to thank Dr. Andrew Musser for helping me into the field of organics and singlet fission, always there to answer questions at exhaustive frequency. The polariton work during my PhD was some of the most enjoyable of the whole PhD experience. Also thank you to Oleksandra Korychenska for always making me feel less alone in the experience of the PhD. Conferences were a lot more enjoyable with us both there, I will miss our conference trips. The help provided by all of you has allowed me to improve in a way I didn't think possible when I started my PhD.

As well as those in my department I would like to thank my dungeons and dragons group here in Sheffield. Creating a world and story for you all to play in and test me with has given me some of the best nights in the last few years. Without the weekly goof sessions, I would never have been able to cope with the stressful times when things went wrong. Particularly I would like to thank Tamsyn Fraser, moaning with you about PhD's through the last 4 years has been a release very much needed. I am glad we tried to make the PhD society, even if it did fail terribly, we got friendships and a DnD group out of it. On that note, thanks to Steven Parslow for being the out of town PhD support and conference partner. Our chats lamenting our issues in research made me feel a lot less alone.

Music has always been what keeps me sane and happy and that goes double for my degree which I think wouldn't have been completed without it. I would like to thank Chloe Slater for renewing my love of music before my degree started, James Town for being the best band mate I could ask for (St Paul's Parade lives on) and the whole of our camp at 2000 trees. The yearly trip to the centre of the forest to listen to music and hang out with you all was the highlight of my summers.

Last but not least I would like to thank those closest to me. My best Friend, Thomas Lees for always being a phone call away to tell me something stupid and make me laugh. My Partner, Chloe Slater for telling me I am an idiot when I thought I might not be capable and encouraging me to believe in myself. Putting up with a stressed me is bad enough but doing so with encouragement and love is a truly incredible act. Your love and support mean everything to me. Also, my parents Jayne and Glenn Polak for raising me to believe in myself, without ever making me feel pressured. Your love and support regardless of what I chose to do with my life made my path all the more manageable.

Finally, to my grandparents who since the moment I was born have done everything they can for me. Ann Hancock the support and love you gave me with no caveats went to form my personality; I hope to live even half as kindly to others as you do. Ralph Hancock, it hurts more than I could ever express in words that you won't be able to see me finish my PhD. The trips to tram, plane and car museums when I was small made me care for how things work and gave me the early love of science that's put me where I am. Your obsession with how machines worked rubbed off on me. You had more of an impact on me than you could ever know, I blame all of you for who I am.

Thesis Abstract:

Singlet fission is the process by which a singlet exciton splits into two 'free' triplet excitons. This was the definition of singlet fission up to the last few years when advances in the understanding of singlet fission in acene and heteroacene materials sparked a change in nomenclature in the field. Techniques such as electron paramagnetic resonance spectroscopy have allowed researchers to improve the understanding of singlet fission by visualizing the intermediate states in the singlet fission process. Currently in acene literature, it is common for the initial step of a singlet exciton converting to a singlet character triplet-pair state to be considered singlet fission. This change has interesting ramifications when it is applied to polyenes, another class of singlet fission material, where internal conversion from the absorbing state is thought to occur to a singlet state of triplet-pair character. We contribute to the above discussion by investigating the intermediate triplet-pair states in three systems using innovative techniques.

We start by investigating the well-studied TIPS-tetracene system using strong light-matter coupling to manipulate the character of the intermediate states. The results here point to a whole field of research, manipulating state energies and radiative character to enhance triplet-fed emission. In Chapters 5 and 6 we investigate the question posed above by studying two polyene systems. First, we measure a series of oligo(thienylene-vinylenes) which allow us to study the conjugation length dependence of singlet fission. Then in the final chapter we use an exciting new design philosophy of man-made proteins to form carotenoid aggregates. Through this chapter we are able to show experimental evidence for the triplet-pair nature of the $2A_g^-$ singlet state in polyenes. Furthermore, we find the

surprising result that singlet fission is incredibly robust in carotenoid aggregates being invariant with protein environment and intramolecular structure. We finish by discussing the implications of the results presented here and point to possible future avenues to further demystify the decay processes of singlet fission materials.

Contents

1. Introduction

As energy consumption continues to rise year on year (2.3% in 2018), we still produce nearly 80% of our energy from fossil fuels[1]. Without significant change, global temperatures are reaching dangerous highs. Already some parts of the world have experienced a temperature rise of 1.5^oC from 1880 to 2019, with significant environmental changes such as draughts and floods[2]. Clearly it is of huge importance for us to create clean and sustainable energy in the near future to avoid catastrophe[2]. While renewable energy production grew by 4.4% last year[1], it's a slow process, with a small proportion of the produced energy each year coming from renewable energies (~10%[1]). It has been argued that the most promising renewable technology is solar cells[3].

Silicon solar cell technology is the most prominent, with a substantial drop in cost, 8-1$/Watt[4], and rise in power conversion efficiency, 5-23%[4], over the last 25 years. To continue to improve, new design philosophies are emerging to overcome the intrinsic Shockley-Queisser limit on power conversion efficiency defined as $\frac{\text{Total optical power in}}{\text{Harvested power out}}$ of 33%[5]. The major limiting factor in the harvesting process is the thermalisation of energy absorbed above the band gap. As a result, methods to sensitise silicon cells to improve the range of absorbed wavelengths are being investigated. One possible route for improving light harvesting is the inclusion of a singlet fission active layer on top of a silicon cell[6–8]. Singlet fission converts a spin-0 singlet electron-hole excitation to two spin-1 triplet electron-hole excitations[9,10]. Sharing the energy between two lower energy excitations reduces loss from thermalisation. Calculations suggest the increased light harvesting could lead to a new maximum power conversion efficiency of ~44%[11].

Since including singlet fission materials in solar cells was proposed, there have been many studies into the process. The majority of these studies have revolved around two polyacenes materials, tetracene[12–14] and pentacene[15–17]. Using these molecules singlet fission has been successfully incorporated in a device with over a 100% external quantum efficiency ($\frac{\text{no. charge carriers collected}}{\text{no. incident photons}}$)[8].

Despite this success there are still significant gaps in the knowledge base, which require further investigation.

The first issue concerns the harvesting of the triplets created via singlet fission. As the triplets are produced on adjacent molecules, and in an overall singlet character triplet-pair state, recombination back to the parent singlet state can be efficient[14,18,19]. Interestingly, recently it was reported that despite this recombination channel, both triplets can be harvested sequentially without recombination[20]. However, the mechanism that allows sequential transfer of the triplets without recombination is unclear[20]. Another possibility for triplet harvesting is 2-electron transfer which could potentially allow both triplets of the pair to be extracted simultaneously[21]. Regardless of the progress made in harvesting triplets, a more fundamental issue in the field is the lack of ideal singlet fission materials.

As we stated above, singlet fission studies have mostly concerned only two molecules. While pentacene undergoes fast and efficient singlet fission (~80fs, 200%)[17], the yield and rate vary over orders of magnitude between different sample structures[22]. As such, we must widen the range of material systems being investigated. In recent years alternative systems have begun to be studied including carotenoid aggregates[23–26], polyene-like polymers[27–30] and the zethrenes[31]. Throughout these systems a common thread is the importance of the intermediate triplet-pair states. New techniques such as electron paramagnetic resonance have allowed for a clearer picture than has ever been attainable before. The prominence and importance of this topic is evidenced by 5 review articles, all discussing triplet-pair character states in singlet fission materials, which have been published in the last year[32–36]. Herein we investigate these triplet-pair states in three molecular systems.

We start by discussing the background required to understand the studies in Chapter 4, 5 and 6. Chapter 2 addresses organic semiconductors, their interaction with light and eventually the singlet fission process. In Chapter 3 we discuss the sample preparation and measurement techniques used

throughout the remaining chapters. As each chapter addresses different molecular systems and sample structures, we postpone discussion of chapter-specific techniques and molecules till the individual chapters.

In Chapter 4 we investigate how triplet-pair states behave in a microcavity in which a photon trapped within the cavity strong-couples to the singlet exciton. In order to probe the behaviour of these states, we measure delayed (triplet-fed) polariton emission from the microcavities. In so-doing, we study the properties and dynamics of (TT) states in a variety of small-molecule systems (TIPS-tetracene, DPA: PtPOEP, DPP, INDP). We demonstrate that long-lived high-spin states can populate the lower polariton branch, resulting in long-lived delayed emission.

In Chapter 5 we investigate a series of oligomers (oligo(thienylene-vinylene)) originally synthesised for solar cell applications. There is continued debate as to the electronic nature of these molecules[27,37,38], including to which class of molecules they belong. In the dimer it has been shown that intersystem crossing produces triplets, with no sign of 'dark' symmetry forbidden states. Meanwhile for the polymer, it has been shown that singlet fission occurs with clear evidence of the symmetry forbidden $2A_g^-$ state of polyenes. We investigate a series of oligomers from dimer to octamer forming a conjugation length dependence that bridges the gap between the dimer and the polymer. We confirm that the OTVs can be described as polyenes before investigating the conjugation length dependence of triplet production.

In Chapter 6 we turn to carotenoids, a polyene molecular class, known for their photo-protective role in photosynthetic proteins. While the polyacenes are well studied, relatively few studies have investigated singlet fission in these molecules. We start by addressing a long-standing debate[32,36,39] in the literature surrounding which states are relevant to the photophysics of carotenoids. We then confirm the triplet-pair nature of the $2A_g^-$ state, before moving to carotenoid aggregates bound to synthetic proteins to establish the effect of protein environment and intramolecular structure on the singlet fission process.

Finally, in Chapter 7 we discuss the current nomenclature surrounding triplet-pair states and the singlet fission process. We summarise the contribution this thesis gives to this debate before concluding with some possible avenues for further research.

2. Theory and Background

2.1 π-Conjugated Organic Molecules

The topic of this chapter is π-conjugated molecules, also known as organic semiconductors, and their interaction with light. Organic semiconductors are defined as molecules containing carbon, that absorb light in the visible wavelength region[40]. We start the chapter with molecular orbitals and their interaction with light. We then move to the experimental and theoretical background of singlet fission. The aim is to build all the necessary knowledge to understand the investigations into singlet fission in Chapters 4,5 and 6. A full treatment of the underlying concepts within this chapter is out of the scope of this text but for those interested we recommend Barford for a physics viewpoint and Turro for a chemistry representation[41,42].

2.1.1 Molecular Orbitals

In the following section we wish to build a picture of the molecular orbitals within a conjugated organic semiconductor. We start by considering the electron configurations of a single carbon atom[40]. The carbon atom has 6 electrons associated with s and p atomic orbitals[40]. In orbital notation; $1s^2 2s^2 2p_x^1 2p_y^1 2p_z^0$ meaning 2 electrons in the 1s and 2s orbitals, 1 electron in the p_x and p_y and none in the p_z[40]. If an electron is promoted from the 2_s to the p_z orbital, there are four unpaired electrons available to form covalent bonds[40]. For carbon the binding energy gained for creating these bonds is larger than the energy required to populate the p_z orbital[40]. Thus, when a carbon atom is incorporated into a molecule the occupation of the atomic orbitals changes to $1s^2 2s^1 2p_x^1 2p_y^1 2p_z^1$, minimizing the energy of the system[40–42].

When another atom such as hydrogen or carbon binds with the carbon atom the 2s orbital hybridizes with the p orbitals forming one of three hybridisation states: 2sp (as in linear molecules, such as acetylene), $2sp^2$ (as in planar molecules, such as those discussed here) or $2sp^3$ (as in 3D molecules, such as methane)[42]. It should be noted that the superscript corresponds to the number of

p orbitals involved in the hybridisation with the 2s orbital, not the number of electrons[40]. Here, we are interested in $2sp^2$ hybridisation as is found in the molecules studied within this thesis. In the $2sp^2$ orbital the three constituent orbitals separate by 120 degrees due to electrostatic repulsion with the remaining orbital (p_z) being perpendicular to the molecular plane[40] (Figure 2.1a). To illustrate the result of $2sp^2$ hybridisation we consider a simple molecule, butadiene, which is formed of 4 carbon atoms and 6 hydrogen atoms, shown in Figure 2.1b[40–42].
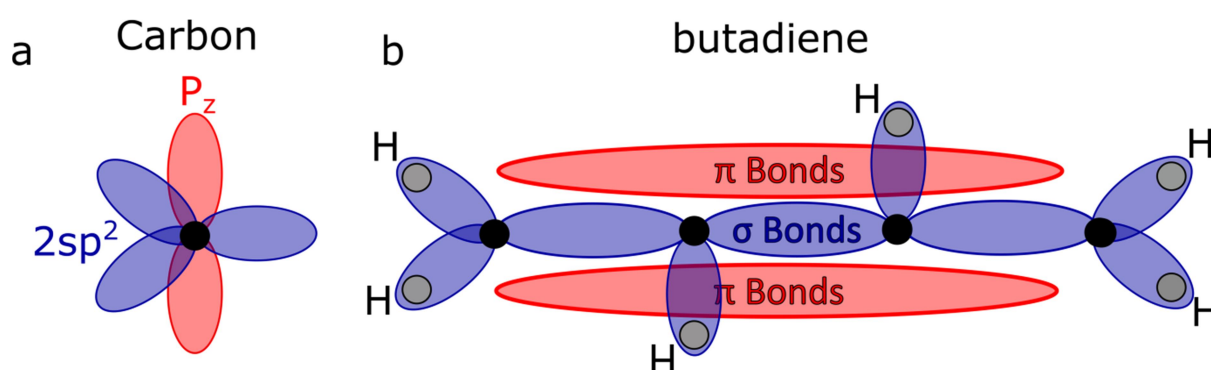
Figure 2.1: Atomic orbitals of carbon and the molecular orbitals of butadiene. (a) $2sp^2$ hybridized carbon atom, for each orbital only the large lobe is shown for simplicity. (b) Black dots are carbon atoms while grey dots represent hydrogen atoms (H). The molecular orbtials/bonds are presented by ovals between the dots. Blue shading represents σ orbitals which are in the plane of the molecule, while red shading represents π orbitals that are perpendicular to the molecule (out of/into the page), and delocalised over the whole carbon chain.

When the carbon/hydrogen atoms of butadiene are brought into close approach the atomic orbitals of the individual atoms combine to form new shared orbitals called molecular orbitals. In order to understand the newly formed molecular orbitals we employ the approximation that they can be described by a linear combination of the atomic orbitals ($\psi_1 \pm \psi_2$)[40–42] (LCAO-method). The addition of the atomic orbitals can be seen as a constructive interference of the charge densities of the atomic orbitals, while the subtraction is a destructive interference[40]. For addition of the orbitals, the increased electron density screens the coulomb repulsion between the positive nuclei, stabilising the system and forming bonds (bonding orbitals). For subtraction, the electron density between the atoms is reduced, increasing coulomb repulsion between the positive nuclei[40,41]. The stronger

coulomb repulsion destabilises the system, weakening the inter-atom bonds, hence the name anti-bonding orbitals. In a simple view, the energy difference in the system between population of the bonding or anti-bonding orbitals is proportional to the overlap of the two atomic orbitals. This leads to a profound effect when we consider the different combinations of atomic orbitals in butadiene[40–42].

First, we consider the 3 $2sp^2$ hybrid orbitals of the carbon atoms which form molecular orbitals with s orbital-like electron density, in a cylinder around the molecular axis. As the charge density is found in between the carbon atoms, an addition of the atomic orbitals leads to a large stabilisation energy. Thus, the so called σ orbitals are responsible for the strong bonds that hold the molecule together. In symmetry with the bonding orbitals, the anti-bonding σ* orbitals cause a large de-stabilisation of the molecular framework. To populate the anti-bonding orbital, and break the strong σ bonds a large perturbation is required on the order of 10eV[40–42].

With the $2sp^2$ orbitals paired, only the unpaired electrons in the p_z orbitals of each carbon atom remain. The electrons in the p_z orbitals delocalise, no longer belonging to a single carbon atom. Instead the electrons delocalise over n carbon atoms, which is referred to as the effective conjugation length. The delocalised electrons are known as π orbitals (or π-conjugation) and have p orbital-like electron density only above and below the molecular axis[40]. Formation of π bonds hinders rotation around the molecular axis causing the molecule to be more planar. The charge density overlap for π bonds is low and they contribute relatively little to the bonding of the carbon atoms. This results in only a small perturbation being required to change the occupation of these orbitals (2-3eV) [40–42].

With the orbitals identified we now turn to the occupation of these orbitals, still in the butadiene molecule. While the method of combining the atomic orbitals yields a good approximation for understanding chemical bonding, for large molecules, calculations become computationally demanding. To reduce the complexity of calculations, while retaining accuracy, we treat the π and σ

orbitals separately; this is known as the Hückel approximation[40]. The convenient separation of energy scales for π and σ bonds makes this and other π-electron models accurate approximations. As with the π-electron models discussed later, we now omit σ orbitals from our state diagrams[40–42].

In Figure 2.2 we show a schematic of the chemical structure of butadiene. Butadiene is comprised of 4 carbon atoms and so has 4 electrons that delocalise over the carbon chain. In a simple view the conjugation can be considered a sum of the individual π orbitals, with one orbital and electron per carbon atom (Figure 2.2b). The total energy of these orbitals is proportional to the spatial second derivative of the molecular wavefunction, thus the energy ordering of the orbitals is proportional to the number of nodes in the wavefunction[42]. Here a node refers to a point in the chain where the spatial wavefunction changes phase from positive to negative[40,41]. The number of nodes also changes the wavefunction's parity, that being an even or odd number of nodes. An even or odd number of nodes leads to a symmetric or antisymmetric wave function respectively[40,41]. Symmetry has a profound effect when light is introduced to the system, discussed later in Section 2.2.

With the relevant orbitals placed in energy order we now occupy these orbitals with the 4 delocalised π electrons. The Aufbau principle states that in the ground state, low energy orbitals must be filled before the high energy orbitals are occupied[41]. Each orbital can contain two paired electrons, meaning the two lowest energy orbitals are populated (bonding) leaving the anti-bonding orbitals (higher energy) empty. As stated above, for π orbitals the charge overlap is low and so only a small perturbation is required to promote an electron from the highest occupied molecular orbital (HOMO), to the lowest unoccupied molecular orbital (LUMO). As these orbitals are responsible for the light absorption characteristics of the molecule, they are known as frontier orbitals[40–42]. We will return to the interaction of molecular systems with light in Section 2.2.
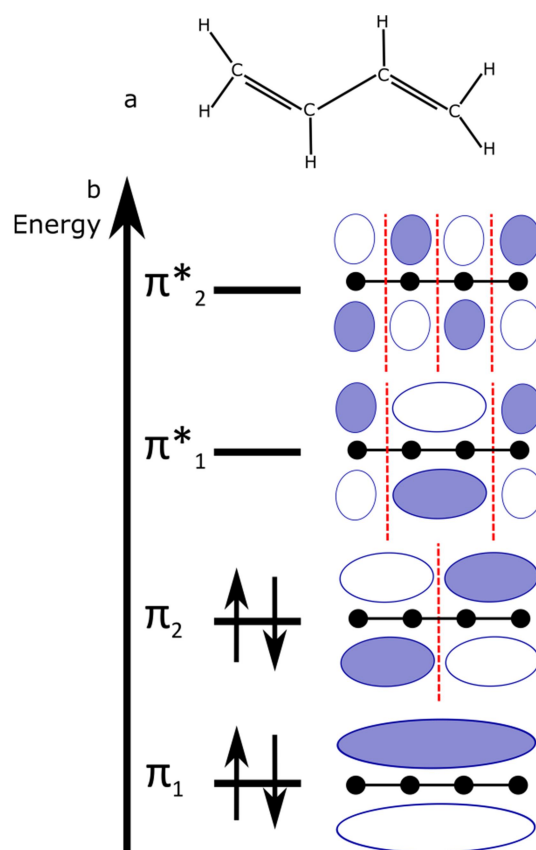
Figure 2.2: Atomic orbitals of butadiene. (a) Chemical structure of butadiene, H = hydrogen, C = carbon, Black lines = bonds (b) Approximate relative energy levels of the π orbitals. To the right are representations of the orbital wavefunction of the π-electrons for each π orbital. Red dotted lines indicate a node in the wave functon. As the energy is increased so is the number of nodes causing an alternation in symmetry. The shaded and unshaded orbitals represent the phase of the wavefunction with a switch from positive to negative for each node.

It is important to make the distinction between the orbitals discussed above and states, which we probe experimentally[40–42]. In order to describe the full energy states of a molecule we must include the kinetic energy of the π electrons, along with the potential energy from electron-electron interactions, electron-nuclear interactions, and nuclear-nuclear interactions. To solve this analytically is almost impossible for all but the simplest one electron systems. As such to build states, researchers construct one-electron wavefunctions, taking account of the other factors as a collective background field. However, this omits electron-electron interactions and in some systems can cause large deviations from experimental observations. We will see later the effect electron-electron interactions have on highly electron correlated molecules such as polyenes in Section 2.4.5[40].

2.1.2 Excitons

There are several conventions on how to describe the change in orbital occupation however the most common is the exciton[40]. In a simplistic view, when the electron is promoted from the HOMO to the LUMO, a hole is left were the electron once was[40]. A hole is thought of as having the same characteristics as an electron but with a positive charge[40,41]. This creates a coulombic attraction between the electron and hole, the two together make a neutral quasi-particle termed an exciton[40,41]. To fully describe an exciton in a medium we must include two components of the wavefunction[42,43]. In short, the exciton is described by two length scales and associated wavefunctions with the total wavefunction equal to $\psi_n(r)\psi_K(R)$. $\psi_K(R)$ represents the centre of mass wavefunction which is related to the delocalisation of the exciton. Delocalisation can be thought of as the distance over which you may find the exciton within a lattice of sites, and so is related to the probability density of finding the particle on a lattice site. The second term, $\psi_n(r)$, is the electron-hole separation wavefunction which describes the relative motion and distance between the electron and hole of the exciton. To illustrate this model we consider two generalised cases of high dielectric constant (inorganic materials) and low dielectric constant (organics materials)[42].

The dielectric constant represents the ratio of the permittivity of a medium and the permittivity of free space. As a result, a large dielectric constant leads to a smaller electric flux for a given charge than a small dielectric constant[40]. For inorganic molecules their large dielectric constants (ε_r~10) screen the coulomb attraction between the electron and hole. Thus, there is a relatively small binding energy between the electron and hole on the order of 10s of meV[40]. In this regime, coulomb interactions between molecules allow electrons and holes to move freely between sites. As such, excitation entails a transition of an electron from the valence band, to the conduction band and is not associated with any individual site/atom. However, at low temperature and in some inorganic materials exciting below the valence to conduction band transition yields an electron-hole

excitation. The electron and hole are loosely bound but sit far apart (large exciton radius) and move

freely in the material[40], these excitons are termed Wannier-Mott excitons (Shown in Figure 2.3a).

In organic materials the dielectric constants are low (ε_r~2-4), leading to a large coulombic attraction

between the electron and hole. The large coulombic attraction leads to large binding energies from

0.1-1eV[40,42]. Additionally, intermolecular interactions between sites are through weak van der waals

forces not coulombic force (discussed further in Section 2.3). The higher binding energies and lower

intermolecular interactions lead to a small exciton radius with electron hole separation on the scale

of one molecule. However, despite the small exciton radius, it is possible for Frenkel excitons to

delocalise with delocalisation lengths on the scale of 10 sites in some molecules[44]. This type of

exciton is called a Frenkel exciton, shown in Figure 2.3b[40,42].

A third type of exciton commonly encountered is also localised but has the electron and hole on

separate molecules. These are known as charge-transfer excitons, shown in Figure 2.3c. Throughout

this thesis we use the term excitons when discussing organic molecules. For simplicity, unless

explicitly named, we are referring to Frenkel excitons[40,42].
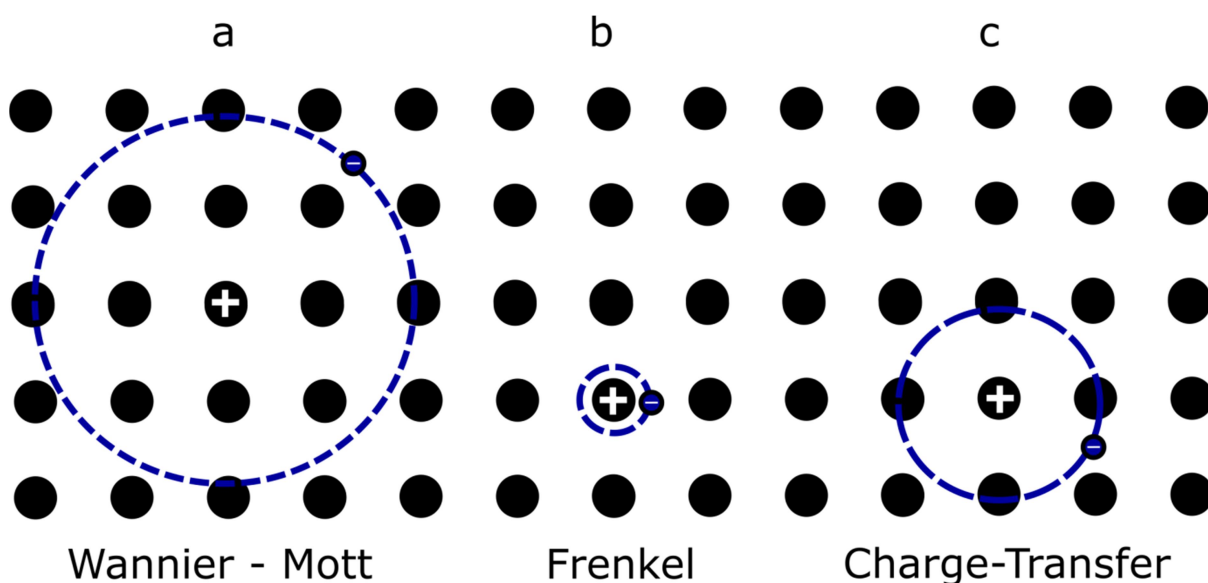
Figure 2.3: Toy model of exciton excitations. Cartoon depiction of the three types of exciton discussed in the text. Each black point represents a site. (a) Wannier-Mott exciton with electron and hole separated by many sites. (b) Frenkel exciton with electron hole separation on the order of a single molecule (c) Charge-transfer Frenkel exciton with the electron and hole sitting on adjacent molecules.

2.1.3 Spin States

A final consideration for this model is the spin state of the excitation. As the excitation is fundamentally a two particle state, interactions between the spins of these particles must be taken into account, known as exchange coupling[40,41]. The spins of these two particles can either be aligned anti-parallel or parallel giving singlet and triplet spin states respectively. There are several possible combinations that yield these states defined by their M_s value, which is the projection of their absolute spin (S) in the Z axis[41]. When the spins are aligned anti-parallel there is a single combination with overall spin S=0, M_s = 0, labelled a singlet (multiplicity of one) [40,41]. For parallel there are three possible combinations yielding an overall spin of 1 with Ms = 1, 0, -1, labelled triplets (multiplicity of three) [40,41]. These are represented in a vector diagram form in Figure 2.4. While the vector diagram is instructive, these are not eigenstates of the spin Hamiltonian. Instead the spin angular momentum operator $\hat{S}^2 = (\hat{S}_1 + \hat{S}_2)^2$ must be diagonalised resulting in the wavefunctions shown below, Equations 2.1-2.4 ($\psi_{S,Ms}$).

$$\psi_{0,0} = |S_0\rangle = \frac{1}{\sqrt{2\pi}}(\uparrow_1\downarrow_2 - \downarrow_1\uparrow_2) \tag{2.1}$$

$$\psi_{1,1} = |T_1\rangle = (\uparrow_1\uparrow_2) \tag{2.2}$$

$$\psi_{1,0} = |T_0\rangle = \frac{1}{\sqrt{2\pi}}(\uparrow_1\downarrow_2 + \downarrow_1\uparrow_2) \tag{2.3}$$

$$\psi_{1,-1} = |T_{-1}\rangle = (\downarrow_1\downarrow_2) \tag{2.4}$$
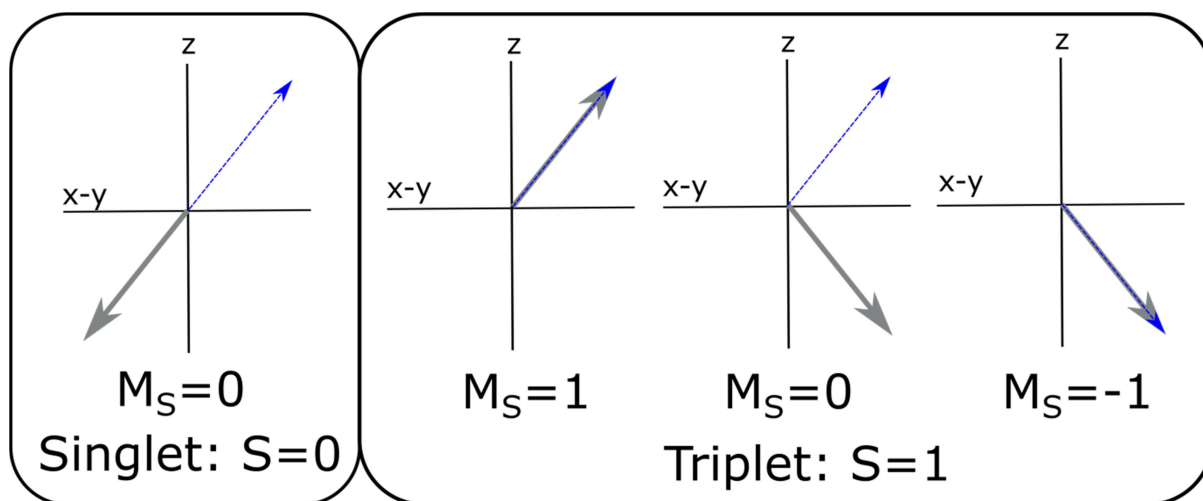
Figure 2.4: Vector diagram representation of 2 electron spin states. The vertical axis represents the chosen Z axis upon which the measured spin or Ms is projected. The horizontal axis represents the total spin taking on the value of either 0 for singlet or 1 for triplets. The electrons are differentiated by colour and solid versus dashed for clarity.

The Pauli exclusion principle states that the overall wavefunction must be anti-symmetric upon exchange of electrons[40,41]. The total wavefunction is the product of the spin component (relative orientation of the spins) and the spatial component (relative position of the spins). In the case of singlet states, the spin component is antisymmetric meaning the spatial component must be symmetric[40,41]. For the triplet configuration the spin component is symmetric so the spatial component must be antisymmetric[40,41]. Described in another way; the electrons are able to approach each other in the singlet as they have opposite spin and so can be distinguished, the opposite is true for the triplet state[40,41]. As singlet states are able to approach each other the electron-electron repulsion is large, whereas for triplets they are unable to approach and as such will have much lower electrostatic repulsion[40–42].

The reduced repulsion leads to triplet states having lower energy than singlet states constructed from the same orbital configurations[40,41]. The difference between the singlet and triplet state energies is given in Equation 2.5, where e is the charge of the electron, r_{12} is the distance between the electrons, π_n is the orbital of the nth π electron and E_K is the exchange energy (Equation 2.5).

$$\Delta E_{ST} = \frac{2e}{r_{12}} \langle \pi_1 \pi_2 | \pi_2 \pi_1 \rangle = 2E_K \qquad (2.5)$$

From inspection of the equation we can see that the exchange energy depends on the overlap of the occupied orbitals[40,41]. For Wannier-Mott excitons, their large electron-hole separation causes the relative orientation of the spins to be ill-defined[40,45]. However in organics, Frenkel excitons are tightly bound and have significant exchange interaction[41] separating the spin states in energy[40–42].

For singlet excitons dipole coupled to the ground state a coulombic dipole-dipole coupling between the neighbouring molecules, allows the energy to transfer via a *virtual* photon. No absorption or emission event occurs during the energy transfer however the efficiency of the process is related to the overlap of the absorption and emission spectrum. The probability of energy transfer occurring is also related to the dipole moments of these transitions. This energy transfer mechanism, known as Förster transfer, can occur relatively fast, and over distances of up to ~3nm.

A second mechanism of energy transfer is known as Dexter energy transfer. The rate of Dexter transfer is still related to the spectral overlap of the absorption and emission spectrum of the two molecules, however here there is no dependence on transition dipole moment. The lack of dependence on dipole moment originates in the different physical mechanisms of the two transfer processes. In Dexter transfer there is no virtual photon and instead the transfer requires a direct transfer of electron and hole. As a result, this process requires wavefunction overlap (exchange interaction) to occur which lowers its effective radius to ~1nm. While singlet states can transfer via either mechanism, triplets are not dipole-coupled to the ground state and so can only hop via Dexter transfer[40–42,46]. As triplet excitons are only able to transfer by this mechanism, triplet excitons diffuse much slower than singlet excitons[40–42,46]. Having described a general background to excitons in conjugated organic molecules, we will now move to the interaction of molecules with external perturbations (light).

2.2 Optical Excitation of Organic Semiconductors

The interaction of light with the electronic dipoles of a material can be described by applying first-order perturbation theory to the time-dependent Hamiltonian[42]. Applying perturbation theory yields Fermi's golden rule for state transitions shown below in Equation 2.6. The rate of transitions (k) between the initial ψ_i and final state ψ_f depends on the density of states in ψ_f (ρ) and the perturbation to the Hamiltonian $\hat{H}'$. We continue from here and insert the perturbation which contains the transition dipole moment (μ) and the perturbing electric field (E_0) respectively.

$$k_{if} \propto \frac{2\pi}{\hbar}\ |\langle\psi_f|\mu\cdot\hat{e}E_0|\psi_i\rangle|^2\rho \tag{2.6}$$

Fermi's golden rule shows us that the transition rate depends on the density of available states in the final state and the perturbation of the applied electromagnetic field. However, the most important factor is the transition dipole moment ($\hat{\mu}$) which couples the initial and final states. Evaluating the matrix elements of the transition dipole moment is extremely complex for almost all systems however a qualitative understanding can shed light on the spectroscopic properties of a system.

The first simplification, the Born-Oppenheimer approximation, states that for visible light absorption, the nuclear and electron motion can be separated. Due to the large mass difference between electrons and nuclei, the absorption of visible frequencies causes an instantaneous response in the electrons, with no change in the nuclear component. A limitation of the Born-Oppenheimer approximation is that within the approximation two potential energy surfaces can never cross, meaning transitions between electronic states cannot occur due to nuclear motion alone[40,41]. As we will see later, transitions of this type are possible, leading to a break-down of the Born-Oppenheimer approximation in these situations[40,41].

In addition to applying the Born-Oppenheimer approximation (separation of nuclear and electronic components), we can also separate out the spin component. As the oscillating electric field does not

affect the electron spins, only the relatively small magnetic field does, the effect is negligible. These considerations allow us split the wavefunction (ψ_n) into the electronic (ψ_{el}), vibrational (ψ_{vib}), and spin (ψ_{spin}) components (Equation 2.7)[47]. In equations below the rotational component (ψ_{rot}) has been neglected, due to the small energies of rotational modes which have little effect on the experimental observables discussed here[47].

$$\psi_n = \psi_{el}\psi_{vib}\psi_{spin} \tag{2.7}$$

Separation of the wavefunction into vibrational, spin, and electronic components allows us to rewrite an approximate expression for the transition dipole moment, shown in Equation 2.8[48]. The formulation shows that the transition dipole moment relies on three factors, the spin component, the vibrational component and the electronic component. As we will see in the following sections these terms have a profound effect on the available transitions and their spectroscopic properties. As such an understanding of these terms is required for the analysis of spectroscopic measurements in Chapters 4, 5 and 6.

$$\hat{\mu}_{i-f} = \langle\psi_j|\mu\cdot\hat{e}|\psi_i\rangle \approx |\langle\psi_{el,j}|\mu\cdot\hat{e}|\psi_{el,i}\rangle| \; |\langle\psi_{vib,j}|\psi_{vib,i}\rangle| \; |\langle\psi_{spin,j}|\psi_{spin,i}\rangle| \tag{2.8}$$

2.2.1 The Electronic Component

The electronic component ($|\langle\psi_{el,f}|\hat{\mu}|\psi_{el,i}\rangle|^2$) governs the spatial symmetry requirements for state transitions. If the value of this component is zero, the transition is considered dipole-forbidden and formally cannot occur. However, if the states are of opposite spatial symmetry the electronic component is non-zero and the transition can occur. To understand the origin of this spatial symmetry requirement we return to considering the spatial symmetry of the molecular wavefunction[40,42].

When constructing molecular orbitals in Section 2.1.1, we saw an alternation of symmetry as the orbitals increased in energy[40,41]. We have now moved to states, however in the limit of no electron-

electron interactions the symmetry considerations are roughly preserved[40,42]. However, we now have to consider a larger range of possible symmetries represented by a point group[40,41]. To illustrate we choose polyenes as an example, starting with their point group, C_{2h}.

In the C_{2h} point group we have to consider two forms of symmetry, rotation and inversion[40–42]. Molecular states that are symmetric or antisymmetric about a 180 degree rotation of the molecular plane are labelled A and B respectively. In addition, upon horizontal spatial inversion, states that are symmetric and antisymmetric are labelled g (gerade) and u (ungerade)[40–42]. It can be shown that some of these representations are equivalent leaving either A_g or B_u state symmetries as the irreducible representations[42]. The eigenvalues upon application of a spatial inversion operator to the A_g and B_u states yields a value of +1 and -1 respectively.

Molecules with a centre of inversion are known to have a ground state of A_g symmetry[42]. For the majority of molecules the symmetry alternates in the ladder of states as was the case for the molecular orbitals above[40]. This becomes important when we consider that the dipole operator is odd under spatial inversion[42]. In Equation 2.9 we apply the inversion operator to the transition dipole moment yielding: $\hat{\imath}^{\dagger}\hat{\mu}_{i-f}\hat{\imath} = -\hat{\mu}_{i-f}$. Furthermore, $\hat{\imath}|j\rangle = i_j|j\rangle$ where i_j is the spatial symmetry eigenvalue for the j state, a similar formulation can be made for the initial state i. By applying these relationships, we arrive at the result in Equation 2.9. In quantum mechanics parity conservation requires the parity to be equal before and after the transition[42]. By inspection we can see that this conversation law will only be held, and as such the transition dipole moment will only be non-zero, for $i_i i_j = -1$ (Equation 2.9). In order for $i_i i_j = -1$ we require a change of symmetry between the initial and final states[42].

$$\hat{\mu}_{i-f} = \langle i|\hat{\mu}_{i-f}|j\rangle = \langle i|\hat{\imath}^{\dagger}\hat{\mu}_{i-f}\hat{\imath}^{\dagger}\hat{\imath}|j\rangle = -i_i i_f \langle i|\hat{\mu}_{i-f}|j\rangle \tag{2.9}$$

While the above symmetry groups are enough when neglecting electron-electron interactions, for real polyene molecules it is insufficient. When considering electron correlations, a third symmetry known as electron-hole symmetry or Pariser alternancy symmetry is required. There are two

requirements for a material to possess electron-hole symmetry. The first is that the material must be constructed of two interpenetrating sub-lattices with nearest neighbour hybridization. For polyenes the two sub-lattices represent the weak and strong bonds which alternate and hybridize into a conjugated backbone. The weak bonds are longer (single bonds) as a result, while the strong are shorter (double bonds). This bond length alternation leads to a repeat unit of single and double bond pairs known as a dimerised ground state. These materials are sometimes known as alternant materials (discussed further in Section 2.4.5).

The second criterion for electron-hole symmetry is that all sites in the chain are equivalent. For a finite chain, electrons occupying sites at the centre of the chain feel a stronger attractive potential due to the nuclei than electrons occupying sites at the edge of the chain. Additionally, the electron-electron repulsion felt at the centre of the chain is larger than at the edge of the chain. When these two competing forces cancel all sites feel the same coulomb potentials and become equivalent[42]. In the majority of literature electron-hole symmetry is indicated with a + (non-covalent) or a − (covalent) if they are symmetric or anti-symmetric respectively upon exchange of electrons and holes[49]. It should be noted that while this is an exact symmetry in models of conjugated systems, in real molecules this is only an approximate symmetry[42].

Non-covalent or sometimes named ionic states are generally the first optically allowed state carrying high oscillator strength. Inversely, covalent states are generally forbidden from the ground state and have energies heavily reliant on electron correlations. For polyenes (highly electron correlated) the lowest energy excited covalent state sits below the lowest energy ionic state (discussed further in Section 2.4.5). By including particle-hole symmetry and C_{2h} group symmetry we have a picture of the possible symmetries of states for polyenes, summarized in Table 2.1.

Table 2.1: Irreducible state symmetries for the polyene class of organic molecules[42].

Representation	Rotation (A or B)	Inversion (g or u)	Particle Hole (+ or -)
A_g^-	+1	+1	-1
A_g^+	+1	+1	+1
B_u^-	-1	-1	-1
B_u^+	-1	-1	+1

2.2.2 The Vibrational Component

The vibrational component of the transition dipole moment ($|\langle \psi_{vib,f}|\psi_{vib,i}\rangle|^2$) can be thought to dictate the shape of the absorption and emission spectrum[40]. In addition to the electronic states there are also many vibrational modes active within a molecule. As described above, the Born-Oppenheimer approximation states that nuclear movement (vibrations) can be considered separate from the electronic change. The electrons are modelled as moving in a stabilisation force produced by the static nuclear configuration. Afterwards the nuclear movement occurs in a potential defined by the electron configuration[41]. Nuclear movement does not change the electronic energy and instead changes the potential energy of the state as the positive nuclei move in the negative potential[41]. By calculating the potential energy at each of these nuclear configurations it is possible to build up a potential energy surface (energy against nuclear configuration (Q)) [41]. The potential energy surface picture allows an intuitive representation of nuclear motion, as vibrations create cyclical movement up and down the potential energy surface akin to a harmonic oscillator[40,41].

However, an energy versus Q plot is only an approximation. In real molecules many vibrations contribute to the spectra, each with their own set of Q coordinates. As such, when constructing a potential energy surface diagram, we must choose a vibration or set of vibrations termed the effective vibrational modes, to restrict the multi-dimensional plot, to a 2D plane. In most molecules

this is a large energy mode such as the carbon-carbon stretching modes ($\sim$2000cm^{-1}). While this approximation is not technically accurate for real molecules, it allows for a relatively simple analysis of the spectra of real molecules. As a result, in the proceeding discussion we are applying the approximation of a single vibrational mode[40,41].

The high energy of the effective vibrational mode implies that at room temperature only the zeroth vibrational level will be populated in the initial state. Furthermore, the Kasha-Vavilov rule states that emission occurs from the lowest energy excited state and has efficiency independent of excitation wavelength[40,41]. This enforces that emission occurs from the zeroth vibrational level of the initial state. However, it is possible for transitions to occur to all levels of the final state, resulting in the highest energy emission peak and the lowest energy absorption peak being equivalent in energy[40–42]. The series of peaks formed from the transitions to each vibrational level is known as a Franck-Condon progression[40,41]. The intensity of these peaks is governed by the Franck-Condon factor, which is the square of the Franck-Condon overlap integral shown in Equation 2.12. The Franck-Condon factor gives a measure of the overlap of vibrational levels as a function of nuclear coordinate, Q, with a larger intensity for greater overlap[40]. If a molecule is stiff, when an electron is excited, and the negative electronic distribution changes, the geometric reorganisation is minimal. This leads to a small change in Q between the excited and ground state geometries. As a result the minima of the excited and ground state potential energy surfaces are at similar Q values[41]. States of this kind are known as 'nested' states (Figure 2.5). For nested states the overlap between vibrational wavefunctions is largest for the 0-0 transition, that being between the ground vibrational level of both the initial and final state[40]. As such the 0-0 peak is the most intense, with a drop off moving to the 0-1 and 0-2 peaks.
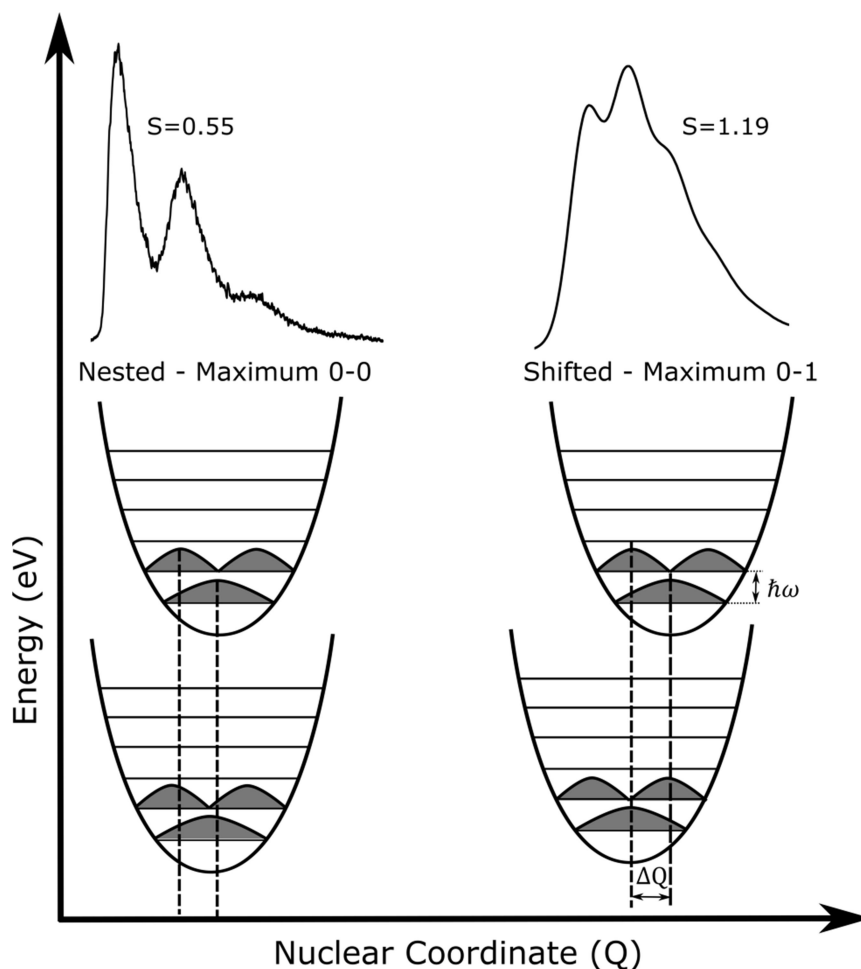
Figure 2.5: Potential energy surface diagrams for nested and shifted states. In both diagrams the shaded sections correspond to the wavefunction, and S is the Huang-Rhys Factor. On the left, the potential energy surfaces of the initial and final state are nested, meaning there is a small shift between the surface minima. In this case the ground vibrational levels of each state have the largest overlap causing the 0-0 peak to be the largest. On the right is the opposite case where the states are shifted in Q, causing large overlap between the ground vibrational level in the initial state and the first excited level of the final. This leads to the largest peak being the 0-1 transition as shown in the spectrum.

If the molecule is flexible, large changes in Q are possible and the state minima can become displaced. Now in Figure 2.5 the first vibrational level (0-1 peak) overlaps well with the minima of the ground state potential energy surface, making it the largest peak[40,41]. The influence the Franck-Condon factor has on peak intensities is why the vibrational component is thought to dictate the absorption and emission spectral shape[40]. By analysing the overlap integral, it can be shown that the peak intensity can be related only to the Huang-Rhys parameter (S), shown in Equation 2.10.

$$I_{0-n} = |\langle \psi_{n,f} | \psi_{0,i} \rangle|^2 = \frac{S^n e^{-S}}{n!} \qquad (2.10)$$

The Huang-Rhys parameter (S) is the ratio of the energy absorbed above the state minima (E_{rel}) and the active vibrational mode ($\hbar\omega$). As such, it is proportional to the displacement between the minima of the ground and excited state potential energy surfaces (ΔQ).

$$S = \frac{E_{rel}}{\hbar\omega} \tag{2.11}$$

$$S \propto \Delta Q^2 \tag{2.12}$$

Before moving on we wish to take a moment to consider the actual measured spectral shape. The above discussion implies that the vibrational component dictates the spectral shape entirely. However, while vibrational overlap dictates the intensity and position of the absorption peaks, the above discussion suggests there should be lines of intensity at each of the vibrational peaks. In real systems this is not what we see[40,41], instead we observe broad peaks that overlap as shown in Figure 2.5. The experimentally measured broadening comes in two categories homogeneous and inhomogeneous.

Homogeneous broadening occurs when all emitters are affected equally. An example of this comes from the uncertainty principle which gives an uncertainty in the energy of a state dependent on its lifetime[50]. As a result the linewidths with only homogeneous broadening are sometimes referred to as "natural linewidths" and take on a lorentzian shape[50]. The second, inhomogeneous broadening, occurs when each emitter is affected differently. Inhomogeneous broadening comes from a combination of disorder and interaction of the molecules with the surrounding medium [40,41]. As an example, we consider a single chromophore in a solvent solution. The electronic dipole of a chromophore induces an electric dipole in the surrounding solvent molecules. The more readily the induced dipoles align with the dipoles of the molecules, the higher its polarizability (α) and hence the larger the induced dipole ($\mu_{induced} = \alpha E$) [41]. It is possible to show that the interaction energy (V) of dipole-dipole coupling between the solvent and molecule under test is proportional to the expression shown below (Equation 2.13).

$$V \propto \frac{\mu^2\alpha}{r^6} \tag{2.13}$$

The interaction energy depends on three quantities, the strength of the transition dipole moment, the polarizability of the solvent and the distance between the interacting dipoles[41]. The dipole-dipole interactions stabilise the state relative to free molecules lowering state energies. As the dipole in the excited state is large, so is the interaction and as such the state is stabilised significantly. In the ground state the only dipoles are small oscillating dipoles caused by zero-point fluctuations. As such the stabilisation of the ground state is much smaller than it is in the excited state. This produces a red-shift in the transitions between the ground and excited states known as solvation. Taking into account disorder we see that this shift will be different for each individual chromophore in solution (different r)[41]. Building up these lines of intensity at slightly different energies (summing over all interactions) creates the spectral broadening we see experimentally with a gaussian distribution[41].

2.2.3 Non-Radiative Transitions

Thus far we have only considered radiative transitions, which require the absorption or emission of a photon. However, after absorption of light, transitions between potential energy surfaces by nuclear motion alone is possible. These transitions are important when considering emission dynamics through the Kasha-Vavilov rule[40,41]. The Kasha-Vavilov rule states that emission occurs from the lowest energy excited state and has efficiency independent of excitation wavelength[40,41]. The consequence of this rule is that after excitation to a high lying excited state S_n, non-radiative deactivation to the lowest excited state must occur before emission[40,41]. These non-radiative transitions can be described by a variant of Fermi's golden rule shown in Equation 2.14[40,41].

$$k_{if} = \frac{2\pi}{\hbar}\rho J^2 F \quad , \tag{2.14}$$

where J is the electronic coupling between states, F is the Franck-Condon overlap factor and ρ is once again the density of states in the final state[40,41]. To evaluate the non-radiative transition rate we must account for coupling of many vibrational modes, which quickly becomes unsolvable[40,41]. To simplify the model, we treat the non-radiative transition as a two-step process. The first step is an electronic transition from the initial state to the final state's potential energy surface[40]. Transitions

of this kind are explicitly forbidden by the Born-Oppenheimer approximation as they involve a change in nuclear and electron configurations simultaneously[40,41]. As no energy is lost through emission of a photon, there must be no overall change in energy hence the transitions are horizontal on an Energy-Q plot[40,41]. A transition between electronic states with no change in energy requires population of high-lying vibrational levels within the final state[40,41].

From inspection of Equation 2.14, we can see that the transition rate relies on the electronic coupling of the states as for radiative transitions. The state transition should then follow the same selection rules as the radiative process[40,41]. However as the transition occurs to a high lying vibrational level in the final state it is possible for vibrations to distort the molecular structure and in doing so change the symmetry of the molecule causing the transition to become partially allowed[40,41]. As a result rigidity of the molecule has an effect on the available non-radiative transitions and the non-radiative transition rate[40,41]. This is important when we consider that non-radiative transitions can also occur between the first excited state and the ground state. As a rule of thumb, rigid molecules are able to access a small number of configurations (Q) meaning non-radiative transitions are unlikely, leading to strong emission[40,41]. However, the opposite is true for flexible molecules that are able to achieve the desired geometry for a given non-radiative transition, increasing non-radiative transition rates and creating a competing route for decay to the ground state, reducing emission efficiency[40,41].

Following the initial change of the electronic states, high energy vibrations are populated requiring energy be dissipated to return to the equilibrium of the state's potential energy surface[40,41]. As the density of states is known to increase with energy, the energy spacing between high energy vibrational levels reduces, meaning redistribution of energy between the various vibrational modes can be efficient[41,51]. The process of sharing energy to all vibrations in a molecule is known as intramolecular vibrational redistribution which occurs in 0.1-10ps[41]. Afterwards the energy is dissipated to the environment by emission of phonons[40]. For a solution samples this involves

transfer of energy to the surrounding solvent molecules which become vibrationally excited[40,41].

Transfer to the solvent usually occurs within 10-100ps in the majority of systems[41]. The consequence of these simplifications is the experimentally verified energy gap law for non-radiative transitions (Equation 2.15)[40,41,52].

$$k_{if} \propto e^{\left(-\gamma\frac{\Delta E}{\hbar\omega_M}\right)} \tag{2.15}$$

In this expression γ represents various molecular properties, such as the vibrational coupling and the displacement between the initial and final state potential energy surfaces[52]. ω_M is the highest energy vibrational mode available and ΔE is the energy gap between the initial and final state[40,41,52]. While the energy gap law is relevant for many transitions it relies on approximations and should be used with caution[40,41]. One such approximation is that the transitions occur between nested states (Figure 2.5)[53]. In the shifted case it is possible for the shift to cause an intersection of the potential energy surfaces[41,53]. This point can form a conical intersection which no longer abides by the energy gap law[41,53].

Conical intersections are points where two potential energy surfaces intersect with a linear dependence between energy and nuclear co-ordinate (Q)[41]. A linear dependence creates a cone shape above and below the intersection in a particular nuclear coordinate or group of coordinates (Q_{ci}) hence the name conical intersection[41]. At the point of intersection both states are isoenergetic and at the same position in the given reaction coordinate or set of reaction coordinates (Q) [41]. The point of intersection leads to a breakdown of the Born-Oppenheimer approximation, and coupling becomes non-adiabatic, meaning states are no longer separate and defined[41,54]. A molecule is in a superposition of the two states and no nuclear motion or change in energy is required to transfer population between these states[41,54]. The transition can be viewed as an electronic transition between states with 0eV energy gap[41]. This results in very fast interconversion with the rate limiting factor being the movement down the initial state's potential energy surface to reach the intersection point, depending on specific vibrations known as tuning modes[41,54]. Conical intersections have been

shown to occur in carotenoids both between the S_2-S_1 states experimentally[54,55] and the S_1-S_0 state theoretically[56,57].
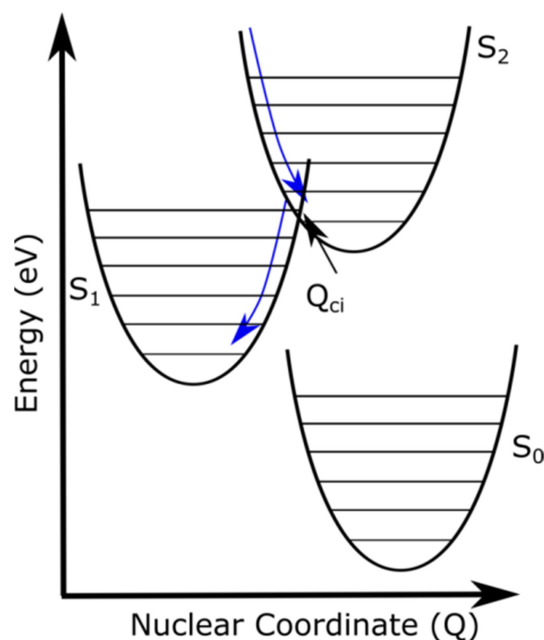
Figure 2.6: Diagram showing the intersection of two potential energy surfaces. The vibrational modes which move the electron to the intersection point are known as the tuning modes while those that form the intersection Q_{ci} are coupling modes. Coupling modes mix the potential energy surfaces and drive the population transfer between the states.

2.2.4 The Spin Component

In a simple model, the spin component of the selection rules, ($|\langle\psi_{spin,j}|\psi_{spin,i}\rangle|^2$) can take a value of either 1 or 0 depending on whether the initial and final states have the same or different spin quantum number respectively[40–42]. As transitions between states of different spin are formally forbidden (value of 0), this forms the selection rule of spin conservation[40–42]. Thus, a direct absorption event from the ground singlet state to the excited triplet state is formally forbidden. However, it has been shown that transitions can occur between triplet and singlet states through a non-radiative process, termed intersystem crossing[58]. In order for the spin component to be non-zero we must induce mixing of the singlet and triplet state wavefunctions[40–42]. We can once again apply Fermi's golden rule to intersystem crossing, now with a new perturbation which mixes the singlet and triplet wavefunctions, shown in Equation 2.16.

$$K_{isc} \approx |\langle \psi_f | \hat{H}_{SO} | \psi_i \rangle|^2 [FCWD] \qquad \text{where } \hat{H}_{SO} = \frac{Z^4}{(n^3(l+1)(l+0.5)l)} \qquad (2.16)$$

Here [FCWD] is a Franck-Condon weighted density of states, ψ_i and ψ_f are the wavefunctions of the initial and final state respectively and n/l represent orbital and angular quantum numbers[40]. This perturbation is known as spin-orbit coupling and as the name suggests it involves the coupling of the spin and orbital angular momenta. The motion of the negatively charged electrons orbiting the positively charged nucleus induces an orbital magnetic dipole moment[41]. This magnetic dipole moment is then able to interact with the intrinsic spin magnetic dipole moment of the electron[40–42]. Total angular momentum is then S+L and a change in the spin state (S) can be compensated by a change in orbital angular momentum (I)[40–42]. From inspection we can see that the rate of non-radiative transfer (intersystem crossing) is related to the strength of the perturbation and the overlap of the initial and final state. As with absorption we require the perturbation to be large enough to transfer population from the initial to the final state. In other words, for efficient intersystem crossing we require either a small singlet-triplet energy gap or a large spin-orbit coupling perturbation.

From inspection of the perturbation (Equation 2.16) we can see that the strength of the spin-orbit coupling goes with atomic number (Z) to the power 4. This result can be rationalised by considering the effect Z has on the molecule[40–42]. First, we consider a simple model of an atom with a single electron orbiting the nucleus. If the electron can approach the nucleus in its orbital, the electron accelerates due to the increased attractive force. As the magnetic dipole moment is proportional to the electron's velocity, for a larger Z there is a larger attractive force and the electron has a larger magnetic dipole moment[41]. The coupling between the spin and angular momenta is related to the magnitude of the dipoles, increasing the spin-orbit coupling term. As such, for larger Z the perturbation is larger, and the intersystem crossing process is more efficient. This is the so called 'Heavy' atom effect (High Z)[40,59,60]. In real systems with many electrons, shielding must be

considered, however this simple model gives us insights into the factors that affect spin-orbit coupling.

In a zero order approximation only transitions which involve compensation in orbital angular momentum are able to occur[41] regardless of the magnitude of the heavy atom effect. These usually take the form of a transition between a π and n (non-bonding) orbital as these require a 90 degree rotation to interconvert[41]. A 90 degree orbital rotation causes a change of angular momentum that can compensate for the change in spin (as in nitro-naphthalenes)[41,61]. This type of spin orbit coupling is described by the El-Sayed rules[41,62,63].

While the above mechanisms are formally the only allowed singlet-triplet transitions, the El-Sayed rules are relaxed when vibrations are considered which introduce distortions to the molecular geometry. For example the benzene molecule is planar and has no orbital transitions (such as n-π*) that can compensate, meaning spin interconversion is formally forbidden[41]. However by including out of plane vibrations that distort the molecule's planar geometry, mixing of the π and σ* orbitals is made possible[41]. The σ* orbital is spatially and energetically separate from the π orbital causing the mixing to be small[41]. Therefore transitions are only partially 'allowed' with transition times on the order of microseconds[41]. In other systems large scale distortions can lead to efficient intersystem crossing, in fact for oligo-thiophenes moving from the singlet to the triplet state involves a torsional rotation of the molecule compensating for the change in spin[64]. In real systems each of these factors interact giving a set of requirements summarised below that affects the efficiency of singlet-triplet interconversion.

1/ The transition must occur between singlet and triplet states that are of a similar energy. As the non-radiative transition occurs with no overall change in energy, the overlap factor reduces quickly with energy gap[41,62,63].

2/ The spin and orbital angular momentum must be coupled by the spin-orbital coupling factor. This can be enhanced by inclusion of heavy atoms either in the structure or in the vicinity of the molecule[40] (external heavy atom effect[59,60]).

3/ The singlet-triplet transition must cause a change in orbital angular momentum that compensates for the change in spin angular momentum. This usually takes the form of a transition between π and non-bonding orbitals[41,62,63].

4/ In the absence of large spin-orbit coupling and n-π transitions, compensation is possible through vibrations. In some cases torsional rotations cause a similar effect to n-π transitions allowing very efficient intersystem crossing[41,64].

Now we have considered all components and transitions, to conclude we build a diagram in Figure 2.7 detailing the most common transitions in organic molecules[40,41].
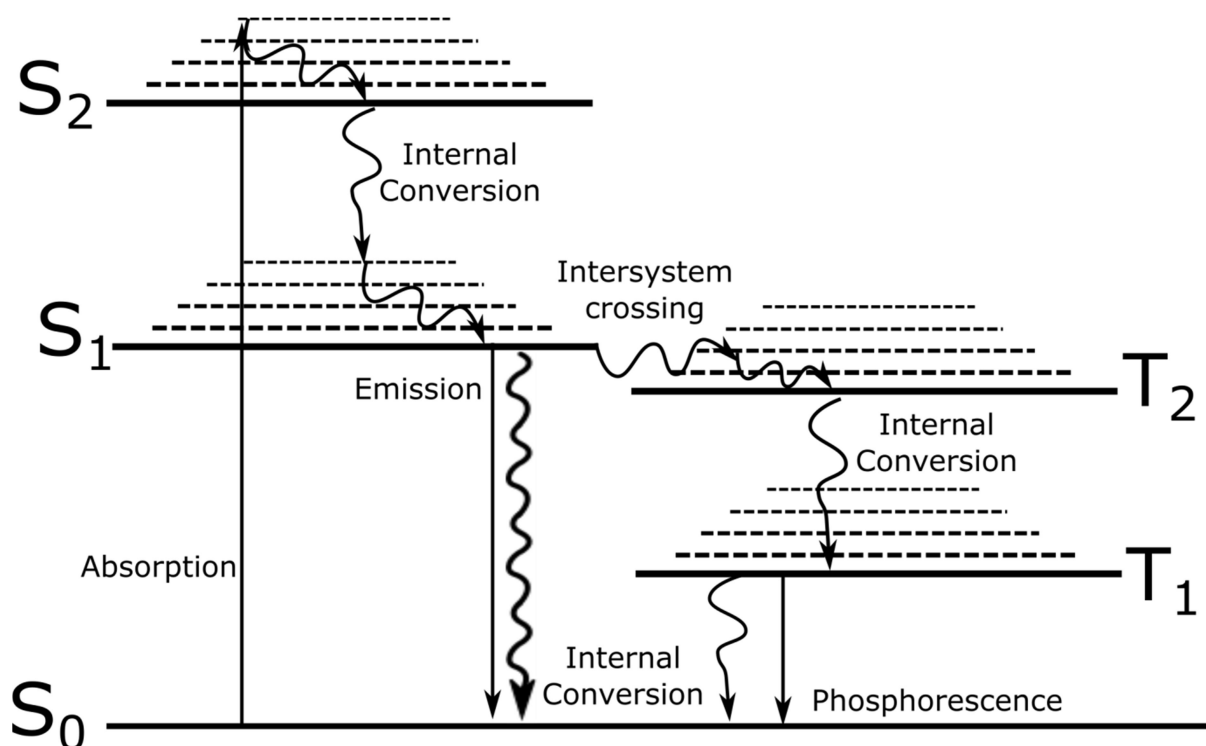
Figure 2.7: Example Jablonski diagram. Jablonski diagrams summarise the basic decay channels in organic molecules. Solid lines represent electronic ground and excited states of either singlet (S_0, S_1, S_2) or triplet (T_1, T_2) spin. For each of these states there is also a ladder of vibrational sub levels represented by dashed lines. Transitions between these states have been grouped into two categories radiative (solid arrow) and non-radiative (oscillating arrow). Energy levels here are only an example and so are arbitrary.

2.3 Intermolecular Interactions

In the previous sections we discussed the processes that can occur on a single molecule. Before discussing singlet exciton fission, we first address the interaction between multiple molecules (intermolecular interactions). We start by considering two molecules in close proximity in the ground state. For simplicity we start by ignoring the vibrational and spin components of the wavefunction and presume the wavefunction overlap between the molecules is small (negligible exchange interaction). As such, we presume the molecules do not share conjugation and concentrate only on the electronic component (Kasha treatment[65,66]). As was discussed above, while in the ground state the only contributions to the molecule's electric dipole is from random oscillations in the ground state electron density. However at small enough distances, the small dipoles in the ground states of the two molecules can interact, yielding a ground state energy for the two molecules collectively shown in Equation 2.19[40].

$$E_g = E_1 + E_2 + D \tag{2.19}$$

Here E_1 and E_2 are the ground state energies of the two molecules and D is the negative polarisation energy (stabilising) analogous to solvation interactions with the surrounding solvent discussed above. As with solvation, the extent of the stabilisation is related to the magnitude of the dipoles and their separation. The reduction in the ground state energy for a smaller dipole separation is the origin of molecules condensing from gas to liquid, or as we will see here from monomer to aggregates. This is the so called Van de Waals or dispersion force that forms weak intermolecular bonds between molecules in the ground state[40].

We now include an excitation on one of the two molecules leaving the other in the ground state. If both molecules are identical (aggregate rather than a complex), the wavefunction is a combination of the two equivalent situations: $\psi_{agg} = \frac{1}{\sqrt{2}}(\psi_1\psi_2^* \pm \psi_1^*\psi_2)$, where ψ_n is the wavefunction of

molecule n and a * indicates the molecule is in the excited state. Inserting this into the Schrodinger equation yields the equation given in Equation 2.20[40].

$$E_{exc} = E_1^* + E_2 + D + k_{mn}\beta \qquad (2.20)$$

In Equation 2.20 E_1^* is the energy of the excited molecule, E_2 is the energy of the ground state molecule, and D is the polarisation energy as for the ground state. The final term on the right is the resonance integral, related to the overlap of charge densities between the molecules. Within this term β is the magnitude of the interaction, related to the distance between the molecules. In real systems β is a combination of dipole-dipole interactions and exchange interactions. However, for simplicity here we presume negligible wavefunction overlap and as such remove exchange interactions from our treatment. Thus, β represents the dipole-dipole interactions between the two molecules. The second term k_{mn} is an orientation factor (Equation 2.21), which changes sign based on the relative orientation of the molecules. It should be noted that the derivation of the orientation factor requires the assumption of the point-dipole approximation[40].

$$k_{mn} = (\hat{r}_m \cdot \hat{r}_n) - 3(\hat{R}_{mn} \cdot \hat{r}_m)(\hat{R}_{mn} \cdot \hat{r}_n) \qquad (2.21)$$

In Equation 2.21, $\hat{r}_j$ is the unit vector of the dipole of molecule j, and $\hat{R}_{mn}$ is the unit vector of the intermolecular interaction. The second term on the right is related to the relative orientation of the intermolecular interaction and the dipoles of the molecules. As a result, the interaction is heavily dependent on the relative orientation of the molecules. The first term, $(\hat{r}_m \cdot \hat{r}_n)$, is then the relative alignment of the dipoles involved in the interaction, which can take two extreme values for alignment (1) and anti-alignment (-1) of the dipoles. As such two states are produced above and below the monomer energy level split by 2β (Shown in Figure 2.8). Likewise, the transition dipole moment is a linear combination of the individual molecule's transition dipole moment giving 2μ for alignment and 0 for anti-alignment, where μ is the transition dipole moment of the monomer. The energy in Equation 2.20 is the total energy of the system, to find an expression for the observed

absorption/emission we must subtract the ground state energy (Equation 2.19), yielding Equation 2.22[40].

$$E_{\pm} = (E_1^* + E_2 + D \pm \beta) - (E_1 + E_2 + D) = \Delta E_1 + \Delta D + k_{mn}\beta \qquad (2.22)$$

The absorption of the two molecules is the monomer excitation energy (ΔE_1), shifted by the difference between the dispersion force in the ground and excited states (ΔD) and the resonance integral. To relate this model to real molecules it is instructive to consider the limiting cases of weak, strong and intermediate wavefunction overlap[40].

The first limit of β approaching 0 is met for large intermolecular distances where charge density overlap is minimal. In this regime the two molecules act as individual chromophores with an energy equal to the monomer state. Next we consider the opposite limit of large β. In this regime the coulomb overlap is strong enough to cause the molecules to reorient to an optimal configuration. Due to the reorientation of the molecules the excited state potential energy surface is shifted relative to the ground state. Emission from these intermolecular states is generally red-shifted and broad compared to the monomer emission. As the molecules are closer in the excited state than the ground state, absorption takes place at larger intermolecular distances between the molecules than emission. As such it is possible for there to be minimal interaction in the ground state as in the weak resonance integral limit. In this case an intermolecular state is only distinct in the excited state, hence the name Excimer or 'excited dimer'[40].

The first report of excimer formation was by Forster *et al*. in 1955, who showed that increasing the concentration of pyrene in solution caused the appearance of a broad red-shifted emission[67,68]. This proves that excimers can form upon random diffusional motion within solution, with an increased chance of a collision at higher concentration. After emission, the excimer returns to the ground state at the geometry of the excited state. If the stabilisation energy of dimerising in the ground state is lower than the stabilisation from solvation (surrounding itself with solvent molecules) the molecules move apart.

For intermediate values of β in the range of 1000s cm^{-1}, the molecules form an aggregate in the ground state held together by Van de Waals forces, sometimes termed a physical dimer (Covalently bound dimers are then known as chemical dimers). As discussed above the relative orientation of the molecules has a profound effect on the absorption characteristics of the dimer. To illustrate this, we take three examples in Figure 2.9, co-planar, head-to-tail and arbitrary.

We first consider two molecules arranged in a co-planar geometry, known as H-aggregates, shown in Figure 2.8a[40]. In the co-planar geometry, the angle between the dipole moments of the molecules and the intermolecular interaction is 90 degrees. Thus, the orientation factor takes on a positive value for aligned dipoles and a negative value for anti-aligned dipoles. In other words, the low energy state has anti-aligned electric dipoles, while for the high energy state the dipoles are aligned. The low energy state carries no transition dipole moment while the high energy state has double the transition dipole moment of the monomer. Absorption then only occurs into the high energy state causing a blue-shift in the absorption spectrum. As we saw previously, the Kasha-Valivov rule states that emission can only occur from the lowest energy excited state. As such emission from H-aggregates is explicitly forbidden and population instead decays non-radiatively[40].
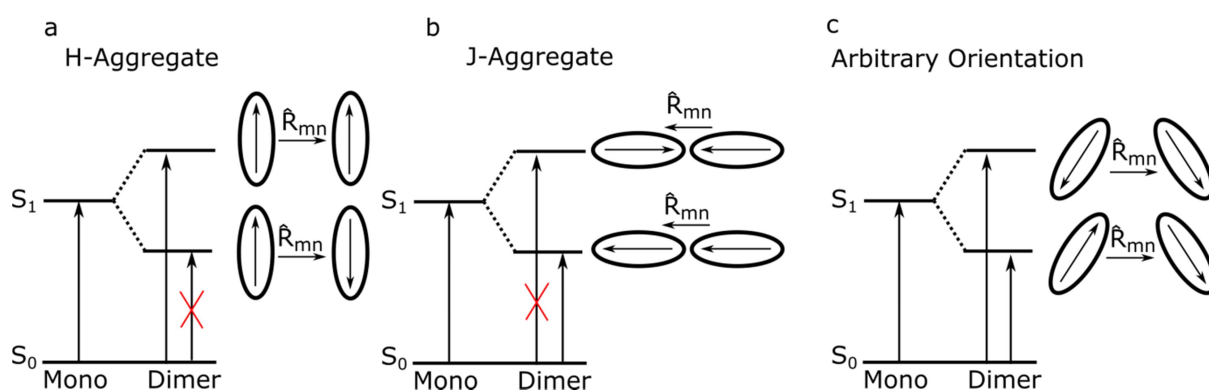
Figure 2.8: Summary of Kasha's model of intermolecular interactions. Jablonski diagrams for a H-aggregate (a), J-aggregate (b) and an arbitrary alignment (c). Next to the aggregate energy levels we show two molecules with their dipole moments aligned to the molecular axis and with a relative parallel and anti-parallel alignment. An arrow is included labelled $\hat{R}_{mn}$ which represents the unit vector of the intermolecular dipole-dipole interaction for each pair of molecules.

At the other extreme, the molecules are in a head-to-tail arrangement, known as a J-aggregate, shown in Figure 2.8b. Here the angle between the intermolecular interaction and the molecules dipoles is either 0 or 180 degrees depending on the orientation of the dipole moments. As a result, the orientation factor is positive for anti-alignment of the dipoles and negative for alignment, opposite to H-aggregates. In the low energy state, the transition dipole moments are aligned giving a transition dipole moment twice that of the monomer. Thus, the absorption of J-aggregates is red-shifted and produces strong emission. A third and final geometry is an arbitrary orientation somewhere between a H- and J-aggregate, shown in Figure 2.8c. In this geometry, the arbitrarily aligned transition dipole moments form a double peak in absorption, with both H- and J-aggregate energy levels being partially allowed[40].

This distinction implies we should be able to identify structure from the absorption and emission spectrum of the aggregates. However, in real systems the distinction is not so clear[69–71]. While the above model is instructive it fails to capture the real behaviour in aggregate samples. For example, in the case of weakly coupled H-aggregates (small blue-shift) solvation can overwhelm the aggregate shift. To extend and improve on the model by Kasha we must also include the influence of vibrations on the system. By incorporating the effect of vibrations into an aggregate model, the structure and interaction strength can be attained from the vibrational progression in the absorption spectrum[69–71]. This was achieved in a model constructed by Spano and co-workers. This model is used in Chapter 6 to model aggregates of carotenoids. The model will be briefly discussed below.

The model constructed by Spano and co-workers involves solving the Holstein Hamiltonian using a two-particle state basis set. First the monomer spectrum is fit with a Franck-Condon progression presuming equal full-width-half-maximum (FWHM) of all the peaks and a single dominant vibrational mode. Then we construct the one-particle basis states, those being; one molecule in the electronically and vibrationally excited (vibronic) state with surrounding vibrationless ground state molecules[69–71]. The Hamiltonian is then solved for two-particle basis states which in addition to the

vibronic excitation also include a neighbouring vibrationally excited molecule in the ground state. Spano *et al.* found that truncating the basis set at two-particle states gives a good agreement with experimental results. This can be conducted for a series of aggregate sizes (number of molecules), with relative angles and nearest neighbour coupling strengths used as fitting parameters[69–71].

A consequence of taking vibrations into account is that the spectral shape can be related to the coupling strength within the aggregate. For the weak regime transfer from the monomer to surrounding sites is slow compared to relaxation causing a spectra similar to that of the isolated monomer[69–71]. In other words, two particle excitations have little effect on the spectral shape indicating the excitations are still localised on the single molecule. When we increase coupling to the intermediate regime and the strong regime we see an increased effect of two-particle states leading to large deviations from the monomer spectral shape[69–71]. The higher energy vibronic replica are more intense relative to 0-0 in H and vice-versa in J type aggregates, providing a powerful method for characterising aggregates[40,71,72].

We now briefly consider the interaction of two excited molecules, the most relevant cases being interaction of two singlet excitons and the interaction of two triplet excitons. For two singlets meeting in solution, energy transfer occurs from one to the other forming a ground state molecule and a high lying singlet state (S_n)[40]. This process is known as singlet-singlet annihilation[40]. As singlet states are relatively short lived, this process is only relevant at high laser intensities where excitation densities are large (as is discussed briefly in Section 2.5). In the case of two triplets meeting in solution the situation is much more complicated. Due to the long lifetimes of the triplet states, triplet-triplet interactions are much more likely to occur at lower power and lower concentration than singlet-singlet interactions. We discuss triplet-triplet interactions in the following section.

2.4 Singlet Fission and Fusion

2.4.1 Fission and Fusion

In the previous section we established that at high power and high concentration intermolecular interactions become important. One of these, the interaction of two triplets, leads to a wealth of new physics. As we saw in Section 2.2.4 when two ½ spin electrons interact they may form one of four spin states, 1 singlet and 3 triplets. The same is true when 2 triplets meet (4 electron state), leading to an even larger set of possible states. In a naïve view the four spins are able to combine into one of 9 combinations, one singlet of spin 0, three triplets of spin 1 and 5 quintets of spin 2 (singlet and quintet states shown pictorially in Figure 2.9)[40,47,73].
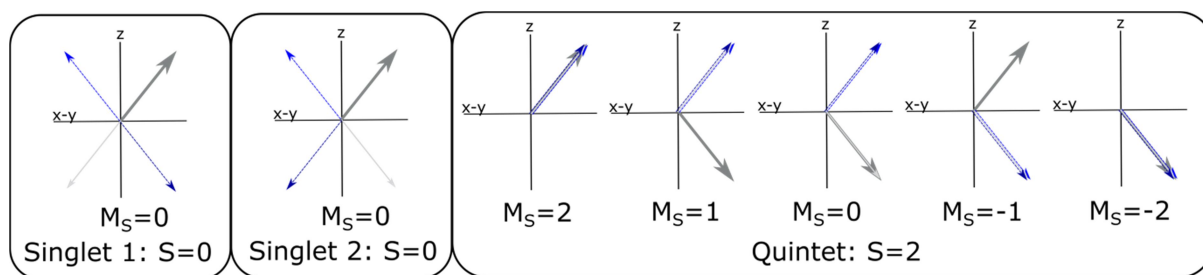
Figure 2.9: Vector diagram representations of Singlet and Quintet 4 electron states. The vertical axis is set to the Z axis and is representative of the M_s value or projected spin. The horizontal axis then represents the phase of the spins relative to each other. The colour and dashed versus solid lines are to differentiate the 4 electrons involved in the state. In diagrams where all four electrons overlap, we offset the arrows for clarity.

Of particular interest is the possibility of forming a singlet state (spin-0) from two triplets which could lead to singlet emission after the decay of the initial singlet population. Indeed, it has been shown that emission with the same line shape as prompt singlet emission is observed on the time scale of triplet decay, this is termed delayed fluorescence[10,40]. Further interest was sparked in the 1960's when it was shown by Johnson *et al*. that the delayed fluorescence of anthracene crystals is sensitive to a magnetic field[74]. In a later paper the authors extended the study and explained the observed magnetic field effects through the model shown in Equation 2.23[75].

$$T_1 T_1 \underset{k_{-1}}{\overset{k_1}{\leftrightarrow}} [TT] \underset{k_{-1}}{\overset{k_2}{\leftrightarrow}} S_1 S_0 \tag{2.23}$$

The intermediate state between the pair of individual triplets and the pair of individual singlets is known as a triplet-pair state. While in the triplet-pair state, the spin character of the coupled triplets is a superposition, formed of the 9 possible spin states. The triplet-pair is formed when two triplets collide occurring with a rate k_1, the triplet-pair can also separate to free triplets once again with the rate k_{-1}. As discussed above the triplet pair can also form a singlet state with rate k_2 reliant on the spin state of the triplet-pair[75]. The picture described above suggests 1/9 triplet-pair states form singlets i.e. ^{1}[TT], however these are not true eigenstates of the system.

Describing the true eigenstates of the system analytically is very complex and as such we must use a model Hamiltonian to simplify. This is achieved by pairing up electrons and considering the interaction between the constituent 2 electron states, which can be in any of the three triplets or one singlet states discussed in Section 2.1.3[76–79]. The four states can then form 16 possible combinations (for example S_0S_0, T_0T_0, T_-T_+ etc.). These states formed of a combination of 2-electron states are not eigenstates of the spin Hamiltonian either. The model Hamiltonian must be diagonalized yielding true eigenstates[76–79]. The wavefunctions of a selection of these spin states are shown below in Equation 2.24-2.26[34,80]. Here A and B represent the two interacting triplet states, and the subscript 0, -1 and +1 represent the M_s level of the state.

$$\text{Singlet 1:} \, S = S_A S_B \tag{2.24}$$

$$\text{Singlet 2:} \, ^1[TT] = \frac{1}{\sqrt{3}}(T_{0A}T_{0B} - T_{-A}T_{+B} - T_{+A}T_{-B}) \tag{2.25}$$

$$\text{Quintet} \, (M_s = 0): \, ^5[TT] = \frac{1}{\sqrt{3}}(2T_{0A}T_{0B} - T_{-A}T_{+B} - T_{+A}T_{-B}) \tag{2.26}$$

In addition to spin character, we must also consider the coupling strength between the triplets in the triplet-pair. For triplets spaced by many molecules the orbital overlap is negligible (weak coupling)[77]. Scholes *et al.* showed that in this regime the singlet and quintet states are isoenergetic[77]. This regime is described by the Merrifield model where singlet and quintet states mix, causing a superposition of M_s=0 singlet and quintet states[80]. The opposite is true of large orbital overlap (strong exchange coupling) where mixing with charge-transfer character configurations splits the

singlet and quintet energy levels[77]. When strongly exchange coupled, the states become pure spin states with no mixing between singlet and quintet states expected (Merrifield's model no longer holds)[77,80], while in the weak coupling regime (superposition of spin states), the rate of singlet formation from the triplet-pair state is related to the number of possible singlet spin configurations that are accessible. As a result Merrifield suggests that the application of a magnetic field changes the relative number of singlet pathways and so modulates the delayed fluorescence of the anthracene crystals[75]. Despite its simplifications this model proves useful in explaining experimental observations[77,80].

Returning to the model presented in Equation 2.23, we have not yet discussed k_{-2}. In addition to the forward process of two triplets forming a singlet (triplet-triplet annihilation), the reverse process of forming a triplet-pair from a singlet state could be possible. By considering the two possible 4-electron singlet character states this becomes clear. Singlet 1 (Equation 2.24) is formed of two singlet states, for example S_1S_0 , that being one molecule in the excited state and the second in the ground state[34,80]. Singlet 2 (Equation 2.25) is formed of three combinations of two triplets in an overall singlet character state[34,80]. Due to the pure spin character of strongly exchange coupled triplet-pair states, interconversion between a singlet state and a strongly exchange coupled triplet-pair of singlet character is possible without a spin flip[78]. This process is known as singlet fission and is defined as the conversion of a singlet exciton into two free triplets through a bound triplet-pair intermediate. After its discovery in the 1960s, singlet fission received relatively little attention in the following years[75,81–83].

This was until the early 2000s when interest was renewed by possible applications in solar cell technology. The majority of the energy absorbed from high energy photons is lost to heat as the excitation relaxes to the band gap, analogous to Kasha's rule for organics[41]. The singlet fission material converts high energy photons into two lower energy excitons reducing losses[11]. It was shown in 2006 that this could increase the maximum possible efficiency from 34% to 44%[11].

Following this prediction, further computational studies investigated possible materials for singlet fission studies[84–86]. In these studies authors investigated materials using two basic energy criteria. The first criterion is that the parent state energy must be above 2 times the triplet to ensure that singlet fission is exoergic and efficient[84–86]. The second criterion is that there are no higher lying triplet states or a lower energy singlet state to facilitate triplet decay. By ensuring neither of these states are at energies accessible to the triplet-pair it is possible to maximize the number of triplets harvested[84–86].

Several studies since have reported inclusion in a solar cell with Congreve *et al*. even reaching more than one electron per photon absorbed (over 100% external quantum efficiency)[7,8,87–92]. However, all of these are with a single class of molecule, which form the majority of singlet fission literature. In fact only two materials and their derivatives are widely used, pentacene and tetracene[11–14,16,19,93–96]. In the following sections we will first discuss the physical mechanism connecting the singlet and triplet-pair states before discussing two classes of singlet fission materials, the acenes and the lesser studied polyenes.

2.4.2 Direct Versus Mediated Mechanism

In the field of singlet fission there has been much debate as to the mechanism for the conversion of a singlet excitation into a multi-exciton (triplet-pair) state. Several studies have put forward mechanisms, which we briefly discuss below[9,10]. The first is the direct mechanism which proposes the initial and final state couple with no intermediates in the process (Figure 2.10). The direct mechanism thus requires a transfer of 2 electrons simultaneously. The rate of the 2-electron process is related to the coupling between the initial and final state under the perturbation of a 2 electron transfer ($\langle S_1|\hat{H}_{2e}|^1[TT]\rangle$)[9,10]. Modelling of these coupling terms is incredibly complex, leading to few studies on the topic. Zimmerman *et al*. conducted *ab initio* quantum chemical calculations as opposed to using a model Hamiltonian, to describe pentacene and tetracene singlet fission. The authors found that the direct coupling terms between the singlet and $^1[TT]$ states were surprisingly

low (5meV)[97–99], however their model was capable of adequately describing experimental findings. In agreement with the above results, Renaud *et al*. found a correlation between the direct coupling term and the singlet fission yield measured experimentally for a series of perylenediimide derivatives[100].
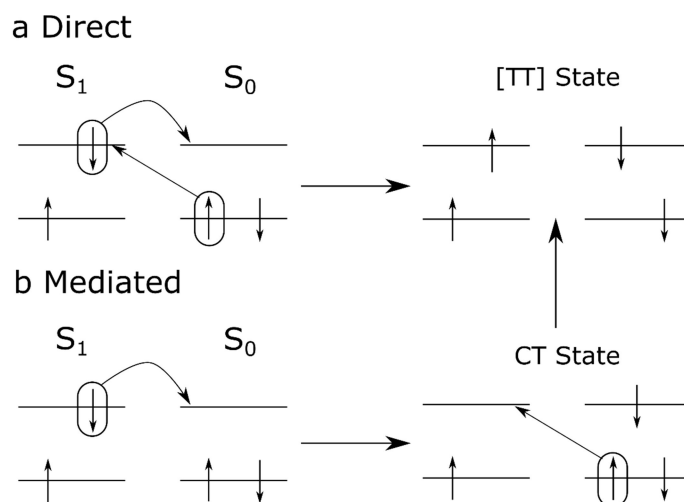
a Direct

b Mediated

Figure 2.10: Mediated verus Direct mechanism for singlet fission. (a) The direct mechanism requires a two-electron transfer moving directly to the [TT] state. (b) The mediated mechanism requires two one electron transfers reaching the [TT] state via a charge-transfer state.

The second proposed mechanism involves an intermediate charge-transfer (CT) state called the mediated mechanism (Figure 2.10). The excited singlet state first undergoes a single electron transfer to an intermolecular charge-transfer state, followed by a second electron transfer event forming the ^{1}[TT] state. Instead of a single coupling element, there are now two describing each step of the process $(\langle S_1|\hat{H}_{1e}|CT\rangle \langle CT|\hat{H}_{1e}|^1[TT]\rangle)$[85,97,101]. In ground breaking work, Berkelbach and co-workers confirmed that for an energy ordering $E_S > E_{CT} > E_{TT}$ and both singlet fission mechanisms available the mediated mechanism dominates[102]. The authors used a system-bath Hamiltonian which describes both the electronic and vibrational components, including coupling to the environment (bath) via phonons[102]. As we will see in the following section, it has been shown that CT states form as observable intermediate states[16].

In recent years a modified version of the mediated model has been proposed in which the CT state never forms, instead mediating as a virtual state. Berkelbach and co-workers also tested the mediated mechanism by removing the direct mechanism and moving the charge-transfer state to above the singlet state energy to mimic previous studies. They found that singlet fission occurs efficiently even for charge-transfer state energies 1eV above the singlet state[102]. Despite the charge-transfer state being inaccessible it is able to mediate in a mechanism termed super exchange[103]. In the super exchange mechanism both the singlet and the triplet-pair mix with a virtual charge-transfer state, increasing the overall effective coupling of the states which is given by; $\frac{\langle S_1|\hat{H}_{1e}|CT\rangle \langle CT|\hat{H}_{1e}|^1[TT]\rangle}{E_{CT}-E_{TT}}$.[103] As this route forms with no intermediate states it is kinetically a direct process from singlet to triplet-pair, making it difficult to distinguish between this and the direct mechanism experimentally[103]. However, as we will see in the next section a distinction can be made through indirect observations[16].

Before moving on we wish to discuss a recent addition to the proposed mechanisms of triplet-pair formation. The quantum coherent mechanism was introduced to explain time resolved two electron photoemission spectroscopy measurements[101]. In this technique, the sample is ionised, and the kinetic energy of the ejected electrons is collected. The difference in kinetic energy between electrons that originate from the ground and excited states then gives a relative measure of the state energies. Chan *et al*. found that a signal around the energy of the triplet transition appears instantaneously along with the singlet signal[101]. The authors suggest that this is a signal of the triplet-pair state and that both the singlet and triplet-pair are formed together in a superposition state. The formation of the triplet-pair state seen in optical measurements is then characteristic of these states dephasing first to the triplet-pair and then to individual triplets[101]. While it is not clear if one mechanism dominates, as we will see in the following sections, there is growing experimental evidence for the mediated model. In fact even the quantum coherent model attains its coupling through an intermediate virtual charge-transfer state[104].

2.4.3 Polyacene Singlet Fission

Most singlet fission studies revolve around polyacenes materials, specifically tetracene and pentacene and their more soluble derivatives that include TIPs groups (Figure 2.11). These two molecules also represent two archetypal cases for relative singlet and ^{1}[TT] state energies. In pentacene the singlet state is above 2 times the triplet (^{1}[TT] below parent singlet state) making singlet fission exoergic. In pentacene, singlet fission has been shown to occur with 200% efficiency in ~80fs, expected for the energetically favourable process[17,105].
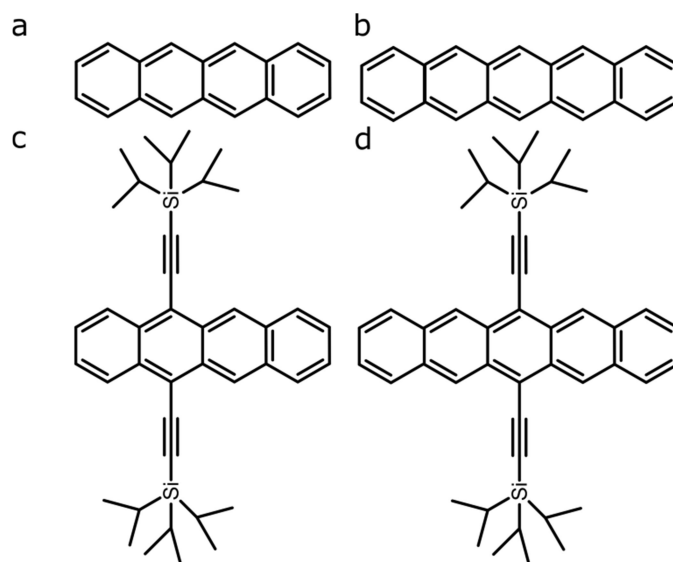
Figure 2.11: Summary of singlet fission in tetracene and pentacene. Chemical structures of tetracene (a) and pentacene (b), TIPS-tetracene (c), TIPS-pentacene (d).

A study conducted by Lukman *et al*. looked to change the charge-transfer state energies through end groups and choice of solvent to investigate its effect on the singlet fission process in pentacene derivatives[16]. They found that in some of the pentacene derivatives they were able to directly measure population of the intermediate charge-transfer state confirming the mediated mechanism[16]. In addition, for some derivatives, while a charge-transfer state was not directly formed, a dependence on solvent was found for the singlet fission rate/yield[16]. This confirms a

charge-transfer state has an influence on the singlet fission process even for systems where it is not directly formed, suggestive of the super exchange mechanism[16].

The energy landscape of tetracene is thought to give endoergic singlet fission (^{1}[TT] above parent singlet state). This assertion originates from temperature dependent studies of the singlet fission triplet yield that puts the activation energy at 200meV[83,106], and direct measurements of the triplet energy of tetracene[107]. Recently, transient absorption measurements taken by Wilson *et al.* tracked the singlet and triplet population at temperatures from 4-300K[19]. Wilson and co-workers found that the rate of formation of the triplet-pair is independent of temperature down to 4K. However, the authors found that there is a temperature dependence in the separation to free triplets. At low temperatures there is reduced triplet diffusion which leads to higher geminate recombination, reducing free triplet population[19]. Through this observation it is possible to explain the observed temperature dependence from the 1960's without singlet fission being endothermic.

Further evidence came from a study by Yong *et al.* who identified quantum beating in the emission kinetics of tetracene and other related singlet fission materials. Using 300fs resolution photoluminescence measurements the authors identified oscillations in the emission kinetics after subtracting the exponential decay. As was discussed above when in the weak exchange coupling regime, the spin character of the triplet-pair state is a superposition of singlet and quintet states. As the triplet-pair state is more emissive when of dominant singlet character, an oscillation in the emission kinetics can be assigned to oscillation in the spin character of the superposition state. As the emission is directly related to the triplet-pair population and cannot be through delayed fluorescence (different spectral shape to the singlet) the emission can be linked to the triplet-pair state directly. This surprising observation is still debated however the authors suggest the triplet-pair emits through coupling to nearby bright states, in a mechanism known as Herzberg-Teller coupling. Herzberg-Teller coupling will be discussed further in Chapter 5.

The fact that the triplet-pair emits allows Yong and co-workers to measure the triplet-pair energy directly. The authors are then able to confirm that the absorbing state and triplet pair states are approximately isoenergetic, and singlet fission is not a strongly exoergic process as was originally thought[94]. A complication in polyacene singlet fission comes from the drastic range of singlet fission rates and yields that have been reported for different sample structures. For example, it has been shown that triplet separation to independent triplets can be a very slow process in polycrystalline TIPS-tetracene films (μs) [14].

A study by Stern and co-workers found that in polycrystalline TIPS-tetracene separate triplets never form and instead the triplet-pair state lives for microseconds decaying non-radiatively[14]. The explanation for this is that the TIPS-tetracene molecules pack with very little orbital overlap (evidenced by lack of change in ground state absorption upon entering the solid state)[14]. As such triplet mobility is very low and triplets are not able to separate and reduce exchange coupling[14]. Indeed, Korovina *et al*. have shown that in a covalently linked dimer of 5-ethynyl-tetracene, separation of triplets occurs through triplet hopping[18].

The authors measure emission and transient absorption of the dimer in the solid state and solution. In the solid state, triplet-pairs form within 1ps and separate to form free triplets with an efficiency of 154%. However, in solution where hopping is not possible, the triplet-pair state forms within 2ps but never separates to free triplets. Korovina *et al*. then form heterogeneous films of the dimers with diphenyl-tetracene, in which they observe separation to both 5-ethynyl-tetracene and diphenyl-tetracene triplets from the triplet-pair state of the 5-ethynyl-tetracene dimer[18]. It should be noted that while this model is consistent with results discussed here, there are some studies reporting separation to free triplets within a single dimer. Tayebjee *et al*. measure a pentacene dimer in solution and find triplet lifetimes equivalent to those of individual triplets on a single pentacene unit[15]. The exact dynamics of the triplet-pair state are still under debate and will be discussed further in Chapter 4.

2.4.5 Polyene Singlet Fission

A second class of materials known to undergo singlet fission are polyenes[9,10]. Owing to their complex photophysics we first take a moment to discuss the models for describing polyenes, and how they lead to the suggested route for singlet fission in these materials.

As discussed above, polyenes are formed of double and single bonds in an alternating pattern, a dimerised ground state[42]. In a dimerised chain two phases coexist and are degenerate, those being A-phase (short-long-short) and B-phase (long-short-long) [42]. For chains with odd site numbers (even number of bonds) it can be shown that there must be a change in phase in the chain to allow double bonds at the chain ends favoured due to edge effects. At the point of conversion of A to B phase conjugation, a defect forms known as a soliton[42]. For a chain with an even number of sites both ends of the chains can be double bonds without the inclusion of a soliton (Figure 2.12)[42]. In order to correctly predict the low energy physics of polyenes it is necessary to include electron-electron interactions. Below we briefly discuss the low energy states of conjugated polymers as a function of the degree of electron correlations[42].

Firstly we define the ground state ($1A_g^-$) as having one π-electron associated with each site of the conjugated backbone[42]. The spacing between each of these sites (or the length of the bond between them) alternates from short to long leading to the double and single bond alternating structure shown in Figure 2.12[42]. For many molecules, the first excited state is $1B_u^+$, an ionic state indicated by the + sign. Following excitation, an electron transfers to a neighbouring orbital leading to a doubly occupied orbital and a corresponding empty orbital surrounded by singly occupied orbtials[42]. The doubly occupied orbital forms a negatively charged soliton, while the empty (or occupied by holes) orbital forms a positively charged antisoliton[42]. The pair then form a bound soliton-antisoliton pair that localise in the centre of the chain. In the weak interaction limit the soliton pair are only weakly bound, forming a charge-transfer Wannier-Mott exciton. At the intermediate to strong interaction

limit the state becomes a strongly bound Frenkel exciton[42]. Excitation energies of the $1B_u^+$ state increase linearly as a function of increasing electron correlations in the system.

Intermedaite Coupling regime
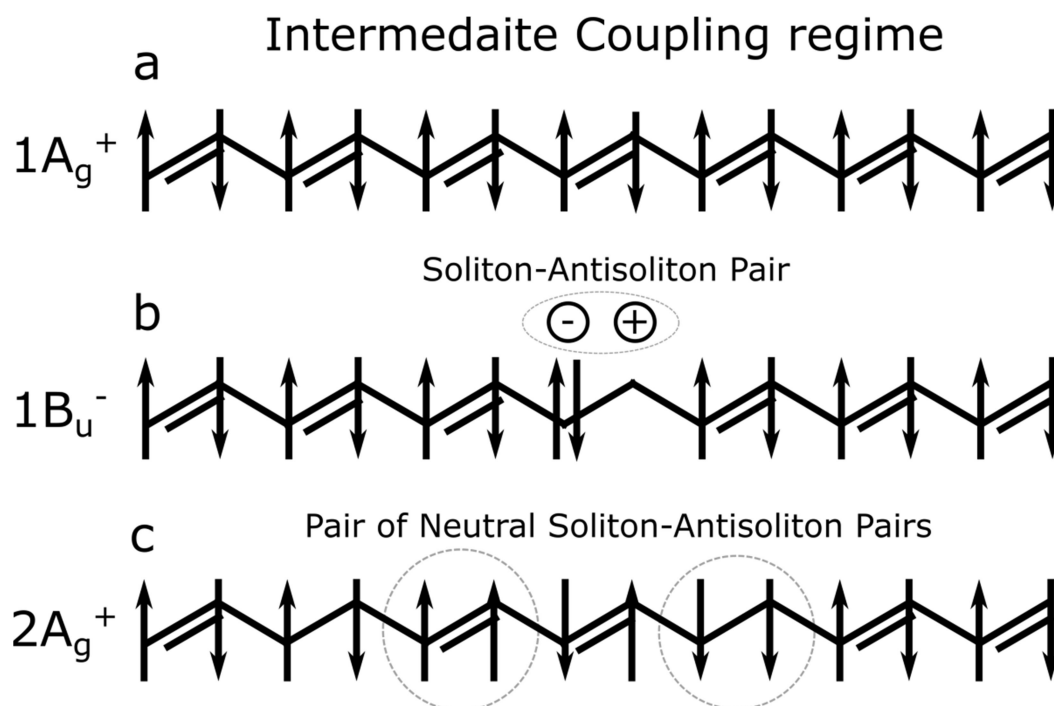
Figure 2.12: Diagram representing the soliton structures of polyene states. (a) Represents the ground state in which each orbital contains a single π-electron. (b) Soliton structure of the $1B_u^+$ excited state. The double occupied and empty orbitals form positive and negative spinless solitons which are bound by their coulomb attraction and self-localise to the centre of the chain. (c) Soliton structure of the $2A_g^-$ state. In the intermediate regime, two spin-1 negative soliton-antisoliton pairs form which are bound into an overall spin-0 state. At strong coupling the two spin-1 objects become unbound forming two triplets.

The second commonly considered excited state ($2A_g^-$) is a covalent state meaning all orbitals are singly occupied after excitation[42]. Unlike the $1B_u^+$ state, $2A_g^-$ changes character significantly as a function of electron correlations. At the weak interaction limit the $2A_g^-$ state is a bound Frenkel exciton whose energy scales linearly with interaction energy[42]. However, as the interaction strength increases the character of the state changes from Frenkel exciton to bi-magnon. A magnon is a spin-density wave and can be thought to represent the movement of energy between the spin degrees of freedom. In the strong coupling limit the $2A_g^-$ state becomes explicitly a bi-magnon or triplet-pair state formed of two spin 1 objects[42]. At any non-zero interaction strength the description of the state as being formed of two spin 1 objects is relevant, with an increased prominence at the strong

coupling limit. In Figure 2.12 we show the structure of the $2A_g^-$ state in the intermediate coupling regime. Each of the spin 1 objects that form the state are constructed of two singly occupied solitons (spin ½), in a soliton-anti-soliton pair of spin 1 with negative charge. The two negatively charged soliton pairs then repel each other causing a reorganisation with the soliton pairs at the ends of the chain.

The bi-magnon character inverts the dependence of the $2A_g^-$ state energy on electron correlations reducing its energy[42]. Another factor that effects the energy/character of the $2A_g^-$ state is the dimerization constant δ. δ is related to the hybridization integrals of the single (t_s) and double bonds (t_d) by Equation 2.27 and 2.28 where t is the transfer integral in the non-dimerised case ($t_d = t_s = t$)[42].

$$t_d = t(1 + \delta) \tag{2.27}$$

$$t_s = t(1 - \delta) \tag{2.28}$$

As the dimerization becomes more pronounced (δ -> 1) electrons become localised on the short (double) bonds ($t_d = 2t$), isolated by the much longer (single) bounds ($t_s = 0$) [42]. In Figure 2.13 we reproduce the phase diagram from a book by Barford showing interaction energy versus dimerization constant[42]. In the intermediate regime (10-15eV) for δ~0.1 as for polyenes the $2A_g^-$ state actually drops below the $1B_u^+$ state and has significant bi-magnon character[42]. A strikingly simple test for this theory is to compare the $2A_g^-$ state energy with double the triplet energy of the molecule.

Interestingly, while the $2A_g^-$ state does sit below the $1B_u^+$ state, this is only true of its relaxed energy (at the excited state geometry). In contrast, at the ground state geometry (vertical excitation), the $2A_g^-$ state is slightly above the $1B_u^+$ state. This curious relationship between the state energies of the first and second excited states in polyenes is due to the structures of the excited states. For the $1B_u^+$ state, after excitation, self-localisation leads to a polaron-exciton with minimal distortion of the

nuclei. As such the state requires very little reorganisation to minimise the energy of the state (0.2eV). Whereas the $2A_g^-$ state is formed of 4 solitons, which due to their negative charge, impart a repulsive coulombic force at short range, separating the two soliton-anti-soliton pairs. This leads to a large geometric reorganisation of excitation density to the ends of the polyene chains. The large reorganisation leads to a large change in energy from vertical to relaxed (1.2eV)[42,43,108].
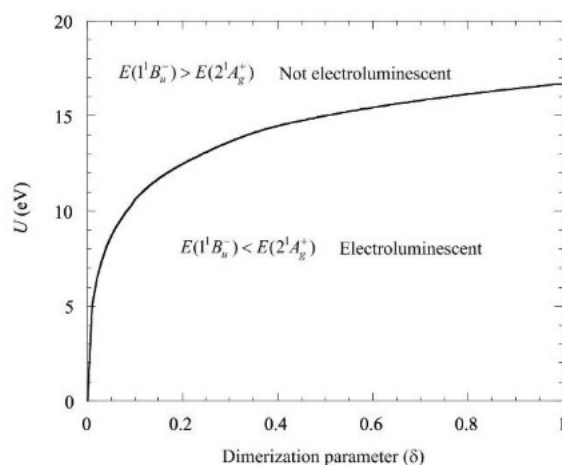
FIG. 5.4. The phase diagram of the Pariser-Parr-Pople model at half-filling. $t = 2.5$ eV.

Figure 2.13: The phase diagram of the Pariser-Parr-Pople model at half-filling. t = 2.5eV. Figure reproduced from the book by Barford[42].

In their seminal paper Tavan and Schulten proposed separation of the $2A_g^-$ state into two triplets as the mechanism for singlet fission in polyenes[9,10]. Tavan *et al*. suggested a small perturbation could lead to separation and localisation of the $2A_g^-$ state into separate triplets[49]. This was based on the observation that the $2A_g^-$ state energy is approximately the sum of 2 triplets implying the binding energy is small[49]. Tavan *et al*. found that localisation is preferred as the conjugation length is increased implying that at a given critical length the triplets will localise and separate[49]. We postpone further discussion of polyene intramolecular singlet fission for Chapter 5.

Of these polyene materials, carotenoids are of particular interest. They are a widely studied set of molecules which have been shown to undergo singlet fission in light harvesting complexes and

solution based aggregates[23–25,109] (discussed further in Chapter 6). Over 600 carotenoids exist in nature [110–112], covering a wide variety of functions from photo-protection in human vision to energy harvesting in photosynthesis [113–120]. The complex energy landscape in carotenoids has led to decades of controversy in the assignment of the excited-state processes[39]. As a result, clarifying which states are present and relevant is of importance. We present below a brief discussion of the current understanding of carotenoid excited-state energies and photophysics. For more in-depth discussion, we refer the reader to references [39,112].

2.4.6 Energy Landscape of Carotenoids

Tavan and Schulten and later Schmidt and Tavan calculated the optically accessible states for polyenes [49,121]. Their calculated energies match experimentally determined gas-phase energies remarkably well[121] and we plot their collated experimental vertical gas-phase $2A_g^-$ and $1B_u^+$ energies[121] in Figure 2.14.

In addition to $2A_g^-$ and $1B_u^+$ states, calculations reveal several other low lying excited-states[39,49]. The most relevant of these is the $1B_u^-$ state that is optically inaccessible from the ground-state (similar to $2A_g^-$). As shown in Figure 2.14, calculations of the vertical gas-phase energy of $1B_u^-$ indicate that at conjugation lengths below N=6, the $1B_u^+$ state lies below the $1B_u^-$ state [121], while at longer conjugation lengths (N>6), these states switch order so that the $1B_u^-$ state is lower in energy than $1B_u^+$. This state ordering suggests that – in the gas phase – both the $1Bu^+$ and the $1B_u^-$ states must be considered when describing excited-state decay pathways in carotenoids with N>6 [39,122].

Experimentally, the $1B_u^-$ state was first invoked to explain the dependence of transition rate on energy gap for the $1B_u^+$ to $2A_g^-$ internal conversion, which doesn't follow the expected exponential energy gap law [123,124]. Since then a raft of literature has suggested the involvement of $1B_u^-$ in energy transfer [112], internal conversion [39,125], triplet generation [126,127], and charge-transfer[128] both in solution and embedded within a protein [32,39,49,112].
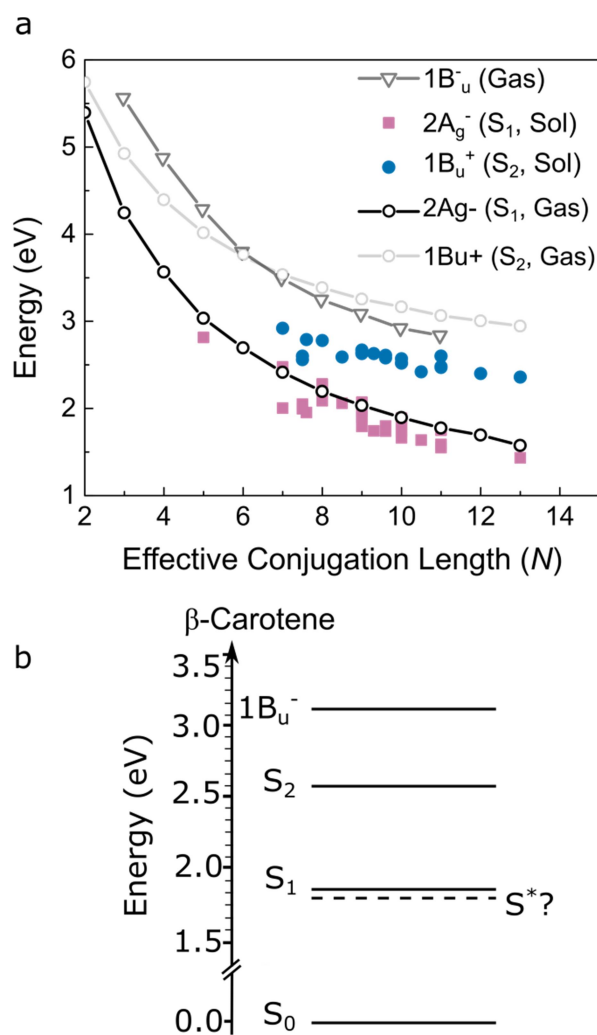
Figure 2.14: A summary of published, experimentally determined or calculated carotenoid energy levels. (a) The measured solution phase energies of excited states in carotenoids with varying degrees of conjugation. $1B_u^+$ (S_2) energies (blue) were measured through ground state absorption while $2A_g^-$ (S_1) energies (pink) were measured through emission [112,129–135]. In addition, experimentally determined vertical gas phase energies (open markers) have been included for the $1B_u^+$ (S_2) and $2A_g^-$ (S_1) excited state [121,136–139]. Finally, the calculated values of the vertical $1B_u^-$ state energies are shown in open triangles [121]. (b) The energy levels of β-carotene taken from literature, including the 'controversial' S* state (Dashed Line) [39].

However, in condensed-phase environments such as solution or protein, the $1B_u^+$ state should be stabilised more than the covalent states ($1B_u^-$, $2A_g^-$) because of its large oscillator strength (suggested to be up to an order of magnitude larger[121]), see Figure 2.14 [112,121,137–139,129–136]. This stabilisation suggests that $1B_u^-$ should play no role in condensed-phase carotenoid photophysics. In other words, for all-*trans* carotenoids excited into the lowest-energy absorption band in solution or protein,

calculations and empirical evidence of solvation suggest the photophysics should depend on only three states: $1A_g^-$ (S_0), $2A_g^-$ (S_1) and $1B_u^+$ (S_2).

This 3-state model is supported by recently published work from Liebel *et al.* who used vibrational coherence spectroscopy to measure β-carotene in solution, suggesting that internal conversion occurs via a conical intersection which implies it does not involve any other electronic states [54]. Indeed, at the ground-state geometry, $2A_g^-$ is calculated to lie higher in energy than $1B_u^{+}$[43]. On reorganisation to the relaxed $2A_g^-$ geometry, it lies > 1eV below $1B_u^{+}$[43,108]. This large geometric reorganisation is reflected in the large Huang-Rhys parameter required to fit the weak $2A_g^-$ emission spectra at low temperature [140,141]. These are both indicators of large geometric reorganisation which implies a shift in the potential energy minima of the $1B_u^+$ and $2A_g^-$ states. A large displacement between the potential energy surfaces of the $1B_u^+$ and $2A_g^-$ states would result in an internal conversion rate between S_2 and S_1 that does not depend exponentially on energetic gap, as is observed [123,142] and discussed in Section 2.2.3. Further evidence for a conical intersection comes from two dimensional electronic and vibrational spectroscopy (2DEV) by Oliver et al. who measure trans-β-apo-8'-carotenal (similar in structure to β-carotene). By resolving both the excitation (electronic) and probe (vibrational) information, 2DEV spectroscopy can follow the wave packet as it interacts with each electronic potential energy surface. The authors found that backbone vibrations remain correlated with the initially excited S_2 state after transfer of population to the S_1 state. As a result, this points to a direct transfer of energy with no vibrational redistribution, indicative of a conical intersection near the vertical excitation of the potential energy surface of the S_2 state[55].

One problem with the 3-state model comes from transient absorption measurements where a photo-induced absorption, to the blue wavelength side of the S_1-S_n absorption spectrum, has been observed with lifetimes longer than the $2A_g^-$ state (S_1). In order to explain this feature, a new state called 'S*' has been proposed (Figure 2.15b). S* was first observed in light harvesting complex 1

containing sprillioxanthin [143,144], and was later suggested to be a precursor to triplet formation via singlet fission in these complexes [126,127]. A similar photo-induced absorption, with a pronounced excitation-energy dependence, was also measured in dilute solutions of β-carotene by Larsen *et al.* [122] and assigned to S*.

There is, however, growing evidence, both in solution and in protein, that S* is not a separate excited state. In light-harvesting protein complexes, for example, the presence of energy donors and acceptors near the carotenoids (e.g. bacteriochlorophyll or other carotenoid pigments) can complicate analysis of the carotenoid photophysics. Recent work by Niedzwiedszki *et al.* demonstrates that the S* feature in LH2 can be attributed to radical pair formation, and the consequent Stark shift induced by the electric field, rather than a pure neutral carotenoid excited state[145].

In solution, several studies have investigated the origin of the S* feature. For example, Wohlleben *et al.*, investigated several carotenoids using pump-deplete-probe spectroscopy and concluded that the S* feature is a vibrationally excited ground state [125]. The pump-deplete-probe technique uses a third pulse between pump and probe to selectively depopulate the $1B_u^+$ state. It was shown that S* is not depleted by the pulse while the $2A_g^-$ state is. As a result, the authors suggested that the S* feature is due to population of an excited vibrational level of the ground state [125]. To explain this, they suggest that the ground state is populated by either impulsive stimulated Raman scattering or non-radiative decay from the $2A_g^-$ state.

The notion of S* as a hot ground state was later disproved by Jailaubekov *et al.* [146] who compared narrowband and broadband excitation conditions. Impulsive stimulated Raman scattering efficiency is expected to scale with bandwidth of the pump [146]. The authors demonstrate that S* is not populated sequentially from S_1 and that, crucially, population of S* does not depend on pump spectral breadth [146]. The latter implies that impulsive stimulated Raman scattering does not populate

S* [146]. Weerd *et al.* and others [144,147–149] instead suggest that a sub-population of carotenoids undergo a photo-induced change in conformation during relaxation from $1B_u^+$ (S_2) [144,147–149] yielding the S* feature.

Recently Ostroumov *et al.* reported transient absorption measurements before and after purification of all-*trans*-β-carotene [150]. The long-lived component in the transient absorption spectra is entirely absent in the pure all-*trans* sample regardless of excitation conditions [150]. This suggests that the so-called S* feature is due to a population of impurities in the sample [150]. The authors also collected spectra from each isolated impurity, finding similar ground-state absorption spectra to all-*trans*-β-carotene [150], suggesting the impurities are isomers that don't adopt a pure all-*trans* conformation [151]. Isomers are known to form over time in solution at room temperature, with a 20% population of a central carbon-carbon double bond *cis* isomer at equilibrium [152]. With the isomers removed, the entire transient absorption spectrum after 1ps can be described by a single transition (S_1-S_n). This is supported by work from Balevicius *et al.*, who were able to model the whole transient absorption spectrum of β-carotene (after purification) including only three states: $1A_g^-$ (S_0), $2A_g^-$ (S_1) and $1B_u^+$ (S_2) [150,153]. We confirm the above model in several carotenoids before exploring the singlet fission process in these molecules in Chapter 6.

2.5 Polaritons and Strong Light-Matter Coupling

In Chapter 4 we use strong light-matter coupling to investigate triplet dynamics in several systems. Here we wish to give the basic background required to understand the methods used during this study. We start with a description of strong-light matter coupling and the structures used to produce it. Strong light-matter coupling has applications in optoelectronics, such as polariton lasers which emit coherently by forming a Bose-Einstein condensate. As such polariton lasing does not require population inversion and can be prompted at much lower input powers[154,155].

2.5.1 Exciton-Polaritons

We start by considering the interaction between light and the exciton of an active medium. After excitation the exciton can relax via emission of a photon, which travels away from the active material. As there is a very low chance of the same exciton reabsorbing the photon the emission process is considered irreversible[156]. However, when the active material is placed in a Fabry-Perot resonator, the light and matter are confined together. A Fabry-Perot resonator is a microcavity constructed of two mirrors around the active medium[156]. As light enters the cavity, it becomes trapped and bounces back and forth interfering with itself, which forms standing waves (Figure 2.15) [156]. At non-normal incidence the total wave vector (K) is a combination of the perpendicular ($K_\perp$) and parallel ($K_\parallel$) wave vector components (Figure 2.15), given by Equation 2.29[156,157]. This can be modified to give the relation between the cavity thickness (L_c) and the wavelength of the cavity (λ_c) photon mode it produces given in Equation 2.30[156], where N is the order of the standing wave. As a result the photon mode energy is reliant on the angle of incidence (θ_{ext}) and gains an angular dispersion[156].

$$\mathrm{K} = \mathrm{K}_\perp^2 + \mathrm{K}_\parallel^2 \qquad (2.29)$$

$$\mathrm{L_c} = \frac{\mathrm{N}\lambda\cos(\theta_\mathrm{Ext})}{\mathrm{K}_\perp} \qquad (2.30)$$
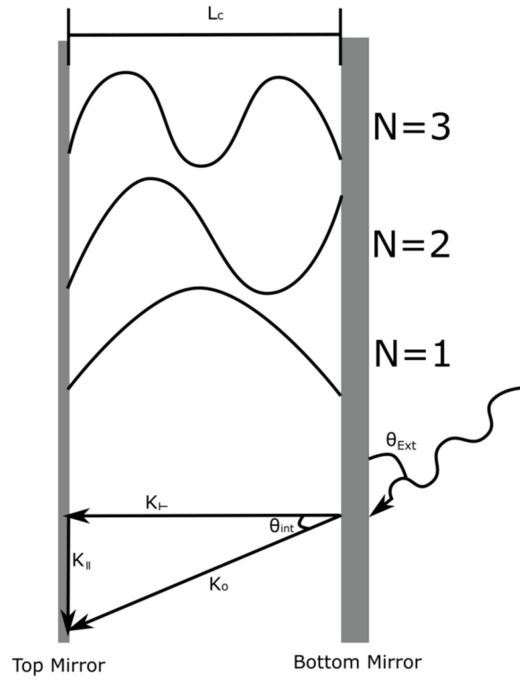
Figure 2.15: Diagram of a microcavity. The top mirror is thin to allow partial penetration of the incident light. The standing waves formed, and wave vector components are labelled.

Once the cavity mode is tuned to the energy of the exciton the two can interact, until the photon escapes the cavity[156]. The time the cavity traps the photon for is known as the cavity lifetime which it is related to the cavity quality factor (Q=$\frac{\text{Cavity mode central wavelength}}{\text{FWHM of the cavity mode}}$) [156,157]. The Q factor is governed by the reflectivity of the mirrors, with the probability of finding an excited electron in the cavity given by Equation 2.31, where γ_c is the cavity linewidth and t is time[156].

$$P_{\text{Exc}} = -e^{\gamma_c t} \tag{2.31}$$

At low Q, i.e. poor confinement, we do not change the photophysics of the active material significantly; this is called the weak coupling regime. In the weak coupling regime, the emission process is still irreversible however the presence of the photon mode changes the density of available states. As the photon mode must be aligned to the peak of the material's absorption to prompt coupling this increases the density of states around the absorbing state. As we saw in Section 2.2 the probability of a transition occurring is related to the density of available states[40,41,157]. As a result, the increase in the density of available states enhances the emission from the cavity. The

enhancement of spontaneous emission in the weak coupling regime is known as the Purcell effect[157].

As the quality factor is increased, we improve the confinement of the electromagnetic wave. This increases the chance of reabsorption before the photon escapes the cavity. At a high enough reabsorption rate, emission becomes a reversible process[156].

Once emission is a reversible process, the system is said to be in the strong coupling regime. The exciton and the photon form a superposition state, a new quasi-particle known as a polariton[156]. The polariton contains both light (boson) and matter qualities, splitting the excitonic state into an upper and lower polariton state[156]. It is possible to model this splitting in energy with a two level coupled oscillator model described by Equation 2.32[158]. If we consider two classical coupled oscillators such as two masses attached by springs, the total system oscillates with a frequency that is a superposition of the two masses. In analogy, the exciton and photon are the coupled oscillators while the polariton is the superposition state which yields a new frequency (or energy)[159]. By expanding the matrix in Equation 2.32, we arrive at Equation 2.33, and then solving using the quadratic formula gives Equation 2.34 [156], where E_c is the angle dependent photon energy, E_{exc} is the exciton energy, E is the polariton energy, A is the interaction potential ($\frac{\hbar\Omega_{rabi}}{2}$) in which Ω_{rabi} is the Rabi splitting defined below[158]. a_c and a_{exc} represent the contribution of the cavity mode and exciton to the polariton state respectively and are known as the Hopfield coefficients discussed below[156].

$$\begin{bmatrix} E_c & A \\ A & E_{exc} \end{bmatrix} \begin{bmatrix} a_c \\ a_{exc} \end{bmatrix} = E \begin{bmatrix} a_c \\ a_{exc} \end{bmatrix} \tag{2.32}$$

$$E = (E_c - E)(E_{exc} - E) - \hbar\Omega = 0 \tag{2.33}$$

$$E_\pm = \frac{E_c + E_{exc}}{2} \pm \frac{1}{2}\sqrt{(E_c - E_{exc})^2 + 4(\hbar\Omega_{Rabi})^2} \tag{2.34}$$

As the equation for the polariton state energies contain the photon mode energy, the polariton gains an angular dispersion while the exciton does not. At normal incidence the energetic difference between the photon and exciton is defined as the detuning of the cavity (δ) [156]. By changing the

angle of incidence of the light we change the relative energies of the modes[156]. When the photon and exciton modes approach and cross each other, they overlap. At this point while the individual modes overlap the polariton branches form an anti-crossing[156]. An anti-crossing, or an avoided-crossing, is a point which two eigenvalues (photon and exciton contributions) of a Hermitian matrix (representing the polariton) cannot have the same value. This can be rationalised with a simple calculation of the energy gap between the upper and lower polariton branch ($E_+ - E_-$). We apply the criteria $E_c - E_{exc} = 0$ and simplify Equation 2.34 arriving at $2\hbar\Omega$. The energetic split at point of closest approach is known as the Rabi splitting (Ω_{Rabi}). Simply put, when the photon and exciton modes meet in energy, the gap between the upper and lower polariton branch is governed by the coupling strength between them. At zero coupling the two are able to meet and cross over each other ($\Omega_{\text{Rabi}} = 0$), while at non-zero coupling we find an energetic split. At strong coupling the Rabi-splitting becomes larger than the absorption linewidth of the exciton and an anti-crossing forms ($\Omega_{\text{Rabi}} > 0$)[156,158]. Scanning a wide range of angles, we produce a range of relative exciton and photon mode energies allowing us to visualise the anti-crossing (example given in Figure 2.16). An anti-crossing in the angle dependent reflectivity of a cavity is a proof of the presence of strong coupling[156].
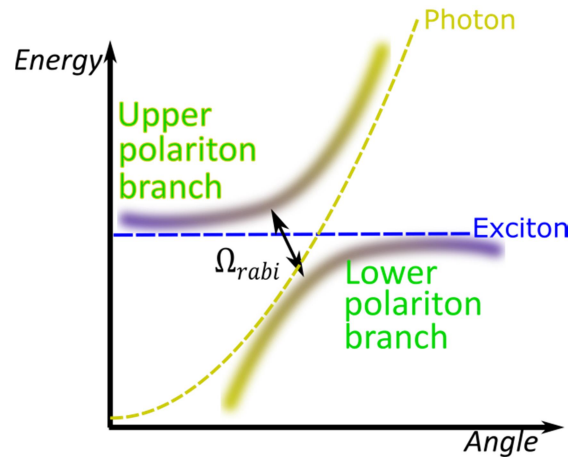
Figure 2.16: Diagram of an anti-crossing. Interaction of the Exciton (blue, dashed) and photon mode (green, dashed) produces an anti-crossing between the upper and lower polariton branch. We represent the dominant character of the polariton states through colour gradient. At the bottom of the lower polariton branch the character is mostly photonic (green) while at the top it is mostly excitonic (blue). The point of closest approach here shown at normal incidence then gives the energetic spacing between the branches (Rabi splitting) denoted as Ω_{rabi}.

The detuning not only affects the energy of the polariton branches but also the contributions from the exciton and photon components[156]. As the detuning is varied we change the relative contribution of the photon and the exciton to the polariton states, known as the mixing fraction[156]. This information is contained in the so-called Hopfield coefficients found in the eigenvector in Equation 2.32. The square of the Hopfield coefficients (a_c and a_{exc}) give the relative contribution of photon and exciton to the polariton with the sum always equal to 1[156].

In Figure 2.17 we show a summary of the modes and their angular dependent energies for the photon, exciton and polariton[156]. By inspection we can see how the photon and exciton fraction changes with angle. At normal incidence the polariton branch is the furthest from the exciton and has the largest photonic character[156], while states close in energy to the bare exciton show enhanced excitonic character. These highly excitonic states are sometimes known as the exciton reservoir; however, this is a hotly debated topic in the field of polariton research. Below we discuss the concept of the exciton reservoir and the currently competing theories.
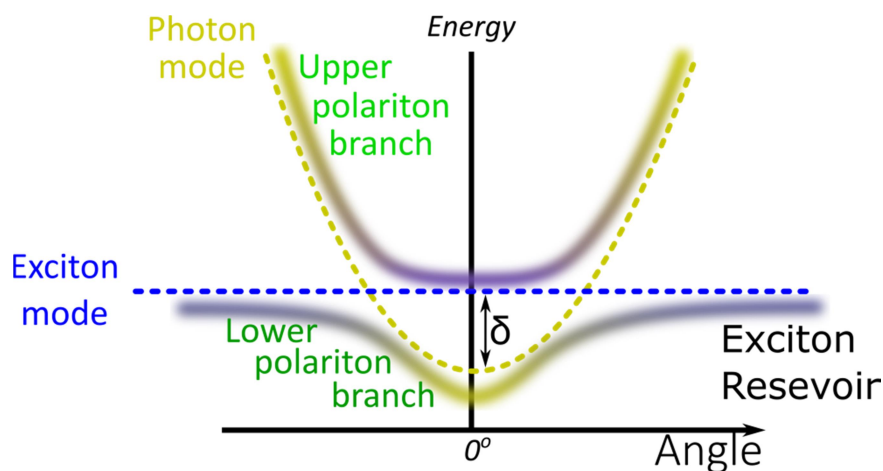
Figure 2.17: Angular dispersion of the polariton, photon and exciton states. Interaction of the Exciton (blue, dashed) and photon mode (green, dashed) produces the upper and lower polariton branch. We represent the dominant character of the polariton states through colour gradient. At the bottom of the lower polariton branch the character is mostly photonic (green) while at the top it is mostly excitonic (blue). The energetic spacing between the photon and exciton at normal incidence (detuning) is labelled, denoted with δ. The exciton reservoir defined as a pool of incoherent exciton states, is usually labelled at the top of the lower polariton branch.

The exciton reservoir and how it relates to the coupled exciton-polaritons is still a topic of discussion in the field of organic polaritonics. Some suggest that the majority of the excited molecules are not coupled and coherent in the delocalised polariton state[158,160], while others suggest the majority are coupled[161]. However, it should be noted that these studies are investigating molecules in different strong coupling regimes. The studies indicating most of the excited states are coupled and coherent are in the ultra-strong coupling regime defined as having a Rabi-splitting a significant fractions of the absorption energy [161,162].

In either case, in addition to the lower and upper polariton branches, a proportion of the excited states are localised and incoherent, with population thought to be mostly around the exciton at the top of the branch[163–167]. Studies have investigated the interplay between these three states. Virgili *et al*. used transient absorption with 15fs pulses to track the population of the UPB. After population, the UPB depopulates through emission of phonons to the exciton reservoir with a decay constant on the 100's fs time scale[168]. This is consistent with many polariton studies that find only weak emission from the UPB[158,169,170], unless measuring at low temperature where vibrations are supressed[171].

Afterwards, the lower polariton branch is the sole source of emission, with emission from the exciton reservoir only able to escape the cavity via some form of population mechanism into the polariton state[156,157]. In several systems it has been shown that the LPB emits with a lifetime similar to that of the bare film[158,172–174]. In these systems despite emission occurring through the polariton the relaxation dynamics of the exciton reservoir is unchanged from those of a bare film[173]. The similarity between the lifetime of the bare film and micro-cavity is related to the drastically different radiative rates of the polariton and the bare exciton. As the polariton lifetime is dictated by the cavity (~50fs)[174], they emit practically instantly compared to population of the polariton from the reservoir. As such the population of the LPB from the reservoir becomes a limiting factor in the lifetime of the system[175]. If the population from the reservoir is much slower than the intrinsic decay of the active material, we would expect the predominant population decay time to equal that of the bare exciton. However, it should be noted that it has been shown in some systems that the polariton can have decay constants nearly twice as long as the bare film[176]. Here authors compare their measured lifetimes to measured PL yields confirming the longer lifetime is consistent with their observations[176]. Once again this is in the ultra-strong coupling regime, so applicability to the other system discussed here is not clear. To understand the possible population mechanisms from the exciton reservoir it is instructive to compare two extreme cases of BODIPY-Br[158] (emissive) and a squaraine dye[177] (non-emissive).

For the BODIPY-Br, authors report efficient emission from the bare film with a PLQY of 15% (3ns lifetime)[158]. Moving to the strongly coupled geometry they measure approximately the same radiative lifetime and PLQY for the cavity[158]. Grant and co-workers suggest that after excitation there is a substantial population of excimers which are only weakly coupled to the light modes. These weakly coupled sites are able to emit and pump the polariton directly termed radiative pumping. As this is the dominant decay channel we expect similar lifetimes and PLQY for the cavity and the bare film[158], as is observed.

In the squaraine dye system, authors instead report an increase in the radiative lifetime and PLQY when moving from bare film (<0.01%) to microcavity (0.03%)[177]. As the radiative lifetime of the bare film is slower than that of the micro-cavity (and the PLQY is smaller) the radiative pumping mechanism cannot explain these observations. Ballarini and co-workers instead assign a vibrational scattering model in which population transfers from the exciton reservoir to the LPB via emission of phonons[177]. This model gained further evidence from Coles *et al*. who measured the emission from a series of cyanine J-aggregate filled microcavities[160]. The authors found that there was an enhancement in the emission intensity at four specific energy spacings between the LPB and the exciton reservoir. The authors found that the energy gaps which caused the enhancements aligned with Raman modes of the active material. As such the enhancement occurred when the energy difference between the reservoir and the polariton was at a phonon mode energy, suggesting a vibrational contribution to the population of the lower polariton branch[160].

The significant deviation between these two material systems can be explained via an interplay between the two mechanisms of population transfer. In the BODIPY-Br which undergoes efficient emission, the emission is channelled through the polariton in a radiative pumping mechanism. As such the high radiative rate of the polariton does not increase the emission lifetime of the system. However, in the squaraine dye where the radiative rate of the bare film is low, scattering to the polariton causes an increase in the population able to undergo radiative decay increasing the PLQY. The emission lifetime is then dictated by the population of the radiative states via vibrational scattering, increasing the time over which they measure emission.

The exact nature and interplay of these population mechanisms is still in debate, however, in all cases the dynamics of the polariton are dominated by the exciton reservoir, which is not thought to be affected by strong coupling[158,172–174,177]. Through this chapter we have introduced all the concepts required to understand the studies into singlet fission in Chapters 4,5 and 6. We now address the materials and methods used in these investigations in Chapter 3.

3. Materials and Methods:

3.1 Materials

Materials listed below were stored in an ambient atmosphere in the dark unless specified otherwise. Excluding anhydrous solvents which were kept in a nitrogen atmosphere, all solvents, polystyrene and bathocuproine (BCP) were communal and exposed to oxygen. Throughout this thesis solvents and molecules were either purchased at spectroscopy grade from Sigma-Aldrich or were synthesised by collaborators where stated. In general, solutions are made in oxygen and held in a quartz 1mm path cuvette with stopper and parafilm. Solutions were used on the day of creation where possible. If stored for longer periods, UV-Vis absorption of the sample was checked for degradation before measurements were taken, in addition to after the measurements. Below details of each molecule are given along with details of sample preparations.

3.1.1 Carotenoids

Carotenoids used for monomer and solution aggregate measurements where either purchased from Sigma Aldrich at 97% purity and used without further purification (β-carotene, astaxanthin, echinenone) or isolated from *Rhodobacter sphaeroides* as described in Chi *et al.*(Spheroidenone)[178] by Jack Chidgey (University of Sheffield). Structures for each carotenoid are shown in Figure 3.1, β-carotene (a), astaxanthin (b), echinenone (c), spheroidenone (d).

3.1.2 Oligo(thienylene-vinylene)

OTVs (or oligo(thienylene-vinylenes)) are an oligomer variant of the PTVs (or poly(thienylene-vinylenes)). These molecules were synthesised for possible use in solar cell technology[27,179–183]. Oligomers of different lengths used here were synthesised by Iain Andrews in the Heeney group (Imperial College London). The structure of the repeat unit in the OTVs is shown in Figure 3.1e.

3.1.3 Diphenyl-anthracene

Diphenyl-anthracene (or DPA) is an anthracene derivative commonly used in up-conversion studies in conjunction with Pt-porphyrin[184,185]. DPA was purchased from Sigma-Aldrich at 97% purity and were used without further purification. The chemical structure of DPA is shown in Figure 3.1f.

3.1.4 Platinum-Porphryin

Pt-porphryin is commonly used as a triplet sensitizer and to enhance emission through the heavy atom effect. Pt-Porphyrin was purchased from Sigma Aldrich at 98% purity and were used without further purification. The structure of Pt-Porphyrin is shown in Figure 3.1g.

3.1.5 DPPT

DPPT (or diketopyrrolopyrrole-thiophene), was synthesised by Kealan Fallon (Columbia University). For details of the synthesis process we refer the reader to Ref[186]. The structure of DPPT is shown in Figure 3.1h.

3.1.6 INDB

INDB (or 3,10-dibromo-7,14-bis(4-((2-octyldodecyl)oxy)phenyl)diindolo[3,2,1-de:3',2',1'-ij][1,5]naphthyridine-6,13-dione), was synthesised by Kealan Fallon (Columbia University). For details of the synthesis process we refer the reader to Ref[186]. The structure of INDB is shown in Figure 3.1i.

3.1.7 TIPS-tetracene

TIPS-tetracene (or 5, 12-bis((trilsopropylsilyl)ethynyl)-tetracene), was synthesised and provided by John Anthony (University of Kentucky). Due to the oxygen sensitivity of this molecule it was always kept in a nitrogen atmosphere. For details of the synthesis process we refer the reader to Ref[186,187]. The structure of TIPS-tetracene is shown in Figure 3.1j.
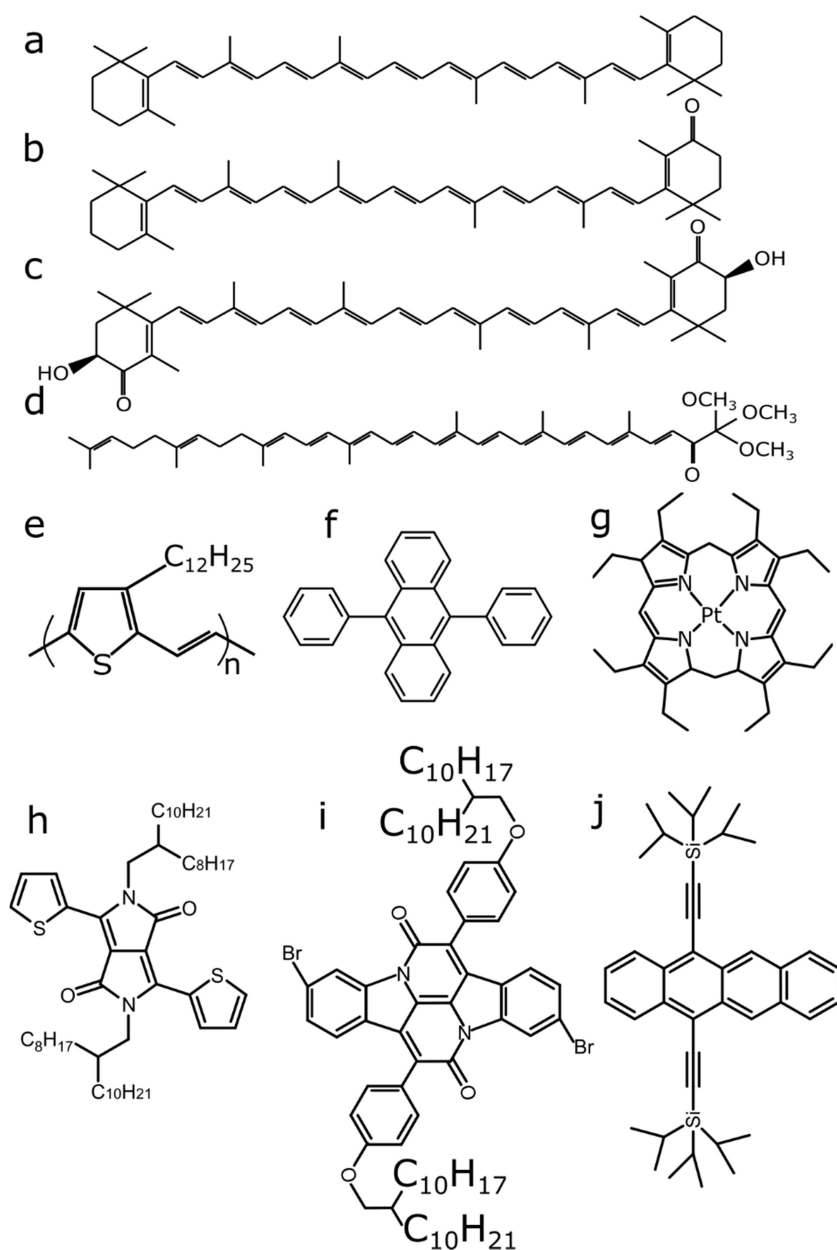
Figure 3.1: Chemical structures of materials. The chemical structure of the molecules used during this thesis are shown. (a) β-carotene, (b) echinenone, (c) astaxanthin, (d) spheroidenone, (e) OTVs (oligo(thienylene-vinylene)), (f) diphenyl-anthracene, (g) platinum-porphryin (h) DPPT, (i) INDB, (j) TIPS-tetracene.

3.1.8 Polariton Film and Cavity Samples:

In Chapter 4 we investigate the effect of strong light-matter coupling on triplet production pathways in a series of systems. The sensitisation up-conversion system of diphenyl-anthracene blend solutions were prepared in a nitrogen-filled glovebox with anhydrous toluene, at a diphenyl-anthracene concentration of 30 mg/mL and a diphenyl-anthracene:Pt-porphyrin:polystyrene ratio of 50:1:15 (wt/wt). Solutions were heated at 90°C for 1 day and then filtered with a polytetrafluoroethylene filter (400 μm). Films were spin-coated from hot solution.

Solutions of DPPT and INDB were prepared in air, at a concentration of 6.25 mg/ml in toluene with an additional 25 mg/ml of polystyrene. To control for the effects of oxygen, DPPT solutions were also prepared in a nitrogen-filled glovebox with anhydrous toluene. TIPS-tetracene solutions were prepared in a nitrogen-filled glovebox with anhydrous toluene, at a concentration of 50 mg/ml. Thin films of all materials were spun on quartz-coated glass substrates for reference measurements. For oxygen sensitive samples we used the additional encapsulation protocol. Within a nitrogen-filled glovebox, films were covered with a glass microscope coverslip of larger dimension than the substrate, using strips of 100 μm-thick carbon tape to prevent the surfaces from touching. We mixed a two-part fast-drying epoxy (araldite) within the glovebox and applied this liberally around all four edges of the sample substrate, ensuring a complete seal with the coverslip. A second coverslip was applied to the reverse of the substrate to create a full encapsulation and a flat surface on either side of the sample.

To prepare microcavities, we first deposited a thick (150-200 nm, 0.1nm/s deposition rate) Ag mirror on quartz-coated glass substrates with a thermal evaporator. Substrates were first cleaned before use by sonication in Hellmanex lll, Acetone and then IPA for 10 minutes each. Films of the desired thickness (~200 nm, aiming for λ-mode microcavities) were spin-coated on top, within a glovebox in the case of oxygen-sensitive systems. To determine film thickness for a given spin speed we deposited a test film of each material at 2000 and 4000rpm (50 seconds) and measured the film

thickness with a stylus profilometer (Dektak 150 surface profiler). Using this calibration, a series of spin speeds (1000-6000rpm, 50 seconds spin) were used to create cavities at different thicknesses. We then evaporated the semi-transparent top Ag mirror (25-30 nm, 0.01nm/s deposition rate) to complete the microcavities. Because of the high sensitivity of triplet-related dynamics to atmospheric oxygen, all samples were encapsulated prior to removal from the glovebox, except for select DPPT films and microcavities used to study the oxygen dependence of our observations. We used the same protocol as for the spin cast films described above.

Some reference samples were also prepared entirely within the thermal evaporator used for mirror deposition. These were prepared with either a 'thick' (73 nm) or 'thin' (20 nm) layer of TIPS-tetracene. For thick samples the organic layer consisted of a 20-nm layer of bathocuproine (BCP, Sigma Alrich), the layer of TIPS-tetracene and a final 20-nm capping layer of BCP. BCP was evaporated at a rate of 0.3 Å/s, and TIPS-tetracene at a rate of 0.3 Å/s. For the 'thin' samples the organic layer consisted of a 90-nm layer of BCP, a layer of TIPS-tetracene of 20 nm and a final 90 nm capping layer of BCP. BCP was evaporated at a rate of 1 Å/s for these samples, and TIPS-tetracene at a rate of 0.3 Å/s. Mirror deposition and encapsulation were performed identically to the other samples. To ensure accuracy in the organic deposition layers, a film of approximate thickness is deposited and measured with a Dektak system as above. This calibration is used to tune the tooling factor which is a measure of the speed at which the material evaporates. Once again samples were encapsulated with the same method described above.

In Chapter 4 we also include a series of control measurements, details of these preparations are summarised in Appendix C.

3.1.9 Maquette Proteins

Protein-bound carotenoid aggregates studied in Chapter 6 were produced and characterised in collaboration with Dr. George Sutherland (University of Sheffield). Previous studies of carotenoid aggregates have found production of aggregates time consuming and unreliable[23–25]. Aggregates form different structures depending on a variety of factors, such as relative concentration, temperature and PH[25,188,189]. Furthermore, aggregates tend to continue to grow, eventually growing large enough to fall out of solution. To circumvent this issue, we use simplified man-made proteins known as Maquettes.

Maquette proteins consist of 4 α-helical structures which when exposed to water fold into a pocket-like structure. This is achieved by engineering the binding of amino acids, and placing hydrophobic and hydrophilic acids on specific binding sites[190–192]. The overall structure of the maquette protein is a single chain of 4 α-helices joined by linkers (shown in Figure 3.2)[193]. As the carotenoids are hydrophobic they preferentially enter the pocket causing aggregation[193]. As the protein pocket is small, we expect a consistent aggregate structure and size with an increase in stability due to the lack of continued growth. In the current study we use the single chain protein variant to greatly increase the stability, reproducibility and practicality of carotenoid singlet fission studies. The method of protein bound aggregate production is discussed in detail in Ref[194] and in brief below.
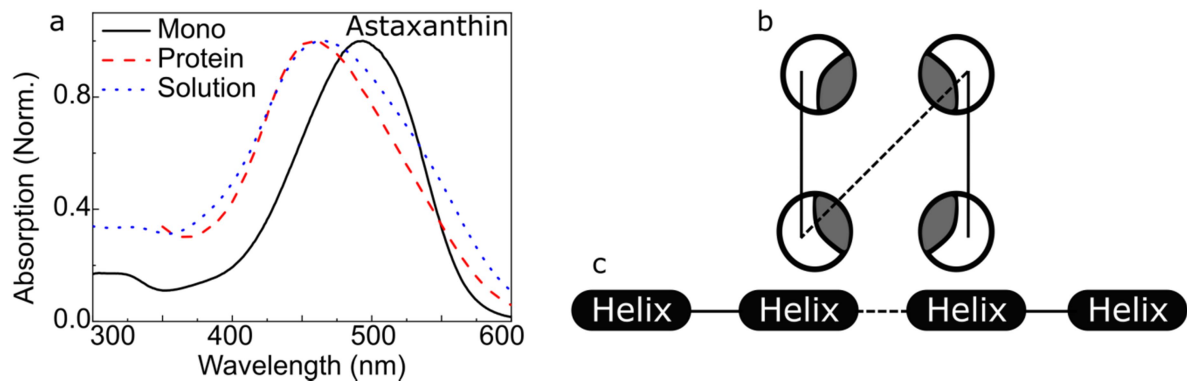
Figure 3.2: Protein and aggregate structure. (a) Comparison between monomer, solution based aggregate and protein-bound aggregate ground state absorption spectra for astaxanthin. (b) Protein structure with single chain design (unfolded structure shown in (c)). In (b) the white sections represent hydrophilic amino acids, while the coloured inner sections representing hydrophobic amino acids.

Plasmid DNA was prepared from JM109 cultures using FastGene™ (Nippon Genetics) plasmid purification kit, according to the manufacturer's instructions. Specific changes to plasmids were achieved with the QuikChange II Site-Directed Mutagenesis kit (Agilent), according to the manufacturer's instructions. For all samples the desired strains of *Escherichia coli* were grown as single colonies in agar media containing the produced plasmids and expressed the desired protein. Afterwards the protein was purified by immobilised metal affinity chromatography[195]. Immobilised metal affinity chromatography involves washing the protein sample with a metal (Nickle Sulfate) that binds selectively with the protein of interest (Histidine in the maquette). The solution is then washed through a column of resin pellets removing anything that doesn't bind. Afterwards the column is rinsed with buffer containing 5mM imidazole that breaks these bonds, allowing separation and so purification of protein types[195].

The purified protein is suspended in buffer (causing it to fold) and mixed with a solvent solution of carotenoid monomer and DMSO (1 carotenoid: 10 protein). Due to hydrophobic forces the carotenoids form aggregates and sequester themselves within the protein, creating molecular clusters of a stable size. Excess pigment found outside of the protein pocket is then removed using ion exchange chromatography leaving only protein bound aggregates. It is well known that proteins

have a charge state dependent on the pH of their surroundings. This is due to the ionisable structures within the protein causing a charge enhancement at given pH values[196]. Anion exchange chromatography uses this protein specific net charge to bind the desired protein as it is passed through a column of charged resin[197]. Afterwards the column is washed with buffers of progressively higher salt content (0-1M NaCl), as the salt concentration increases (brings the pH closer to 7 reducing the charge of the protein) more of the proteins unbind leaving pure samples at high salt content[197].
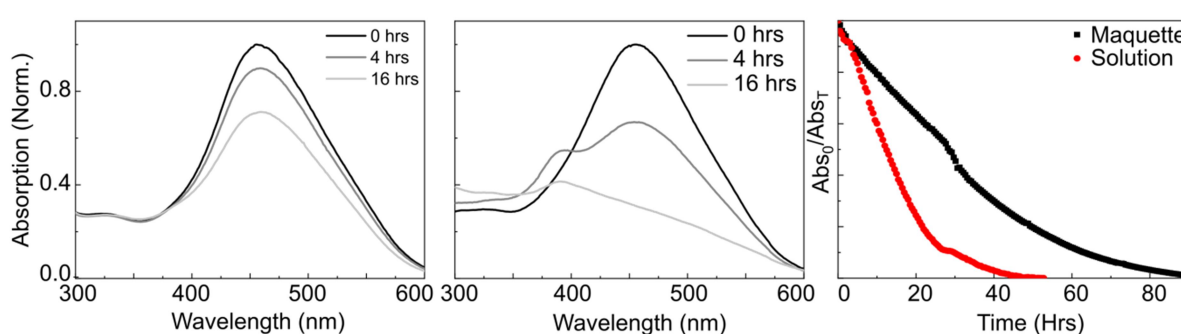
Figure 3.3: Protein aggregate stability measurements. Absorption comparisons for solution-based aggregates (a) and protein bound aggregates (b) after 0, 4 and 16 hours of light exposure, normalised to time zero. Also included is a normalised change in peak absorption against exposure time for both samples (c). Measurements carried out by George Sutherland (University of Sheffield).

To characterise the influence of the protein environment we expose both solution and protein-bound samples to light to investigate their stability (measurements performed by George Sutherland (University of Sheffield)). Figure 3.3 shows normalised absorption spectra at 0, 4 and 16 hours exposure for both samples, normalised to time zero. While the solution aggregates decay to zero absorption by 40 hours, the protein samples survive for almost 100 hours. Furthermore, aggregates formed in solution continue to grow over time causing a significant change to the ground state absorption spectrum within 4 hours of production. Measurements then sample the aggregates as they change in structure causing potential artefacts. However, for protein-bound samples we see the same line shape for the entirety of the decay suggesting the samples remain the same size and viable for over 50 hours, long enough for measurements to be completed.

In addition to stability measurements, reconstitutions were repeated to ensure factors such as freeze thawing during storage don't degrade the proteins. In Figure 3.4 we present ground state absorption, transient absorption spectra and transient absorption kinetics for each reconstitution method. We find no change in any of these measurements with the different preparation methods (summarised in Table 3.1). These measurements confirm that the maquette sample preparation creates reproducible and stable carotenoid aggregates.
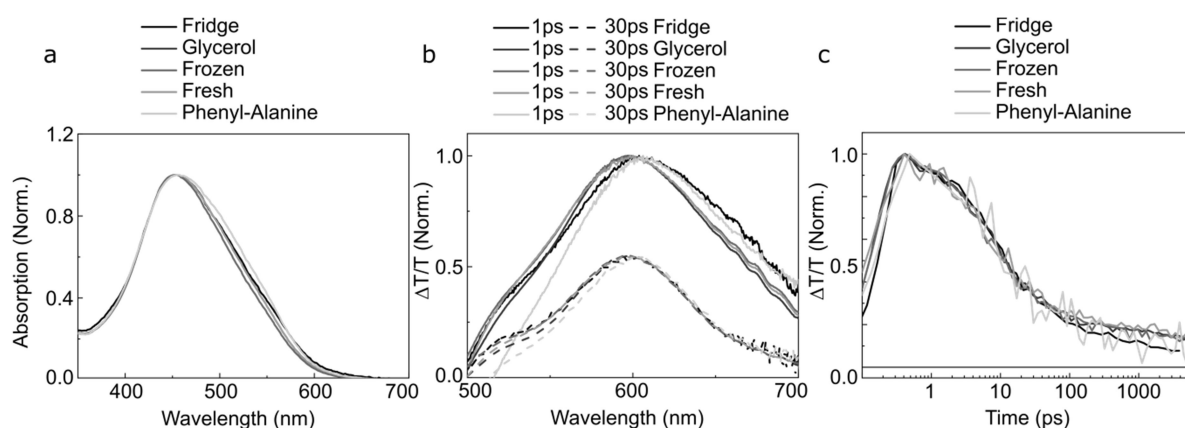
Figure 3.4: Comparison of storage and preparation techniques. (a) Ground state absorption of all samples prepared, we find no change in the ground state absorption suggesting we have minimal degradation or change between the samples. (b) Transient absorption spectra taken following 400nm excitation (3mW power) at 1-3ps and 30-40ps delay. (c) Transient absorption kinetics averaged over 600-610nm following 400nm excitation (3mW power). Sample preparation methods are detailed in Table 3.1.

Table 3.1: Summary of sample preparation methods.

Sample name	Preparation	Storage Conditions
Fridge	Alanine maquette[1]	Stored for ~1 week in a fridge
Glycerol	Alanine Maquette reconstituted in a ~50% Glycerol solution	Made on day of measurement
Frozen	Alanine maquette	Stored for ~1 month at -80 degrees
Fresh	Alanine maquette	Made on day of measurement
Phenyl-Alanine	Phenyl-alanine	Made on day of measurement

[1] Alanine maquette is used throughout chapter 6.

3.2 Methods

Here we discuss the experimental methods used throughout this body of work. Specifics of measurements are given in each chapter where necessary, in the following section we given a more general insight into the methods used.

3.2.1 Ground State Absorption

Ground state absorption is a steady state technique which measures the optically allowed transitions from the ground state to higher-lying states. As such it is a measure of the energy of the lowest optically accessible states with relative intensities governed by the transition dipole moment of the transition[40]. Throughout this thesis ground state absorption measurements were taken using a fluoromax spectrofluorometer (Horiba Jobin Yvon) in the 200-800nm spectral range. Light is directed at the sample from a lamp and the transmitted light is measured (I_T). We also measure a reference sample of solvent in a cuvette to find light transmitted without the molecules (I_0). The absorbance (OD) is then given by the below Equation (3.1), which can be related to the parameters of the molecule under test through the Beer-Lambert law[40].

$$A \, (\text{OD}) = \, -\log_{10} \left(\frac{I_T}{I_0} \right) = \, \varepsilon \text{cl} \qquad (3.1)$$
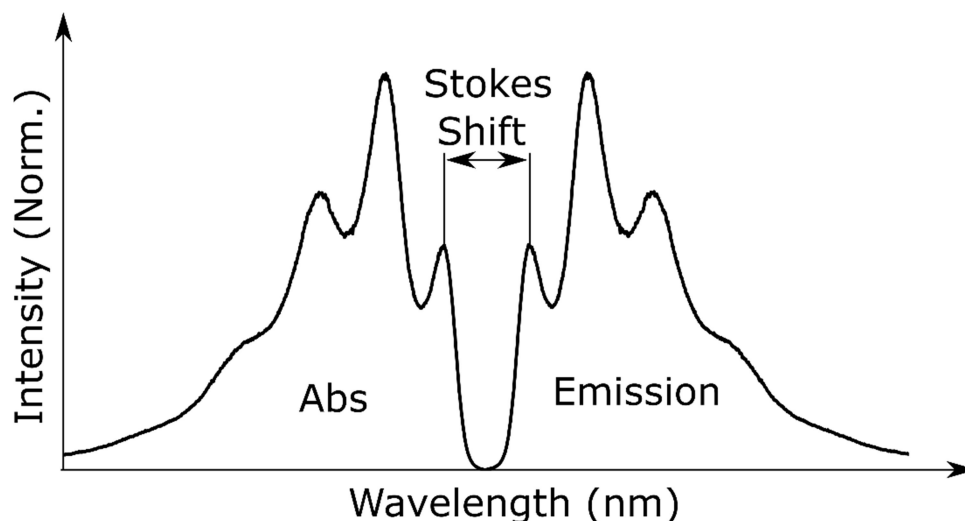
Figure 3.5: Example absorption and emission spectra. Absorption and emission are a mirror image with a stokes shift between the energies of the 0-0 peaks. In real samples, geometric reorganisation leads to changes in the absorption and emission spectra which reduces the mirror image relationship.

3.2.3 Photoluminescence Spectroscopy

Photoluminescence spectroscopy can be thought of as the inverse of ground state absorption as it involves the deactivation of an excited molecule to the ground state by emission of a photon. These photons are then collected. Photoluminescence gives an estimate of the emissive state energies. According to Kasha's rule, emission occurs from the lowest excited state, meaning photoluminescence describes the lowest energy optically allowed transition. If the emitting state and absorbing state are the same, with only minor geometric reorganisation, the absorption and emission are a mirror image of each other[198]. Emission occurs from the bottom vibrational level of the excited state to all vibrational levels of the ground state. This is the reverse for ground state absorption causing a reverse in the peak intensity pattern shown in Figure 3.5. The above consideration suggests the 0-0 peaks of emission and absorption should be isoenergetic. However, if there is a difference between the excited and ground state geometries, relaxation occurs after light absorption. As a result, the vertical transition (absorption, at the ground state geometry) and relaxed (emission, at the excited state geometry) energies differ causing a Stokes shift between the 0-0 peaks.

Time-resolved photoluminescence measurements were acquired with an Andor iStar ICCD (Intensified charge coupled device), coupled to a Shamrock 303i spectrograph. Excitation was provided by an Nd:YAG Q-switched laser (Innolas Picolo) tuned for second-harmonic (532 nm) or third-harmonic (355 nm) output and synchronized with the ICCD. Nominal pulse duration is 600 ps, at a typical repetition rate of 5 kHz. Excitation and collection were through the same aspheric condenser lens (focal length=3.2 mm, Numerical Aperture=0.76), with the excitation incident on the sample at 40°.
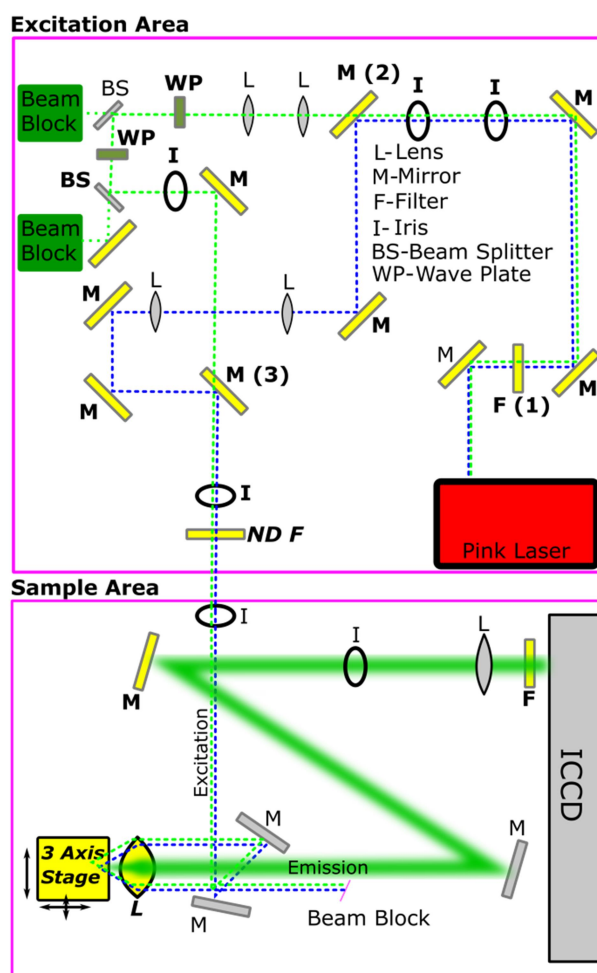
Figure 3.6: Diagram of the photoluminescence spectroscopy setup. The setup is used throughout Chapter 4 and 5. Letters correspond to optical components as stated in the legend, ICCD refers to the intensified charge coupled device detector.

3.2.3 Transient Absorption Spectroscopy

The basic components of a transient absorption setup are summarised in Figure 3.7. In short, a pump pulse excites the sample creating a significant excited state population. The pump is followed by a second pulse, which probes the absorption spectrum of the excited states. Pump and probe pulses are spatially overlapped in the sample with pump much larger than probe to ensure the probe only measures the excited region of the sample. A mechanical chopper is used to block half of the pump pulses, effectively collecting a probe spectrum with (T^{on}) and without (T^{off}) the pump. The two are then processed using Equation 3.2, which gives the measured differential transmission signal. The transmission is then normalised by T^{off} to allow a comparison between different excitation conditions and experimental setups. By varying the delay between the two pulses we can probe the population of the excited states over time.

$$\frac{\Delta T}{T} = \frac{T^{on} - T^{off}}{T^{off}} \tag{3.2}$$

As the technique measures a differential signal it becomes sensitive to small changes in population (10^{-5}). In addition to differential transmission it is also common to present data in differential absorption. The derivation of differential absorption is shown below.

Starting with Equation 3.1 and setting transmittance before hitting the sample (I_0) to 1 we arrive at the relation $A = -\log_{10}(T)$, where A is the absorption and T is the transmission. Rearranging and making the distinction between pump on and off we arrive at Equation 3.3 and 3.4.

$$T^{on} = -10^{-A_{on}} \tag{3.3}$$

$$T^{off} = -10^{-A_{off}} \tag{3.4}$$

Putting these into the expression for $\frac{\Delta T}{T}$ and rearranging we arrive at the expression for differential absorbance (ΔA) (Equation 3.5). For small intensities ($\frac{\Delta T}{T} \sim 10^{-3}$) the conversion can be approximated as Equation 3.6.

$$\Delta A = -\log_{10}\left(1 + \frac{\Delta T}{T}\right) = -\left((-A_{on}) - (-A_{off})\right) \tag{3.5}$$

$$\Delta A = -\frac{\Delta T}{T} \div 2.3 \qquad\qquad (3.6)$$

An additional component that can be included is a reference beam which reduces noise in the measurements. The probe beam is split into probe and reference with reference passing through the unexcited volume of the sample for both pump on and off. Each acquisition is divided by the reference which reduces noise from shot-to-shot fluctuations in the laser and allows lower powers to be used and as such reduces the artefacts we discuss below[199].
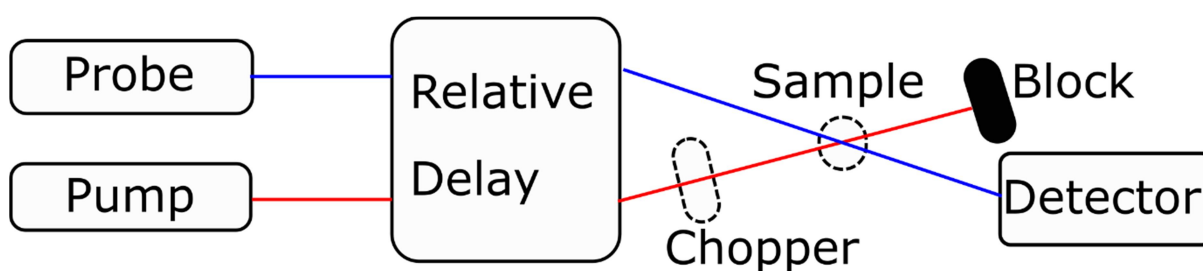
Figure 3.7: General components of a transient absorption setup.

During a transient absorption measurement there are generally three categories of signal, ground state bleach, stimulated emission, and photo-induced absorption[200]. The first, ground state bleach, is a measure of the depletion of the ground state population[200]. After excitation (pump) some molecules are excited, leaving less population in the ground state, meaning fewer probe photons are absorbed compared to pump off[200]. In differential transmittance this is represented by an increase in transmission with the pump compared to probing without the pump, as such it is a positive signal[200]. Likewise, when plotting differential absorption, ground state bleach results in a reduced absorption and is a negative signal (Figure 3.8) [200]. As the ground state bleach is directly due to a depletion of the ground state, the TA feature matches the ground state absorption of the excited molecule[200]. The rise of the ground state bleach describes the instantaneous event of photon absorption and as such will be instrument-limited. However It is also possible for ground state bleach signals to form dynamically by processes that excite molecules after the initial pulse[200]. An example of this is heterogeneous combinations of materials such as in sensitization. By exciting one of the molecules,

only the ground state bleach of that molecule is visible. After some time, transfer of energy to the second molecule occurs, exciting them from their ground state to an excited state, resulting in a ground state bleach signal after time zero at the ground state absorption wavelengths of the second molecule[200].
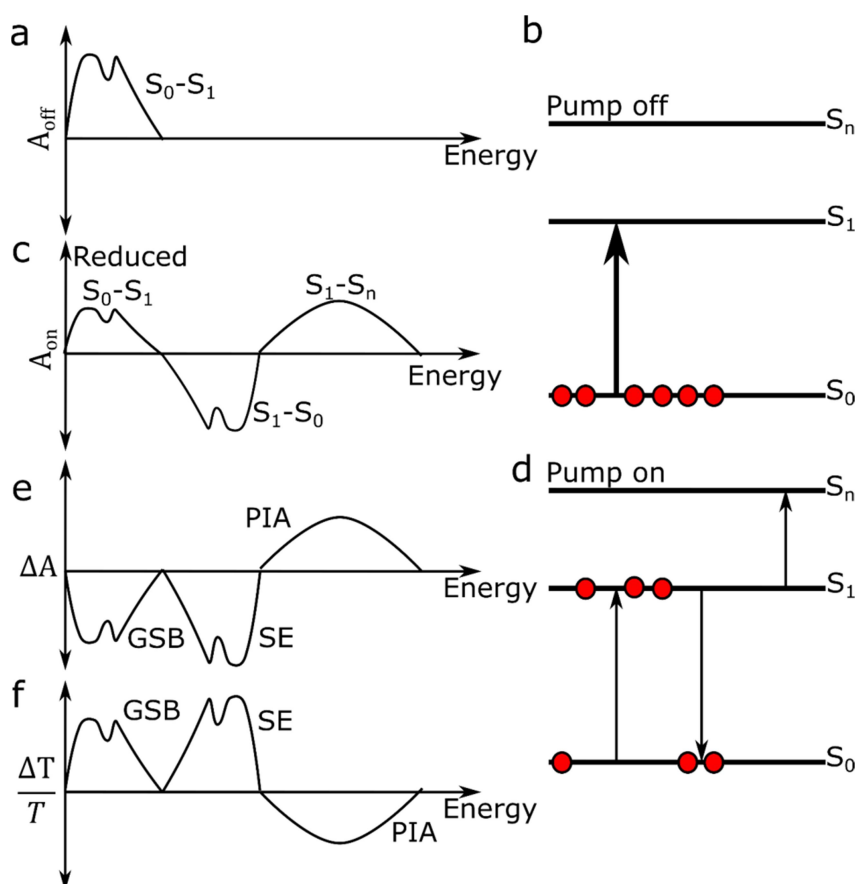
Figure 3.8: Example signals collected in a transient absorption experiment. (a) shows the expected signal for pump off with only the ground state absorption visible. (b) shows (a) represented by state population. The only transitions are from the ground state to the first optically active state. (c) shows the signal with pump on. Here due to depopulation of the ground state the overall ground state absorption is lower. Additionally, there are signals from stimulated emission and excited state absorptions. (d) shows (c) represented by state populations. A reduced ground state absorption, emission from first excited state to ground and absorption from the first excited state to a higher lying state. Panel (e) and (f) represent the combination of pump on and off in both differential absorption (e) and differential transmission (f) units. Through we use GSB, PIA and SE to stand for ground state bleach, photoinduced absorption and stimulated emission respectively.

The second category of signal is due to emission stimulated by the probe. After excitation the probe pulse interacts with the excited state population causing photons of the correct energy to stimulate a transition from the excited state to the ground state[200].

Stimulated emission is observed as a positive signal in differential transmission (negative in differential absorption, Figure 3.8) [200]. The third signal, photo-induced absorption, represents the absorption of an excited state[200]. Photo-induced absorption results in a negative signal in differential transmission (positive in differential absorption, Figure 3.8) [200].

In addition to the signals described above there are also several sources of artefacts that complicate the spectra. These are broadly characterised as thermal effects and coherent artefacts. The first only occurs in materials which exhibit a temperature dependant absorption spectrum such as P3HT[201]. In P3HT it has been shown that the ground state absorption, and therefore the ground state bleach, exhibit a blue-shift at high temperatures[201]. When the pump pulse hits the sample, the temperature rises locally causing a different response upon probing[201]. The shift will then cause a residual signal when comparing pump on and off that adds an artefact to the measurement. By measuring temperature dependant ground state absorption it is possible to model the features and correct them[27,201]. Another method is to take transient absorption measurements on substrates with different thermal conductivities. The substrates then remove heat from the sample at different rates identifying thermal artefacts by the change in their kinetics[202].

The second source of artefacts are grouped under the name coherent artefacts. Signals relevant to the electronic states of the molecule only exist when the probe pulse is incident after the pump. During the pump-probe overlap the signals are no longer sequential and instead excitation and measurement occur simultaneously. As a result, these signals do not represent the true population dynamics of the system and signals within the overlap should be carefully analysed[200]. During pump-probe overlap cross phase modulation occurs which is a change in the refractive index of the cuvette or surrounding medium as a result of the strong pump pulse[203]. This modulation causes a change in phase of the weak probe pulse which modulates its spectral response[200,203,204]. It is possible to characterise this signal and remove it from the data however for most measurements it is enough to discount the pump-probe overlap region from data analysis.

A final consideration is the effect molecular geometry has on the signal. The response of the molecule to the incident electromagnetic field depends on the orientation of the molecules transition dipole moment relative to the field. A distribution of dipole orientations in the solid state can affect the measurement depending on the relative polarisation direction of the pump. As a result the polarisation of the pump and probe are set to the 'magic angle' of 54.7^{o} which cancels out the effect[200,205].

3.2.4 Transient Absorption Systems

The pump pulses were created by non-colinear optical parametric amplification (NOPA) or in a commercial OPO (Spectra Physics). The probe pulses were created via white light supercontinuum. White light generation occurs when a weak seed pulse (800nm) is focused onto a sapphire crystal. As the pulse travels through the non-linear medium, the refractive index varies with the pulse intensity[206]. The phase of the pulse is then modulated by the oscillating refractive index of the medium[206]. As a result, the pulse itself modulates its own phase known as self-phase modulation. As the wave front of the pulse has a spatial intensity profile, so does the magnitude of the phase modulation[206]. This spatial component of the modulation distorts the wave front causing the well-studied phenomenon of self-focusing and self-defocusing. For pulsed lasers there is a temporal change in laser intensity giving a temporal phase modulation[206]. As the time derivative of the wave is the angular frequency, a change in the phase also modulates the frequency. Thus self-phase modulation causes a self-broadening effect, which in conjunction with self-focusing provides an intense and broad probe spectrum[206].

The majority of the experimental data was taken using a modified version of a commercial Helios Fire system (Ultrafast Systems). The Helios is pumped by a Ti:Sapphire regenerative amplifier (Spitfire, Spectra-Physics) providing 800 nm pulses (~40fs, 10kHz, 1.2mJ). The pump was produced

by a commercial OPA (TOPAS prime, Light Conversion) pumped by the 800nm pulses from the Ti:Sapphire laser. The probe was produced by white light generation in a sapphire crystal. The Helios setup does not include a reference beam and uses magic angle before the sample.

The second setup, from the University of Cambridge, is a homebuilt system pumped by a Ti:Sapphire laser (Solstice, SpectraPhysics) producing 3.5W, of 1kHz repetition rate, ~90fs pulses at 800nm. The home-built system includes a reference beam and uses a NOPA for the probe and pump pulses. This setup was operated and maintained by Andrew Musser (University of Cambridge). The high resolution (<30fs pulse) data was taken in collaboration with Giulio Cerullo and Frederico Branchi at the Politecnico di Milano. The system is the same as the home-built system at the University of Cambridge, however the pump pulses are optimized to the broadest possible range (~100nm). As the time resolution is limited by the time-bandwidth product[200], the larger bandwidth allows a shorter pulse. The pulses are compressed with chirp mirrors to achieve near transform limited pulses (~no chirp).

The following chapter describes an investigation of singlet fission, intersystem crossing and triplet up-conversion in the presence of strong light-matter coupling. I produced and measured all samples within the work, however, the project was a collaboration across several universities with molecules synthesised by Kealan Fallon (Columbia University) and John Anthony (University of Kentucky), and code provided by Rahul Jayaprakash (University of Sheffield). Where these aspects are discussed in the text, credit is given to the appropriate researchers.

4. Manipulating Matter with Strong Coupling: Harvesting Triplet Excitons in Organic Exciton Micro-cavities

4.1 Summary

Exciton-polaritons are quasiparticles with mixed photon and exciton character that demonstrate rich quantum phenomena, novel optoelectronic devices and the potential to modify chemical properties of materials. Organic semiconductors are of current interest for their room-temperature polariton formation. However, within organic optoelectronic devices, it is often the 'dark' spin-1 triplet excitons. These triplets have been largely ignored in treatments of polariton physics. Here we demonstrate polariton population from the triplet manifold via triplet-triplet annihilation, leading to polariton emission that is longer-lived (>µs) even than exciton emission in bare films. This enhancement arises from spin-2 triplet-pair states, formed by singlet fission or triplet-triplet annihilation, feeding the polariton. This is possible due to state mixing, which – in the strong coupling regime – leads to sharing of photonic character with states that are formally non-emissive. Such 'photonic sharing' offers the enticing possibility of harvesting or manipulating even states that are formally dark.

4.2 Background

The exploration of new material properties typically faces significant practical constraints from cumbersome synthesis and morphological control. In recent years, however, it has been shown that many materials properties can be non-synthetically tuned with confined light to form exciton-polaritons[161,207,208], pointing the way to an entirely new field of microcavity-controlled materials[176,209–212]. These exciton-polaritons are quasi-particles mixing light (photon) and matter (exciton) components, leading to rich quantum effects[213–217] and potential optoelectronic applications[154,207–209,218–221]. Exciton-polaritons are formed by placing a semiconductor between two metal mirrors to create a Fabry-Perot microcavity in which light of the correct angle and wavelength can be trapped (Figure 4.1a). If the material within the cavity has a strong exciton absorption, in resonance with the trapped photon mode, the exciton and photon can couple and form hybrid polariton states (Figure 4.1b). As a consequence of the mixed exciton-photonic character of these states, a measurement of reflected light as a function of incident angle demonstrates the typical dispersion shown in Figure 4.1c, with the upper polariton branch (UPB) and lower polariton branch (LPB) split around the excitonic energy, as discussed in Chapter 2.

Most studies of exciton-polariton physics have focussed on inorganic semiconductor systems[154,213,214,217,218]. However, organic semiconductors have the advantage of high oscillator strengths[222], which leads to Rabi splittings in the range 0.1-1eV[161,162,207,222–224]. Organic semiconductors also have low dielectric constants (ε_r typically 2-4)[40]. Consequently, photoexcitation results in bound electron-hole pairs known as Frenkel excitons. Such high binding energies allow for room temperature polariton formation observed now in several organic semiconductor microcavities[170,215,225]. The tightly bound Frenkel excitons also exhibit complex photophysics, with numerous radiative and non-radiative decay pathways possible following initial photoexcitation (Figure 4.1d)[226]. These pathways are rarely treated in detail in organic exciton-polariton studies, where the focus is primarily on 'bright' singlet (spin-0) excitons. However, intermolecular relaxation

to form weakly emissive excimers can significantly influence microcavity emission dynamics[158], and theoretical attention increasingly has started to focus on the impact of other non-radiative photophysical processes[210–212]. We focus here on the role in these systems of triplet (spin-1) excitons. Triplet excitons and their management are critical in organic semiconductor devices such as solar cells[8,73,227,228]. For example, 75% of excitons formed by electron-hole recombination in optoelectronic devices are triplets due to spin statistics.
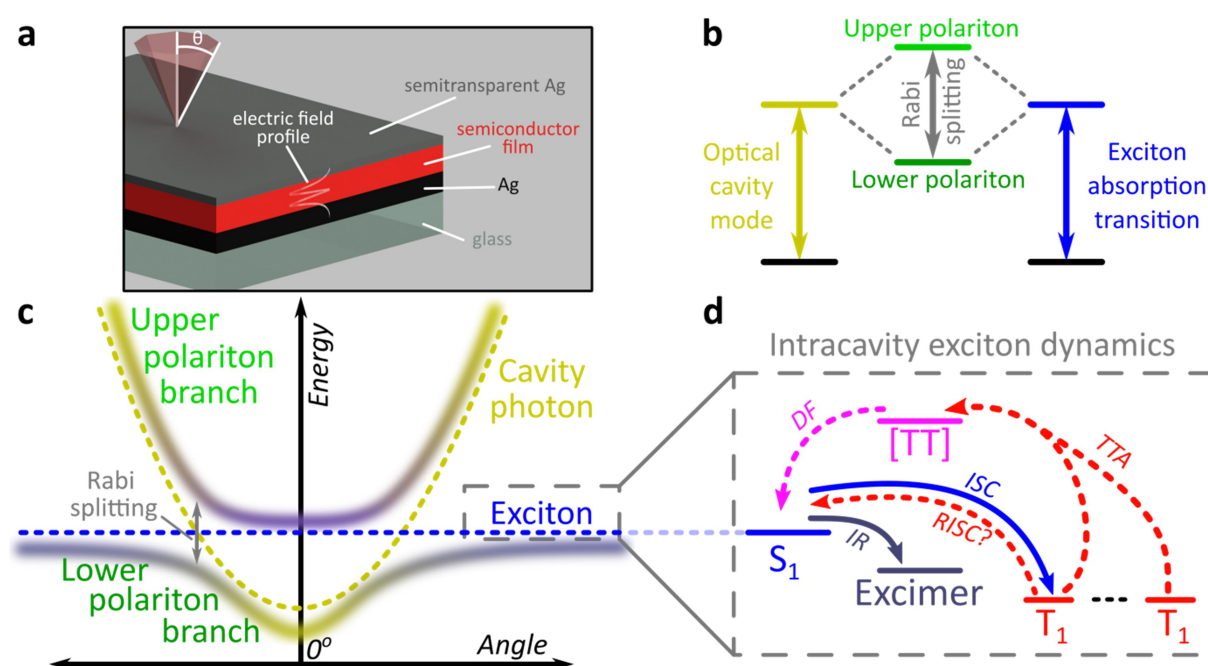
Fig 4.1: Strong light-matter coupling in optical microcavities. (a) Microcavity structure. A thin film of organic semiconductor or dye dispersed in neutral polymer matrix is deposited between two mirrors, here Ag. The thickness determines the energy of the confined photonic mode and thus the profile of the electric field inside the cavity, shown here for the λ-mode. Reflection and emission from the cavity are measured as a function of angle θ, with 0° defined as normal to the cavity surface. (b) When the cavity mode and the excitonic transition of the semiconductor are near resonance, these two states can couple, forming hybrid upper and lower polariton states. (c) Unlike the exciton (blue), the cavity mode (gold) exhibits distinct angular dispersion. Coupling between the two yields dispersed polariton branches, with characteristic anti-crossing at the exciton energy. Shading indicates the degree of photonic (gold) vs excitonic (blue) character in the state. (d) Typical excitonic processes possible within organic semiconductor films. IR: intermolecular relaxation, (R)ISC: (reverse) intersystem crossing, TTA: triplet-triplet annihilation, DF: delayed fluorescence. Solid arrows indicate processes known to modify exciton-polariton emission dynamics, while dashed arrows show processes not explored within microcavities.

It is generally thought that only states with large oscillator strength couple to the photon in a microcavity, with triplet states considered a loss channel in organic exciton-polariton systems[224]. Because of progress in electrically injected polariton devices[154,219,220], however, it is important to consider in more detail the fate of these states and how they interact with polaritons. Similar to electrical injection, a very large reservoir of triplets can be generated by photoexcitation in some materials. Large triplet populations can be optically generated by using systems with strong spin-orbit coupling resulting in fast intersystem crossing[224] or in singlet fission active materials[10,226].

Herein we use both intersystem crossing and singlet fission to optically generate triplets to show how triplet excitons interact with polariton states and find that strong coupling creates new radiative channels that are unavailable in the film. This results in ultra-long-lived polariton emission and the potential for harvesting triplets in devices. We propose a mechanism based on the widespread phenomenon of excited-state mixing, which could open the way to using strong light-matter coupling to manipulate dipole-forbidden, formally dark states.

4.3 Up-Conversion - Diphenylanthracene

A common way to study triplet excitons is through delayed fluorescence, which occurs through the spin-allowed conversion of two triplets into a singlet exciton, known as 'triplet-triplet annihilation'[226,229]. One of the best-characterised triplet-triplet annihilation systems is the diphenyl-anthracene/metal-porphyrin blend used for up-conversion[184,185], the chemical structure of the molecules are shown in Figure 4.2a. We depict the photophysics of this system schematically in Figure 4.2b: directly exciting the Pt-porphyrin at 532nm initiates efficient intersystem crossing (<100fs)[184], producing triplets that can transfer to diphenyl-anthracene where triplet-triplet annihilation produces delayed fluorescence.

In order to understand how triplets behave in microcavities, we need to study delayed fluorescence in the solid state, rather than solution. We therefore prepared films of diphenyl-anthracene/Pt-porphyrin/polystryene blends with a ratio of 50:1:15. The polystyrene is used to aid mixing between the two active materials and reduce film roughness. Films and microcavites were encapsulated in inert atmosphere to protect against oxygen quenching.
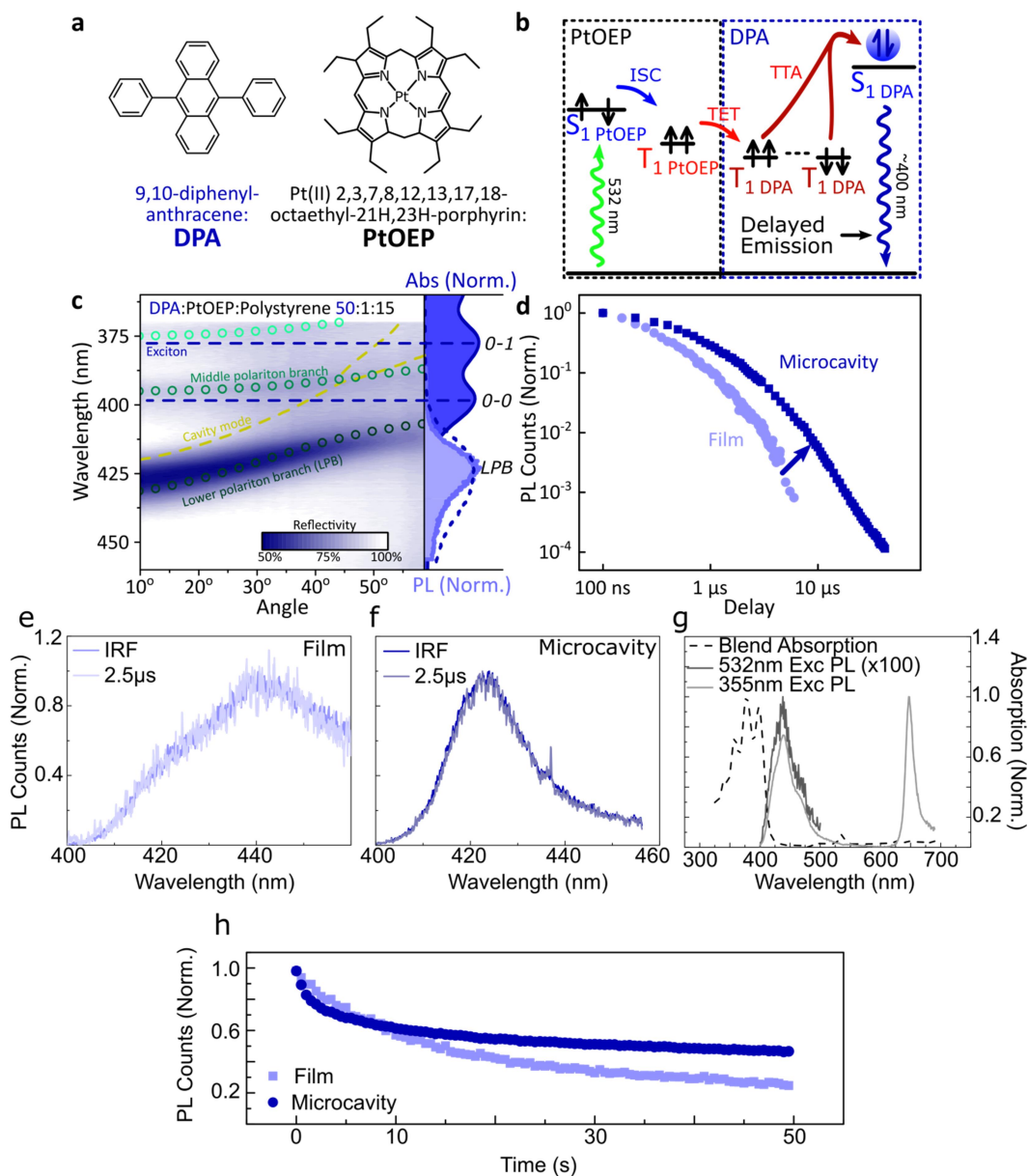
Fig 4.2: Sensitised photon up-conversion system. (a) Molecular structures of active components used in photon up-conversion system. (b) Simplified schematic of photon up-conversion. ISC: intersystem crossing, TET: triplet energy transfer, TTA: triplet-triplet annihilation. (c) Reflectivity map of photon up-conversion blend within an Ag-Ag microcavity. Comparison with absorption spectrum (right) and transfer matrix modelling (lines, circles) confirms strong coupling, characterised by anti-crossings at the 0-0 and 0-1 energies (dashed). Details of transfer matrix model in Section 4.8.1. All emission comes from the lower polariton branch (LPB), whether excitation is resonant with diphenyl-anthracene (355nm, dashed) or PtOEP (532nm, shaded). Emission is collected with a NA=0.76 lens and thus effectively integrates along the entire dispersion (±45°). (d) Decay kinetics of diphenyl-anthracene/exciton-polariton emission following excitation of PtOEP at 532nm reveal enhanced lifetime in microcavity (dark) vs bare film (light). All emission on these timescales arises from triplet-triplet annihilation. Incident power (film: 50μW, microcavity: 150μW) was chosen to give similar absorbed power in both samples, details in the main text. Photoluminescence spectra of diphenyl-anthracene blends in neat films (e) and microcavities (f), revealing no change in emission profile over time. (g) Absorption spectrum (dashed) of blend film, and photoluminescence spectra (solid) following excitation at 355nm and at 532nm. As indicated, the diphenyl-anthracene emission following excitation at 532nm is scaled 100x. (h) Integrated diphenyl-anthracene emission spectra measured continuously over 50 s reveal clear signal degradation in films and microcavities. The strength of Pt-phorphyrin phosphorescence during this period does not decrease.

Figure 4.2g shows the steady-state absorption and emission from the blend film. The vibronic progression of diphenyl-anthracene can be clearly distinguished, while the absorption 500-550 nm of the porphyrin dopant is markedly weaker. At this low loading the porphyrin is too weakly absorbing to enter the strong-coupling regime itself. Following excitation at 355 nm (Exciting diphenyl-anthracene directly), we measure diphenyl-anthracene fluorescence 400-500 nm, as well as substantial Pt-porphyrin phosphorescence due to rapid energy transfer from dipyhenyl-anthracene followed by intersystem crossing[184,230]. Following 532nm excitation (Pt-PEOP excitation) we measure up-converted emission at 400-450nm from diphenyl-anthracene, shown in Figure 4.2g. As this is a solid-state blend, phosphorescence at 650nm dominates the spectrum due to significant phase-separation, which prevents Pt-PEOP triplets from reaching the diphenyl-anthracene regions of the film[184,230]. The spectra in Figure 4.2 reveal there is no evolution in the spectral emission profile from early times (< 100 ns) to the longest timescales, ~2.5 μs, in either bare films (Figure 4.2e) or microcavities (Figure 4.2f). In both cases the emission is mediated by the same state over all time delays: either S_1 for DPA in the film, or the lower polariton branch in the microcavity. During the measurement, the film and microcavity show a non-reversible change in emission intensity, shown in Figure 4.2h. The effect is more pronounced in the film. Interestingly, the energetic position of the polariton emission does not change over the same measurement time (Figure 4.2f). The lower polariton branch emission energy is governed by the cavity thickness (expected to be constant) and Rabi splitting. The latter is governed by the optical density in the film. Hence, we conclude that there is no change in optical density of the film over the measurement time.

We therefore attribute the apparent degradation in Figure 4.2h to laser-induced phase separation, causing a reduction in diphenyl-anthracene delayed fluorescence. This observation is consistent with the typical observation of reduced photon up-conversion efficiency in such blend films relative to solutions, due to the separation of Pt-porphyrin and diphenyl-anthracene into relatively pure domains[184,230]. To ensure that this does not affect our observations, the kinetics in Figure 4.2 were

measured during the saturation regime when laser-induced phase-separation reaches a steady state, i.e. after 50s. Overall the emission behaviour of the films is consistent with literature[184,185].

Figure 4.2c shows a reflectivity map of a microcavity containing the diphenyl-anthracene blend, as a function of incident angle and wavelength. The dips in microcavity reflectivity never cross the bare exciton energy (blue dashed). This 'anti-crossing' is a signature of strong light-matter coupling and polariton formation, and the absorbing states are thus split into polariton branches. Transfer-matrix modelling based on measured optical parameters confirms strong coupling in this structure (Figure 4.2c, lines and circles). Microcavity emission originates from the lower polariton branch (Figure 4.2c, right), whether we excite the diphenyl-anthracene directly (355 nm, dashed) or the Pt-porphyrin (532nm, shaded). In the latter case emission is due to up-conversion through triplet-triplet annihilation.

We explore how this triplet harvesting process is affected by strong coupling using time-resolved measurements. To correctly compare the film and cavity kinetics, the incident excitation power was scaled to ensure similar absorbed power in both cases. To do this, we considered multiple passes of light through the microcavity due to internal reflections, accounting for transmission through the semi-transparent top mirror (~25%, due to the presence of a nearby cavity mode) and attenuation by the Pt-porphyrin absorption. This yields a 1.6% absorption of incident light at 532 nm within the microcavity, compared with 5% by the film. Therefore, we compared measurements taken with 50 µW incident laser power for the film samples with 150 µW for the microcavities in Figure 4.2d. The lifetime of emission in the microcavity is distinctly longer than in the film (Figure 4.2d). The predominant species on these timescales are triplet excitons, so we conclude that additional long-lived triplets are harvested in the microcavity. This change in lifetime is surprising and requires further investigation. However, the two-molecule nature of the system combined with laser-induced phase separation, makes a detailed study on this system difficult. We therefore apply the same approach to a simpler system with a single active component.

4.4 Triplet-Triplet Annihilation - DPPT

Diketopyrrolopyrrole thiophene (DPPT, Figure 4.3a) is the base unit for polymers exhibiting high charge-carrier mobility in thin-film transistors, recently used in electrical-injection polariton OLEDs[220]. DPPT monomers are also known to undergo intersystem crossing in the solid state[231], shown schematically in Figure 4.3b. Films were prepared containing DPPT dispersed in polystyrene matrix (1:4 DPPT:polystyrene). Figure 4.4c shows the steady-state absorption and PL spectra of a DPPT:polystyrene blend (1:4) in solution (<1mg/ml) and in the thin film. The solution photoluminescence spectra are representative of singlet emission from isolated molecules. Within the films, we observe a distinct red-shift and increase in intensity beyond 600 nm, which we attribute to excimer emission[232]. The slight increase in absorption at the 0-1 peak (~510 nm) within the films is likewise consistent with a sub-population of H-aggregated sites within the film[71], which can lead to excimer emission[232]. It is likely these are the primary sites of triplet-triplet annihilation, as this process requires two DPPT molecules to be in proximity.
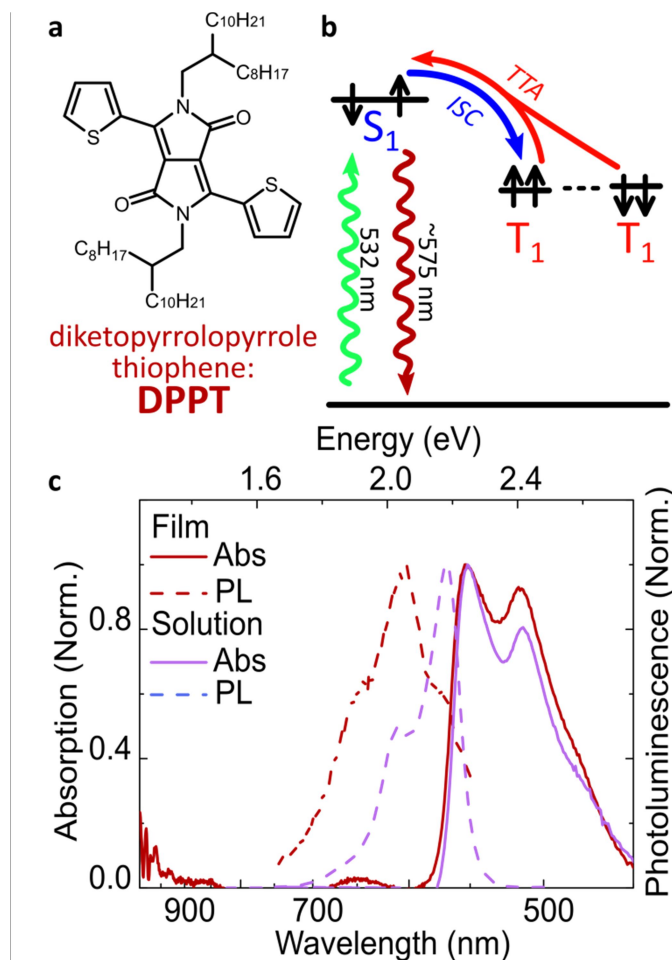
Figure 4.3: Steady state characterisation of DPPT. (a) Molecular structure of DPPT. (b) Simplified schematic of DPPT film photophysics, details in main text. ISC: intersystem crossing, TTA: triplet-triplet annihilation. (c) Absorption (solid) and photoluminescence (dashed) spectra of DPPT in toluene solution (red) and embedded in polystyrene matrix (purple). Excitation for photoluminescence spectra was at 532nm.

Figure 4.4 shows time-resolved emission data of DPPT:polystyrene blend films and microcavities. Within the instrument response (0-2 ns), the spectrum resembles emission in dilute solution (Figure 4.4a), so we assign it to prompt singlet emission. By 15 ns the spectrum is dominated by a red-shifted species which decays in tandem with the initially excited singlet and can be attributed to excimer emission. We observe no time-dependence in the polariton emission in microcavities (Figure 4.4b), indicating that all emission is from the lower polariton branch.

Figure 4.4c shows a comparison of the normalised bare film emission spectra at 15 ns after photoexcitation, in the presence and absence of oxygen. We see a much smaller relative population of the excimer state in the oxygen-rich samples, compared to oxygen-free. It is well known that

triplets are quenched in the presence of oxygen, making oxygen dependence a standard test for triplet states[233]. The quenching of excimer emission suggests that the excimer is populated by triplet states. Previous reports of DPPT and similar chromophores are ambiguous about the presence of triplets and mechanism of their formation. Some DPP derivatives are claimed to be capable of singlet fission, which would suggest rapid and efficient triplet formation[234]. An analogue of DPPT with slightly different side-chain structure, however, yielded no long-lived triplet signal in time-resolved EPR measurements on a pure film[231], suggesting singlet fission does not occur. The latter measurement indicates that any triplet formed by intersystem crossing must be short-lived and/or in low yield. To verify that our delayed fluorescence is from triplet-triplet annihilation, we performed intensity-dependent measurements. Figure 4.4d shows the intensity dependence of DPPT:polystyrene film emission within the instrument response and between 500-600 ns. The non-linear scaling is consistent with triplet-triplet annihilation to reform both the singlet and the excimer, and closely follows the dependence in a diphenyl-anthracene solid-state system[235]. All subsequent measurements were performed on films or microcavities encapsulated in an oxygen-free environment.
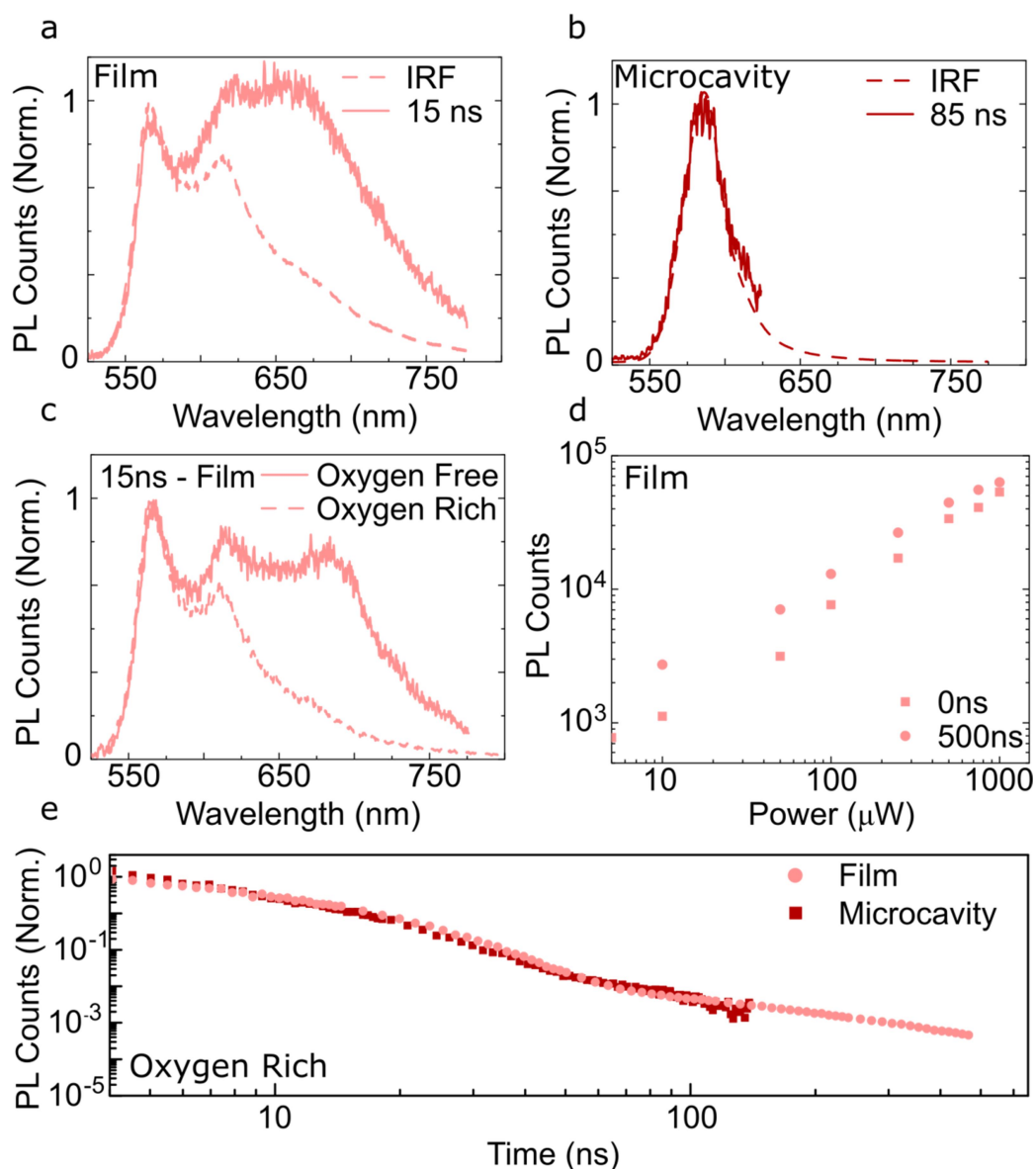
Figure 4.4: Oxygen dependent time resolved photoluminescence of the DPPT samples. (a) Spectra of DPPT:polystyrene film following excitation at 532 nm, collected within the instrument response (dashed) and at 14-16 ns (solid) after excitation. b Equivalent spectra for microcavity, within the IRF (dashed) and at 80-90 ns (solid) after excitation. (c) Time-resolved emission spectra of DPPT:polystyrene film at 14-16 ns, in the presence (solid) and absence (dashed) of oxygen. The oxygen-free film was prepared and encapsulated within a nitrogen-filled glovebox. (d) Laser intensity dependence of emission from DPPT:polystyrene films at short (squares) and long (circles) time delays, revealing similar dependence whether the emission is dominated by S_1 (IRF) or excimers (500 ns). (e) Bare film (red) and microcavity (pink) emission kinetics integrated over full emission band, in the presence of oxygen.

Within DPPT-based microcavities, Figure 4.6a, we observe a clear anti-crossing at the 0-0 peak, while

the second peak in the absorption appears to be in the weak/intermediate-coupling regime. Similar

to the diphenyl-anthracene cavities, we attribute the anti-crossing states to polariton branches, and

emission is again entirely from the lower polariton branch. Comparison of the film and microcavity

emission kinetics in Figure 4.5b reveals that the prompt fluorescence dynamics remain unchanged. However, delayed fluorescence from triplet-triplet annihilation is once again longer-lived in the microcavity. By contrast, in a reference material INDB in which we observe no contribution to emission in the bare film from triplet-triplet annihilation, we observe no enhancement of long-lived emission in microcavities (Appendix A). Likewise, when we quench the triplets in DPPT through exposure to oxygen, the enhancement observed in Figure 4.5b disappears (Figure 4.4e).
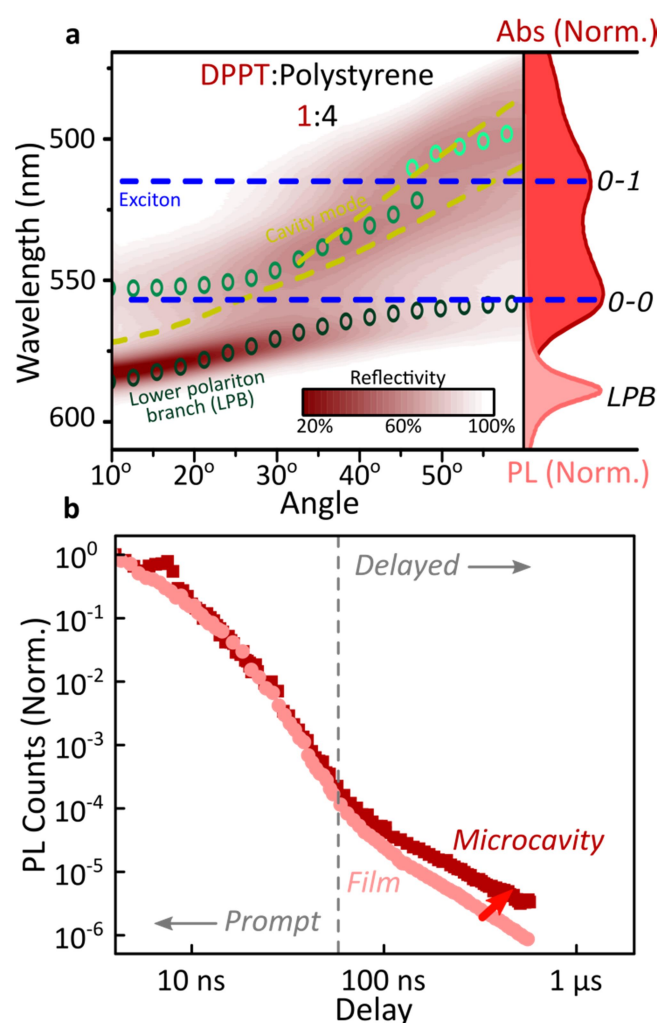
Figure 4.5: Delayed emission in single-component DPPT film. (a) Reflectivity map of DPPT:polystyrene film within a Ag-Ag microcavity. Comparison with absorption spectrum (right) and transfer matrix modelling (lines, circles) confirms strong coupling to the 0-0 transition. All emission arises from the lower polariton branch (LPB). Emission is collected with a NA=0.76 lens and thus effectively integrates along the entire dispersion (±45°). (b) Integrated photoluminescence kinetics over full emission band for bare film (light) and microcavity (dark) following excitation at 532nm. Enhanced microcavity emission matches the 'delayed' regime, in which contributions from triplet-triplet annihilation are significant.

To understand the possible origin of this longer-lived emission, we consider the mechanism and spin physics of triplet-triplet annihilation. Emission in this process comes from the encounter of two triplets as they diffuse through the film, forming an 'encounter complex' called a triplet-pair state (TT)[80]. As discussed in Chapter 2, spin conservation means ^{1}(TT) is the only spin state enabling transfer from the dark triplet-pair manifold to emissive S_1. We note that the same pair states that make up ^{1}(TT) also compose two of the five ^{5}(TT) configurations[80], such that the spin states are a mixture of singlet and quintet. The rate of transfer from the (TT) encounter complex to S_1 is weighted by its overlap with ^{1}(TT), e.g. $\left| \langle \, ^1TT | \varphi \rangle \right|^2$, where φ is the mixture of spin states in the encounter complex. Simple spin considerations (9 combinations of 4 electrons in the triplet-pair) would imply a maximum quantum efficiency of ~ 11% (1 of 9). In practice, up-conversion efficiencies of >11% have been observed in solution systems, suggested to be due to the higher spin-states such as ^{5}(TT) dissociating back to free triplets without significant loss, later reforming ^{1}(TT)[229,236]. We propose that the enhanced long-lived emission in our microcavities can also be explained by considering these high-spin states.

The quintet triplet-pair states have only recently been observed in organic solid-state systems[12,15,237,238], both in 'pure' configurations and in a complex mixture with ^{1}(TT) governed by dynamics of the exchange interaction (see discussion below). These states have been shown to have a lifetime of a few microseconds, presumably because any relaxation to the ground state from ^{5}(TT) or the ^{1}(TT)-^{5}(TT) mixture would be spin-forbidden. On the other hand, ^{1}(TT) has a typical lifetime on the order of only 10ns in the absence of fast dissociation into 'free' triplets[31,94]. Moreover, it can directly recombine into S_1 in a spin-allowed process. Given this significant difference in pair-state lifetimes, a channel to harvest the quintet states for delayed fluorescence would significantly increase the emission lifetime. To more directly probe this possibility, we study a material system capable of singlet fission, the inverse of triplet-triplet annihilation in which a singlet exciton forms two triplet excitons via ^{1}(TT)[10,13,31,94,226]. We use polycrystalline films of TIPS-tetracene, a system which has been very well studied with a range of complementary time-resolved techniques (optically

detected magnetic resonance, transient and/or magnetic field-dependent absorption, photoluminescence and EPR)[12,13,96,239]. These measurements have established a detailed picture of the excited-states and, importantly, spin-dependent dynamics of TIPS-tetracene. The triplet-pair state produced via singlet fission is initially a pure singlet ^{1}(TT) which can then evolve into ^{5}(TT) and ^{1}(TT)-^{5}(TT) on sub-microsecond timescales[12,15,237,238]. This evolution does not depend on exciton diffusion, allowing us to isolate the contribution of high-spin states in microcavities.

4.5 Singlet Fission - TIPS-tetracene

To investigate singlet fission, we use TIPS-tetracene, a well-studied singlet fission material, structure shown in Figure 4.6a. In polycrystalline TIPS-tetracene films, singlet fission occurs within 50 ps[13], well within our instrument response of 4 ns. The singlet and ^{1}(TT) states are very similar in energy resulting in a dynamic equilibrium and delayed fluorescence, schematic shown in Figure 4.6b. Over time, spin evolution of the bound triplet-pair state forms ^{5}(TT)[12] and the films become non-emissive. On very long timescales (>μs), spin dephasing yields independent triplets[12]. We note that even on these long timescales, the predominant triplet-triplet annihilation processes in TIPS-tetracene are geminate[13] because annihilation occurs between triplets formed from the same parent singlet state. As a result, the delayed fluorescence kinetics show no dependence on excitation density.

Within microcavities we observe strong coupling throughout the TIPS-tetracene absorption band and clear polariton branches, Figure 4.6e. As above, emission is entirely from the lower polariton branch. Relative to the bare film, the prompt microcavity emission is only weakly perturbed, Figure 4.7f. However, beyond 100ns the microcavity shows a significantly enhanced long-lived tail. As in previous systems, the film and microcavity spectral shapes exhibit negligible evolution over this decay (Figure 4.6c-d). In the film this is because all emission we detect is from S_1, populated by triplet-triplet annihilation from ^{1}(TT). Likewise, in the microcavity the constant spectral shape indicates that the emission is mediated by the lower polariton state, also populated by triplet-triplet annihilation. However, the clear delineation into two kinetic regimes in Figure 4.6 suggests that on long times (>100ns) this process follows a distinct pathway unavailable in the film.
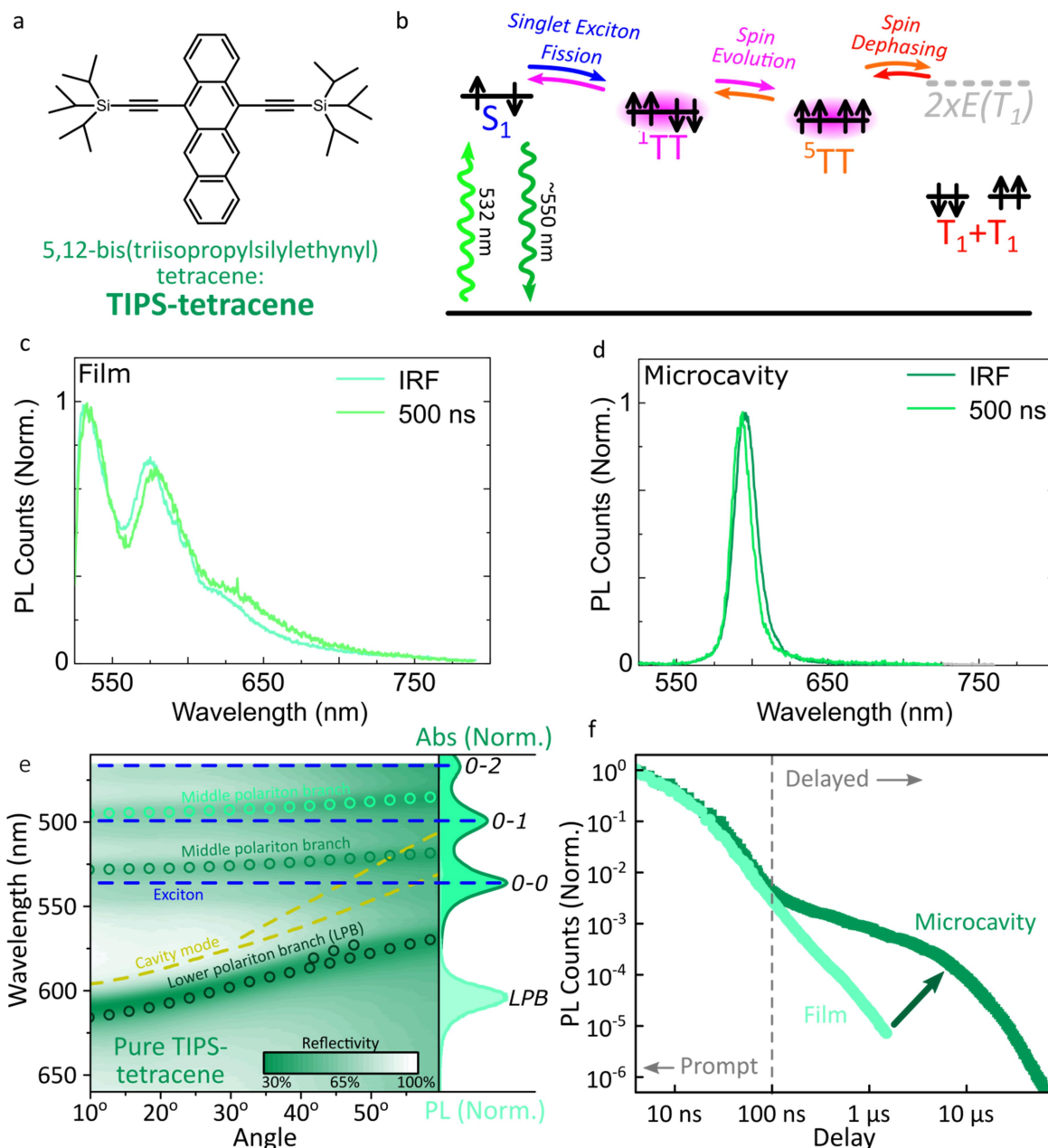
Figure 4.6: Singlet fission into bound TT within a microcavity. (a) Molecular structure of TIPS-tetracene. (b) Simplified schematic of TIPS-tetracene photophysics. All processes are potentially reversible, leading to delayed fluorescence from triplet-triplet annihilation. (c) Emission spectra of pure TIPS-tetracene film following excitation at 532 nm, collected within the instrument response (IRF) and at 500-600 ns after excitation. (d) Equivalent spectra to (c) but for the microcavity. (e) Reflectivity map of a pure TIPS-tetracene film within an Ag-Ag microcavity. Comparison with absorption spectrum (right) and transfer matrix modelling (lines, circles) confirms strong coupling to multiple transitions. On the left the emission spectra of the microcavity is shown consistent with emission from the lower polariton branch (LPB). Emission is collected with a NA=0.76 lens and thus effectively integrates along the entire dispersion (±45°). (f) Integrated photoluminescence kinetics over full emission band for bare film (light) and microcavity (dark) following excitation at 532 nm. All emission on these timescales arises from triplet-triplet annihilation.

Initially we wish to rule out changes in film morphology due to the various sample preparation methods. A summary of the control sample measurements is given in Appendix B, but in brief. Spin-cast control films were prepared from chloroform solutions with the same parameters as toluene in Figure 4.7, to determine if the slight changes in morphology that result[13] have any effect on the delayed emission dynamics. Films identical to those in Figure 4.6 were subjected to thermal annealing or ultrahigh vacuum in the evaporation chamber. These measurements allowed control for whether any incidental effects of microcavity preparation (e.g. changes in morphology under vacuum or higher temperatures) could be the origin of the enhanced delayed emission reported in the main text. Finally, a film was produced on top of a mirror to investigate if organic-metal interactions could cause the effects we measure. All samples were encapsulated and measured following the same procedures used for all other samples. We observe no systematic change in the photoluminescence decay kinetics following these solution-based processing steps. We observe slight variation in the PL lifetime across all samples including those without additional treatments (Figure 4.7). Similar variation can be obtained by scanning across the same film, which can be attributed to slight changes in the film crystallinity. Following annealing, vacuum treatment or position on a mirror we observe variation on a similar scale (Figure 4.7), in some cases with increased prominence of the 'kink' as the kinetics transition from cleanly exponential behaviour to a less-defined power-law-type decay weakly detectable above the noise floor. In no instance do we detect changes in the film behaviour on the same scale as the effects of microcavity formation, confirming that the effect we report does not arise from our processing or metal-organic interactions.
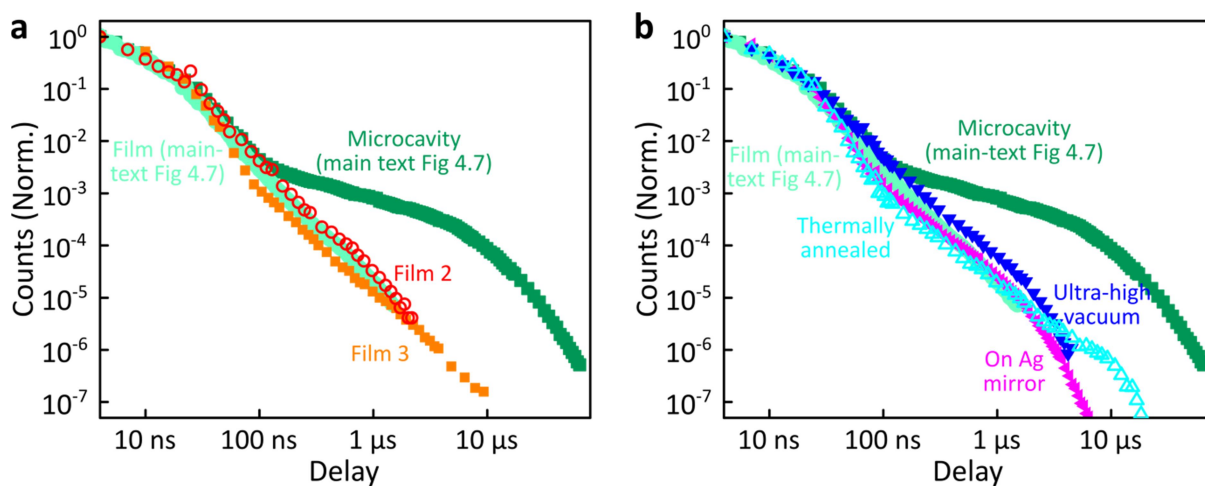
Figure 4.7: Control measurements on TIPS-tetracene films. (a) Films prepared from different batches of solution or different solvents at the same TIPS-tetracene concentration exhibit the same qualitative behaviour. The slight spread of lifetimes indicates slight variations in film crystallinity; similar variation can be obtained scanning within the same film. (b) Exposure of the films to heat or ultra-high vacuum does not significantly change the kinetics beyond the standard film-to-film variability. Similarly, deposition on an Ag mirror does not result in a major change in lifetime due to metal-organic interactions. No processing steps result in an enhancement that can explain the behaviour observed in full microcavities. In each kinetic only every third data point is shown for clarity.

We additionally prepared fully evaporated sample structures to ensure that direct contact between TIPS-tetracene and Ag is not responsible for the observed delayed emission. We first confirmed that evaporation of TIPS-tetracene does not yield films with significantly different emission properties (Figure 4.8). Multilayer BCP:TIPS-tetracene:BCP films on glass exhibit a redshift of the overall PL spectral weight, consistent with a minor contribution from excimer-type sites previously reported to exist in disordered samples[14]. These features do not dominate the emission and are presumably a minority species in the film, and we expect they are formed at the TIPS-tetracene:BCP interface where disorder will be greater. There is no accompanying change in the PL decay dynamics: evaporated and spin-coated samples are fully equivalent (Figure 4.8). Likewise, subsequent coating with an evaporated Ag mirror does not significantly enhance the delayed emission and results in changes comparable with film-to-film variation. We then complete a full microcavity structure, with a sufficiently thin layer of TIPS-tetracene and a sufficiently large negative detuning that no strong light-matter coupling is possible. This sample exhibits effectively identical dynamics to other

reference films, demonstrating that the full microcavity processing steps are insufficient to induce major enhancement to the delayed emission if polariton formation is not possible.
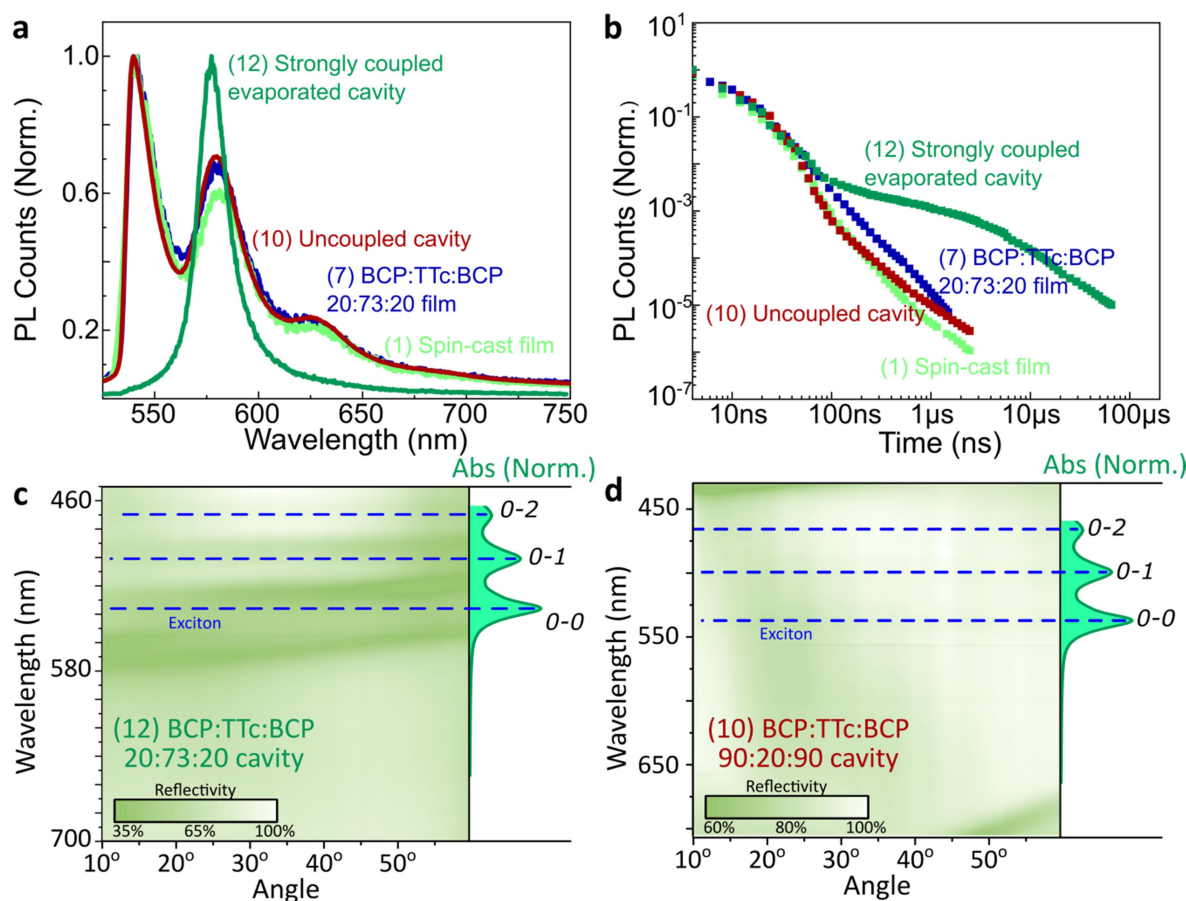
Figure 4.8: Fully evaporated TIPS-tetracene samples. (a) Emission spectra and (b) integrated kinetics of each sample. Data is acquired and processed as above. Comparison of samples produced by evaporation and spin casting shows little variance. A strongly detuned microcavity with low oscillator strength ('Uncoupled cavity') also exhibits no enhancement in the delayed emission. (c) Angle-dependent reflectivity of the 'thick' TIPS-tetracene evaporated cavity shows strong coupling as in solution-processed cavities. (d) No strong coupling is evident in the 'thin' TIPS-tetracene evaporated cavity.

However, when we prepare full microcavities with a thick evaporated layer of TIPS-tetracene we observe clear strong light-matter coupling in the angle-dependent reflectivity (Figure 4.8c), with well-defined polariton emission and the same substantial enhancement to delayed emission for spin-cast microcavities (Figure 4.8b). The enhancement is clearly independent of physical contact between the TIPS-tetracene and metal mirrors or any of the sample processing steps but is instead uniquely caused by strong light-matter coupling (Figure 4.7/4.8).

To identify the new pathway available in the microcavity, in Figure 4.9 we compare our results with published data from TIPS-tetracene polycrystalline films that show identical absorption spectra and fluorescence lifetimes and are thus equivalent[12,13]. Transient absorption spectroscopy (solid line, dark red) has shown that triplet photo-induced absorption signatures generated by singlet fission appear well within our instrument response and do not decay significantly until >10μs[13]. The same sample shows emission with 10ns lifetime, attributed to delayed fluorescence during the initial S_1–^{1}(TT) equilibrium[13]. This decay (open circles) closely matches our pre-100ns emission decay. Importantly, the combination of these two data sets shows that the pre-100ns decay in delayed fluorescence is caused by the change in the emissive character of the triplet-pair states, rather than a loss in population. This change in character is attributed to spin evolution[12,13]. Indeed, time-resolved electronic paramagnetic resonance spectroscopy shows the presence of quintet states[12], reproduced by the dashed line in Figure 4.9. Interestingly, the bulk of our microcavity-enhanced emission coincides with this time frame. Finally, on still longer timescales, it has been observed that the triplets within the bound pairs become spin-independent. In this regime, we detect no emission from the microcavity, presumably due to a reduction in triplet-triplet annihilation. As a result, we assign the enhanced delayed emission to quintet states populated on the microsecond time scale.
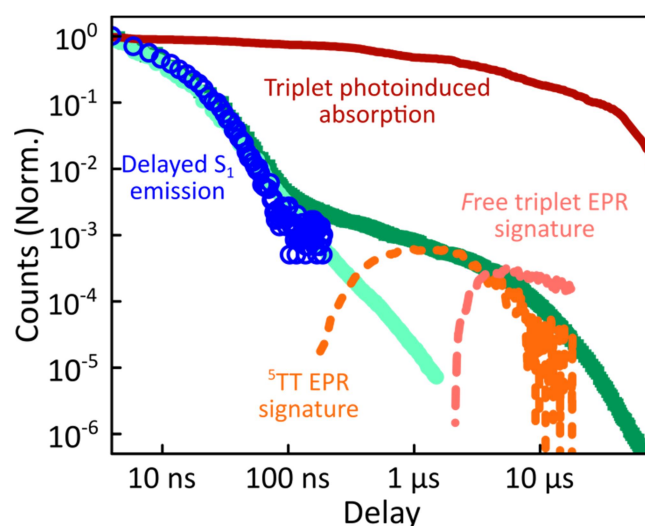
Figure 4.9: Identification of the ^{5}TT contribution. Reproduction of the TIPS-tetracene film and microcavity emission kinetics from Fig 4.7, compared with time-correlated single photon counting[44] (circles), transient absorption[44] (solid) and electron paramagnetic resonance[38] (dashed) kinetics previously reported for similar polycrystalline films. The long-time enhancement in microcavities coincides with observations of high-spin ^{5}TT .

We have also measured the dependence of the observed enhancement on the energy offset between cavity mode and S_1 (the 'detuning'). Figure 4.10 shows that across the entire detuning series we observe the same qualitative effect, though the magnitude and lifetime of the enhancement appear to vary. There is no systematic dependence on energy offset. Interestingly, the least and most negatively detuned cavities (-71 and -545 meV) exhibit nearly the same long-time kinetic. The extremes of dynamic behaviour are instead obtained with two similar 'intermediate' negative detunings, -342 and -418 meV. The fairly short energy scale for such changes in behaviour is consistent with earlier studies of squaraine microcavities[177], where the detuning scans the LPB over relatively sharp energetic resonances within the exciton reservoir. The complex structure observed here suggests the presence of multiple resonances, likely related to the more complex vibronic structure of TIPS-tetracene. With all the data assigned, we now discuss the results presented herein.
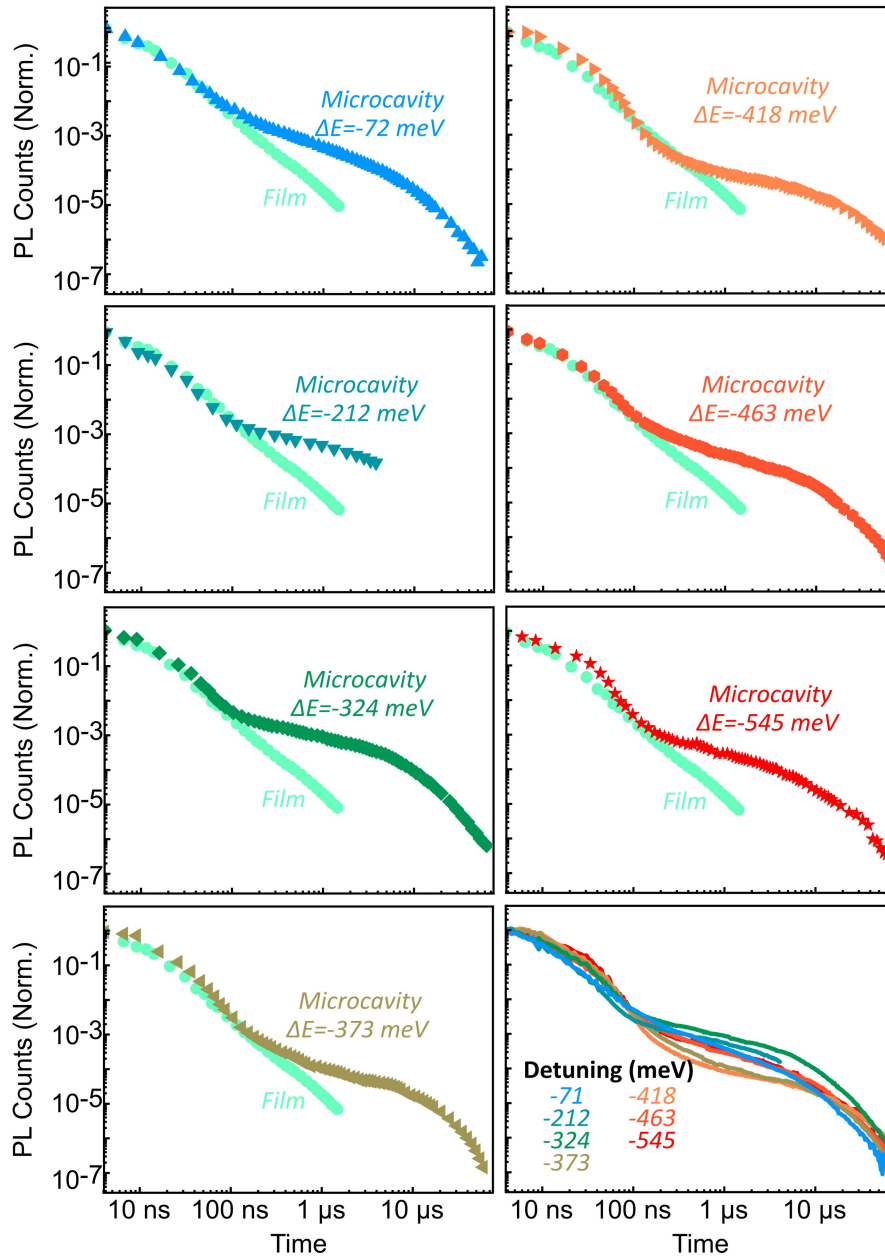
Figure 4.10: Detuning dependence in TIPS-tetracene microcavities. Integrated PL kinetics acquired and processed as in previous Figures. The same qualitative behaviour is observed over the full range, but there is no systematic dependence of the relative magnitude or lifetime of the enhanced emission. In each kinetic only every fifth data point is shown for clarity.

4.6 Interpretation of the Enhanced Emission

In all the systems we have studied in which triplets are formed, triplet-triplet annihilation leads to longer-lived emission in the microcavity compared with the bare film. Because of the long timescales involved, this is a significant effect even though the instantaneous emission from these states is weak. To illustrate this point, in Figure 4.11 we integrate the emission decay kinetics from the main text, normalising both curves for each material to the 'film' value for ease of comparison. Based on this simple metric, the degree of enhancement due to strong coupling (shaded) is 21% for DPPT, 64% for TIPS-tetracene and 133% for DPA. If we extend the integration in TIPS-tetracene and DPA cavities to longer delays, beyond the measurable lifetime of their reference films, the enhancement rises to 72% and 152%, respectively. Based on the model system, TIPS-tetracene, and the fact that in all systems in which we observe microcavity-enhanced emission on these timescales the primary species are uncoupled triplet excitons, we suggest that the enhanced emission comes from harvesting ^{5}(TT) into the lower polariton.
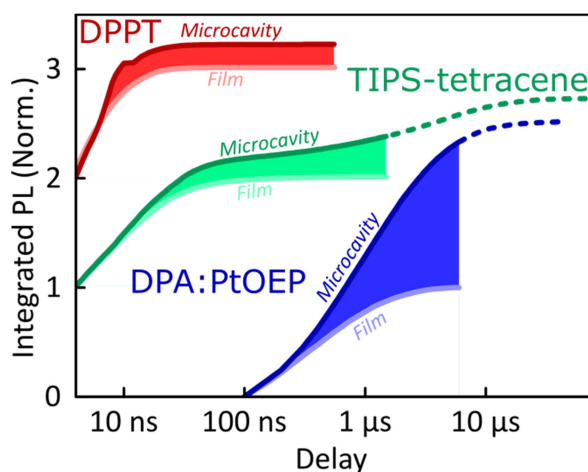
Figure 4.11: Time-integrated emission kinetics. Integral of emission kinetics presented in the text above. For each material, both curves are normalised to the final value of the film integral, as a proxy for total film emission. Shaded region corresponds to the enhancement achieved through strong coupling. Dashed lines show continuation of microcavity emission beyond the range when film emission falls into noise.

This result is entirely unprecedented: direct interaction between the quintet and the polariton should be spin- and symmetry-forbidden. Our observation shows that strong coupling can alter the photophysics even of states that cannot interact with light. We start the discussion by returning to our model system TIPS-tetracene. Polycrystalline films of this material have been very well studied and understanding its photophysics in detail is important for the results reported here. The process of singlet fission is generally described in simplistic terms, where a singlet exciton splits into a pair of triplet excitons which are initially coupled into a triplet pair. These excited states are not pure diabatic states but rather mixed adiabatic states. Thus the nominal S_1 state is often substantially mixed with higher-lying charge-transfer excitons (CT)[240] and even attains some TT character. The ^{1}(TT) state is also substantially mixed with CT and S_1, resulting in significant binding with respect to two free triplets[31,94,241,242] (essential for fission to even be possible in TIPS-tetracene[13]) and providing a channel for this formally dark state to emit directly[13,31,94]. The mixed character of both states enables ultrafast singlet fission[13,94,243,244] and efficient equilibration between (adiabatic) S_1 and ^{1}(TT)[13]. Once formed, the adiabatic ^{1}(TT) state can exhibit significant further evolution. The constituent triplets within the pair can interact through exchange coupling. In the regime of weak exchange coupling, the initially created ^{1}(TT) state mixes with other spin configurations via dipolar coupling, resulting in a triplet-pair with mixed singlet and quintet character[80]. This regime has been detected in TIPS-tetracene using magnetic resonance techniques[96], and it is likely that the formation of this dark ^{1}(TT)-^{5}(TT) mixed state is responsible for the ~10ns loss of delayed fluorescence[13]. The recent observation in the same and other materials of strongly exchange-coupled triplet pairs after loss of emission suggests that the exchange interaction must fluctuate over time, as described in other systems by Troisi *et al*[12,15,237,238,245]. The coexistence of these two regimes on similar timescales indicates that the weakly and strongly exchange-coupled triplet-pairs are in dynamic equilibrium[245]. Importantly, the physical mechanism behind the fluctuating exchange coupling is not linked to singlet fission but is an intrinsic property of organic materials, and we can thus expect the same processes to occur on formation of TT encounter complexes in triplet-triplet annihilation.

To understand the mechanism of ultra-long-lived polariton emission, we have constructed a basic toy rate model for the TIPS-tetracene data. The model, shown in Figure 4.12a, is based on the current photophysical model of polycrystalline films of TIPS-tetracene presented in Weiss *et al.*[12] and Stern *et al.*[13] In this model singlet fission from S_1 (k_{SF}) creates a population of spin-entangled triplet-pairs ^{1}(TT), given by Equation 4.1.

$$\left|^1\mathrm{TT}\right\rangle = 3^{-1/2}(\left|xx\right\rangle + \left|yy\right\rangle + \left|zz\right\rangle) \qquad (4.1)$$

where $\left|xx\right\rangle$, $\left|yy\right\rangle$ and $\left|zz\right\rangle$ are the zero-field triplet-pair basis states. ^{1}(TT) is not an eigenstate of the spin-Hamiltonian in the regime of weak exchange coupling. In our model we term ^{1}(TT) 'TT$_{bright}$' as this population is in equilibrium with S_1 through k_{-SF} and is observed through delayed emission from S_1. Over ~10ns, the ^{1}(TT) states lose their spin-entanglement, and probably some S_1 character, and evolve into dark triplet-pair states, 'TT$_{dark}$'. As there have been no spin-flips, the triplet-pairs are still made up of $\left|xx\right\rangle$, $\left|yy\right\rangle$ and $\left|zz\right\rangle$, and are initially weakly exchange coupled with mixed singlet ($\left|^1\mathrm{TT}\right\rangle = 3^{-1/2}(\left|xx\right\rangle + \left|yy\right\rangle + \left|zz\right\rangle)$) and quintet [$\left|^5\mathrm{TT}_a\right\rangle = 2^{-1/2}(\left|xx\right\rangle - \left|yy\right\rangle)$ or $\left|^5\mathrm{TT}_b\right\rangle = 6^{-1/2}(\left|xx\right\rangle + \left|yy\right\rangle - 2\left|zz\right\rangle)$] character.

These weakly-coupled TT states are thought to co-exist with a population of strongly exchange coupled triplet-pairs[12]. With strong exchange coupling, the triplet-pair states are pure singlet (S=0) or quintet (S=2) states as S becomes a good quantum number in the strong-exchange coupling regime. The latter has been observed in TIPS-tetracene films using transient EPR[12]. The evolution between the initially created weakly exchange-coupled and the observable strongly exchange-coupled triplet-pair states most likely occurs via thermal fluctuations that alter the relative spacing between molecules and thus the wavefunction overlap between them[12]. This has been described in similar systems by Troisi *et al.*[245]

If these fluctuations are responsible for generating strongly exchange-coupled triplet pairs, we can assume an equilibrium exists between weakly and strongly exchange-coupled TT states. Therefore, the dark triplet-pair population TT$_{dark}$ (taken to be the equilibrium combination of weakly- and

strongly-coupled singlet/quintet TT states) should follow the observed EPR quintet dynamics. We note that EPR lifetimes do not necessarily represent the natural lifetime of the system, which is perturbed by the EPR measurement itself. The natural 'TT$_{dark}$' lifetime could be longer than the EPR-measured quintet lifetime. Nevertheless, we take the EPR-measured quintet lifetime as a reasonable estimate of the TT$_{dark}$ lifetime.

Eventually spin-flips can occur, probably through spin-orbit coupling, effectively scrambling the spins within the triplet-pairs. At this point the zero-field basis states include combinations such as $|xy\rangle$, $|xz\rangle$, etc. In this form, instead of all states (in the weakly exchange-coupled regime) showing some singlet character (i.e. containing $|xx\rangle$, $|yy\rangle$ or $|zz\rangle$), only 3/9 now have any singlet character. In this regime the triplets, although possibly still spatially bound in TIPS-tetracene as suggested by transient absorption measurements[13], are no longer correlated ('T$_1$+T$_1$'). There is no signature of quintet pairs in transient EPR at this point, but their excited-state absorption can still be measured using transient absorption spectroscopy[13]. It is likely that some of the triplet pairs have fully dissociated on this timescale, forming spatially separated uncorrelated triplets, but we assume this is a negligible process in TIPS-tetracene.

In TIPS-tetracene-based microcavities we assume that the lower polariton branch dynamics are governed by the exciton reservoir photophysics. Therefore, we use photophysical data from the literature to parameterise our model. The rate constants from our model are shown in Appendix C and comparison of our model to literature data is shown in Figure 4.12b. Our basic model – in the absence of strong light-matter coupling – fits both delayed fluorescence and transient absorption (TA) data. We have attempted to constrain the model by using the fewest free parameters per population, fixing the radiative, singlet fission and fusion rates from literature values and the intrinsic non-radiative rates for S$_1$ and TT$_{bright}$ from estimates based on the gap-law of non-radiative decay. The gap-law has been shown to be a good predictor of non-radiative rates for acene and hetero-acene-type materials[246]. The free parameters are: k$_{dark}$, which is fixed by fitting to the S$_1$

delayed emission; k_{nr} and k_{spin} of TT_{dark}, are fixed by fitting to the tr-EPR and TA data; and k_{nr} of T_1+T_1, fixed by fitting to the terminal decay in the transient absorption data. Only k_{nr} and k_{spin} of TT_{dark} are not independently varying parameters. These are difficult to decouple as not enough is known about the intrinsic non-radiative decay of unentangled triplet-pairs or the time-constant for the formation of uncorrelated triplet pairs.
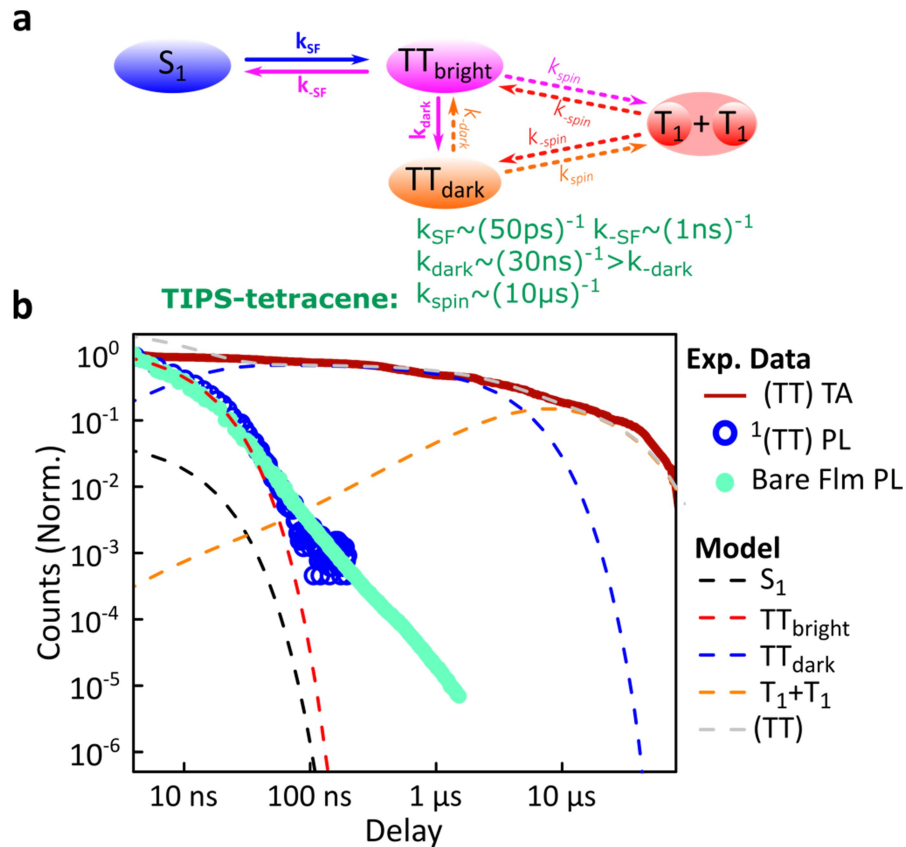
Figure 4.12: Basic rate model used to model TIPS-Tetracene film and microcavity emission. (a) schematic of rate model of bare films, all rates are reproduced in Appendix C. Parameters are set from literature or fit to literature data[12,13,78]. (b) Comparison of our basic rate model with published optical data (TA and PL)[13]. Circles indicate delayed emission from S_1, which tracks TT_{bright} population (red, dashed) as S_1 and TT_{bright} are in equilibrium. Solid brown line shows transient absorption of triplet-pair states which is proportional to the sum of all triplet-pair populations. In our model (TT) = TT_{bright} + TT_{dark} + T_1+T_1 (grey, dashed). We fit the T_1+T_1 lifetime to the decay of the transient absorption signal.

Having parameterised the model using reference data, we turn to modelling our own data. The basic model reproduces the initial exponential decay of the film, as expected, but does not reproduce the power-law-like tail we see after 10ns. To account for this tail, we require a distribution of exponential rates to produce a power law decay ($k_{dark}<(30ns)^{-1}$). To model the microcavity we use

our model for the exciton reservoir and include a new emissive state representing the lower polariton branch. The only new rates that appear, k_{pol_s}, k_{pol_b}, k_{pol_d}, describe the transfer of population from the singlet, bright TT and dark TT to the LPB (Figure 4.13a). We find that the rate of population of the lower polariton branch from S_1 and TT_{bright} (k_{pol_s} and k_{pol_b}) must be on the order of $(100ns)^{-1}$ to avoid rapid depopulation of the S_1 and TT_{bright} populations. A faster rate would result in a significant shortening of the LPB emission lifetime compared with the bare film S_1 emission, which we do not observe. To fit the correct relative intensity of the microcavity-enhanced portion of the delayed emission we used $k_{pol\_d} = 0.005\ k_{pol\_s}$. Using the same model but varying the ratio of k_{pol_s}/k_{pol_d}, we were able to fit microcavity emission from the different detunings.
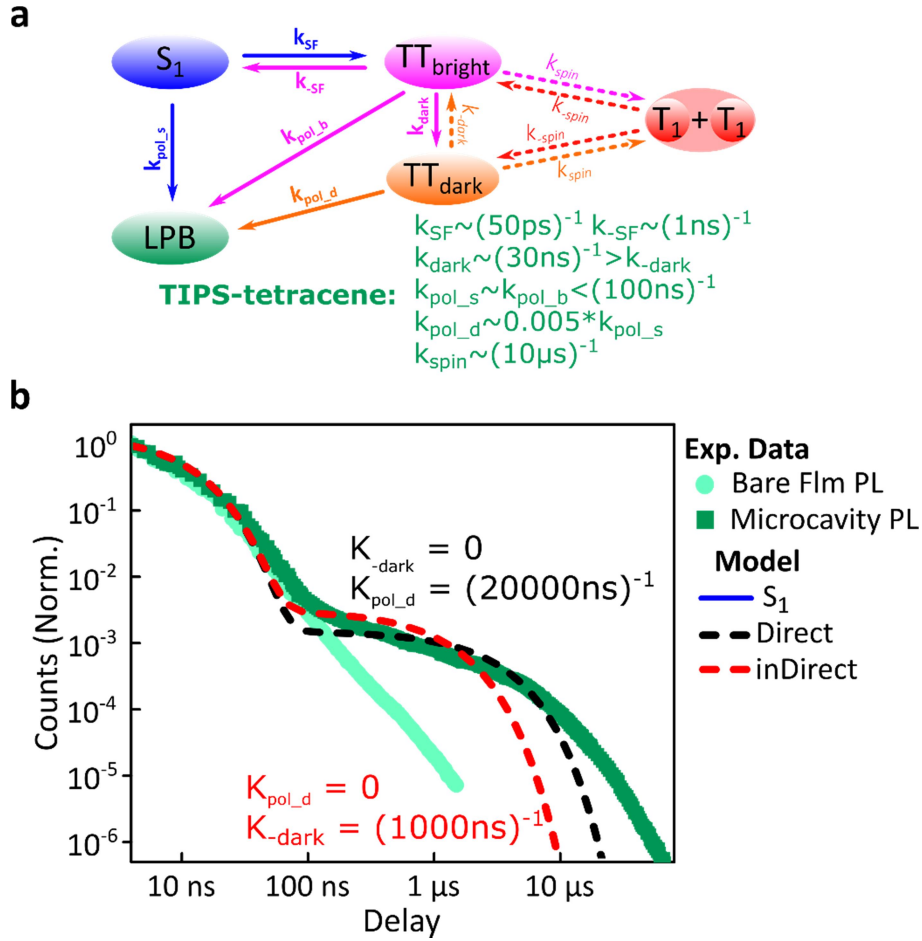
Figure 4.13: Basic rate model used to model TIPS-Tetracene film and microcavity emission. (a) schematic of rate model including polariton states, all rates are reproduced in Appendix C. Parameters are set from literature or fit to literature data[12,13,78]. (b) Comparison of our basic rate model with microcavity data[13]. Squares show emission from the lower polariton branch. We present two models presuming population of the lower polariton branch directly from quintet states and indirectly through TT_{bright}.

This good fit of the model to our data and that of the literature suggests that the LPB emission beyond 100ns originates primarily from TT_{dark}, the equilibrium population of weakly exchange coupled singlet/quintet states and strongly exchange coupled pure quintet states. These states do not significantly contribute to emission in the pure film but are able to populate the LPB. We suggest the reason for this is the enhanced photonic mixing within TT_{dark}.

Finally, we ran the model to determine whether population of the LPB from TT_{dark} was direct or indirect. For this we assumed no distribution of k_{dark} (and therefore a poor fit to the film S_1 emission tail). In Figure 4.13b we show results for direct population of the LPB from TT_{dark} with, as above, k_{pol_d}

= $(20\mu s)^{-1}$ and k_{dark} = $(0ns)^{-1}$, and indirect population via TT_{bright} (assuming a microcavity-induced enhancement of k_{-dark} from 0 to $(1000ns)^{-1}$ and k_{pol_d} = $(0ns)^{-1}$). While both routes are very surprising, we consider the k_{pol_d} pathway to be more probable, and it provides a better fit to the full dataset (Figure 4.13b).

In order to explain the existence of this pathway, we return to the concept of excited-state mixing. Mixed adiabatic states are a critical driver in photophysical processes such as ultrafast intersystem crossing[53], thermally activated delayed fluorescence[247], singlet fission[13,94] and its reverse, triplet-triplet annihilation. This property is a critical distinction from inorganic semiconductors, but in the exciton-polariton field it remains far more common to treat strong coupling in terms of diabatic states.

The potential implications of mixed states for strong coupling are profound. We postulate that when the photon couples to S_1 to form polaritons, it in fact interacts with all the states that mix with S_1. Consequently, all states that mix with S_1 may acquire some photonic character. In polaritonic systems in which triplet-triplet annihilation occurs, this admixture of photon into the triplet-pair states creates a pathway to populate the radiative lower polariton branch and thus a route to harvest light from nominally dark diabatic states. While the above explains any increased microcavity emission from $^1(TT)$, it does not on its own explain our observation of $^5(TT)$ harvesting. Our kinetics reveal a correlation with the strongly exchange-coupled, pure $^5(TT)$ state. This state exists in equilibrium with the weakly exchange-coupled $^1(TT)$-$^5(TT)$ mixed state[12,80,96,245], which itself acquires photon character through its $^1(TT)$ component. Hence, in the strong exciton-photon coupling regime, mixed states gain weak but non-zero photon character which creates a channel to populate the emissive lower polariton branch. Thanks to dynamic fluctuations in the exchange coupling, this allows even completely dark states like $^5(TT)$ to serve as a reservoir for polariton emission. The strong light-matter coupling then opens a new route for the $^5(TT)$ states to emit increasing emission of the system overall.

4.6 Conclusions

Here we incorporated a series of molecules into micro-cavity systems to investigate the effect of strong light-matter coupling on triplet production. We find that for all triplet production processes the long-lived emission of the system is enhanced compared to a bare film sample. This behaviour was observed not only for singlet fission active materials but also for systems undergoing intersystem followed by TTA. When triplets meet an encounter complex forms and a distribution of triplet-pair states are produced with spin of 0, 1 or 2. As the singlet character states are coupled and share character with quintet character states, we suggest the photon character gained by the singlet state is also shared with the ^{1}(TT) and ^{5}(TT) states. While the photonic character gained is small the long lifetimes of the quintet character states allow for a significant enhancement in the emissive character of the quintet state.

Interestingly, this behaviour could allow for an improvement in solid-state up-conversion. In an optimised fluorescence up-conversion system, the ability to directly harvest ^{5}(TT) encounter complexes in the weak spin-interaction regime should boost the maximum efficiency. At the same time, the resulting up-converted polariton emission would be well-directed, thereby simplifying collection. A similar mechanism could be used in electrically-injected polariton LEDs and lasers, where triplet excitons constitute 75% of the population and triplet-triplet annihilation could be used to harvest them. Because these states are very long-lived, they can make a substantial contribution to the total emission even if the instantaneous probability to emit is always low[248]. The ability of these very long-lived states to populate the lower polariton can also enable new applications in polaritonic physics[176,209–212]. For example, it may be possible to use such a reservoir of non-coupled states to feed a polariton condensate, greatly increasing its effective lifetime. This may be equivalent to the continuous pumping of exciton reservoir states in GaAs microcavities to continually repopulate the polariton condensate[214]. Such long-lived condensates would be important for practical applications of room-temperature polariton condensation. This concept also vastly expands

the scope of microcavity-controlled matter, which seeks to alter material properties and light-induced dynamics through strong light-matter coupling[161,176,207–212]. The interactions implicit in the adiabatic picture mean that strong coupling may perturb not only the state that dominates the absorption spectrum, but also any states that mix with it.

4.7 Methods

Below we include details of the transfer matrix simulations provided by Rahul Jayaprakash (University of Sheffield). Steady state absorption and emission, Reflectivity and time-resolved photoluminescence measurements were acquired as described in Chapter 3.

4.8.1 Transfer Matrix Simulations

Microcavity reflectivity data was modelled using transfer matrix simulations as previously reported[169], based on the measured absorption of the organic films. The absorption spectra were fitted to a series of Lorentzian peaks, with the oscillator strength of each individually tuned to correctly reproduce the extinction of the measured film. A uniform film of these absorbers was then modelled between two Ag mirrors (200 nm and 30 nm), using the tabulated value for the Ag index of refraction. The optical properties of the entire system (transmission, absorption, reflectivity) were calculated as a function of angle for comparison to the measured reflectivity maps. For these purposes, the index of the refraction of the organic layer inside the microcavity was treated as a free parameter, and it was adjusted to provide the correct dispersion for uncoupled cavity modes observable at shorter and longer wavelengths than the exciton-polariton bands of interest. Good fits were obtained with typical values ~1.6. The oscillator strength of the organic film was also adjusted slightly compared to the bare-film reference, to allow for slight variation in dye concentration from batch to batch, spatial inhomogeneity (reflectivity measurements are taken over a ~0.5 mm spot, versus 8 mm aperture for absorption) and inevitable partial sample degradation in air for reference

film measurements (due to the need to subsequently measure film thickness). In all materials, an adequately parametrized model which closely describes the film absorption can also closely reproduce the measured reflectivity maps, confirming that all samples are within the strong exciton-photon coupling regime. In addition to the peak positions of the polariton branches which are output by the transfer matrix model, we also include the input exciton peak positions and cavity photon mode dispersions as dashed lines in the Figures. Code and modelling provided by Dr. Rahul Jayaprakash (University of Sheffield).

4.8.2 Micro-cavity Refelctivity

Microcavity reflectivity maps were obtained on a home-built goniometer system, using motorised arms for excitation and collection that allow the angle of incidence to be swept from 10° to 60°. White light was provided by a fibre-coupled lamp with deuterium and halogen sources. Collected light was sent via fibre to an Andor Shamrock CCD spectrometer. Steady-state photoluminescence spectra were obtained with the time-resolved photoluminescence system (Chapter 3), using sufficiently long gate windows to capture the full microcavity or film dynamics.

In the following chapter we discuss the singlet fission process in a series of polyene oligomers. Throughout the work I produced and measured the samples, and carried out analysis on the data. However, the molecules were synthesised by a collaborator in the Heeney group (Imperial college London) and some additional measurements were performed by collaborators. Where these results are discussed, credit is given to the appropriate researchers.

5. Conjugation Length Dependence of Intramolecular Singlet Fission in a Series of Thienylene-Vinylene Oligomers.

5.1 Summary

The OTVs (oligo(theinylene-vinylenes)) were originally synthesised for solar cell applications due to their high hole diffusion rates and low energy band gaps. In 2013 Musser et al. observed activated intramolecular singlet fission in the polymer variant, PTV, providing a new system for the study of polyene intramolecular singlet fission[27]. However, across two studies by Datko et al.[37,38], the assignment of OTVs as singlet fission active polyenes was called into question. The authors investigated an OTV dimer, finding efficient intersystem crossing and no evidence for the dark symmetry forbidden $2A_g^-$ state of polyenes. A difficulty in comparing these studies is the vastly different effective conjugation lengths of the dimer and the polymer, which in polyenes is known to produce vastly different photophysics. Here we investigate a series of oligomers running from dimer to octamer, covering the conjugation length gap between the dimer and polymer. We start by confirming the polyene nature of OTVs, explaining the lack of $2A_g^-$ in the dimer via a switching in the state order at short conjugation lengths. Afterwards we confirm that the polymer and longer oligomers undergo activated singlet fission which switches to efficient intersystem crossing at a length of 3 units.

5.2 Background

In Chapter 2 we discussed polyenes, a class of materials whose conjugated backbone is constructed of alternating single and double bonds. A defining characteristic of polyenes is that the first excited state ($2A_g^-$, S_1) has the same symmetry as the ground state[32,112]. This means that one-photon transitions between S_1 and the ground state are symmetry forbidden. The presence of the S_1 state has been used to explain the lack of emission and fast non-radiative decay in polyenes such as carotenoids. S_1 can also be described as having significant triplet-pair character [49,121]. In 1987 Tavan and Schulten predicted that the triplets within this pair could separate and become isolated with a small energetic push, at a critical conjugation length[49,121]. This implies the possibility of activated singlet fission in long-chain polyenes. Activated intramolecular singlet fission was initially observed in the polyene-like polymer, polydiacetylene[28–30,249]. However, it is notable that the S_1 state was not observed before the formation of triplets in these studies[28–30,249].

A difficulty in the study of polydiacetylene is its propensity to form either blue or red phases depending on its environment[28–30,250]. Kraabel *et al.* for example, measured isolated polydiacetylene chains in a matrix that forces the molecules into a planar geometry ('blue phase')[28–30]. They reported formation of a triplet-pair state within a few ps of excitation[30] that was only formed after excitation above 2eV, as expected for activated singlet fission[30,49,121]. After formation, the triplet pairs all decayed within 30ps, much too fast for non-radiative decay of isolated triplets, as isolated triplets in polydiacetylene have been shown to have a lifetime of ~ 50µs[251]. The authors assign the fast decay to triplet-triplet annihilation, sped up by confinement of triplets on a single chain causing continued interaction between the triplets[30]. However, this behaviour is not universal; in two studies by Lanzani and co-workers, the authors measured a twisted conformation of polydiacetylene known as the red phase[28,29]. In this phase, they observed a long lived triplet population (>400ps) representing at most 50% of the initial transient absorption triplet signal[28,29]. In their report they apply the model by Zozulenko[252] which argues that traps in the one dimensional backbone isolate one of the

constituent triplets reducing their ability to recombine[28,29]. However in these studies no kinetics are presented past 400ps making assignment to isolated triplets, which are expected to have lifetimes on the order of microseconds in the absence of oxygen, difficult to verify[28,29].

Another polymer described as a polyene , PTV (poly(thienylene-vinylene)), has received attention due to its possible use in semiconductor devices[253,254]. PTV was first described as a polyene to explain the observation of fast non-radiative decay (~2ps) and low emission quantum yield (PLQY)[255,256] compared to similar polymers such as PPV (poly(p-phenylene-vinylene))[257,258]. PPV, in common with most other conjugated polymers, does not fit the polyene model as it has lower electron-electron correlations which lead to the first excited state being the bright $1B_u^+$ state. Further evidence that PTV can be described as a polyene was provided by Olejnik and co-workers who measured PTV excited state absorptions in the mid-infrared region[259] and Apperloo *et al.* who measured a series of OTVs (oligo(thienylene-vinylene))[179]. Olejnik *et al.* measure a population which decays with a sub-ps time constant aligning with the rise of a feature in the visible region[259]. As such, the authors assign the mid-infrared feature to the absorbing state and the visible feature to a dark intermediate, the S_1 state of A_g character[259]. This is consistent with previously reported spectra of other polyenes[25].

Apperloo *et al.* characterise a set of oligomers running from 2 units (Dimer) to 12 units (Polymer)[179]. They investigated the series of oligomers for their ability to undergo electron transfer to MP-C_{60} for possible solar cell applications[179]. Throughout, Apperloo *et al*. characterise the conjugation length dependence of absorption energy, triplet energy and excited state transition energies finding a linear dependence with 1/conjugation length as in carotenoids (a polyene) [179]. In all of the above polymer studies[253–256,259], the PTV ground state absorption is broad (FWHM ~2eV). By comparison to the conjugation length dependence by Apperloo *et al*. this suggests a wide range of conjugation lengths are present within the polymer samples[37,179,253–256,259,260]. Recently Musser *et al.* reported a sample of PTV with narrow ground state absorption (FWHM ~1eV), which shows no change with

concentration in solution. The authors of this study suggest they are able to measure an aggregation-free sample with average chain lengths around 12 units long.

In their study, Musser *et al*. extended the model of PTV by investigating its ability to undergo intramolecular singlet fission[27]. Musser and co-workers found that intramolecular singlet fission has a distinct excitation energy dependence[27], similar to blue phase polydiacetylene[30]. The yield of intramolecular singlet fission increases with higher energy excitation suggesting the triplet pair state formed during singlet fission sits above the absorbing state[27]. The authors report no transient absorption signals on the microsecond time scale, indicating a lack of isolated triplet formation[27]. Furthermore, the authors use transient absorption spectroscopy with 18fs pulses to show that both the triplet-pair and S_1 states form in parallel[27]. As a result, the S_1 state cannot be the parent state of singlet fission, a divergence from the proposed mechanism by Tavan and Schulten[27,49,121]. Despite the above work, the assignment of PTV and OTV (oligo(thienylene-vinylene)) molecules as polyenes has been called in to question, most recently by Datko and co-workers, who imply that OTVs should be described with a non-polyene model in which the lowest-lying excited state is of B_u symmetry [38].

Datko *et al.* suggest the current polyene-model of PTVs is incorrect in two papers studying PTVs and an OTV dimer. In the first of these papers, the authors suggest the model presented by Musser *et al*. and others is incorrect due to the reappearance of strong emission when polymer chains are isolated in dilute solution [37]. Similar results have been reported in studies of PTV embedded in PMMA films by Hu *et al*[260]. Polyenes are expected to be non-emissive at all concentrations and so Datko *et al*. explain this concentration dependent reduction in emission as aggregation induced quenching[37]. We reproduce the Figure from the study by Hu *et al*. showing absorption, emission and excitation spectra for a pure PTV film and PTV embedded in a PMMA matrix (Figure 5.1)[260]. For the chains embedded in PMMA matrix (panel b) Hu *et al.* measured a large blue shift in the emission and excitation spectra compared to the absorption spectrum[260]. Datko *et al.* explain this via selective excitation of the isolated chains in the film which have a blue shifted absorption spectrum compared

to aggregated chains[37]. As the concentration is increased to a pure PTV film, data in panel (a), energy-transfer to the non-emissive aggregated chains reduces emission yield. An alternative explanation, which we demonstrate below explains all available data, is that only short (high energy) chain segments are emissive.

This is because, as we demonstrate In this chapter, the emission characteristics of the OTV materials are highly conjugation length dependent; the shorter oligomers are emissive while the longer chains are not. This is similar to behaviour observed in polyenes, in which the shortest conjugation length molecules have emission yields as high as 80%[261]. As such, we find that the observations by Hu *et al*. and Datko *et al*. can be fully explained by the polyene framework. Within this framework, dilute PTV samples can emit from short conjugation length segments (blue-shifted), while at high concentrations, energy can transfer from short to long chain lengths which efficiently dissipates energy non-radiatively.
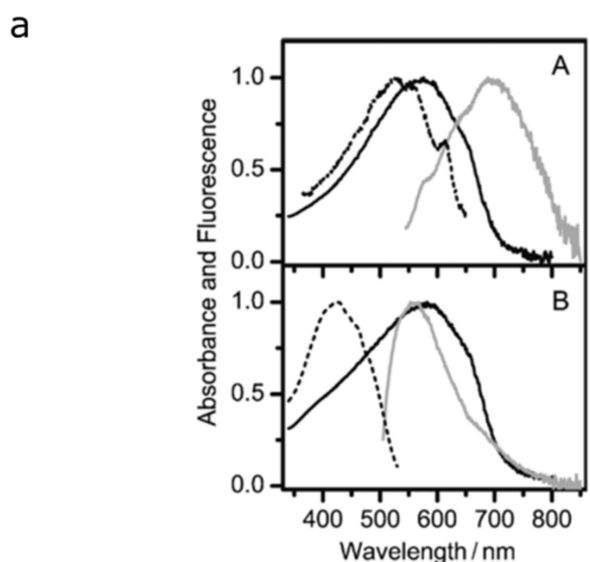
Figure 5.1: Normalised absorption (black solid), emission (gray solid), and fluorescence excitation spectra (bblack dashed) for A) pure rra-P3HTV film and B) highly concentrated rra-P3HTV embedded in PMM. The emission spectra were detected at 488nm excitation. The excitation spectra in (A) and (B) were detected for the emission maxima at 680nm ad 560nm, respectively. Figure reproduced from Ref[260].

The increased emission in shorter oligomers is in agreement with the second paper by Datko *et al.* which describes how an OTV dimer undergoes rapid (100ps) intersystem crossing via a twisting motion[38]. Critically, the intersystem crossing model of triplet production in the dimer does not require singlet fission. Datko *et al.* implies that this model can be applied to the longer oligomers and the polymer, contradicting the established model for PTV[27].

The difficulty in assessing which model is correct stems from the fundamental differences when comparing a short-chain oligomer with a long-chain polymer. The oligomer series characterised by Apperloo *et al.* bridge this gap, with chain lengths ranging from 2 to 12 units. Indeed, they observe triplets in short oligomers with no sign of triplet production in longer chain oligomers. However due to the limited time resolved data presented in their study they were unable to assign triplet production pathways.

Herein, with the use of excitation dependent fs-transient absorption on a series of OTVs, we can confirm that the OTVs are polyenes, and that they undergo activated singlet fission above a critical conjugation length.

5.3 Steady State Spectroscopy
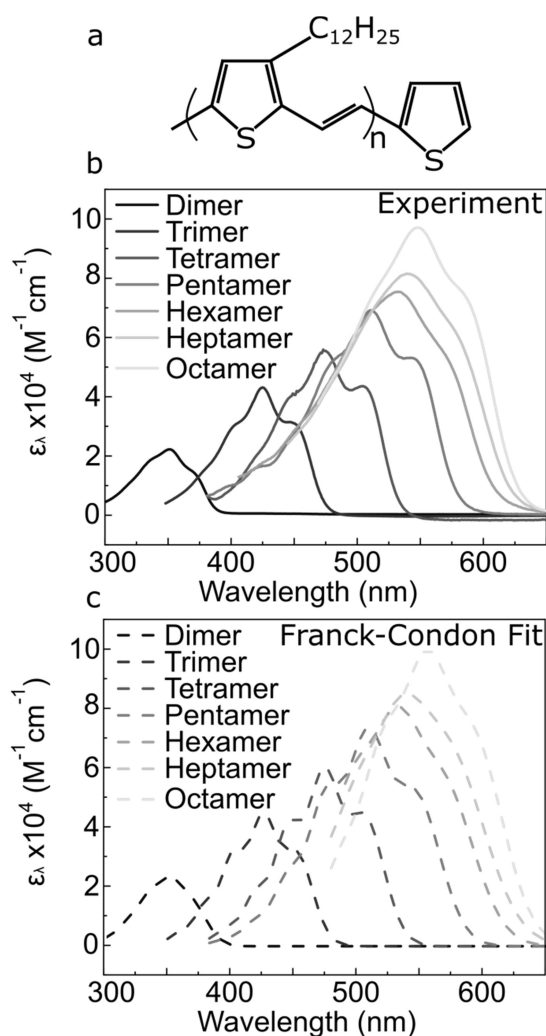
Figure 5.2: Steady state absorption of oligo(thienylene-vinylenes): (a) Chemical structure of the oligo(thienylene-vinylenes), the n represents the number of units in the molecule. (b) Ground state absorption of the 2-8 unit oligomers scaled to their extinction coefficients. (c) Franck-Condon fit of the 2-8 unit oligomer scaled to their extinction coefficients. Parameters used for the fit are given in Table 5.1.

Figure 5.2 presents the structure (a) and the ground state absorption spectrum (b) of each oligomer.

We fit the absorption spectrum of each oligomer with a Franck-Condon progression presuming the same FWHM for each peak and a single vibrational mode, as in refs[40,262]. The spectral fits are presented in Figure 5.2c, while the parameters used to fit the spectra are summarised in Table 5.1. Most of the parameters do not scale systematically with number of units. However, from the dimer through to the octamer, we observe a red-shift in absorption spectrum along with a rise in extinction coefficient as the conjugation length increases, consistent with previously studied molecules[179,263,264].

We find that our extinction coefficients and 0-0 Energies follow the trends calculated for polyenes[111] and DPP based oligomers[263].

Table 5.1: Fitting parameters for the absorption spectrum of the OTV molecules. Conjugation lengths quoted are effective lengths based on comparison to the dependence presented previously for carotenoids.

Name	Conjugation Length	Extinction Coefficient ($M^{-1}cm^{-1}$)	Huang-Rhys Parameter	FWHM (meV)	Vibrational spacing (meV)	0-0 Peak Energy (eV)
Dimer	4.3	22240	1.53	228	180	3.35
Trimer	7.5	43100	1.41	174	176	2.75
Tetramer	11.5	55860	1.36	165	171	2.45
Pentamer	17	69140	1.41	175	175	2.27
Hexamer	22	75380	1.46	190	162	2.17
Heptamer	28	81520	1.28	207	170	2.15
Octamer	33	97080	1.41	181	167	2.11

We observe negligible (~0%) photoluminescence from oligomers with 5-8 units, when exciting at their absorption peak. This is expected behaviour for polyene-like materials where absorption is into S_2, and S_1 is non-emissive[32,39,112]. This is consistent with previous studies of OTV molecules[27,179]. However, in the shorter oligomers (tetramer, trimer and dimer), emission is observed, shown in Figure 5.3a. The tetramer has an emission quantum yield under 0.1% making measurement of the emission difficult. However, we note the similarity between the emission spectrum of the tetramer and the spectrum from dual fluorescence in dipheyl-polyenes[265]. The dimer shows a slightly increased quantum yield of 3.6% and the trimer has the highest quantum yield of 10%.

To assign the emitting state of the dimer and trimer, we present emission spectra taken at 77K in Figure 5.3b/c. To understand the data, we attempted to fit a Franck-Condon model to the emission spectrum. We assume equal FWHM for each vibronic peak and one effective vibrational mode. We use the refractive index of the solvent in the formula which has no dispersion in this spectral region. For the dimer we are unable to fit the emission with a Franck-Condon progression, finding a red shift and suppression of the 0-0 peak. These are changes expected for self-absorption of the emission;

indeed, we find the absorption and emission spectra of the dimer overlap. In order to simulate the self-absorption effect, we multiply our Franck-Condon fit by 1-Absorption (OD), red dashed line in Figure 5.3b. We find an agreement between the Franck-Condon fit and the measured spectra after correction for self-absorption. Interestingly, we find a distinct change in spectral shape (narrowing, change in vibronic structure) between the absorption and emission with a shift of 0.14eV between the 0-0 peak energies. This indicates a substantial geometric reorganisation consistent with a torsion rotation in the excited state[266] in agreement with the study by Darko *et al*[38]. As we can satisfactorily fit the emission with a Franck-Condon progression, we suggest the emission originates from the absorbing state of B_u symmetry.
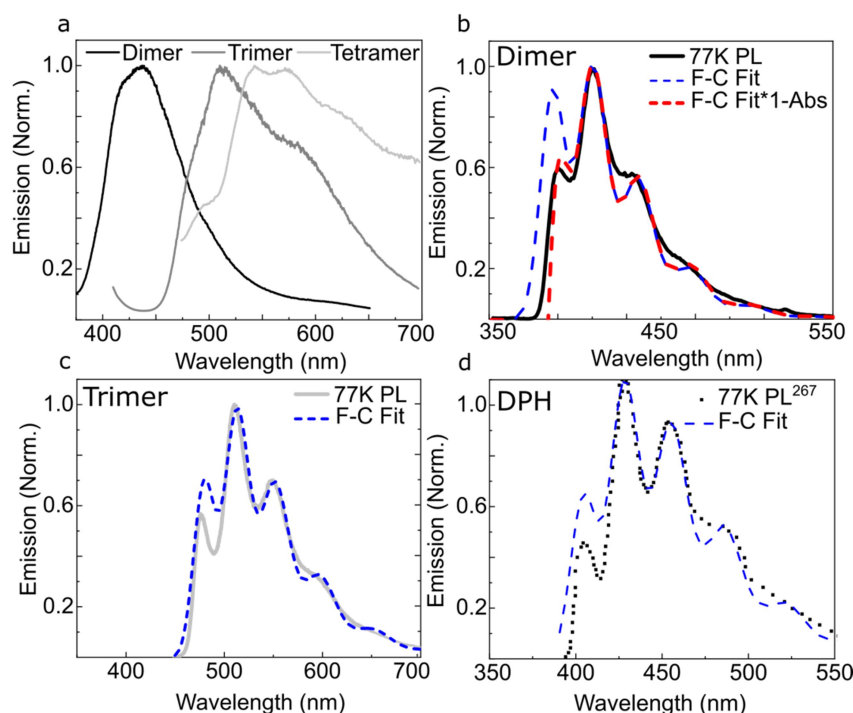
Figure 5.4 Emission of short-chain OTVs and DPH: (a) Steady state emission spectra for the 2,3 and 4 unit oligomers, normalised to peak intensity. (b) Low temperature (77K) emission spectrum of the dimer, in a solvent blend (diethylether:ethanol - 1:1). A Frank-Condon fit to the 77K emission is also included with the following parameters: Huang-Rhys Parameter = 1.1, 0-0 energy = 3.20eV, Vib Spacing = 0.18eV, FWHM = 141meV (blue dashed line). We simulate the effect of self-absorption on the Franck-Condon fit by multiplying the fit by 1-Absorption (OD) (red dashed line) (c) Low temperature (77K) emission spectra of the trimer in a solvent blend (toluene:diethylether:ethanol - 1:1:2). A Frank-Condon fit to the 77K emission is also included with the following parameters: Huang-Rhys Parameter = 1.4, 0-0 energy = 2.59eV, Vib Spacing = 0.17eV, FWHM = 139meV (blue dashed line). (d) Emission spectrum of diphenylhexatriene in a PVA film at 87K reproduced from Ref[267] to which we have fit a Franck-Condon progression. Parameters of the fit: Huang-Rhys Parameter = 1.69, 0-0 energy = 3.08eV, Vib Spacing = 0.17eV, Broadening = 136meV (blue dashed line).

For the trimer we find that we cannot fit the spectrum in its entirety, however, we can fit the 0-1, 0-2, and 0-3 peaks. Compared to the Franck-Condon fit, the measured 0-0 vibronic replica is reduced in intensity and appears *blue-shifted*. In Figure 5.3d we show the emission spectrum of diphenyl-hexatriene (DPH). DPH has been very well characterised and is described as a polyene. We fit the DPH spectrum with a Franck-Condon progression as described above. As with the trimer, DPH has a suppressed 0-0 vibronic transition with an apparent *blue-shift*. Unlike the dimer here we measure a *blue-shift* in the 0-0 peak rather than a *red-shift*. As such it is not possible to explain the observed behaviour via self-absorption. The similarity between the two spectra suggests emission originates from similar electronic states.

A reduced 0-0 emission peak is consistent with emission from a forbidden transition (e.g H-aggregates, S_1 in carotenoids, triplet-pair states[34,70,268,269]). In carotenoids, a class of polyene materials, S_1 emission has been explained by intensity borrowing via a Herzberg-Teller mechanism[270–275]. The Herzberg-Teller mechanism allows states with symmetry forbidden transitions (i.e. dark states) to emit via vibrational coupling to symmetry allowed states (i.e. bright states)[270–275]. As such, the pure electronic symmetry forbidden 0-0 transition is supressed or even entirely lost in some materials[270–275]. An apparent slight blue-shift in the 0-0 peak emission is also consistent with previous reports of emission from S_1 states in polyenes[34,269]. We explain the apparent blue-shift in the 0-0 peak via coupling to vibrational modes required for Herzberg-Teller coupling (Figure 5.4). Emission occurs from the zeroth vibrational level of the forbidden state to all levels of the ground state. As the 0-0 transition is explicitly disallowed, instead emission occurs from above the zeroth level of the forbidden state via coupling to vibrations. As this state is coupled to a vibration it occurs from slightly above the forbidden state, to the ground state and thus appears blue-shifted, as shown schematically in Figure 5.4.

a	b

S_1 S_1+S_2

S_0 S_0

Symmetry Allowed Emission   Symmetry Forbidden Emission
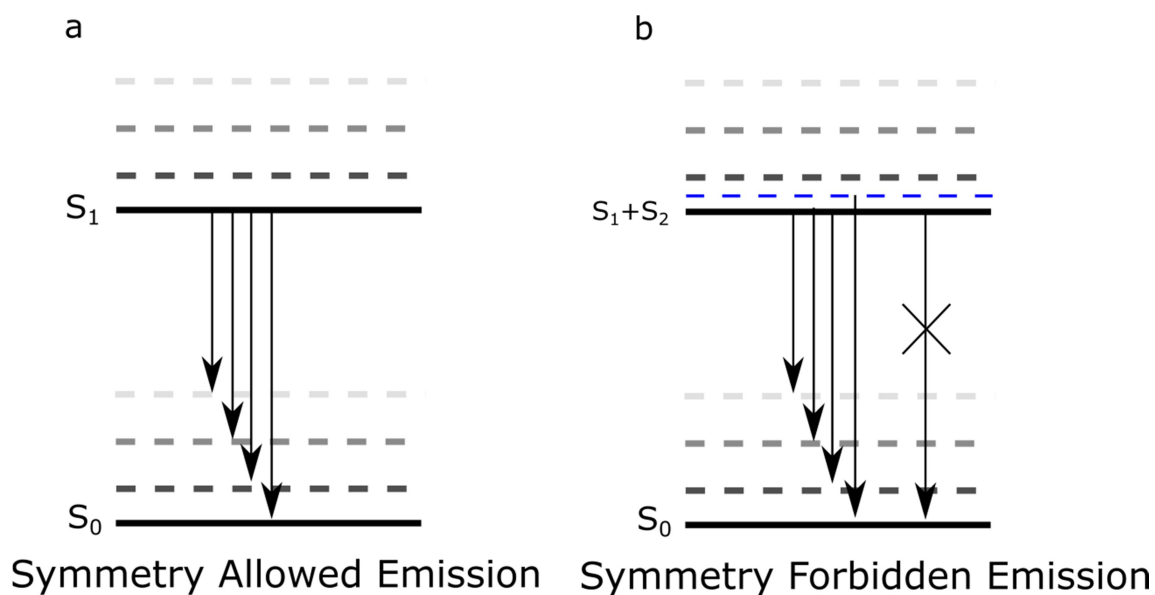
Figure 5.4: Mechanism of the blue-shift in 0-0 emission peak due to H-T coupling. (a) Schematic of symmetry allowed emission, in which emission occurs from the zeroth vibrational level of the emitting state to all vibrational levels of the final state. (b) Schematic of emission from a symmetry forbidden state, allowed via Herzberg-Teller coupling. Emission occurs from the ground vibrational level of the mixed character state to all vibrational levels of the final state. As the 0-0 electronic transition is forbidden, the observed 0-0 emission peak represents a transition from the zeroth level + a vibration of Bu symmetry (Indicated by the blue dashed line) to the zeroth level of the final state. This causes a blue shift in the observed 0-0 emission compared to that of the expected transition.

In two studies by Noguchi *et al*. and Werncle *et al*. the authors investigated state mixing by measuring the carbon-carbon double bond stretching mode of β-carotene and DPH in a variety of solvents[276]. As the S_2 state energy is strongly solvent dependent, while the S_1 state is not, each solvent gives a different S_2-S_1 energy gap[276]. The study found that as the S_2-S_1 gap decreased, the carbon-carbon double bond stretching mode is shifted lower in energy, a signature of strong vibrational coupling[276]. The authors found that the S_1 state gains significant S_2 character when the gap drops below $4,000 cm^{-1}$ (0.48eV) [276]. As we see significant emission from the trimer, the S_2-S_1 gap must be below 0.48eV. Indeed, comparing absorption and emission 0-0 energies gives an energy gap of 0.16eV.

In a similar vein, the radiative rate is likely to be affected by the coupling of the S_2 and S_1 states. Andrews *et al*. investigated this for DPH and found that mixing between the S_2 and S_1 states leads to

a faster radiative rate[277]. To compare with literature on polyenes we calculate the $\frac{(n^2-1)}{(n^2+2)}$ (proportional to polarizability) value for the solvent used (toluene) and the radiative rate (K_r) of the trimer ($K_r = \frac{\phi_{PL}}{\tau_o}$ where τ_o is the measured lifetime of the state and ϕ_{PL} is the PL quantum yield[40,277]). We find a value of $(13\pm2.4\text{ns})^{-1}$ with $\frac{(n^2-1)}{(n^2+2)} = 0.29$, which is similar to the value for DPH at this polarizability $(16\text{ns})^{-1}$ [277]. The above observations suggest that the emission we observe is from a symmetry-forbidden state, which borrows intensity from a nearby bright state. Following previous work on carotenoids and PTVs discussed above, we assign the emission in the trimer to the S_1 state.

5.4 Time Resolved Spectroscopy - Tetramer to Octamer

In the previous section we confirmed that OTVs (and PTVs) are polyene-like. In polyenes almost all of the excited-state processes occur non-radiatively[32,39,112]. Therefore, we now turn to transient absorption spectroscopy. Previous transient absorption spectroscopy on OTV/PTVs has focussed on polymers[27,259] and therefore we begin by studying the polymer-like oligomers (i.e. long chain). Figure 5.5 presents transient absorption spectra and kinetics for the tetramer, hexamer and octamer excited at 500nm and 400nm (pentamer and heptamer in Appendix D). All three oligomers show broadly similar features after 500nm excitation. We measure a ground state bleach (positive feature) and a photo-induced absorption (negative feature) red-shifted relative to the ground state bleach (Figure 5.5).

In Figure 5.5 we also present kinetics taken at the peak intensity of the photo-induced absorptions (PIA) of each molecule. For each oligomer, in addition to an initial decay of 55 ± 5ps (tetramer), 4.2 ± 0.3ps (hexamer), and 2 ± 0.2ps (octamer), we detect a small population with a longer decay constant. We return to this longer-lived population when we discuss high energy excitation below. In all molecules we are unable to resolve the rise of the PIA features as the rise occurs within the

instrument response. As a result, we cannot rule out assignment of the PIA to the absorbing singlet state, although we observe no stimulated emission.
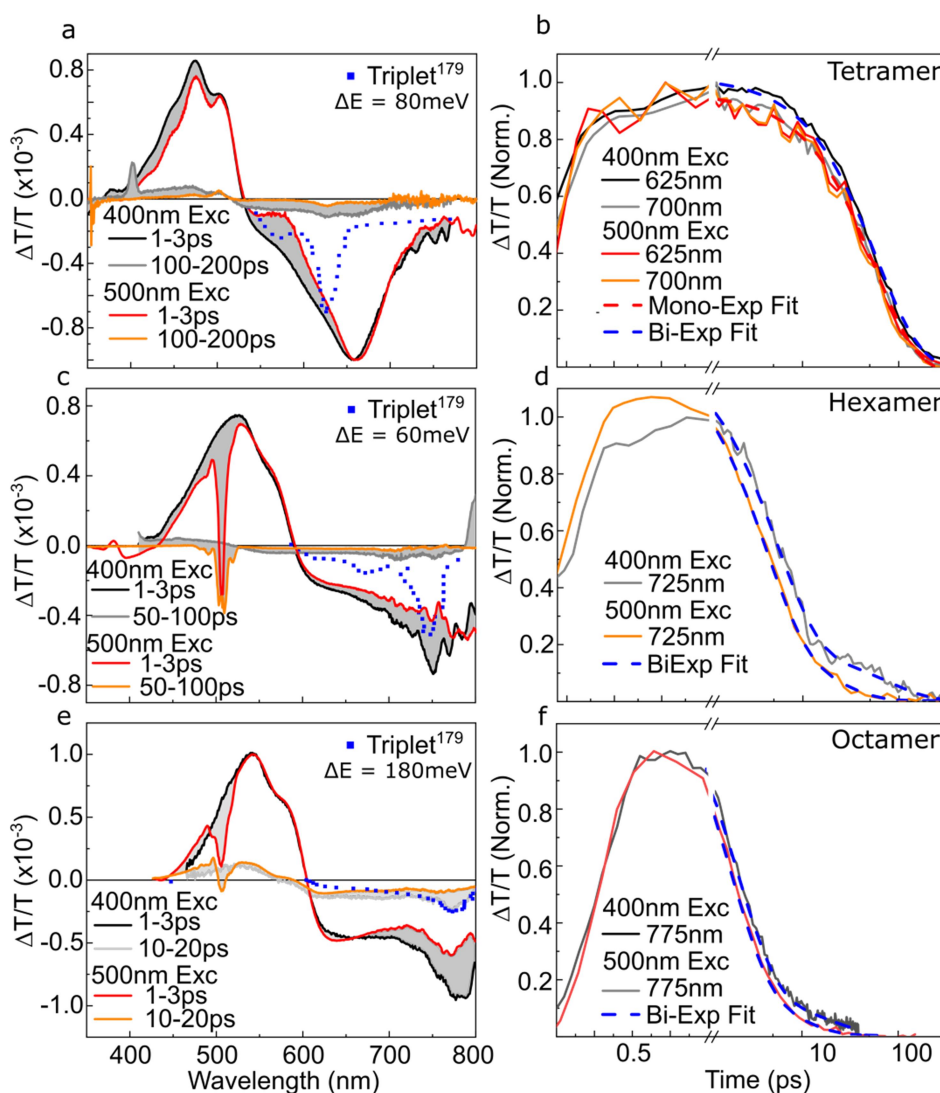
Figure 5.5: Excitation energy dependent transient absorption of 4-8 unit OTVs: (a,c,e) Transient absorption spectra of the tetramer (a), hexamer (c) and octamer (e) excited at 500nm and 400nm (1mW power). Spectral slices are averaged over times marked in the legend. Included are the sensitised triplet spectra taken from Apperloo *et al.*[179], blue-shifted by an energy indicated in the panel. The 500nm spectra have been scaled so that the 0-0 peak of the ground state bleach matches the 400nm excitation data. (b,d,f) Transient absorption kinetics of the tetramer (b), hexamer (d) and octamer (f) at the central wavelengths marked in the legend (10nm window). For the tetramer kinetics were taken in the triplet and singlet PIA regions. Due to a broadening of features in the hexamer and octamer data, we also show a kinetic at the peak of the triplet region. Dashed lines show mono/bi exponential fits. Fit parameters are detailed in Appendix E and in the text.

In their study of PTV, Musser and co-workers demonstrated that intramolecular singlet fission only occurs when activated by excess energy excitation[27], as previously observed in polydiacetylene[30]. In

Figure 5.5 we therefore compare transient absorption data with high- (400nm) and low-energy (500nm) excitation for all three molecules. Starting with the tetramer, after 400nm excitation (high energy) we find an enhancement in the 550-650nm region of the spectrum (shaded). After 200ps most of the spectrum decays revealing a weak long-lived feature which was barely visible after 500nm excitation (low energy). To assign this feature we compare to a sensitised triplet spectrum by Apperloo *et al.* shifted by 80meV (Figure 5.5)[179]. We find a clear resemblance between the shifted sensitised triplet spectrum and the enhancement/long-lived feature (Figure 5.5). We therefore assign this enhanced long-lived feature to triplet-pairs generated via activated singlet fission, similar to the polymer[27]. Recent studies of zethrenes[31] and heteroacene films[34] that undergo singlet fission observe a similar blue-shift between sensitised triplets and singlet fission generated triplets. This shift quantitatively correlates with the binding energy ($E_b = E_{2T_1} - E_{^1(TT)}$) of the triplet pair (^{1}(TT)) generated by singlet fission (binding energy defined in Figure 5.6).
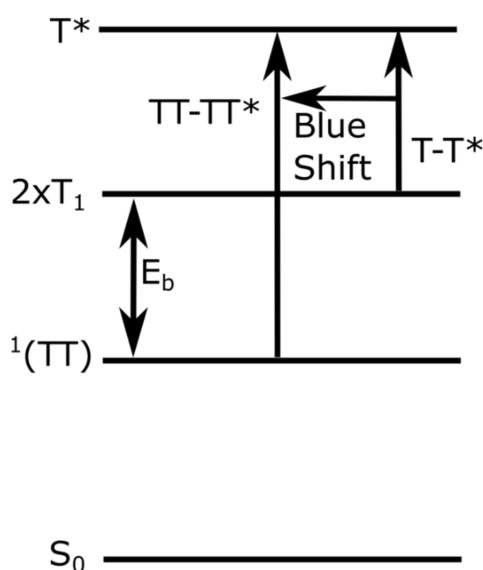
Figure 5.6: Definition of binding energy. We show a schematic with arbitrary energy levels to demonstrate the definition of the binding energy between triplets in the triplet-pair state.

The above evidence allows us to assign the long-lived feature to singlet fission generated triplet-pair states with $E_{binding}$= 80-180meV. As we do not observe a long-lived (µs) population, we suggest that ^{1}(TT) decays without ever separating to free triplets. Figure 5.5 shows equivalent data for the

hexamer and octamer, along with sensitised triplet spectra for each molecule from ref[179]. We also

include equivalent data for the pentamer and heptamer molecules in Appendix D. For all oligomers

we find that with excess energy excitation we observe an enhancement of the longer-lived kinetic

component (Figure 5.5). Considering the similarity between the kinetic and spectral features we

suggest the same model can be used to describe the 4-8 unit oligomers. To summarise, with band-

edge excitation only a singlet state is formed with a single decay constant which is dependent on

conjugation length. At high energy excitation, the weakly coupled ^{1}(TT) states which sit above the

energy of the absorbing state are also formed, which introduce a slower decay component. We find

no evidence of separation to isolated triplets. All these findings are in agreement with previous

studies of the polymer[27]. In Figure 5.7 we show a scheme of the potential energy surfaces and their

energy ordering for the 4-8 unit oligomers.
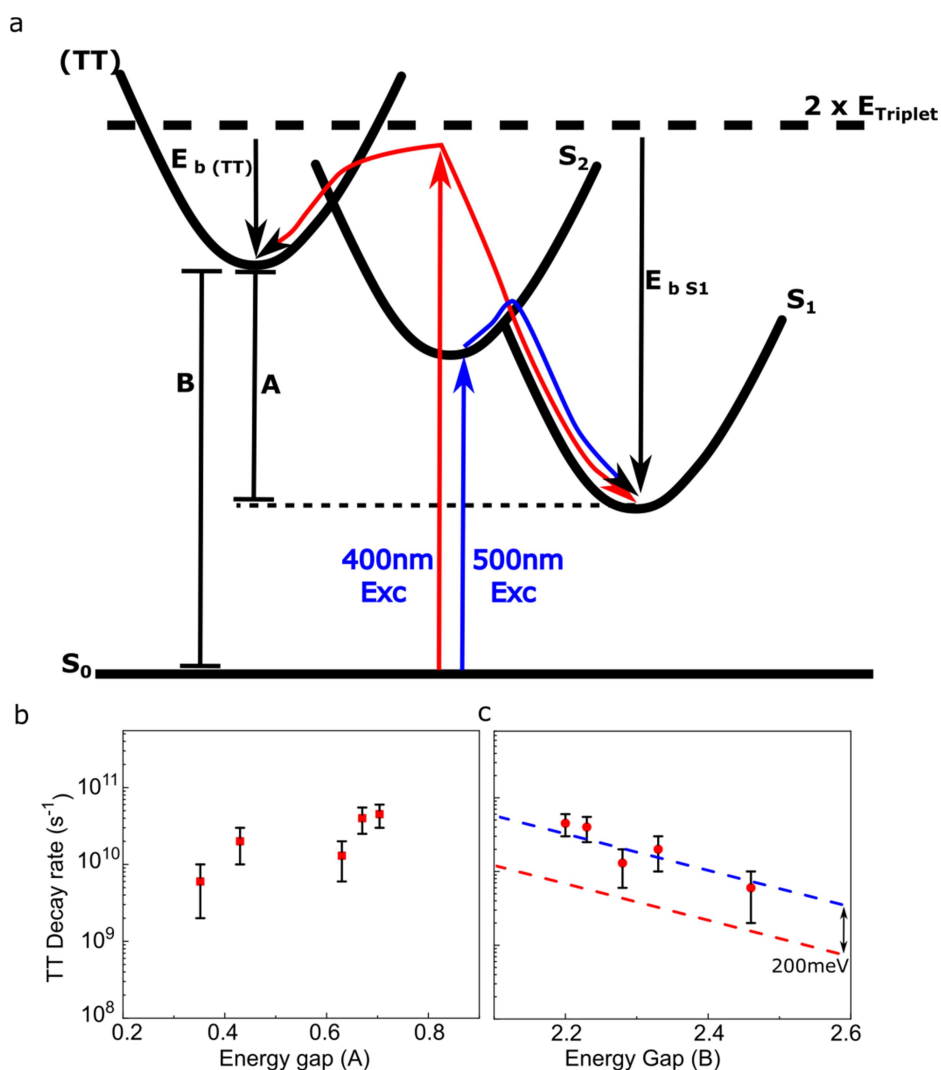
Figure 5.7: Summary of energy level scheme proposed for 4-8 unit oligomers: (a) Estimated relative energies and potential energy surfaces of the 4-8 unit oligomers. Positions and energies are arbitrary and do not represent measured or calculated values. The binding energy of the S_1 and triplet pair ^{1}(TT) states are shown relative to double the energy of sensitised triplets. (b) Decay rate of the ^{1}(TT) state accessed after high energy excitation, plotted against energy gap A (b) and energy gap B (c). Error bars are based on the range of decay constants able to adequately describe the decay kinetics. The dependence of decay rate on S_1 energy for a series of carotenoids in literature is given as a red dashed line[52]. The same dependence blue-shifted by 200meV is shown to fit our triplet decay constants (blue-dashed line).

It is interesting that the triplet features here decay with such a short lifetime of 10-100ps (details in Appendix E). Similar short ^{1}(TT) lifetimes have been observed in polymers[27,30] and carotenoid aggregates[23–25] and have been attributed to rapid geminate triplet-triplet annihilation. However, the ^{1}(TT) state here shows some similarities with the S_1 state in polyenes. In fact, in their review Musser and Clark[34] show that strongly bound triplet-pairs decay following an energy-gap-law-like dependence on conjugation length similarly to the S_1 state. In Figure 5.7 we apply this model to the ^{1}(TT) state for the 4-8 unit oligomers. We fit kinetics for each of the oligomers after high energy

excitation with a bi-exponential, locking the first decay component to that of the S_1 state at band edge excitation. From this we collect a decay component for the new feature which appears only after high energy excitation. We then compare this rate to two different energy gaps shown in Figure 5.7. In panel b we compare the decay rate to the energy gap between the triplet pair and S_1 states ($E_{TT} - E_{S_1}$) (for details of S_1 state energy estimates see Section 5.7). We find no clear dependence of rate on this energy gap, with at most an 'inverted' dependence, a slower rate for smaller energy gap. As such we suggest it is unlikely that the dominant decay channel of the ^{1}(TT) state is through the S_1 state.

In panel c we compare the decay rate to the energy of the ^{1}(TT) state (Estimated as E_{2T_1}, triplet energies taken from the study by Apperloo et al.[179]). We find an energy-gap-law-like dependence with a slower rate for a larger energy gap. In fact, the slope of the fitted dependence (blue dashed line) quantitatively matches the slope of the same dependence for the S_1 state of carotenoids (shown in Figure 5.7, red dashed line), but shifted by 200meV to higher energy. This suggests we over estimated E_{TT} by ~200meV. This is possibly due to inaccuracies in the estimates of triplet energies in the paper by Apperloo et al.[179], or could be due to the binding energy between the triplets in the ^{1}(TT) state which we previously estimated to be (80-180meV).

Here we have shown that the triplet-pair state generated via activated singlet fission has triplet-like excited state spectra but decays with a lifetime similar to S_1 (an energy-gap-law-like dependence). Additionally, according to Tavan and Schulten, the S_1 state has triplet-pair character (discussed further in chapter 6)[49,121]. As a result, the ^{1}(TT) state and the S_1 state appear to have triplet *and* singlet character. We now move to the shorter oligomers that are of a similar conjugation length to the dimer measured by Datko et al.[38]

5.5 Time Resolved Spectroscopy - Trimer

In Section 5.3 we established the energy landscape for the trimer, finding a small gap between the S_2 (Absorption) and S_1 (emission) state energies. We assigned emission to a dark singlet state via Hertzberg-Teller coupling, evidenced by the emission spectral shape. Due to the strong vibrational coupling involved in the Herzberg-Teller mechanism and the small energy gap (0.16eV) between the S_2 and S_1 states we expect the two to be strongly mixed. To investigate the mixed adiabatic state further we turn to excited state dynamics. We first conducted concentration dependent DOSY NMR (measurements by Iain Andrews) and ground state absorption to check for aggregation (Appendix G). We find no change in diffusion coefficient or spectral shape with concentration suggesting we are always measuring isolated molecules. In Figure 5.8 we present transient absorption and fluorescence up-conversion spectra and kinetics taken after 400nm excitation (high energy excitation).

In Figure 5.8a (top panel) we present transient absorption spectra taken in the first 1ps after excitation. At 50fs delay we measure a small stimulated emission (SE) feature at 500-530nm, and a weak PIA in the NIR that decays over the first picosecond. As we only see loss of intensity at the edge of the measurement window this suggests we are measuring the decay of a feature in the IR, with a tail in the NIR. This is similar to previous measurements of astaxanthin[25] (a polyene) and previous studies of PTV[259]. In both studies the authors find a strong PIA in the IR region from the S_2 (absorbing) state[25,259]. Due to the short lifetime and similarity to previous measurements of polyenes we suggest the NIR tail originates from S_2. Over the same time scale (1ps), three features at 550nm, 775nm and 1100nm rise to cover the whole measurement window (Figure 5.8a, bottom panel).

In Figure 5.8b we present fluorescence up-conversion photoluminescence spectra (FLUPS) for the trimer excited at 400nm (taken by George Farrow at the University of Sheffield). This spectrum is similar to the steady state spectrum in Figure 5.3. Over the first 1ps we observe a loss in intensity accompanied by a red-shift (Figure 5.8b, bottom panel). To further investigate, we present kinetics of each feature in the transient absorption and FLUPS measurements. In Figure 5.8c we compare the

rise of the 505nm and 775nm PIA features, the decay of the NIR tail at 1100nm, and the decay of the

emission spectrum at 475nm. The initial decay of the NIR PIA feature and the emission dynamics at

475nm are identical (420±100fs), suggesting they originate from the same excited state. This decay

approximately matches the rise of the PIA features at 505nm/775nm (280±100fs). Therefore, we

suggest the initially excited population evolves from showing stimulated emission and a NIR PIA, to

visible PIA features at 505 and 775nm. Interestingly, on the same time scale the emission spectrum

barely changes shape.
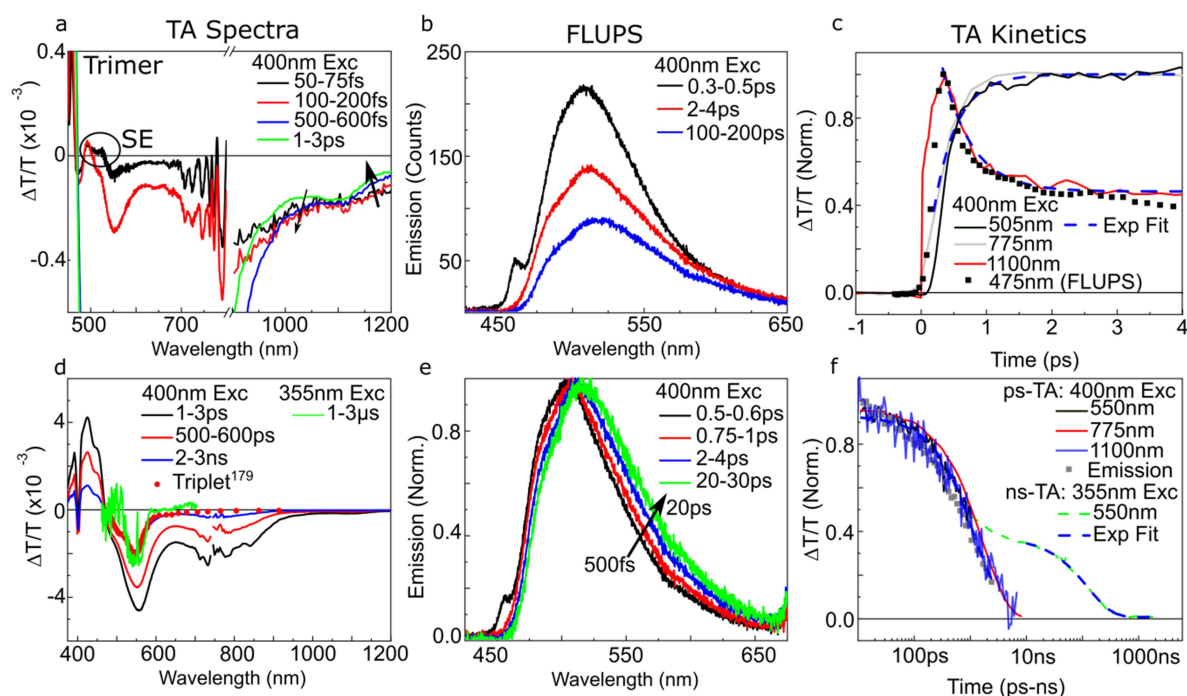
Figure 5.8: Transient absorption and fluorescence up-conversion of the trimer. (a) Transient absorption spectra of the trimer excited at 400nm averaged over times shown in the legend (1mW power) and a 1-3µs delay trace taken with 355nm excitation (ns-TA, 0.5mW). We include the sensitised triplet spectrum from Apperloo *et al.*[179]. (b) Fluorescence up-conversion (FLUPS) spectra excited at 400nm averaged over times shown in legend. The bottom panel shows spectra normalised to their maximum intensity. (c) Transient absorption and FLUPS kinetics averaging a 10nm window around the wavelengths displayed in the panel (excitation at 400nm). We also include a ns-TA kinetic at the triplet peak excited at 355nm (0.5mW power). We show in Appendix H that excitation energy doesn't change dynamics or spectral shapes. Note the overlap of the ps-TA and ns-TA kinetics allowing accurate scaling. The FLUPS kinetic has been scaled to the same intensity at 10ps for comparison to the transient absorption kinetics. Throughout the kinetic panels fits of exponential decays are indicated with a blue dashed line, parameters given in Appendix E.

In Figure 5.8e (bottom panel), we present kinetics taken at the peak of the 550nm, 775nm and

1100nm transient absorption features along with a kinetic taken at the peak of the emission

spectrum. We find identical decay components (1.3±0.2ns) for the three transient absorption features suggesting they originate from the same state. As the decay kinetics of these features match the decay of emission which we previously assigned to the S_1 state, we suggest all three PIA features represent population of the S_1 state. Interestingly, the 550nm S_1 feature appears very similar to the sensitised triplet spectrum found by Apperloo et al. (red squares, Figure 5.8a) but red-shifted by 6meV[179], while the 775nm and 1100nm peaks do not. Mazumdar and co-workers studied the ^{1}(TT) state theoretically for a series of acene dimers. The authors solve the Pariser-Parr-Pople (PPP) Hamiltonian including intermolecular 1e-1h to 4e-4h states to calculate the excited state absorption spectrum of ^{1}(TT)[278,279]. They found that in addition to a triplet character transition in the visible, there are also 2 smaller peaks related to 1e-1h CT configurations[278,279]. These observations qualitatively match the S_1 PIA features measured here for the trimer. We tentatively assign the 775nm and 1100nm features to CT character excited-state absorptions from the S_1 state.

The triplet-like peak at 550nm is qualitatively similar to the observations of triplet-pair states in the longer oligomers but shifted in the opposite direction. To confirm this feature does not represent a triplet-pair state formed via singlet fission as in the longer oligomers we perform excitation dependent transient absorption spectroscopy (Appendix H). We find no excitation dependence confirming the triplet character feature is not representative of activated singlet fission. Instead the three peaks are indeed related to the S_1 state of triplet-pair character.

It is interesting that the emission spectral shape does not change despite considerable change in the PIA features over the first 3ps. We suggest this is due to the mixed character of the adiabatic S_1/S_2 state, see schematic in Figure 5.10. The excited state population moves from a 1e-1h configuration to a predominantly triplet-pair configuration, as such, the PIA line shape changes from 'singlet-like' to 'triplet-like' while the emission only dims and red shifts (Figure 5.8f).

Over the first 2ns we find a decay of the features assigned to the S_1 state, revealing a spectrum which matches the sensitised triplet spectrum taken from the paper by Apperloo et al. After 2ns we

see no emission and find no further evolution of the triplet spectrum with a mono-exponential decay with a 125±20ns decay constant. As our measurements were conducted in the presence of oxygen we expect a triplet lifetime on the order of 100ns[38]. This is due to the well documented quenching of triplets by oxygen[233]. In the longer oligomers (Section 5.4) we found higher ^{1}(TT) population for higher excitation energy, indicative of activated singlet fission. The ^{1}(TT) states generated via activated singlet fission then decayed rapidly (100ps). Here we observe no activated processes and the triplets we observe are long-lived (100ns). To investigate whether these are formed via singlet fission or not we turn to time-resolved electron paramagnetic resonance spectroscopy.

Time-Resolved Electron Paramagnetic Resonance (TR-EPR) is a technique that is sensitive to paramagnetic intermediates such as triplets and charges[12,15]. The time resolution of our TR-EPR experiment is of the order of 100-150ns and allows only detection of species that are long lived on the time scale of transient absorption experiments[12,15]. As a result TR-EPR preferentially probes the long-lived triplets and not the bound ^{1}(TT) state. Importantly the polarization of the spectrum collected provides valuable information on the mechanism responsible for the formation of the triplets. Indeed, all the processes leading to the formation of transient paramagnetic species are anisotropic and selective towards spin sublevels leaving a signature on the polarization of the TR-EPR spectrum. For example it has been shown that singlet fission preferentially populates the $M_s=0$ triplet sublevel[93]. This leads to a distinctive polarisation pattern of AEEAAE (A = enhanced absorption, E = emission) as seen in pentacene and tetracene[12,15]. However for intersystem crossing we expect no preferential population of the $M_s=0$ level leading to a EEEAAA polarisation pattern as seen in anthracene and polythiophene[280,281]. In Figure 5.9 we show the TR-EPR spectrum of the trimer along with a simulation with parameters D = -1500 MHz, E = 90 MHz and triplet sublevel populations $P_X:P_Y:P_Z$=0.39:0.44:0.17. Experimental measurements and simulation of resulting spectra were completed by Dr. Enrico Salvadori (Queen Mary University). We see a clear polarization pattern AAAEEE which along with the fit parameters implies a preferential population of the X and Y zero-field triplet sublevels. This polarisation pattern allows us to exclude that the measured spectrum

results directly from a singlet fission event, however we find a pattern reversed to those in literature (A instead of E and vice versa). A similar effect was found for anthracene and several porphyrins with a flipped polarisation pattern for a sub set of the materials measured[280,282,283]. Throughout these studies it was shown that an increased population of the T_z sub level was found for the molecules with a flipped polarisation pattern[280,282,283]. The preferential population of the T_z sub level can point to the involvement of out-of-plane spin-orbit coupling[283]. This would be consistent with the model of spin-orbit coupling presented by Kolle *et al*. for thiophenes in which a torsional rotation causes much faster than expected intersystem crossing[64], in agreement with the dimer study by Datko *et al*[38]. Overall, while the exact cause of the polarisation pattern inversion cannot be assigned, we can unambiguously assign the triplets to those formed by intersystem crossing and not singlet fission.
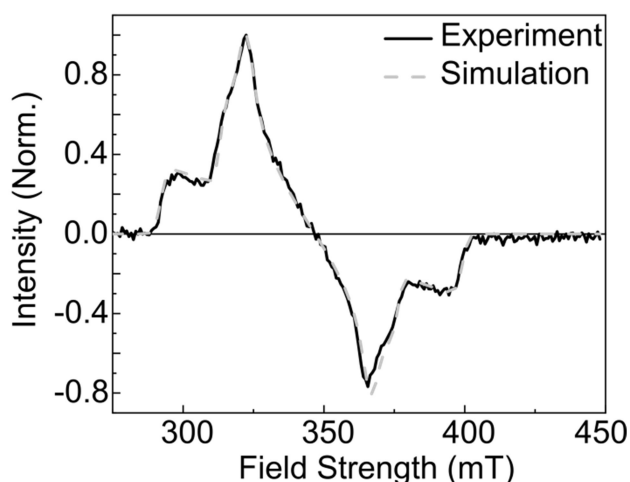
Figure 5.9: Time-Resolved-Electron-Paramagnetic-Resonance spectroscopy of the trimer. EPR measurements were conducted at 9.6GHz after 410nm excitation. Samples were prepared at 77K in a mixture of ethanol:toluene:diethylether in a 1:1:2 ratio. The solution was degassed to remove oxygen. For further details see Methods.

In Figure 5.10 we present the proposed scheme for the trimer with rates and yields (details of calculations in Appendix I). To summarise, excitation occurs into the S_2-character section of the mixed S_2-S_1 state potential energy surface. Following excitation, population relaxes to the S_1 character geometry, with a ~350fs decay constant. The S_1 state is then able to undergo both emission and intersystem crossing forming a population of isolated triplets which decay non-radiatively.
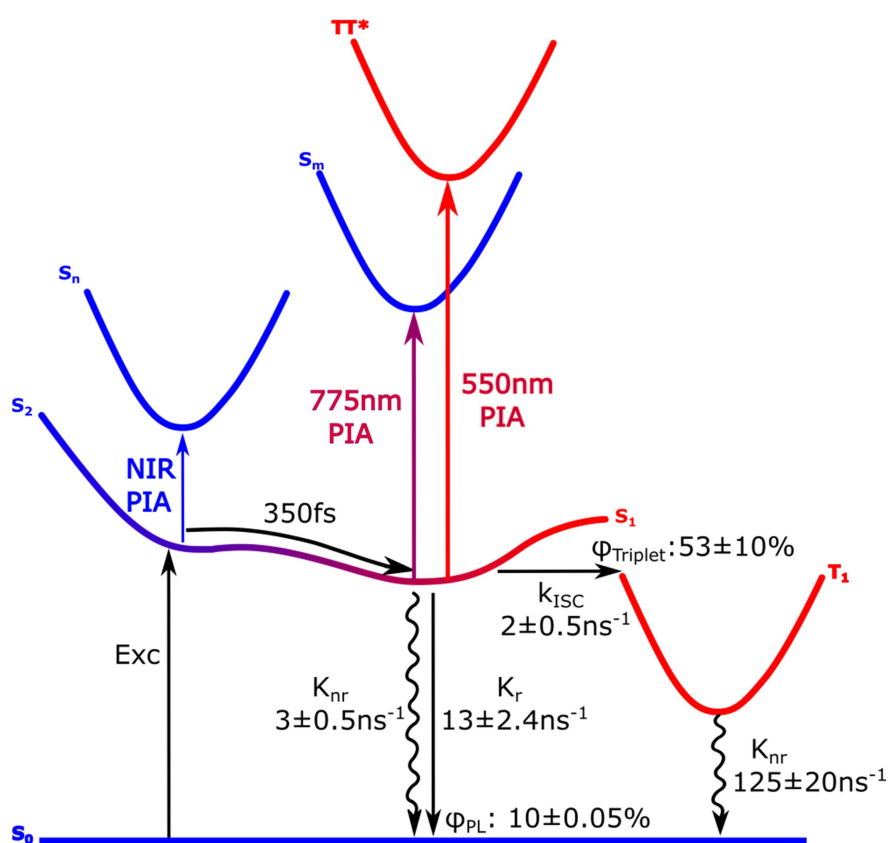
Figure 5.10: Proposed energy level scheme for the trimer. Energy levels and available photo-physical processes for the trimer, energy levels are arbitrary approximations and do not represent exact values. The rate constants and yields presented in the Figure were calculated using equations discussed in Appendix I. Following excitation (Exc) the S_2 (B_u) state interconverts to the S_1 (A_g) state. We measure photo-induced absorption features (PIA) from both states to higher lying singlet states (S_n, S_m) and triplet states (TT*). Here K_{nr}, K_r and K_{ISC} are the rates of non-radiative decay, radiative decay and intersystem crossing respectively. φ_{PL} and φ_{ISC} are the emission and intersystem crossing yields respectively.

5.6 Time Resolved Spectroscopy - Dimer

In Figure 5.11 we present transient absorption spectra and kinetics for the dimer excited at 320nm. We find two clear areas of intensity at 625nm (PIA) and 400-450nm which is a combination of both positive and negative features. At 2ps delay the 400-450nm feature has a line shape similar to that of the dimer emission suggesting the spectra is dominated by stimulated emission. By 200ps we measure a decay of the positive feature revealing a PIA underneath the stimulated emission. After 2ns we find no further evolution with the 420nm PIA showing minimal decay within the measurement window, indicating a ns-μs decay constant. To further assign these states, in Figure 5.11a we show the expected T_1-T_n energy for the dimer extrapolated from the T_1-T_n energy versus conjugation length dependence by Apperloo et al.[179]. We find an agreement between this energy and the PIA which, combined with the long decay constant, suggests the 420nm feature is related to triplets.

In Figure 5.11b we present kinetics taken at 625nm (PIA), 450nm (SE) and at the peak of the feature underneath the stimulated emission (420nm). In order to fit the kinetic for the 625nm feature we must use two exponentials with decay constants 109±5ps and 1.9±0.2ns. These components are consistent with those found by Datko et al. who assign the feature to the absorbing state of B_u symmetry[38]. In Section 5.3 we assigned emission to the absorbing state, as such we compare the decay kinetics of the stimulated emission and 625nm PIA. We find similar decay kinetics, requiring a bi-exponential fit with 110±15ps and 1.5±1ns components. Due to the similarity of the decay of the emission and 625nm features we assign the PIA to the absorbing state in agreement with Datko et al[38].
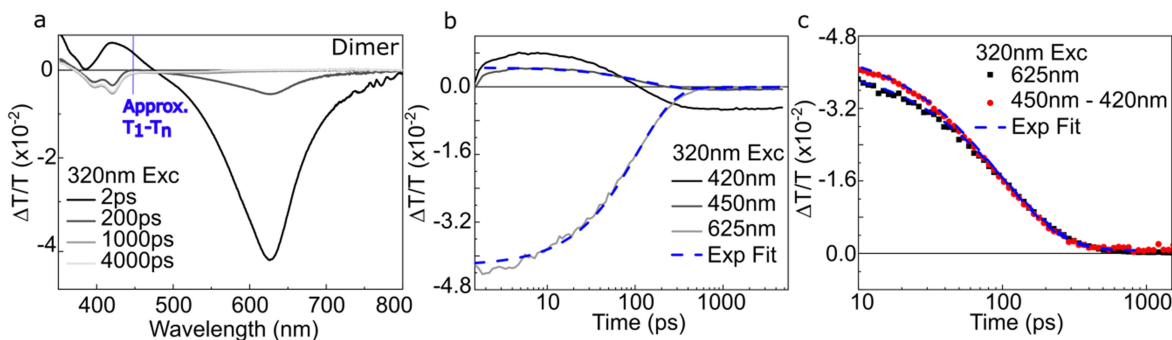
Figure 5.11: Transient absorption spectra and kinetics of the dimer: (a) Transient absorption spectra of the dimer excited at 320nm, shown averaged over 2-3ps, 200-300ps, 1000-2000ps, 4000-6000ps. An estimate of the dimer triplet energy is provided by extrapolating the dependence of T_1-T_n energy against conjugation length in the paper by Apperloo *et al.*[179]. (b) Transient absorption kinetics of the dimer excited at 320nm, the kinetics are averaged over 5nm around the peak of the PIAs (625, 420nm) and the stimulated emission (450nm). (c) Transient absorption kinetics of the dimer after 320nm excitation. The 625nm kinetic is reproduced from panel b and compared to the subtraction of the 450nm kinetic away from the 420nm kinetic. The difference kinetic was then normalised for comparison. Throughout all transient absorption data were taken at 1mW power.

In Section 5.5 we showed that the S_1 state can have features with triplet-like spectral shapes consistent with its description as a bound pair of triplets. As such, the triplet feature in the dimer could be a signature of the dark S_1 state for the dimer. Two open questions remain: (1) What is the nature of the triplet-like state at 420nm? And (2) What causes the initial 100ps decay in the absorbing state which quenches emission?

While we cannot resolve directly the rise of the triplet features, we see a faster decay at 420nm than 450nm (Figure 5.11b). This is caused by the combination of the stimulated emission decay and the rise of the triplet PIA. To pull these apart we subtract the 450nm kinetic from the faster decay of the 420nm kinetic, in order to isolate the rise of the triplet. Figure 5.11c presents a comparison of the rise of the 420nm feature and the decay of the 625nm singlet feature normalised to the maximum value. We find a similarity between the two, with the rise being mono-exponential with rise constant of 106±5ps, very similar to the first decay constant of the singlet state (109±5ps). This suggests there is an interconversion of the absorbing state and the triplet-like state, explaining the quenching of emission. While this is fast for intersystem crossing, it is much too slow for formation of the S_1 state (usually on the order of fs[25,27,32,112]). Combined with the long lifetime of the triplets, we suggest the

feature is not representative of the S_1 state. Additionally, to rule out singlet fission we measure the dimer at 320nm and 370nm excitation (Appendix J). We find no excitation dependence, ruling out activated singlet fission occurring through the same mechanism as the longer oligomers.

We find our measurements agree with the model by Datko *et al.* who assign the triplet population to intersystem crossing, possibly enhanced by a torsional rotation[38,64]. Interestingly, efficient intersystem crossing has been reported previously for dipheyl-hexatriene with a similar mechanism[284]. Here we find no evidence for a dark intermediate state (S_1) between the absorbing and the ground state of the dimer in agreement with Datko *et al.*[38]. However, unlike Datko we suggest the lack of the S_1 state in the dimer is a consequence of its short conjugation length and find the behaviour in agreement with the OTV/PTV family of molecules being polyene-like molecules. A summary of the scheme presented for the dimer including rates and approximate yields are given in Figure 5.12. Now that we have characterised the full oligomer series, we return to the questions posed at the beginning of the chapter.
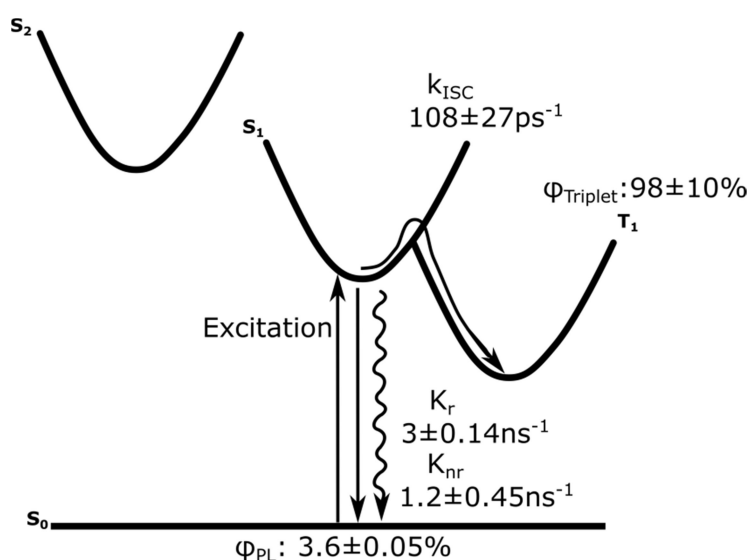
Figure 5.12: Proposed energy level scheme for the dimer. Energy levels and available photo-physical processes for the dimer, energy levels are arbitrary approximations and do not represent exact values. The rate constants and yields presented in the Figure were calculated using equations discussed in Appendix I. Following excitation, the S_1 (B_u) state undergoes intersystem crossing to the triplet manifold. For the dimer, the dark A_g state is then the S_2 state. Here K_{nr}, K_r and K_{ISC} are the rates of non-radiative decay, radiative decay and intersystem crossing, respectively. φ_{PL} and φ_{ISC} are the emission and intersystem crossing yields respectively.

5.7 Conjugation Length Dependence of OTVs

In the preceding sections we characterised a set of oligomers running from 2 to 8 thienylene-vinylene units. We resolved the apparent contradiction in the models presented by Musser et al and Datko *et al.* to describe the photophysics of OTV/PTVs. In the long-chain oligomers we observe polymer-like behaviour in agreement with Musser *et al.* i.e. activated singlet fission[27], while in the short-chain oligomers we observe emission and intersystem crossing similar to the findings by Datko *et al*[38]. We are now able to describe the photophysics of OTV/PTV molecules thoroughly with the polyene framework.
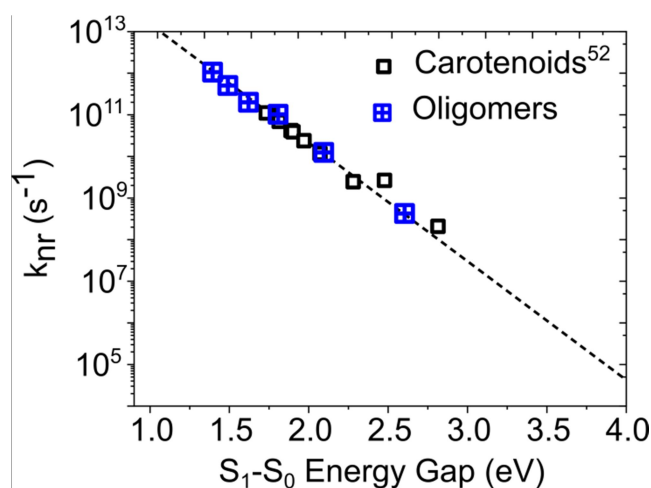
Figure 5.13: Dependence of singlet state lifetime on conjugation length. Series of decay rates for polyene molecules previously found by Chywat *et al.*[52]. Lifetimes are plot as a function of the energy gap between the initial and final state in the transition (S_1-S_0). Kinetics shown in Figure 5.5 and 5.8 were fit with a mono-exponential decay yielding a single decay constant. These K_{nr} values are then fit to the carotenoids dependence to estimate the S_1 energies of the oligomers. Details of kinetic fits and decay constants given in the text and Appendix E and I.

In Section 5.5 we investigated the emission characteristics of the trimer, assigning emission to the symmetry forbidden S_1 state, allowed via mixing with S_2. In Figure 5.4f we suggested that the trimer has a smaller S_2-S_1 energy gap compared with carotenoids of a similar S_2 energy. Interestingly, the K_{nr} of the trimer is similar to K_{nr} of a carotenoid with the same S_1 energy. We can use this fact to estimate the energies of the non-emissive oligomers (2, 4-8 units), if we assume that the OTVs follow an energy-gap law for non-radiative decay with the same slope as carotenoids. In Figure 5.13 we plot

the carotenoid K_{nr} versus S_1 energy (dashed line). We then plot K_{nr} for the oligomers so that they sit

on this line and thus estimate the S_1 energies. Having estimated the S_1 energies of the OTVs we now

compare these energies to those of carotenoids, a well characterised class of polyenes.
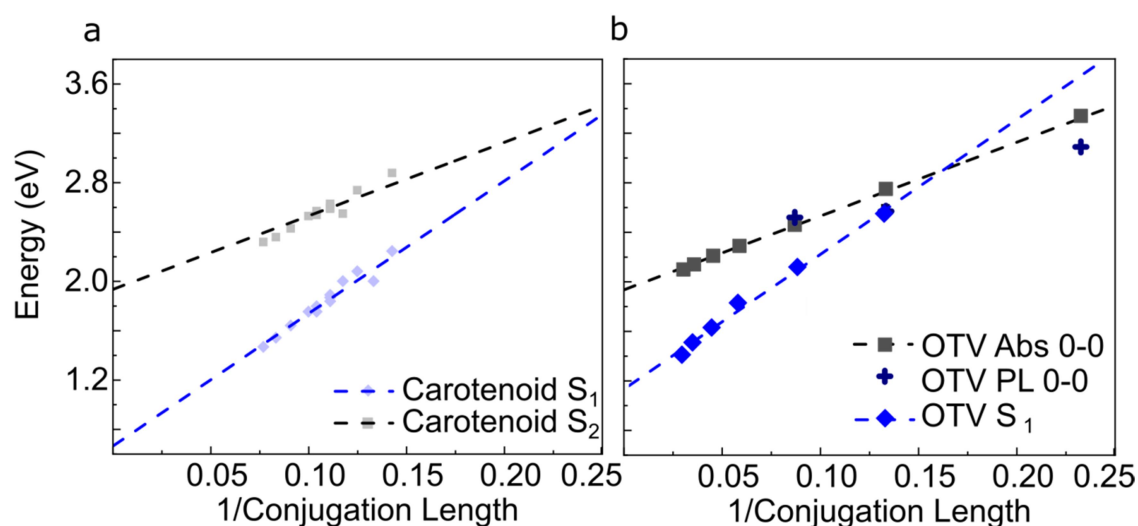
Figure 5.14: State energies for the series of OTVs and carotneoids. (a) Collection of carotenoid state energies taken from various literature sources[112,129–135]. We include a fit for each state based on the relationship discovered by Kohler for polyene molecules[285]. For the $1B_u$ state: $1.8 + \frac{7.8}{N}$, and for the $2A_g$ state: $0.76 + \frac{10.32}{N}$, where N is the conjugation length.(b) We reproduce the literature trend for the $1B_u^+$ state presented in panel a along with the absorption and emission energies of the OTVs. We include the S_1 state energies estimated by application of the gap law to the measured lifetimes of the oligomers (Figure 5.13). The same slope can describe the estimated $2A_g$ energies of the carotenoids and the OTVs with an altered y intercept for the OTVs (1.1eV).

In Figure 5.14a we show S_2 and S_1 state energies against 1/conjugation length for a series of

carotenoids from literature [112,129–135]. We then fit them using the empirical relationship identified

previously by Kohler in 1988 for polyenes ($E_N = E_\infty + \frac{E}{N}$), where E_N is the state energy for N double

bonds, E_∞ is the state energy at an infinite conjugation length and N is the number of double bonds.

Kohler measured a series of oligomers finding a relationship for the $2A_g$ and $1B_u$ states of

poly(acetylene) (Equation 5.1-5.2)[42,285]. We find an agreement in the slope of the dependence with

this relationship however to fit the carotenoid data we require a reduction in the y intercept (energy

of the state at an infinite conjugation length) of ~200meV for both the $2A_g$ and $1B_u$ state [42,285]. While

experimental data has been shown to diverge from this relationship at long and short conjugation lengths, in the region of interest here the simple relationship is surprisingly accurate[42,285].

$$E_{1Bu}^{0-0} = 2.01 + \frac{7.8}{N} \tag{5.1}$$

$$E_{2Ag}^{0-0} = 0.96 + \frac{10.32}{N} \tag{5.2}$$

We then use this quantitative relationship to assign effective conjugation lengths to the OTVs by comparison of carotenoid and OTV S_2 energies. This method for assigning effective conjugation lengths from absorption energies is common in literature on polyenes and other polymer/oligomers[111,286,287]. By assigning conjugation lengths to our oligomers we can compare with literature on carotenoids. In Figure 5.14b, we plot the estimated S_1 and S_2 energies as a function of conjugation length. The blue dashed line has the same slope as the carotenoid S_1 conjugation length dependence, but blue-shifted by 500meV.

Interestingly while the S_1 state has the same conjugation length dependences as carotenoids, the magnitude of the S_1-S_2 energy gap is smaller for the OTVs, 0.16eV for the trimer compared to 0.62eV in a similar length carotenoid. This suggests there are lower electron correlations in the OTVs compared to carotenoids, raising the energy of triplet and triplet-pair states. This is consistent with theoretical work which finds electron correlations are dependent on geometry of the molecules[42,288]. In Figure 5.15 we show the structure of 3 conjugated polymers. Despite the similar structures PTV is a polyene and non-emissive while PPV is emissive with no low-lying $2A_g$ state. The lower electron correlations are directly a result of the rings in the structures of PTV and PPV. The rings allow electrons to avoid each other which reduces electron-electron repulsion. Further the ring causes an increase in the alternation (difference in double and single bond lengths) which in turn localises electrons and reduces correlations.
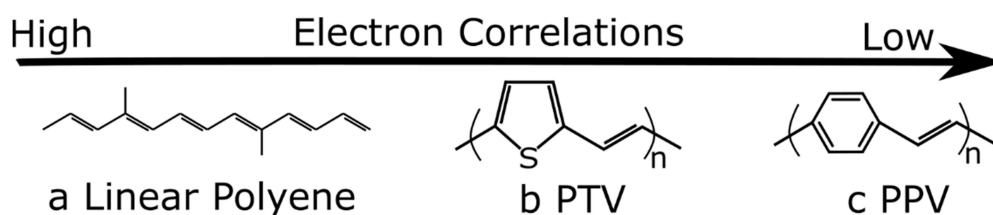
Figure 5.15: Structures of materials with high and low electron correlations. (a) Chemical structure of a generic linear polyene known to possess high electron correlations. (b) Chemical structure of PTV (poly(thienylene-vinylene)), a polyene-like polymer which has intermediate electron correlations, with the polyene energetic structure for long-chains and an inverted energy ordering at short-chain lengths. (c) Chemical structure of PPV, a emissive polymer which shows low electron correlations causing the lowest excited state to be of B_u symmetry.

For polyenes the dark intermediate states are dominated by the triplet-pair or 2e - 2h character pushing the S_1 state to low energies. While in the emissive polymers/oligomers the 1e-1h character is much more prominent, raising the energy of the S_1 state, even pushing it above the absorbing state for low electron correlations[288,289]. As such, the polyene state ordering of $B_u > 2A_g > 1A_g$ is a consequence of strong electron correlations[288,289]. Here we find an intermediate case where the S_1 energy is higher than carotenoids but still well below the absorbing state for oligomers with conjugation length above 7, consistent with polyene molecules [288,289].

Here we take a moment to discuss the definition of intramolecular singlet fission before continuing. Singlet fission is defined as a singlet state converting to two triplets[10]. However in acene literature due to the prominence and importance of intermediate states, a new terminology has been adopted (discussed in Chapter 4)[34]. In this new language singlet fission is sometimes defined as the process of a singlet state converting to the $^1(TT)$ state. In the original description of singlet fission, the polymer and longer oligomers are not undergoing singlet fission due to the lack of separation to free triplets. However, the new language leads to interesting questions for the OTV/PTV materials and polyenes in general. This is due to the predicted triplet-pair nature of the S_1 state[49,121], which causes the S_2-S_1 internal conversion to be defined as a form of intramolecular singlet fission[43,108]. In this model, the longest oligomers undergo singlet fission to two states, where neither separate to free triplets. Afterwards both states decay in parallel to the ground state with decay rates consistent with the

energy gap law for singlet states in polyenes. This model implies that S_2-S_1 internal conversion and intramolecular singlet fission events described above are equivalent but occur to states of different energy.

Interestingly, we find another distinction between these two states for the tetramer where spectral features are narrow enough to distinguish differences between the states. In the tetramer we can resolve both the S_1 and ^{1}(TT) states, finding a triplet-like spectral shape for them both. However for the triplet-pair of singlet fission we find a blue-shift compared to free triplets, as in the longer oligomers and many other singlet fission materials[31,34]. A blue-shift in the transient absorption spectrum of the triplet-pair compared to isolated triplets indicates a bound triplet-pair with a binding energy given by the blue-shift[31]. Whereas for the S_1 state we find a red shift from isolated triplets, similar to the S_1 state of carotenoids (see Chapter 6) and S_1 of the trimer. We postpone discussion of this red-shift until Chapter 6.

5.8 Conclusions

The results presented here form a clear view of OTV molecules, assigning them to the polyene class of materials. In the longer oligomers (>4 units) we find evidence for a symmetry forbidden $2A_g$ state and activated intramolecular singlet fission, as in the polymer[27]. For the trimer we find a clear separation from the longer oligomers with intersystem crossing to form isolated long-lived (µs) triplets. The small S_2-S_1 energy gap (0.16eV) for the trimer leads to significant mixing of the absorbing (B_u) and symmetry forbidden (A_g) states allowing the symmetry forbidden state to emit. Finally, for the dimer we find our data agrees with previous studies by Datko et al[38]. with efficient intersystem crossing and no symmetry forbidden $2A_g$ state. However, here we find this is in agreement with the polyene model in which the $2A_g$ state energy rises faster than the absorbing $1B_u$ state as a function of conjugation length, causing them to switch order at very short (<5) conjugation lengths.

5.9 Materials and Methods

5.9.1 Sample Preparation

OTV molecules were synthesised by Iain Andrews in the Heeney group (Imperial College London). The solutions were prepared in toluene with ~40µM for an OD of ~0.4-0.6 in 1mm path length cuvette unless stated otherwise in the Figures. For the low temperature measurements, a solvent mixture was used to ensure a clear glass formed (details in figure captions).

5.9.2 Spectroscopy

Steady state absorption, steady state emission, and time-resolved emission measurements were taken as described in Chapter 3, Section 3.2. Low temperature emission measurements were conducted as described in Chapter 3 with the addition of a liquid nitrogen Cryostat (Oxford Instruments). After submerging the sample in liquid nitrogen, measurements were only conducted

after the initial cool down was complete. All transient absorption measurements were taken at room temperature with the Helios setup described in Chapter 3. A series of narrow band (~10nm, ~100fs) pumps (under 1mW power) between 300 and 600nm and a visible probe pulse running from 350 – 700nm and 800-1200nm were supplied by a commercial TOPAS (Light Conversion Ltd) and white light generation respectively.

5.9.3 Franck-Condon Modelling

Within this chapter we perform a Franck-Condon analysis on both steady state absorption and emission spectra. To carry out the analysis we applied the below equations (5.1-5.2) as in Refs[40,262]. To fit we presume a Gaussian line shape with a single broadening constant (σ) for all peaks which represents the Gaussian variance and is related to the FWHM via $FWHM = 2.354\sigma$ [40]. We also presume a single active vibrational mode (ω_{vib}). In Equations 5.1-5.2 below, x represents a given absorption or emission wavelength, n_x is the refractive index of the solvent at wavelength x, m is the number of the given vibrational replica and S is the Huang-Rhys factor. To fit organic molecules we use a gaussian rather than Lorentzian line shape function, consistent with inhomogeneous broadening known to occur for organic molecules[40,41].

$$I_{PL} = (n_x x)^3 \, \Sigma_i \left(e^{-s} \frac{S^{m_i}}{m!} \; e^{-\left(\frac{(x-(E_{0-0} - m_i \omega_{vib}))^2}{\sigma^2} \right)} \right) \tag{5.1}$$

$$I_{Abs} = (n_x x) \, \Sigma_i \left(e^{-s} \frac{S^{m_i}}{m!} \; e^{-\left(\frac{(x-(E_{0-0} + m_i \omega_{vib}))^2}{\sigma^2} \right)} \right) \tag{5.2}$$

5.9.4 Time-Resolved Electron-Paramagnetic-Resonance Spectroscopy

Time-Resolved EPR (TR-EPR) experiments at X-band frequency (~9.6 GHz) were recorded on a Bruker E580 pulsed EPR spectrometer and equipped with a Bruker ER4118X-MD5 dielectric resonator. TR-EPR spectra were recorded in direct detection mode without magnetic field modulation, therefore they show characteristic enhanced absorptive (A) and emissive (E) features, as indicated in the reported spectra. A Surelite broadband OPO system within the operating range 410–680 nm, pumped by a Surelite I-20 Q-switched Nd:YAG laser with 2nd and 3rd harmonic generators (10 Hz, pulse length of 5 ns) was used to achieve a pulsed laser excitation at an appropriate wavelength optimized on the signal intensity, with the energy at the sample approximately 5 mJ per pulse. A cryogen-free cryostat from Cryogenic ltd and a Lake Shore temperature controller (model 350) were used to cool the sample and maintain the temperature at 77 K. EPR samples were prepared at a concentration of 0.05mg mL^{-1} in a mixture of ethanol:toluene:diethyl ether in a 1:1:2 ratio (v/v). The solvent mixture was degassed by sonication prior to use. TR-EPR measurements carried out by Enrico Salvadori (Queen Mary University of London).

5.9.5 TR-EPR simulations

TR-EPR spectra were simulated using the EasySpin toolbox in MATLAB™ to extract ZFS parameters – D and E – and sublevel populations (P_x, P_y, P_z). The simulation of the OTV timer considered the ZFS parameters D negative as expected for polyenes. An isotropic g value equal to the free electron g value ($g_x = g_y = g_z = 2.0023$) was used in all simulations. Simulations carried out by Enrico Salvadori (Queen Mary University of London).

5.9.6 Fluorescence Up-conversion Photoluminescence Spectroscopy (FLUPS)

Broadband femtosecond fluorescence spectroscopy experiments were performed on an experimental setup as described in detail in ref[290] by George Farrow at the University of Sheffield. A Ti:Sapphire regenerative amplifier (Spitfire, Spectra-Physics) provided 800nm pulses (40fs FWHM,

10kHz, 1.2mJ). Doubling of the 800nm output pulse in a β-barium borate (BBO) crystal generates the 400nm pump pulses. The pump pulses were passed through a computer-controlled optical delay line (M-IMS400LM, Newport), translation of which gave control of time delay between pump and gate pulses, within a 4 ns window with a temporal resolution of 1.67fs. Polarization was set to magic angle, with respect to vertical, with a half-wave plate. Pump pulses were then focused by a lens (focal length = 200mm) onto the sample cell, to a spot diameter of <0.1mm. The 1320nm gate pulses were the signal pulses generated by an OPA (TOPAS prime, Light Conversion) pumped by the 800nm output of the Ti:Sapphire regenerative amplifier. Fluorescence from the sample was directed onto a 100μm thick β-barium borate crystal (BBO crystal, EKSMA OPTICS) where it was up-converted by sum-frequency generation with the 1320nm gate pulses. In doing so a given time delay can be sampled by altering the delay between excitation and gate pulses. The fluorescence and gate beams met at an angle of ~21° at the crystal. Type II phasematching was used in order to provide the broadest up-conversion spectral window. The upconverted fluorescence was spatially filtered and then focused on the entrance of a fibre bundle (Ceram Optek) with a concave mirror. A homebuilt spectrograph was used to disperse the upconverted fluorescence onto a CCD detector (iDus 420 DU440A-BU2, Andor). The detectable spectral range was 286-500nm, this corresponding to original fluorescence of 360-780nm.

In the following chapter we clarify the photophysics of carotenoids, before discussing the factors that affect the singlet fission process in these molecules. I once again produced and measured all the samples, and carried out the analysis of the data. Throughout the chapter we present several computational models that support the conclusions we present for the data. When these are discussed, credit is given to the appropriate researcher that carried out the modelling.

6. Characterisation of Singlet Fission in Protein-Bound Carotenoid Aggregates: Revealing the Triplet Contributions to the $2A_g^-$ State.

6.1 Summary

The nature of the low-lying electronic states and their decay processes in carotenoids has been debated for decades. To clarify we use excitation-dependent transient absorption spectroscopy to investigate carotenoid monomer, solution based aggregates and protein-bound aggregates. We start by characterising the pertinent states to the low energy physics of the monomer. By comparison with published results on β-carotene we demonstrate that the so-called S* feature in astaxanthin, echinenone and spheroidenone spectra is due to an isomer impurity in the sample. Excitation at the absorption band-edge results in a transient absorption spectrum dominated by the pure S_1 photo-induced absorption, with no contribution from impurities ('S*'). We find that this S_1 absorption resembles the triplet excited-state absorption spectrum, shifted by ~200meV. To explain this, we suggest that the individual triplets that make up the dominant triplet-pair (TT) configuration of $2A_g^-$ contribute strongly to the S_1 absorption band. Comparison with recent literature on molecular polycrystalline films which undergo singlet fission suggests the shift could be related to the binding energy of the triplet-pair state. Afterwards we investigate both solution-based and protein-bound carotenoid aggregates using the emerging technology of man-made maquette proteins. We show that surprisingly, intramolecular structure and protein environment has little effect on the singlet fission process. These findings have implications for understanding triplet-pair states in organic semiconductors and singlet fission in carotenoid aggregates and wider biological systems.

6.2 Background

Over 600 carotenoids exist in nature [110–112], covering a wide variety of functions from photo-protection in human vision, to energy harvesting in photosynthesis [113–120]. These roles are enabled by the complex properties of carotenoids where – assuming C_{2h} symmetry – the lowest-lying singlet excited-state (S_1) is highly electron-correlated, described as a pair of triplets (TT) with overall A_g symmetry (the $2A_g^-$ state) [43,49,295,296,54,108,146,153,291–294]. This state carries the same symmetry as the ground-state ($1A_g^-$), therefore $2A_g^-$ (S_1) has negligible oscillator strength. One-photon absorption is instead predominantly into the $1B_u^+$ singlet state, which is typically assumed to be the second singlet excited-state, S_2 [49,54,153,291–296]. Internal conversion from $1B_u^+$ to $2A_g^-$ occurs in <200fs [295,297], followed by non-radiative decay to the ground-state ($1A_g^-$) within 20ps [49,54,153,291–296]. This rapid non-radiative decay makes carotenoids perfect photo-protective materials for rapidly dissipating electronic energy into heat [113–118].

Interestingly, despite calculations showing the $2A_g^-$ state to have dominant ^{1}(TT) character, to our knowledge no experimental comparison between triplet (T_1) and $2A_g^-$ excited-state absorption spectra have been presented for carotenoids. Similar (TT) states have been observed in acene[12–15,95] and heteroacene polycrystalline films[298], and are of current interest in the field of organic electronics. Such interest stems from the fact that triplet-pair states can transfer charge or energy *independently*, either to an electron acceptor[8] or a triplet acceptor[89,92]. Thus, a single photon produces two excitations that could be harvested in solar cells, potentially increasing solar energy generation efficiency by up to 33%[6] and overcoming the Shockley-Queisser limit[11]. Despite this, very few studies of singlet fission in carotenoids have been conducted, with the majority concerning carotenoids bound to proteins in photosynthetic materials.

The first assignment of singlet fission in photosynthetic materials came from observations of changes in reaction centre emission when the protein complex was exposed to a magnetic field[109]. In

a comprehensive study, Kingma and co-workers investigated the effect of magnetic fields on the triplet yields of several protein strains[299,300]. The authors discovered two distinct regimes related to the reaction centres and antenna complexes[299,300]. The first, associated with the reaction centre, shows an overall reduction in triplet yield, with no dependence on excitation energy or the presence of carotenoids[299,300]; this is assigned to charge recombination in the reaction centre of the complex.

The second regime of magnetic field effects is associated with the antenna complexes and only occur for direct excitation of the carotenoids[299,300]. Here the magnetic field effect takes on the distinctive shape (initial negative change before increasing to a positive plateau) previously measured for acene crystals undergoing singlet fission[83,299–301]. This magnetic field effect has been assigned to a change in the triplet-pair configurations that contain singlet character, which mediates the singlet fission rate and its reverse process[83,301]. As the response is identical to that of singlet fission in acenes and is only observed following direct excitation of carotenoids, the authors assign the observed effect to singlet fission involving two carotenoid molecules[299,300].

The assignment to singlet fission gained additional evidence from Klenina *et al*. who investigated pure carotenoid films and light harvesting complex samples with time resolved electron paramagnetic resonance spectroscopy (TR-EPR)[302,303]. The authors found the singlet fission process was identical in the light harvesting complex 2 of *Allochromatium minutissimum*[303] and a pure carotenoid film, but did not occur in solution. The authors suggest this is due to the larger intermolecular distances in solution compared to the film[303]. However, it has been shown that the average distance between carotenoid molecules in these complexes is 16Å[145]. We therefore expect small nearest neighbour intermolecular coupling between the carotenoids (~meVs)[304] inconsistent with the assignment of efficient intermolecular singlet fission[102,103].

In a later paper the same authors found that the singlet fission yield is reduced if bacteriochlorophylls are photo-bleached, suggesting bacteriochlorophyll plays a role in carotenoid singlet fission[302]. The authors suggest that bacteriochlorophyll molecules mediate the coupling

between the carotenoids in a super exchange mechanism, increasing the overall coupling between carotenoids[302,303]. However, in their study Klenina *et al.* found that even at a full bleaching of bacteriochlorophyll, the measured EPR signal only drops by ~60%[302,303]. As a result, a singlet fission process not involving bacteriochlorophyll must also be occurring within the protein. Since it was previously shown that singlet fission does not occur in monomer samples in solution[302,303], this suggests binding with the protein environment plays a role.

An explanation comes from a twisting of the carotenoid molecule induced by the differing protein interactions for different segments of the polyene chain[126,143]. The twisting is then proposed to isolate the triplets possibly by causing a break in the conjugation of the carotenoid backbone, consistent with the measured µs triplet lifetime[126,143]. A recent paper by Yu *et al.*[305] measured carotenoid triplets produced by both singlet fission and through sensitisation (excitation of bacteriochlorophyll). Yu *et al.* show that the peak intensity ratio of the ground state bleach to the triplet PIA for singlet fission is half of the same ratio measured after sensitisation[305]. As the authors know there is one triplet per molecule for sensitisation they interpret this as indicating two triplets per bleached molecule following singlet fission[305]. As a result they suggest singlet fission in light harvesting complex 1 of *Thermochromatium tepidum* and *Rhodobacter sphaeroides* is an intramolecular process[305]. However within the study, the authors also measure other light harvesting complexes with ambiguous results[305].

The above discussion serves to point out the complexity of investigating these protein systems[178,306,307]. The interaction of carotenoids with bacteriochlorophyll and the protein environment combined with the presence of multiple carotenoids (most proteins contain a distribution of carotenoid structures[178,306,307]) causes ambiguity in these studies. To simplify the sample under test we must separate the carotenoids from the protein environment, forming a well characterised sample structure. However it has been shown that carotenoid monomers in solution do not undergo singlet fission; instead aggregates must be formed[25,32,39,112].

The first study of carotenoid aggregates for singlet fission was published in 2010 by Wang *et al*. who investigated a J-aggregate of zeaxanthin using picosecond raman spectroscopy[23,24]. Using this technique they measured triplet formation with a 90% yield within 4ps, much too fast and at too high yield for intersystem crossing in carotenoid systems[23,24]. Due to their limited resolution (picoseconds) they were unable to assign the parent state of singlet fission, suggesting it was possible a hot S_1 plays a role[23,24]. In 2015 Musser *et al*. extended this study and measured a wide range of packing structures of astaxanthin aggregates[25].

Across aggregate structures the energy of the absorbing state shifts over 1.2eV, from well above to around the expected energy of the intermediate triplet-pair state ($2xE_T$) [25]. Despite the large shifts in energy, and changes in coupling strength between the molecules, the rate of singlet fission remains under 100fs[25]. This rate competes with the fastest singlet fission materials for all aggregate structures and confirms the process is independent of intermolecular structure, a rather surprising result[25]. The authors also use ultrafast (<30fs) transient absorption spectroscopy to detail the dynamics of singlet fission in the aggregates.

The authors found no sign of the S_1 ($2A_g^-$) state, with the triplet-pair forming directly from S_2 ($1B_u^+$)[25]. The intermediate triplet-pair then decays with two distinct decay regimes, the first on the 10-100s ps time scale is assigned to geminate recombination of the triplet-pair[25]. The second, post-1ns, in which the authors measure a much longer decay constant for the remaining 10% of the triplet population (µs)[25] is assigned to localised triplets. The lack of dependence on intermolecular structure is surprising and points to the need for further study of the singlet fission process in carotenoid aggregates. However, a difficulty with these studies is the inability to form reproducible stable samples, leading to large studies being time consuming. To reduce complexity, a new simplified sample preparation method is required. A possible route for reliable aggregate creation are maquette proteins which were recently shown to produce stable and reliable carotenoids aggregate samples[194] (details in Chapter 3).

Dutton and co-workers pioneered the new concept of entirely artificial, *de novo*-designed 'maquette' proteins, which have been shown to replicate and even enhance biological function[190–192]. The maquette proteins are based around a simple structural motif consisting of 4 α-helical structures, connected by short peptide linkers[193]. Through engineering of the amino acids bound to the helix structures, the inner segments are hydrophobic while the outer segments are hydrophilic. When suspended in water the proteins fold to protect the hydrophobic sections creating a water-excluding cavity[193]. As carotenoids are hydrophobic, they preferentially populate the pocket forming consistent carotenoid aggregate structures within the protein.

Herein we use excitation dependent transient absorption to measure carotenoid monomer, solution-formed aggregates and aggregates bound to maquette proteins. We start by studying the photophysics of carotenoid monomers. We find a clear excitation dependence in all four carotenoids: β-carotene, astaxanthin, echinenone and spheroidenone. We assign the observed excitation dependence to the presence of non-all-*trans*-isomers. We then show experimental evidence for the triplet-pair character of the S_1 state for β-carotene, astaxanthin and echinenone. Finally, we present measurements of protein-bound aggregates finding intramolecular structure and protein environment has no effect on the singlet fission process.

6.3 Triplet-Pair Contributions to the S_1 PIA

We start by examining the monomer photophysics of a selection of carotenoid structures. In Figure 6.1 we present ground state absorption spectra, energy levels and structures of β-carotene, astaxanthin, echinenone and spheroidenone. Each carotenoid has a strong absorption in the visible region due to the S_0-S_2 ($1B_u^+$) transition, with a series of red shifts between molecules [308] as the effective conjugation length increases from β-carotene (9.6) to astaxanthin (10.5) [110,112]. Comparing the absorption line shape of β-carotene and astaxanthin we observe a pronounced loss of vibronic structure. This is due to the presence of carbonyl groups that adopt a range of conformations in

polar environments [308]. The small absorption peaks around 375-425nm in spheroidenone are commonly assigned to *cis* isomers [148,308].
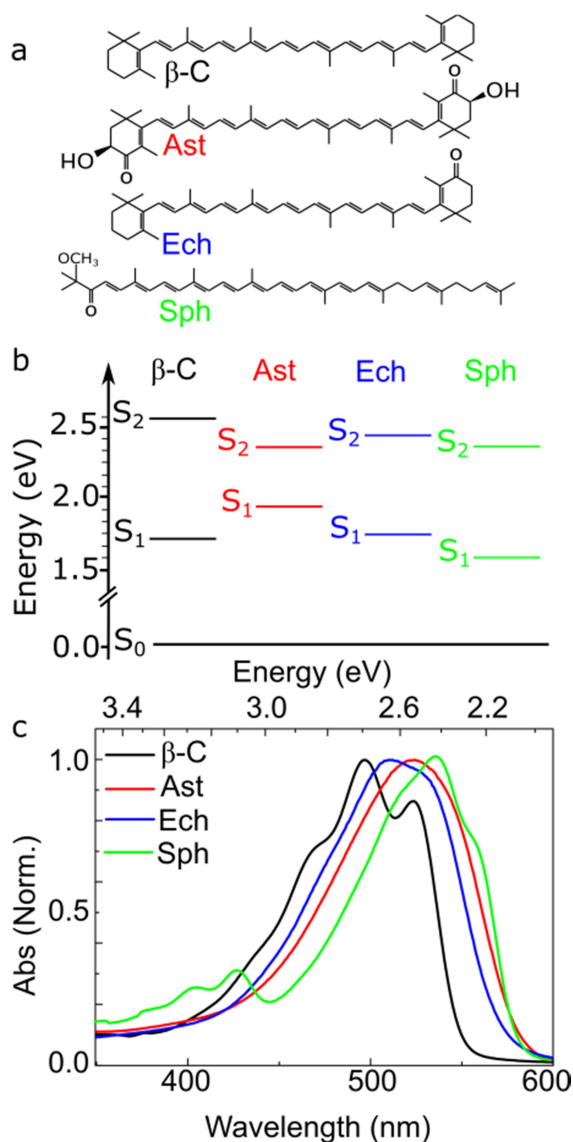
Figure 6.1: Carotenoids studied in this work. (a) Chemical structures of β-carotene, astaxanthin, echinenone and spheroidenone. (b) Measured state energies relative to the ground state. S_2 and S_1 energies are taken from literature by Bachilo *et al.* [309], Musser *et al.* [25], Polivka *et al.* [112] and Cong *et al.* [148] for β-carotene, astaxanthin, echinenone and spheroidenone, respectively. (c) Ground state absorption spectrum of each molecule in dilute (~40µM) toluene solution.

Figure 6.2 shows transient absorption spectra and kinetics for β-carotene and astaxanthin excited low (520nm) and high (400nm) in the absorption band. The photo-induced absorption peaked at 590nm (β-carotene) and 630nm (astaxanthin) is due to the S_1-S_n transition [25,310]. This feature decays with a time constant of 9.6±2ps and 5.3±1ps for β-carotene and astaxanthin respectively, in agreement with literature [25,150]. A summary of the parameters used to fit kinetics throughout this chapter is given in Appendix L. With high excitation energy (400nm), a shoulder on the blue side of the S_1-S_n peak, consistent with features assigned to S* in β-carotene, appears at 560nm and 540nm for β-carotene and astaxanthin, respectively [150,153].

This S* peak decays slower than the rest of the spectrum, with time constants of 95±25ps (β-carotene) and 45±15ps (astaxanthin) shown in Figure 6.2. The presence of a decay component much longer than the S_2 or S_1 states is usually used as proof for the assignment of S* [122,125,146–149,311]. However, as discussed in Chapter 2, Ostroumov *et al.* discovered that a series of impurities (*cis* isomers) form in solution that are responsible for this feature in β-carotene [150]. In Appendix K we conduct excitation energy dependent transient absorption confirming this assignment for both β-carotene and astaxanthin.
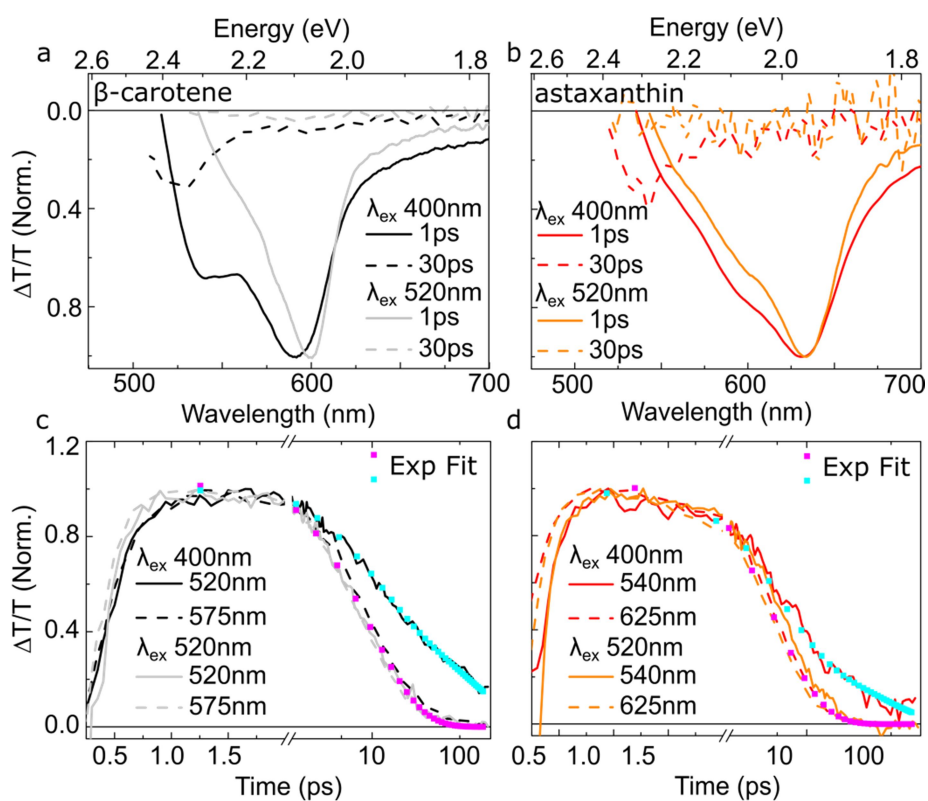
Figure 6.2: Excitation photon energy dependent transient absorption (β-carotene and astaxanthin). (a, b) Transient absorption spectra of β-carotene (a), astaxanthin (b) excited at 400nm and 520nm (<1mW power). Spectral slices are averaged over 1-3ps and 30-40ps. The 520nm spectra have been scaled so that the peak of the photo-induced absorption at 1ps matches after both 400nm and 520nm excitation. (c, d) Transient absorption kinetics of β-carotene (c), astaxanthin (d) taken after 400nm and 520nm excitation. Kinetics were taken in the S_1 and proposed S* PIA regions (averaged of a 10nm window).

Figure 6.3 presents equivalent data for echinenone and spheroidenone, excited above and below the onset energy for isomer absorption (480nm). A peak at 610nm (6.4±1ps lifetime) is measured for echinenone and a peak at 585nm (7.2±0.4ps lifetime) is measured for spheroidenone matching values for the S_1-S_n transition from literature [307,308,312]. The small side peak visible at ~670nm for spheroidenone has been suggested to be due to the charge-transfer state character of the S_1 state, although this is contested [308,312].
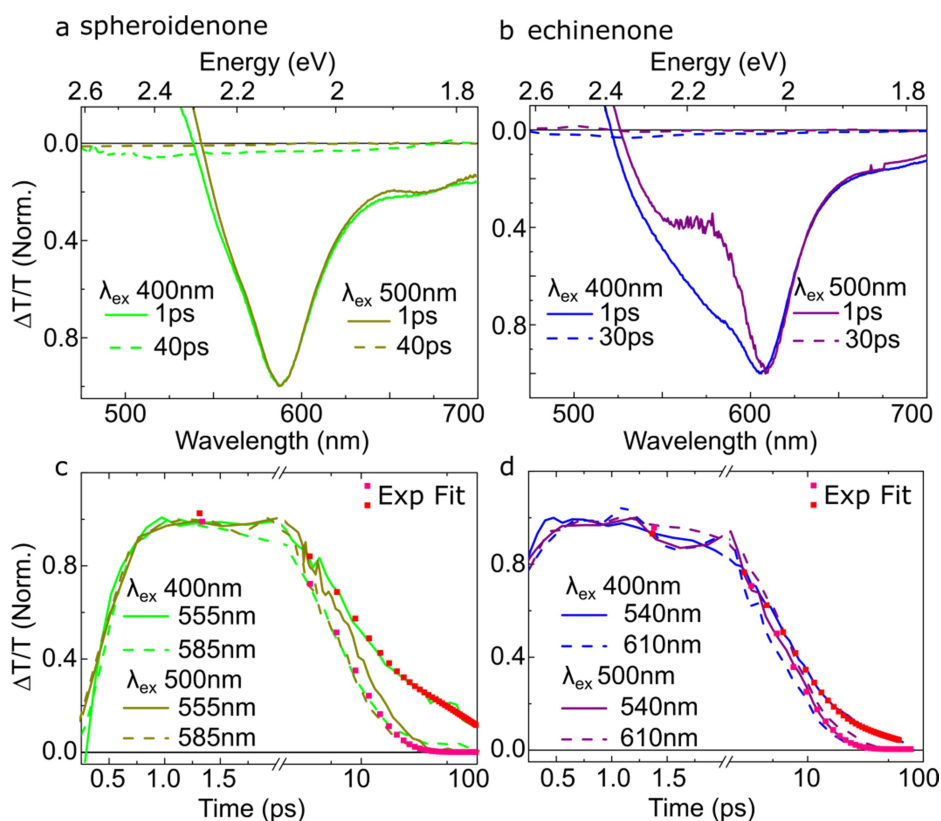
Figure 6.3: Excitation photon energy dependent transient absorption (spheroidenone and echinenone). (a, b) Transient absorption spectra of spheroidenone (a), echinenone (b) excited at 400nm and 500nm (1mW power). Spectral slices are averaged over 1-3ps and 40-50ps in (a) and 1-3ps and 30-40ps in (b). The 520nm spectra have been scaled so that the peak of the photo-induced absorption at 1ps matches after both 400nm and 520nm excitation. (c, d) Transient absorption kinetics of spheroidenone (c), echinenone (d) taken after 400nm and 500nm excitation. Kinetics were taken in the S_1 and proposed S^* PIA regions (averaged over a 10nm window).

When comparing spectra excited above and below the onset absorption energy of the isomer identified above, we see a new feature appear with a lifetime of 41±10ps and 80±20ps in echinenone and spheroidenone respectively (Figure 6.3). The relatively small change in spheroidenone compared to the other carotenoids is due to overlap of the supposed S^* feature and the ground state bleach (Figure 6.3). In analogy with β-carotene and astaxanthin above we suggest that the longer-lifetime component is produced by a separate population of non-all-*trans* isomers and is not a sign of a new electronic state. Indeed, with low-energy excitation the entire spectrum decays with the same dynamics, requiring no need to invoke S^*. We conclude that the S_1-S_n

transition is the only feature present in the transient absorption spectra in this spectral window with band-edge excitation of β-carotene, astaxanthin, echinenone and spheroidenone presented above.

We now turn to examine the spectral shape of the S_1 ($2A_g^-$) state following band-edge excitation presented in Figures 6.2 and 6.3. To understand the spectrum in more detail, we note that the dominant configuration in the wavefunction of $2A_g^-$ is a pair of triplets ^{1}(TT), with other contributions from charge-transfer and electron-hole particle excitations [49,121,293]. Recent work by Khan and Mazumdar [279] suggests that a triplet-pair ^{1}(TT) should absorb with a similar spectral shape to a triplet exciton (T_1). Barford *et al.* likewise suggest that the visible photo-induced absorption in linear polyenes is a T-T* transition[43]. More recently, empirical work by Lukman *et al.,* [31] suggests that the ^{1}(TT) absorption should be blue-shifted compared with the isolated triplet T_1-T_n photo-induced absorption spectrum by an energy proportional to the triplet-pair binding energy $E_b = 2E_T - E_{TT}$ [31].
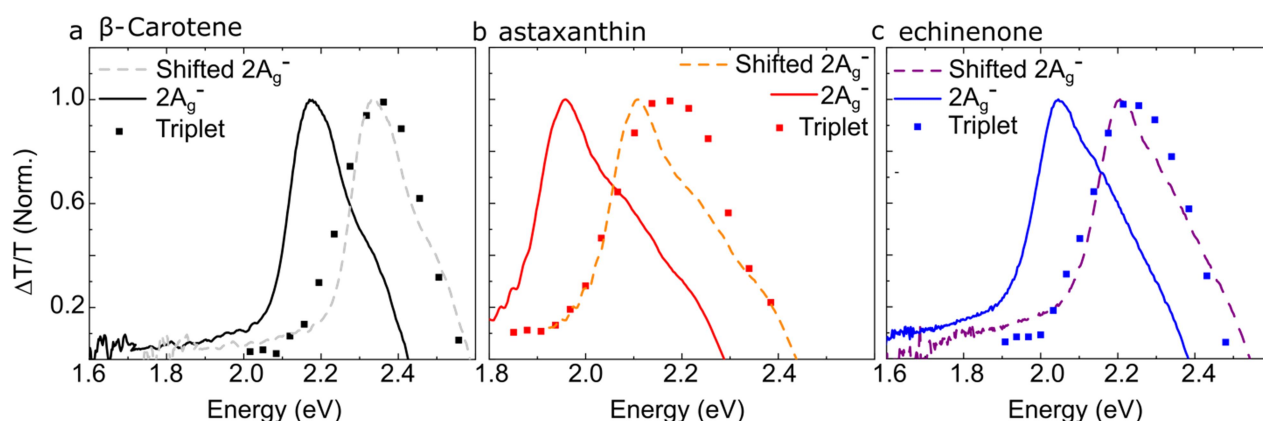
Figure 6.4: S_1 absorption is similar to T_1-T_n. S_1-S_n and T_1-T_n transitions for (a) β-carotene, (b) astaxanthin and (c) echinenone, dashed lines show the S_1-S_n photo-induced absorption spectrum shifted by (a) 190meV, (b) 100meV and (c) 220meV to higher energies. T_1-T_n spectra were acquired via sensitisation by Fullerene-C_{60} (200:800μMol Carotenoid:C_{60}). Details of the sensitisation measurements are given in Section 6.8.3, measurements were conducted with Jose Marin Beloqui (Univeristy College London).

In carotenoids, as the triplets which make up $2A_g^-$ are on the same chain, they should be strongly exchange-coupled and bound [9]. We estimate the binding energy for the β-carotene ^{1}(TT) state (i.e. $2A_g^-$) from the difference between the energies of $2A_g^-$ (1.75eV ± 25meV [140]) and $2 \times T_1$ (1.88eV ± 80meV [112,140,313]) to be 130 ± 105meV. With such strong binding between triplets, ^{1}(TT) is expected to

be a pure spin-singlet state [78–80]. As a singlet state, it does not require a spin flip to return to the ground state, with its lifetime dominated by the standard gap-law for non-radiative singlet transitions [52].

In Figure 6.4 we present a comparison between the transient absorption features of the S_1 state and a sensitized triplet spectrum (T_1-T_n). Shifting the S_1-S_n absorption spectrum by 190meV to higher energies for β-carotene (dashed) demonstrates a striking similarity between the spectral line shapes of S_1 and T_1. This suggests that, as expected, the $2A_g^-$ state can be described as a bound triplet-pair with triplet-like photo-induced absorption[49]. A similar shift is visible in astaxanthin and echinenone, however the spectral shape diverges on the high-energy edge due to overlap with the ground state bleach. We have omitted spheroidenone from the remaining experiments due to lack of access to the molecule.

To investigate if the comparison of T -> T* and the $2A_g^-$ photo-induced absorption features is valid we calculate state energies by solving the Pariser-Parr-Pople-Peierls Hamiltonian for an 18 site chain (9 double bonds)[42,43]. The model was constructed by William Barford (Oxford University), the results of which are shown in Figure 6.5. The model includes the relaxed (at $2A_g^-$ geometry) and vertical (at ground state geometry) energies for the S_0, S_1 ($2A_g$), S_2 ($1B_u$), and T_1 (B_u) states along with the final states for the observed photo-induced absorptions (X, T* and nB_u). We have labelled three state transitions: (1) the initial absorption event, (2) the S_1-S_n photo-induced absorption, here labelled $2A_g^r$ to X^r, and (3) the T_1-T_n photo-induced absorption, here labelled T^r to T^{*r}. For the S_0-S_2 transition the model gives energies approximately 650meV larger than the transitions measured for β-carotene above. The discrepancies in the measured and modelled S_0-S_2 state absorption energies are consistent with solvation calculated by Schmidt and Tavan. The $2A_g^r$-X^r and T^r-T^{*r} transitions also have similar solvation values (520meV and 510meV respectively). As a result, we find that this model is appropriate for describing the photophysics of β-carotene.
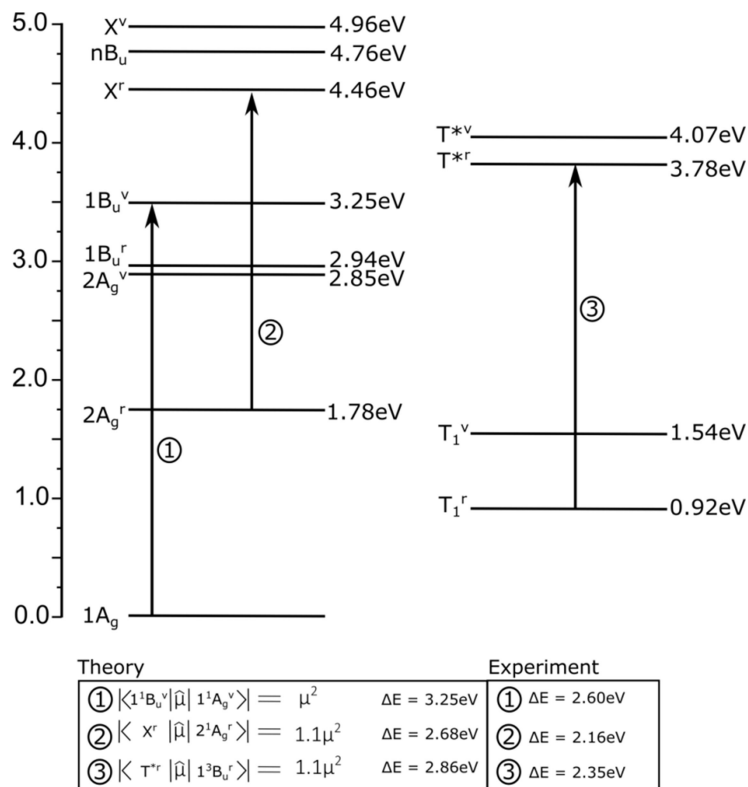
Figure 6.5: Energy level scheme of an 18 site polyene chain. Energy levels and oscillator strengths calculated by solving the PPPP Hamiltonian are presented (calculated by William Barford (Oxford University), details in ref[42,43]). States with the designation r are the relaxed energies ($2A_g^-$ state geometry). States with the designation v are the vertical energies (ground state geometry).

In Figure 6.6 we present the spin-spin correlations for the 4 lowest energy singlet states in the PPPP model. The spin-spin correlation maps are symmetric about the diagonal, hence only half of the map has been calculated. For both the $2A_g^-$ and X ($3B_u$) states we find a large negative value in the bottom left corner (indicating spin correlation between the ends of the chain) which is not present in the maps of the ground ($1A_g$) and first optically allowed state ($1B_u$). This indicates both states are of triplet-triplet character and that the assignment of triplet character to the $2A_g^r$-X^r state transition above is valid. Interestingly, we also find that the $2A_g^r$-X^r and T^r-T^{*r} transitions have the same transition dipole moment, as expected if they are both due to T to T* type transitions. Even though both (2) and (3) are due to T-T* transitions, they have different energies $\Delta E=187$meV. This is similar to the experimentally observed shift between the two transitions (190meV).
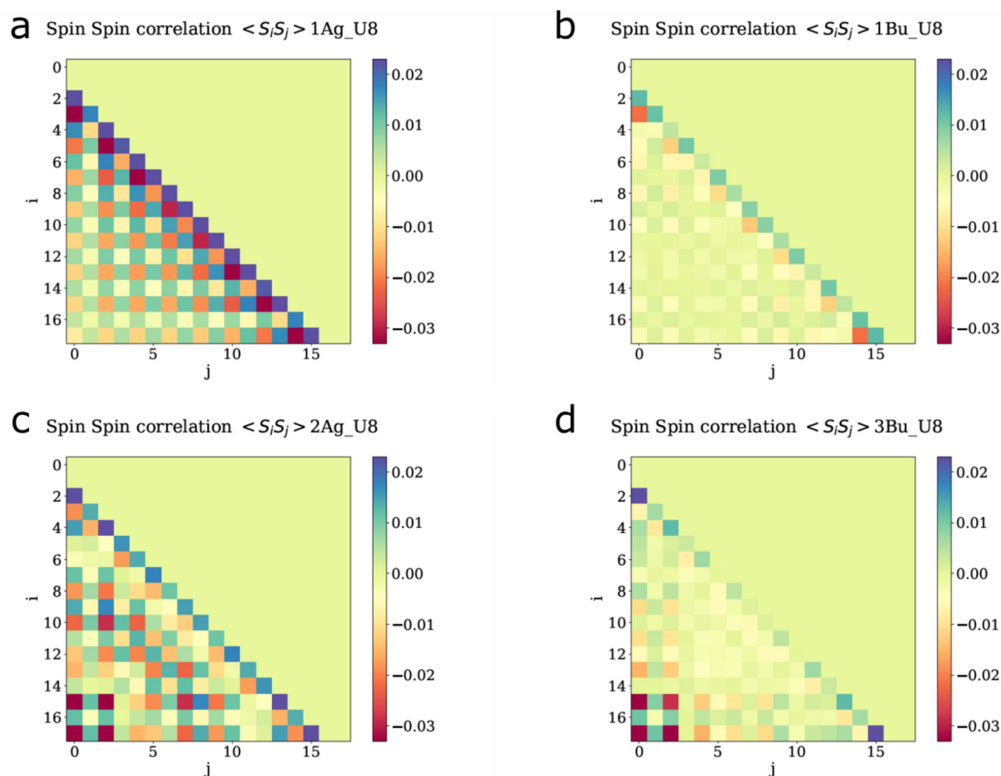
Figure 6.6: Spin-Spin correlations of the 4 lowest energy singlet states of an 18 site polyene chain. (a) spin-spin correlations of the $1A_g^-$ state which corresponds to the ground state (S_0). (b) spin-spin correlations of the $1B_u^+$ state which corresponds to the first optically allowed state (S_2). (c) spin-spin correlations of the $2A_g^-$ state which corresponds to the first excited state (S_1) which is optically forbidden from the ground state. (d) spin-spin correlations of the $3B_u$ state which corresponds to the X or S_n state. For all 4 maps I and J represent sites on the chain that are considered in the spin-spin correlation calculation. The negative signal in the bottom left of the $2A_g^-$ and $3B_u$ maps is indicative of triplet-pair character. As a result, we can confirm that the X state (labelled S_n) is the $3B_u$ state which contains triplet-pair character. The above PPPP model was constructed and the figure was provided by William Barford (Oxford University), details in ref[42,43].

Now that we have established that S_1-S_n is a triplet-like transition we return to the discussion of triplet-pair binding energies. In their study of zethrene molecules Lukman *et al*. found that the triplet-pair PIA shift (ΔPIA) has an approximate 1:1 relationship to the inter-triplet binding energy in the triplet-pair[31] ($E_b = E_{2T} - E_{2Ag}$). Although the magnitude of the photo-induced absorption shift here is similar to the empirical relationship demonstrated in Ref.[31] (130meV compared to 190meV), the shift is in the opposite direction. In other words, for carotenoids, the $2A_g^-$ photo-induced absorption is shifted to lower energies compared with the T_1 photo-induced absorption. Assuming interaction between triplets does not change the T_n energy (E_{Tn}), we would expect the $2A_g^-$ photo-induced absorption to be shifted by 130 ± 105meV to *higher* energy (as estimated above), instead of lower energy as we observe. This suggests the assumption of a constant T_n energy is not valid.

To explain this, we return to our model, now only considering relevant states to the PIA shift in Figure 6.7. By comparing the energy of the triplet-pair character $2A_g^-$ state and double the triplet energy we can find the predicted binding energy for the state. Our model predicts a binding energy in the $2A_g^-$ state of 50meV. This is within our experimentally determined range of 130±105meV from $E_b = E_{2T} - E_{2Ag}$. However, if we compare the S_n state (X) to T+T* (the energy of the triplet-pair after one triplet has been excited by an absorption event) the model also estimates a binding energy in the final state of 237meV. As a result, the PIA red-shifts by 187meV in agreement with the experimentally measured shift (190meV), explaining our observations. The above model provides a quantitative explanation for the observed shifts in the $2A_g^-$ state and confirms the triplet-pair nature of the $2A_g^-$ state experimentally.

Thus far we have considered only isolated monomer in which the triplet-pair never separates to free triplets. We now move to carotenoid aggregates to compare intra and intermolecular singlet fission in polyene systems.
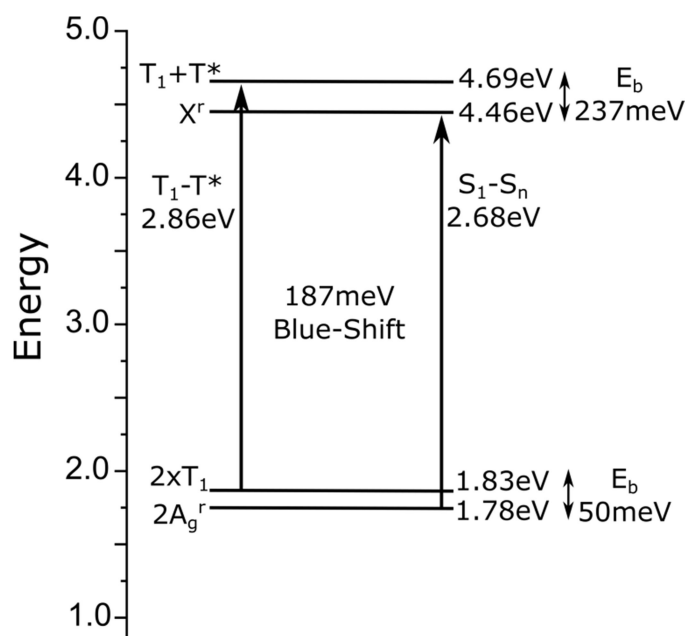
Figure 6.7: Model for the measured triplet-pair PIA blue-shift. (a) We reproduce the energy levels modelled by William Barford (Oxford University) from Figure 6.5. Here we only include the energy levels pertinent to the blue-shift in the PIA. The model predicts a overall blue shift of the triplet-pair PIA of 187meV compared to the triplet transition.

6.4 Characterising Protein bound aggregates

Before continuing we wish to establish the structure of the aggregates embedded in the proteins. Details of sample production and characterisation carried out in collaboration with George Sutherland (University of Sheffield) are given in Chapter 3. Below, we carry out modelling to assess the specific structure of the carotenoids within the protein (model provided by Frank Spano (Temple University, USA)). The simulations of aggregate absorption spectra are based on methods described in Chapter 2, Section 2.3 and in a 2010 study[71]. In short, the Holstein Hamiltonian is solved for one and two particle states. One particle states have an electronic + vibrational (vibronic) excited state on one molecule surrounded by molecules with no vibrational or electronic excitations. Two particle states have a vibronic excited state on one molecule and a vibration in the ground state on a neighbouring molecule. Spano has found that truncating the basis at two particle states is a good approximation for most systems[70].

To obtain the parameters for the model, the monomer ground state absorption spectrum is fit with a Franck-Condon progression (Appendix M) presuming equal FWHM for each peak and one vibrational mode (details of the Franck-Condon fit given in Section 5.9.3). The parameters of the Franck-Condon fit are fed into the Hamiltonian along with nearest neighbour coupling strength (V) and the relative angle (ϕ) between the transition dipole moments of the molecules included. In Appendix M we show predicted spectra when considering 2,3 and 4 molecules for β-carotene. When considering a dimer, the parameter space is sufficiently small that we are able to rule out the possibility of a dimer being responsible for the spectral shape we measure. For any combination of parameters, we find a two peak structure inconsistent with the ground state absorption measurements. For larger collections of molecules, the parameter space becomes intractable and we are unable to explore every possibility. Nevertheless, it is possible to simulate the measured absorption spectrum with a trimer with nearest neighbour coupling of 1200cm^{-1}, spacing of 3.5$\mathring{A}$ and

a relative angle of 0.3π (Figure 6.8). However, we have been unable to do so for the tetramer and larger. We note that the restricted space within the protein pocket and the excellent agreement between theory and experiment suggest we have a trimer within the maquette. This is supported by stoichiometry measurements which find an average of 2.5 carotenoid molecules per protein (measurements by George Sutherland (University of Sheffield)).

The absorption spectrum of all three carotenoid aggregates can be described with the same model and parameters but with slightly varied FWHM and 0-0 energies. For echinenone we must broaden the peaks ($\text{FWHM}_{\text{bc}} = \frac{\text{FWHM}_{\text{ech}}}{1.5}$) and for astaxanthin we must apply both the broadening and a 170meV red-shift. Therefore, all three carotenoids have the same aggregate structure. This is the same structure as aggregate 2 in the study by Musser and co-workers[25]: a weakly interacting H aggregate.
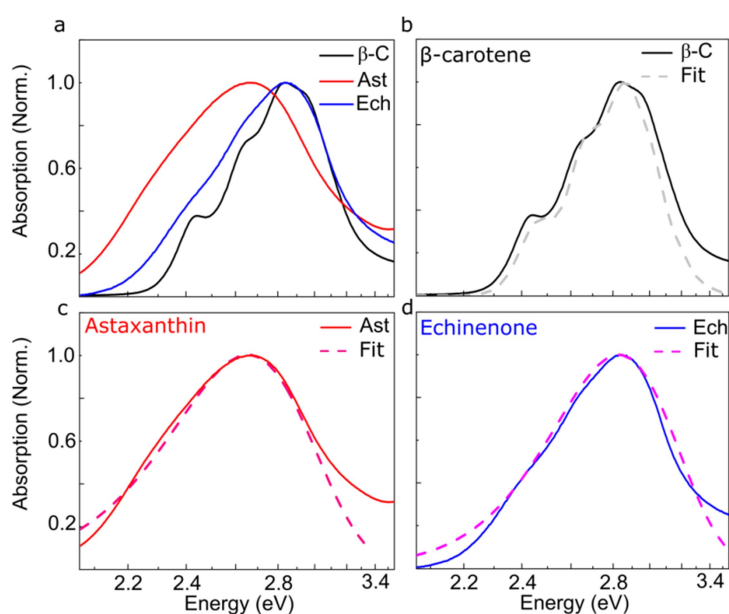
Figure 6.8: Simulation of aggregate structures of each carotenoid. (a) Ground state absorption spectrum of β-carotene (β-C), astaxanthin (Ast) and echinenone (Ech) in maquette protein. We find a similar line shape suggesting the same aggregate structure is formed in all 3 carotenoids. (b) Model developed by Frank Spano[71] (Temple University, USA) applied to the β-carotene aggregate ground state absorption. More extensive results of the model are shown in Appendix M. Here we present results of modelling a trimer of carotenoid molecules with nearest neighbour coupling of 1200cm^{-1} and a relative angle of 0.3π. (c) The same model applied to β-carotene is applied to echinenone with the FWHM of the peaks increased by a factor of 1.5. (d) Model developed by Frank Spano[71] applied to the β-carotene and echinenone aggregate broadened as for echinenone and red-shifted by 170meV.

Having shown that all three carotenoids have the same aggregate structure we now wish to establish whether the protein environment has a significant effect on the decay processes of the aggregates. In Figure 6.9 we show a comparison between monomer, protein bound aggregate and solution-based aggregate ground state absorption for β-carotene and astaxanthin. For both carotenoids we observe very similar line shapes comparing the protein and solution based aggregate, suggestive of a similar intermolecular structure. In Figure 6.9 we also show transient absorption data for carotenoid aggregates in both solution and protein environments. We see no significant difference between the spectra or kinetics of aggregates in solution and protein. As the protein does not perturb the sample dynamics, while increasing stability (see Chapter 3), maquettes present a valuable route to allow fundamental studies of small clusters of molecules. We now move on to examine the effect of intramolecular structure on singlet fission dynamics.
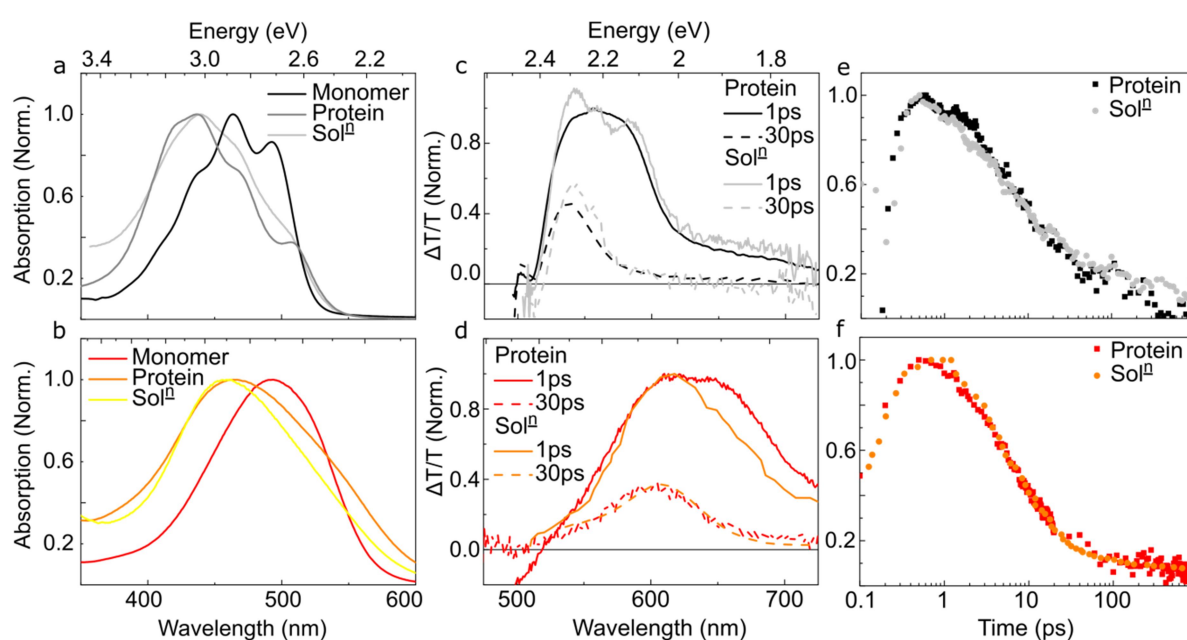
Figure 6.9: A comparison of transient absorption data for aggregates in solution and protein. Ground state absorption spectra of monomer, solution based aggregates and protein bound aggregates of β-carotene (a) and astaxanthin (b). Transient absorption spectra for solution based and protein bound aggregates of β-carotene (c) and astaxanthin (d). Astaxanthin samples where excited at 400nm (<1mW Power), while β-carotene samples were excited at 450nm (<1mW Power). As the stability of solution based aggregates of β-carotene is low, we include the excitation energy over which we see the least degradation. Transient absorption kinetics averaged over a 10nm window for β-carotene at 575nm (e) and astaxanthin at 600nm (f). Kinetics are identical in both cases indicating a similar decay pathway for the aggregates. Through the Figure we designate monomer carotenoids in solution as Monomer, protein bound aggregates as protein and solution based aggregates as Sol^n.

6.5 Effects of Intramolecular structure

In Figure 6.10 we present a comparison of transient absorption spectra for protein-bound aggregates of all three carotenoids excited at 400nm. We find a broad photo-induced absorption for all three carotenoids which in each case narrows over time to leave a long-lived feature. Kinetics averaged over the whole PIA feature for each carotenoid is plotted in Figure 6.10b. There is a remarkable similarity between the protein-bound aggregate kinetics of all three carotenoids. For all three carotenoids the PIA rises within the instrument response, in agreement with previous measurements of astaxanthin aggregates[25]. The kinetics for all three protein-bound aggregate samples can be fitted with a bi-exponential.
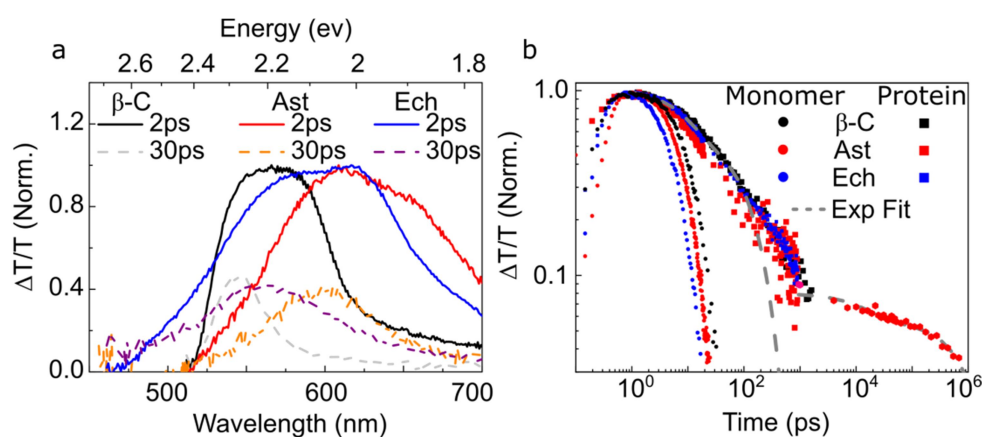
Figure 6.10: Transient absorption data for the protein bound aggregates. (a) Transient absorption spectra of β-carotene, astaxanthin and echinenone protein-bound aggregates excited at 400nm (1mW power). Spectral slices are averaged over 2-3ps and 30-40ps. The spectra have been normalised to the peak of the photo-induced absorption at 1ps for comparison. (b) Transient absorption kinetics of the three carotenoid protein bound aggregates, and carotenoids monomer taken following 400nm excitation. Kinetics were averaged over the whole PIA spectrum for each protein-bound aggregate. For carotenoid monomer samples kinetics are shown following band-edge excitation averaged over a 10nm window around 575nm (β-carotene), 625nm (astaxanthin) and 610nm (echinenone). For astaxanthin we also include a ns-TA kinetic (red circles past 10^3 ps delay) averaged over a 10nm window around 600nm excited at 355nm (0.1mW power). We include fits for the protein-bound aggregate kinetics indicated with a dark grey dashed line, parameters of the fits are discussed in the main text and Appendix L.

The first decay component is invariant with carotenoid structure with a value of 15±5ps. It should be noted that the 15±5ps decay component is similar to the decay constant for the S_1 state in carotenoid monomer. However, it is not possible to fit the aggregate data with the monomer decay

constants which vary from 5-10ps between the carotenoids (shown in Figure 6.10b). As a result, we rule out the low energy peak originating from a sub-population of monomer within the sample. Previously this component has been assigned to vibrational cooling in the triplet-pair state[25].

The second component of 125±50ps describes most of the high energy peaks decay for all three carotenoids, with only a small (10%) population surviving beyond 1ns. We include a ns-TA kinetic of this long-lived population for astaxanthin which decays with a majority time constant of 1. 4±0.2µs. The latter time-constant is too long for a strongly exchange coupled (TT) state, which should decay with similar decay constant to singlet states[34]. However, triplet lifetimes in solution for carotenoids range from 2-30µs, consistent with the measured lifetime here[314,315].

The observed behaviour in the protein-bound carotenoid aggregates shows a strong resemblance to the previous studies of carotenoid aggregates[24,25,316]. In these studies the authors assign the dynamics to singlet fission, with the two time constants representing the distribution of triplet-pair lifetimes within a given sample[25]. We find our observations agree with these studies confirming singlet fission is occurring within these protein-bound aggregates. Before we discuss the photo-induced absorption spectral shapes in detail we return to the spectra and kinetics in Figure 6.10. It is surprising that protein-bound aggregates of all three carotenoids show identical kinetics, given differences in their energetics and monomer photophysics. This suggests that singlet fission in carotenoids is an incredibly robust process. Combined with the work by Musser *et al.*[25] we are able to say that carotenoid aggregate singlet fission is invariant with intramolecular structure, intermolecular structure and protein environment.

6.6 Assigning the Photo-Induced Absorption Spectra

In the previous section we established that there are two distinct decay kinetics within the broad photo-induced absorption (PIA), neither of which match the decay of the monomer. To assign the two photo-induced absorption peaks for each carotenoid we decompose the initial spectrum into two separate features. We suggest one photo-induced absorption matches the longer-lived feature (30ps spectrum in Figure 6.10). The other (short-lived) component can be obtained by subtracting the 30ps spectrum from the 1-10ps spectra (Scaled to the blue-edge of the PIA). These results are presented for each carotenoid in Figure 6.11.
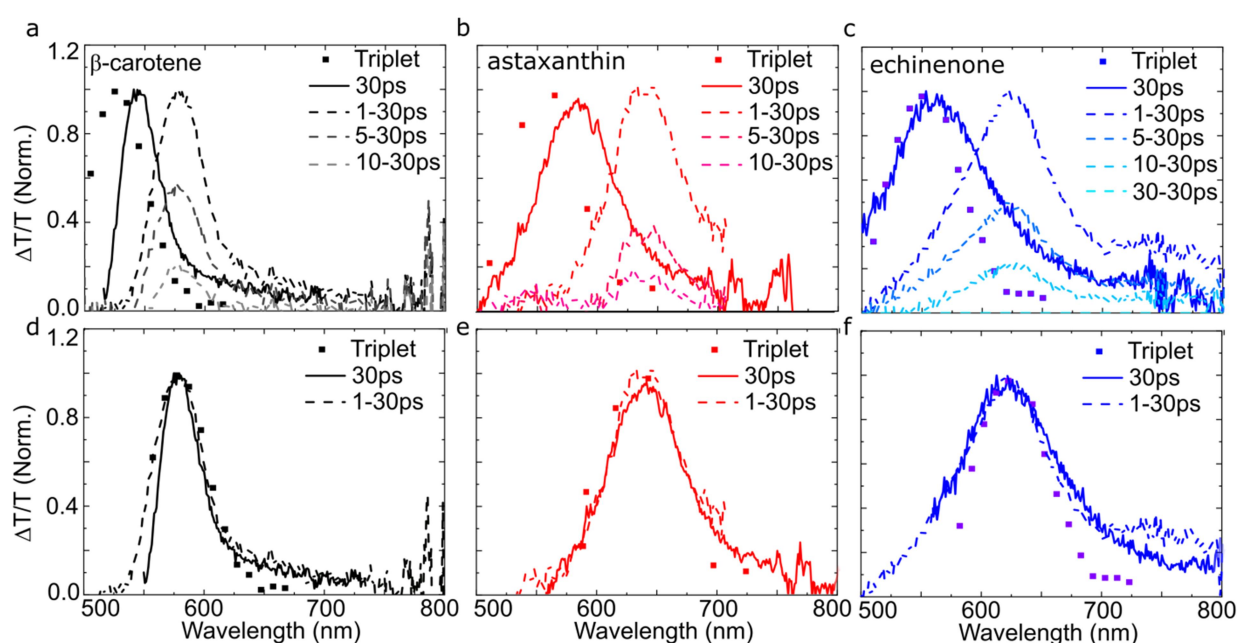
Figure 6.11: Decomposition of the carotenoid aggregate photo-induced absorption. Transient absorption spectra of β-carotene (a) astaxanthin (b) and echinenone (c) aggregates bound to maquette proteins excited at 400nm (1mW power). Spectral slices are averaged over 1-3ps and 30-40ps. We also include difference plots: 1ps-30ps delay, 5ps-30ps delay, and 10ps-30ps delay. For each difference spectra the 30ps delay spectrum was scaled to match the blue edge of the PIA. Spectra were normalised for comparison. The same plots are reproduced for β-carotene (d), astaxanthin (e) and echinenone (f) but arbitrarily shifted for comparison of spectral shapes with sensitised triplet spectra reproduced from figure 6.4, details of triplet sensitisation in Section 6.8.3.

We find an identical spectral shape at all delays with no shift or narrowing over time. The apparent narrowing of the overall spectrum over the first 30ps was measured previously for astaxanthin aggregates and was assigned to 'cooling' of the triplet-pair state[25]. However, we find here that the

two spectral features identified in Figure 6.11 are identical and appear to decay in parallel with no interconversion (no continued rise of the long lived feature). As such, we suggest the more likely explanation is the existence of two distinct triplet-pair states with differing energies and decay kinetics.

In Figure 6.11 we compare the two spectra to an isolated triplet spectrum taken via sensitization by Fullerene-C_{60}. Both photo-induced absorption features are similar in shape to an isolated triplet spectrum. This suggests that both of these transitions are triplet-like (T-T*) in nature, but shifted in energy from isolated triplets, indicative of triplet-pair states[31]. This implies we have triplet-pair states with two different binding energies represented by spectra shifted by two different energies. The lower energy state (larger binding energy) decays with a 15±5ps decay constant, while the higher energy transition (smaller binding energy) decays with a 125±50ps decay constant. It should be noted that we are comparing triplets of isolated molecules to triplet-pairs in an aggregated sample in a protein environment. It is unclear if the triplet state energy will shift with aggregation making quantitative assessments of shifts relative to isolated triplets difficult. However, as we find no further evolution of the long-lived feature, we suggest the spectrum responsible for the μs delay is the isolated/localised triplet spectrum with the triplets on different molecules.

The interpretation described above is qualitatively similar to that of PTV molecules in Chapter 5. In PTV molecules, activated singlet fission occurs from the S_2 state in parallel with formation of the S_1 state. To investigate whether singlet fission in carotenoids is activated, we excite protein-bound aggregates of β-carotene in 10nm steps across the whole absorption spectrum. For each excitation energy, the transient absorption spectrum at 1ps delay is fit with two gaussians to collect approximate peak intensities for the two photo-induced absorption features.

In Figure 6.12 we plot the ratio of these two peak intensities ($\frac{\text{High energy peak}}{\text{Low energy peak}}$) as a function of excitation energy (black squares).We observe an increase in the relative intensity of the high energy peak when exciting with higher energy photons. However, we observe a quantitatively similar

increase in relative intensity of the blue-shifted long-lived feature in isolated monomer (Figure 6.2). The similarity of the excitation dependence between monomer (no singlet fission) and protein-bound aggregates (singlet fission) suggests that the excitation dependence in the aggregate has the same origin as the monomers. This was assigned to the presence of non-all-trans isomers in the sample (Section 6.3). As a result, we can say that singlet fission is not activated in carotenoids aggregates. Instead our results suggest we have a sub-population of β-carotene isomers within our sample. However, as the isomer impurity lifetime is similar to that of the triplet-pair state (95ps compared to 125ps) we are unable to confirm if the isomer is the origin of the excitation energy dependence of the aggregate sample.
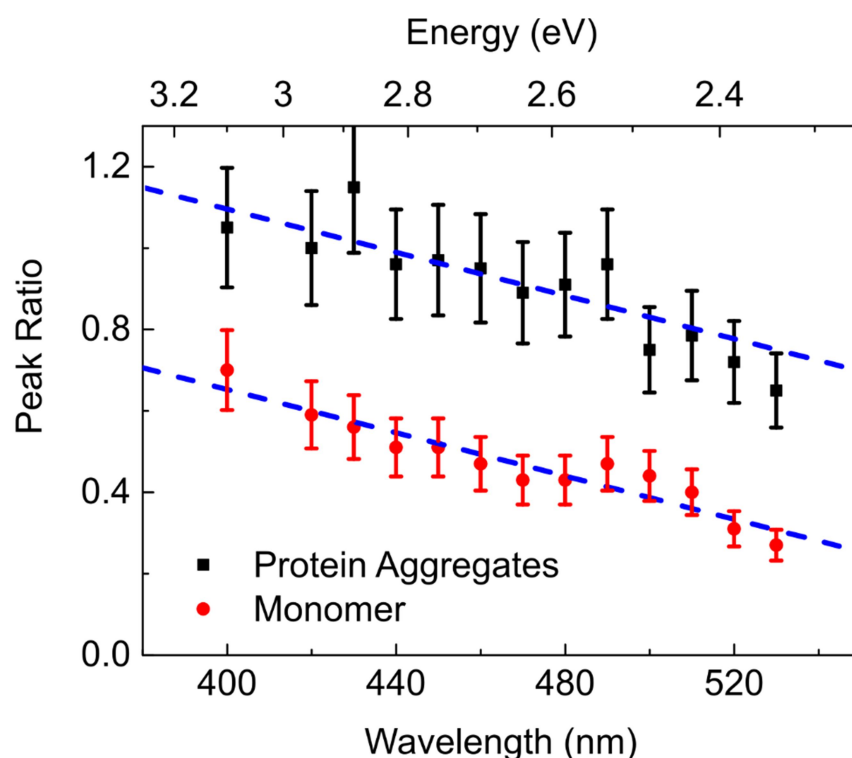
Figure 6.12: Excitation energy dependence of the monomer and aggregates. Protein-bound aggregates of β-carotene were excited in 10nm steps across the ground state absorption spectrum (<1mW Power). For each of the excitation energies the transient absorption spectra averaged over 1-3ps delay were fit with two gaussian functions. From this fit we are able to estimate the peak intensities of the low and high energy PIA peaks. The ratio of these peaks ($\frac{PIA_{High\ Energy}}{PIA_{Low\ Energy}}$) are plotted as a function of excitation energy (black squares). The same procedure was completed for a monomer sample of β-carotene at each of the excitation energies. For the monomer the two gaussians represent the S_1 excited state absorption for the all-*trans* and non-all-*trans* populations of the sample. We plot the ratio ($\frac{S^*}{S_1}$) of these intensities as a function of excitation energy (red circles).

6.7 Conclusion

Here we have used excitation-energy dependent transient absorption spectroscopy of β-carotene, astaxanthin, echinenone and spheroidenone in comparison with published data on β-carotene[150] to show that the so-called S* feature in all four carotenoids is due to impurities in the sample. Fortunately, with band-edge excitation the S* feature vanishes leaving a pure S_1 photo-induced absorption spectrum. The shape of this spectrum in the visible spectral range can be explained as due to a coupled pair of triplets (TT), which is known to be the dominant configuration of $2A_g^-$ [43,49,108,121]. The excited-state absorption spectrum of $2A_g^-$ shifts by ~200meV for β-carotene, ~100meV for astaxanthin and ~200meV for echinenone compared with the absorption spectrum of T_1. We then move to aggregates to prompt intermolecular singlet fission. We find protein environment and intramolecular structure has little effect on the singlet fission process.

6.8 Materials and Methods
6.8.1 Sample Preparation

β-carotene, astaxanthin and echinenone were purchased from Sigma-Aldrich at 95-97% purity and used as received. Spheroidenone was isolated from *Rhodobacter sphaeroides* as described in Chi *et al.* [178]. All carotenoids were dissolved in toluene at ~40µM for an OD of ~0.4-0.6 in 1mm path length cuvette. Protein samples were produced as described in Chapter 3 by George Sutherland (University of Sheffield) as in Ref[194].

6.8.2 Spectroscopy

Steady state absorption and emission measurements were taken as described in Chapter 3. Transient absorption measurements of β-carotene and astaxanthin monomer were taken at room temperature with a setup similar to that described by Cerullo *et al.* [200,317]. A series of narrow band (~10nm) pumps (under 1mW power) from 400 to 560nm and a visible probe pulse running from 500 – 700nm were supplied by home-built non-collinear optical parametric amplifiers (NOPA) (Setup

operated by Andrew Musser (University of Cambridge)). For most results pump pulses were 100fs long, while for 'fast' TA a broadband (50nm) pump pulse centred at 505nm with 10-fs duration was used (Operated by Frederico Branchi (Politecnico di Milano)). Finally, all other transient absorption measurements (other monomer and aggregate samples) were taken on the Helios setup as described in Chapter 3. Throughout the power was kept as low as possible to avoid degradation, in all cases being below 1mW.

6.8.3 Triplet Sensitisation

μs-ms transient absorption kinetics was measured at a given probe wavelength, each kinetic was fit to attain a peak intensity at a given time to build a full spectrum. Excitation was provided by a Nd:YAG laser (6 ns, 10Hz, Spectra-Physics), which pumped a versa-Scan L-532 OPO , providing pump wavelengths in the visible region. The excitation density of the laser was controlled with neutral density filters from 3 to 200 mJ/cm2, and was measured with an ES111C power meter (Thorlabs). Probe light was supplied by a IL1 (Bentham) quartz tungsten halogen lamp. The probe was recorded with Silicon and Indium Gallium Arsenide photodiodes coupled to a preamplifier and an electronic filter (Costronic Electronics) which sent signals to a Tektronix DPO4034B oscilloscope. A Cornerstone 130 monochromator (Oriel Instruments) was used to select the probe wavelength for a given acquisition. μs-ms transient absorption were conducted in collaboration with Jose Marin Beloqui (University College London). Solutions were flushed with nitrogen gas in a quartz glass cuvette prior the measurements. Samples of each carotenoid (β-carotene, astaxanthin, echinenone) where mixed with Fullerene-C_{60} as a sensitizer at a concentration of 200:800μMol, Carotenoid:C_{60}.

7. Conclusions and Further Work

Throughout this thesis we have investigated the intermediate triplet-pair states in the singlet fission process. In Chapter 4 we used strong-light matter coupling to investigate the high spin triplet-pair states in TIPS-tetracene. Due to the coupling between triplet-pair states of differing spin character, the photon character provided to the singlet state is also mixed with the quintet character triplet-pair states. Through this mechanism we were able to prompt emission from the dark quintet triplet-pair state via the emissive lower polariton branch. The coupling of light and matter then not only provides a new method for triplet harvesting but also for investigating these elusive dark states.

In Chapter 5 we investigated a series of oligo(thienylene-vinylenes) whose assignment as polyenes has been up for debate. We first confirm that these molecules do belong to the polyene class of materials before investigating the conjugation length dependence of triplet production from the dimer to the octomer (approximately equivalent to a polymer). We found efficient intersystem crossing in the shortest molecules, which for molecules longer than 4 units switched to energy activated intramolecular singlet fission. Throughout the singlet fission active oligomers, we found decay constants consistent with an energy gap law, suggesting the triplet-pair formed of singlet fission in these materials is relatively strongly bound.

In Chapter 6 we started by clearing up which states are relevant to the low energy physics of carotenoids, a class of polyene materials. We found that at band-edge excitation only three states are required to describe the observed data, those being the ground state, the bright absorbing state ($1B_u^+$) and the dark symmetry forbidden triplet-pair character state ($2A_g^-$). We then compare the $2A_g^-$ photo-induced absorption spectrum (S_1-S_n) to a sensitised triplet spectrum (T-T*), red-shifted by ~200meV. We find a striking resemblance, providing experimental evidence for the triplet-pair character of the $2A_g^-$ state. Interestingly, here we find a red-shift between the singlet state PIA and isolated triplet PIA as opposed to a blue-shift for the triplet-pair of singlet fission in OTVs (Chapter 5) and zethrenes[31]. However, the red-shift is in agreement with the S_1 state of the trimer in Chapter 5.

Solving the PPPP π-electron model for polyenes we find that the designation of S_1-S_n as a T-T* transition is supported by the calculations and that the shift is consistent with the expected state energies for a polyene chain of a similar length to the trimer and β-carotene. We then continue to investigate singlet fission in protein bound carotenoid aggregates. We find the surprising result that combined with the study by Musser et al.[25] we are able to conclude that intramolecular structure, intermolecular structure and protein environment have little effect on the singlet fission process. This points to an incredibly consistent singlet fission process, as opposed to polyacenes which have a very different singlet fission process depending on the structure of the sample[12,15,17,19,77,93,96].

With the contributions of this thesis outlined we would like to conclude by discussing an interesting question that arises when applying the current language surrounding polyacene singlet fission to polyene materials. Originally singlet fission was defined as the formation of two 'free' triplets[9,10]. However, recent studies of acene and heteroacene materials[12–14,77,94–96,239] show that singlet fission creates a strongly exchange coupled (bound) pair of triplets which can either separate to form individual triplets[17], evolve to other spin states (quintets)[12,95] or decay with no further evolution[14]. This has caused the nomenclature in the field of singlet fission concerning acenes to evolve. It is now common for the initial step of forming a bound triplet-pair to be referred to as "singlet fission", with the following steps being "separation" or "spin evolution"[12,15,95]. In order for singlet fission to occur efficiently i.e. without a spin flip, the bound triplet-pair state must be of pure singlet character[34,77]. Therefore, in acene literature singlet fission is defined as the conversion of a singlet state into a strongly exchange coupled singlet character triplet-pair state. When we apply this language to polyenes, an interesting equivalency becomes clear.

As discussed in Chapter 5 and 6, the $2A_g^-$ state can be described as having significant triplet-pair character, with the excited state absorption spectrum resembling a triplet transition. On the other hand it has been shown that the triplet-pair of singlet fission has significant singlet character[34,77], with strongly bound triplet-pairs being shown to following the well-known energy gap law, which

has been previously applied to the decay of singlet states such as the $2A_g^-$ state[34,52]. It is therefore reasonable to suggest there are significant similarities between the bound triplet-pair state of singlet character and the symmetry forbidden $2A_g^-$ state in polyenes which possesses significant triplet-pair configuration. Both states form within 1ps of excitation, can decay following an energy gap law with no formation of free triplets, and both have excited state absorption signatures that have a similar line shape to sensitised triplet absorption signatures.

Considering this similarity, the classification of the transition from the bright singlet ($1B_u^+$) state to the dark triplet-pair character ($2A_g^-$) state in polyenes comes into question. To date this transition has been considered 'internal conversion' as it involves the transition between two singlet states. However, as the final singlet state is considered a strongly exchange coupled triplet-pair of singlet character; this clearly matches the definition of singlet fission outlined above. As a result, the transition between $1B_u^+$ and $2A_g^-$ could also be described as 'intramolecular singlet fission' using the new definition of singlet fission in the acene literature. Indeed a similar suggestion has been made by two separate theoretical studies of polyene systems[43,108]. In Figure 7.1 we show a generalised decay scheme for polyacene solid state samples and a single polyene chain. The two show significant similarities with behaviour dependent on the specific structure of the sample. However, there are some differences that as of yet remain unexplained, these are discussed below.
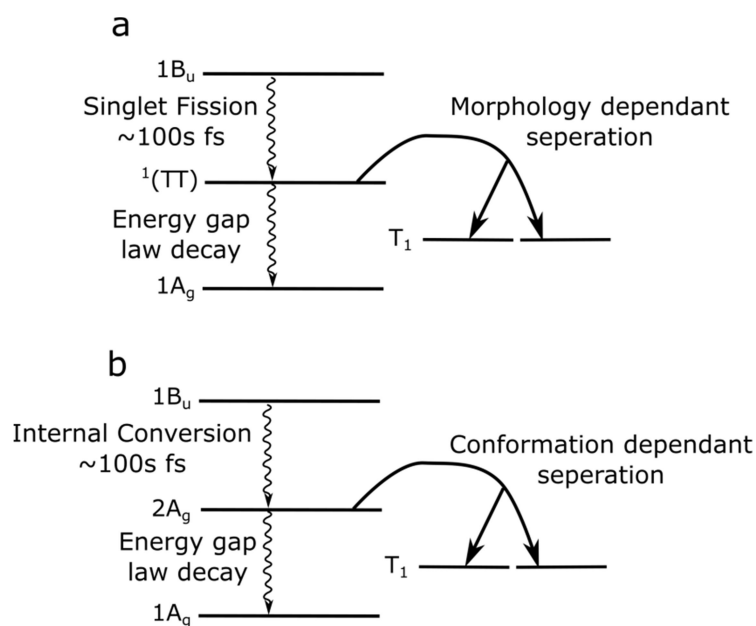
Figure 7.1: Comparison of acene and polyene decay schemes. (a) Following excitation to the first optically allowed state (1Bu) singlet fission occurs to a triplet-pair of singlet character with a time constant dependent on the sample structure. In some material systems such as pentacene this can occur on the 100s fs time scale. After singlet fission the triplet-pair states are then able to separate to free triplets, evolve to other spin states (quintets) or remain bound and decay to the ground state depending on the sample structure. (b) Following excitation to the first optically allowed state (1Bu) internal conversion occurs with a 100s fs time constant to the singlet state of triplet-pair character. Afterwards the $2A_g^-$ state either decays to the ground state or separates to free triplets dependent on the conformation of the carotenoid molecule.

While in some situations free triplets are not formed from the triplet-pair of polyacene materials, in the majority of cases separation to free triplets occurs to some extent[13,14,17,19,77,96]. On the other hand, free triplets have not been confirmed for intramolecular singlet fission of a single polyene chain. Despite increasing the chain length to the maximum attainable conjugation length, there have been no confirmed observations of individual triplets produced via singlet fission in polyene polymers[27–30]. In their seminal work, Tavan and Schulten proposed that a small energetic push could separate the two triplets that comprise the $2A_g^-$ state[49,121]. To our knowledge there has been little evidence found for this mechanism. Hashimoto *et al*. identified a small triplet population (10^{-3} yield) in β-carotene following 355nm excitation that decay within 5ns[318], much faster than is expected for isolated triplets in β-carotene (30µs)[314]. While this is an increase from the intersystem crossing yield at band-edge excitation ($\sim 10^{-6}$)[39,112], the yield is still very low. Furthermore in a later study, Billsten *et*

al. found that for zeaxanthin there was no measurable triplet population despite conducting an excitation energy dependence up to 266nm excitation[147].

While no free triplets have been reported for polyenes in solution, there have been studies indicating the production of individual triplets on a single carotenoid in light harvesting complexes[126,143,305]. It is suggested a twisted conformation of the conjugated backbone could cause a localisation of the individual triplets[305]. While this has gained evidence from studies of light harvesting complexes no simplified solution based study has observed the mechanism directly. In Chapter 6, we used maquette proteins to produce aggregates of carotenoids bound and stabilised by the protein environment. Recent work on man-made proteins has shown potential for creating specific binding motifs, which enforce a particular conformation of the molecule contained within the protein[319]. In theory it may be possible to design a protein able to bind a twisted carotenoid to provide a simple solution based sample to test. Investigation of these protein bound samples could shed light onto the mechanism of triplet formation in light harvesting complexes. If it is indeed possible for the triplet-pair to separate, this points to yet another similarity between the $2A_g^-$ state and triplet-pairs in acene materials.

Regardless of free triplet production in twisted conformations, a more fundamental open question remains. As a strongly exchange coupled triplet-pair and $2A_g^-$ can decay with the same rate for a given energy gap and have similar spectral features a distinction experimentally may not be possible.

In order to investigate further we must first establish if there are any spectroscopic differences between the triplet-pair state and $2A_g^-$ state. A possible route for this is through vibrational spectroscopy, due to the distinctive signatures of the states involved. It has been shown that the $2A_g^-$ state has several distinctive vibrational modes[112], while triplets also have distinctive signatures[320]. However, a recent study of pentacene derivatives in the solid state suggests the strongly bound triplet-pair state has no vibrational signature in the first 10ps following excitation[320]. Instead the authors measure vibrational signatures of triplets rising on the 10-50ps time scale consistent with

separation of the correlated strongly exchange coupled triplet-pair to a weakly bound triplet-pair[77,320–322]. Similar results have been shown for carotenoid aggregates measured via impulsive vibrational spectroscopy (as in Ref[54]) suggesting a wider applicability of the lack of measurable vibrational signatures in the strongly bound triplet-pair state [Musser et al, private communication]. These preliminary results point towards a possible route for distinguishing the two triplet-pair character states.

In competition with these initial studies, vibrational signatures of triplet-pair states have been reported. Chen and co-workers report on a femtosecond mid-IR transient absorption study of a series of terrylenediimide (TDI) dimers[323]. Chen et al. found that in solutions of TDI dimers the triplet-pair state forms via mixing with an intermediate charge-transfer state with no separation to free triplets during their 8ns measurement window. Despite the lack of isolated triplet formation, authors report the vibrational signatures of free triplets, which they assign to the triplet-pair state. Further, the authors measure a shift in the C=O stretching mode ($1579cm^{-1}$) over the first 5ps, coinciding with formation of the mixed charge transfer and triplet-pair character state[323]. A similar observation of a shift in a ring stretching vibrational mode ($1620cm^{-1}$) upon formation of the triplet-pair state (over 5ps) was reported for crystals of hexacene this year[324]. Clearly, further work is required to pick apart the vibrational signatures and possible differences between states of triplet-pair character.

8. Appendix

Appendix A - Indolonaphthyridine benzene (INDB)

Figure 8.1 shows steady-state absorption and PL spectra of INDB:polystyrene blends (1:4 ratio) in solution (<1mg/ml) and thin film. Compared with solution, the film absorption spectrum blue-shifts, showing a reduction in the 0-0 peak intensity, suggesting formation of weakly-coupled H-aggregates within the film[71]. The film PL spectrum likewise shows a red-shifted component, consistent with aggregation and/or excimer emission[232], with more extreme effects than observed with DPPT.
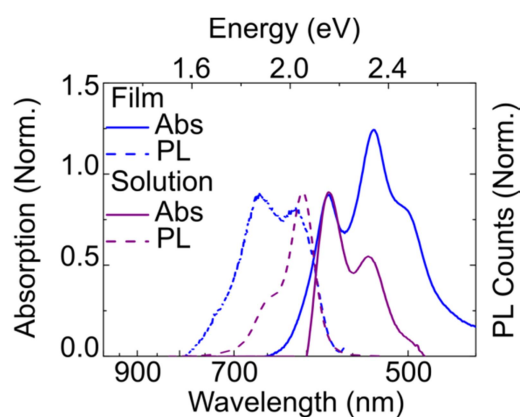
Figure 8.1. Steady-state characterisation of INDB. Absorption (solid) and emission (dashed) spectra of INDB in toluene solution (red) and embedded in polystyrene matrix (green). Excitation for photoluminescence spectra was at 532 nm.

Figure 8.2 shows a reflectivity map of an Ag-Ag microcavity containing an INDB blend film. The clear anti-crossing at the 0-0 absorption energy and transfer matrix modelling (lines) confirm that this microcavity is in the strong-coupling regime. Following photoexcitation of the microcavity, all emission is from the lower polariton branch.
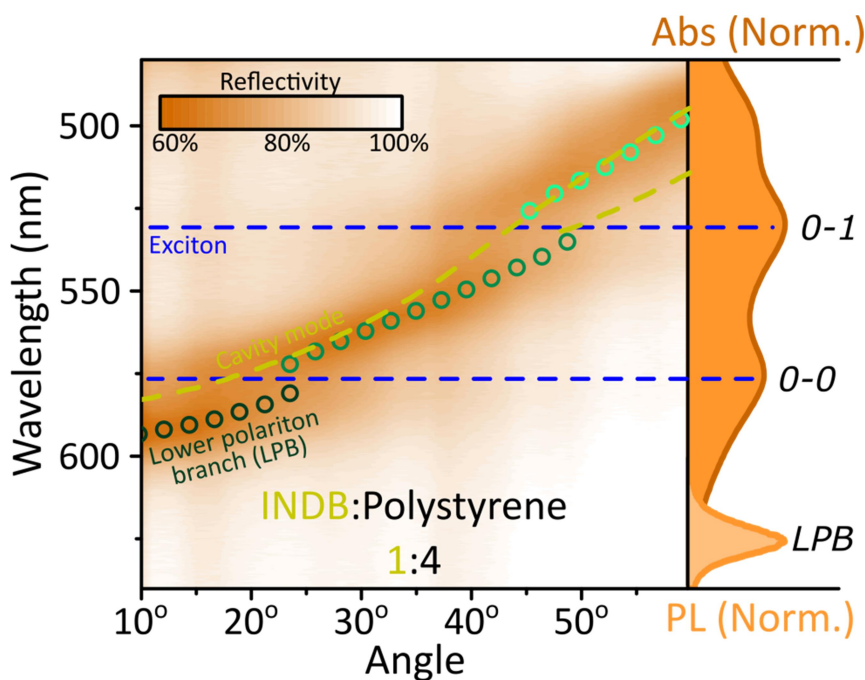
Figure 8.2. Reflectivity map of INDB microcavity. Ag-Ag microcavity containing INDB:polystyrene (1:4 by weight) film. Comparison with absorption spectrum (right) and transfer matrix modelling (lines, circles) confirms strong coupling. All emission arises from the lower polariton branch (LPB).

Time-resolved emission spectra of the film and microcavity are shown in Fig 8.3 within the instrument response (IRF) and between 15-25 ns after photoexcitation. In the film, the prompt emission is from singlet excitons while at later times the broad, featureless, red-shifted emission suggests formation of excimers. Microcavity emission spectra do not change over this timescale, suggesting that emission is from the lower polariton branch. It is noteworthy that we observe microcavity emission even on timescales when the singlet has been fully depleted, and the only excited-state population is that of excimers. The simplest explanation for this observation is that the excimer is able to populate the lower polariton branch, as observed in other systems[158]. INDB film and microcavity emission dynamics are shown in Figure 8.3, integrated over the entire spectral range (i.e. both singlet and excimer bands in the film). Kinetics for the two samples are similar, confirming the excimer can also populate the lower polariton branch. When this excimer-population mechanism (known as 'radiative pumping') is active, the delayed emission lifetime has been shown to increase between film and microcavity[158]. However, the change in emission lifetime between cavity and film measured here on these timescales is negligible. This result confirms that the large

changes in lifetime reported in Chapter 4 are not an artefact of our measurement conditions, and in the absence of triplet-triplet annihilation, we observe no significant lifetime enhancement between film and microcavity.
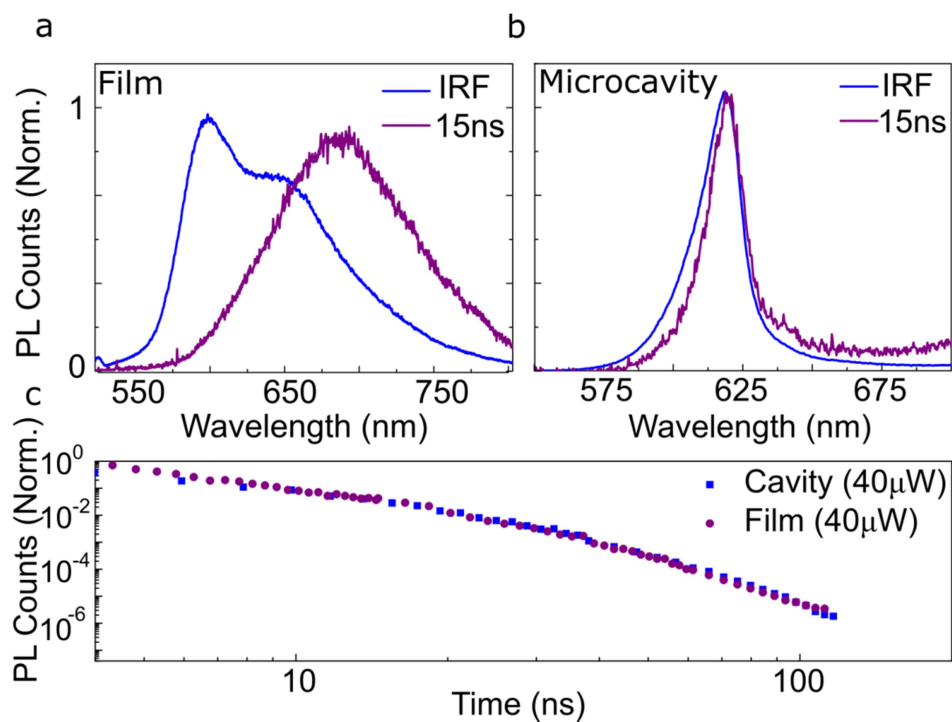
Figure 8.3. Time-resolved INDB photoluminescence. (a) Spectra of INDB:polystyrene film following excitation at 532 nm, collected within the instrument response (IRF) and at 15-25 ns after excitation. (b) Equivalent spectra for microcavity. (c) Emission kinetics integrated over full spectral bandwidth of bare film (circles) and microcavity (squares) of INDB.

Appendix B - TIPS-Tetracene Control Samples

Table 8.1: Summary of sample types and observed behaviour.

Prep. no.	Sample type	Strong coupling?	Strong delayed PL?	Notes
1	Spin-cast thin film (~200 nm) on glass, toluene solution	*no*	*no*	reproduces literature behaviour
2	Spin-cast thin film (~200 nm) on glass, chloroform solution	*no*	*no*	change in morphology does not alter dominant PL dynamics
3	Spin-cast thin film (~200 nm) on glass, toluene solution, thermally annealed	*no*	*no*	improves morphology and reduces disorder but only slightly enhances delayed emission
4	Spin-cast thin film (~200 nm) on glass, toluene solution, exposed to ultrahigh vacuum	*no*	*no*	removes residual solvent and possible quenching sites, improves morphology but dynamic effects are within sample to sample fluctuation
5	Spin-cast thin film (~200 nm) on Ag, toluene solution	*no*	*no*	no effect, reproduces reference film within sample-to -sample variance. Ag promixity does not result in any enhancement
6	Evaporated TIPS-tetracene film on glass	*no*	*no*	reproduces spin-cast film behaviour
7	Evaporated BCP:TIPS-tetracene:BCP film (20 nm:73 nm:20 nm) on glass	*no*	*no*	slight change in spectral shape due to increased disorder at TIPS-tetracene:BCP interface, but evaporation with BCP does not significantly alter photophysical properties
8	Evaporated BCP:TIPS-tetracene:BCP film (20 nm:73 nm:20 nm) on glass, capped with 25 nm Ag	*no*	*no*	minor effect, similar to thermal annealing or ultrahigh vacuum treatment. Microcavity processing procedures are insufficient to cause enhanced delayed emission in the absence of strong coupling
9	Evaporated BCP:TIPS-tetracene:BCP film (90 nm:20 nm:90 nm) on glass	*no*	*no*	no effect, photophysics of thin film are identical to thick films
10	Evaporated BCP:TIPS-tetracene:BCP film (90 nm:20 nm:90 nm) on Ag, capped with 25 nm Ag	*no*	*no*	no effect, encapsulation within a non-coupled microcavity does not enhance the delayed emission
11	Spin-cast thin film (variable thickness) on Ag, toluene solution, capped with 25 nm Ag	**yes**	**yes**	polariton formation results in substantially enhanced delayed emission
12	Evaporated BCP:TIPS-tetracene:BCP film (20 nm:73 nm:20 nm) on Ag, capped with 25 nm Ag	**yes**	**yes**	polariton formation results in substantially enhanced delayed emission, even when there is no physical contact between active layer and Ag

Appendix C - Rate Model Parameters

Table 8.2: Summary of rates used in the rate model

Rate constant	Value	Reference or rationale
G	1/(0.5ns)	Generation of excitons: estimated from instrument response.
LPB k_r	1/(0.1ns)	Radiative decay of the lower polariton branch: Should be roughly equal to the photon lifetime (here we make it longer to speed up computation time, noting that it is markedly faster than other rates on our measurement timescales).
S_1 k_r	1/(15ns)	Singlet radiative lifetime: in solution[14]
S_1 k_{nr}	1/(30ns)	Singlet non-radiative lifetime: Assuming the non-radiative decay is dominated by the gap-law, as for other acenes, with E_{S1} = 2.3 eV [246]
TT_{bright} k_r	1/40 x S_1 k_r	Singlet character TT state radiative decay: Relationship previously determined for a similar heteroacene[94]
TT_{Bright} k_{nr}	1/15	Singlet character TT state non-radiative decay: Assuming $^1(TT)$ decays via the same non-radiative gap-law as S_1, as demonstrated by the authors in an up-coming review. Energy = $2 \times T_1$ = 2.2.eV.
TT_{Dark} k_{nr}	1/5000	TT states not coupled to the emissive singlet non-raditive decay: Fit to the published $^5(TT)$ data[12]. Note this constant is not unique but is correlated with k_{spin} below.
TT_{uncorr} k_{nr}	1/30,000	Non-radiative decay of individual triplets: Fit to the transient absorption data[13].
k_{SF}	1/0.05	Singlet fission: 50ps[13]
k_{-SF}	1/1	Geminate triplet recombination: Taken from a previous determination for tetracene[78]
k_{pol_s}	1/100	Emissive singlet state to lower polariton branch: Fit to data (this is a maximum rate, any faster and the LPB emission would decay faster than we observe. Smaller values are possible but do not change the dynamics, only the relative LPB population).
k_{pol_b}	1/100	Singelt character TT state to lower polariton branch: Fit to data (as above)
k_{pol_d}	x * k_{pol_s}	Quintet character TT state to lower polariton branch: Fit to data. For data in the main text x = 0.005.
k_{dark}	1/30	Spin evolution from TT states that can couple to the emissive singlet to those that cannot: Fit to delayed emission[13]
k_{-dark}	0	Reverse of the above process: In simplest model. Otherwise we used a distribution of rates to model the non-exponential tail of S_1 emission
k_{spin}	1/10,000	Conversion to isolated triplets from all triplet pair states: Fit to $^5(TT)$ EPR data[12] (see note for K_{NR} TT_{dark} above).

Appendix D - Pentamer and Heptamer Transient absorption data
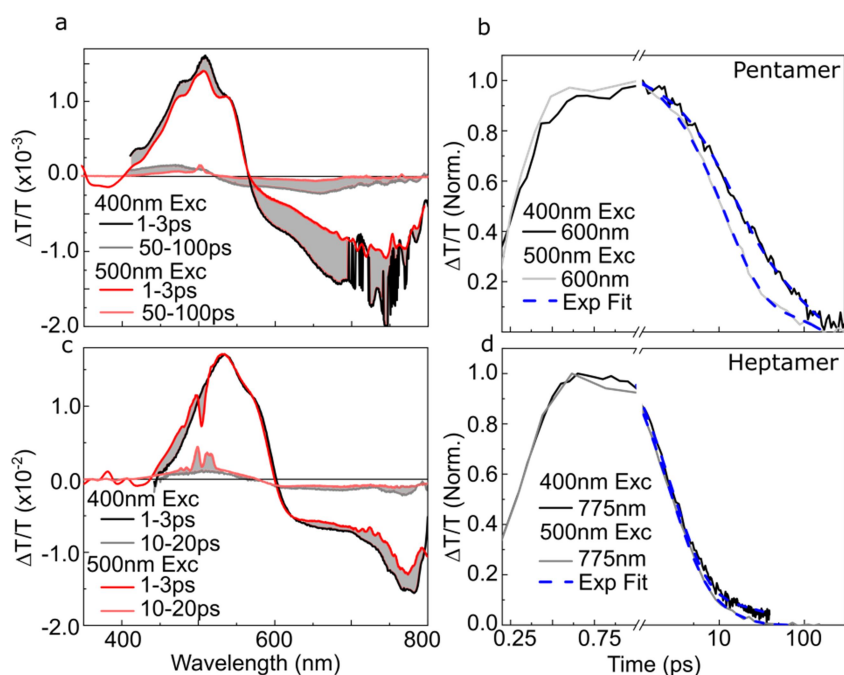
Figure 8.4: Excitation energy dependant transient absorption of 5 and 7 unit OTVs: (a,c) Transient absorption spectra of the pentamer (a), heptamer (c) excited at 500nm and 400nm (1mW power). Spectral slices are averaged over times marked in the legend. The 500nm spectra have been scaled so that the 0-0 peak of the ground state bleach are match the 400nm excitation data. (b,d) Transient absorption kinetics of the pentamer (b), heptamer (d) at the central wavelengths marked in the legend (10nm window). Due to a broadening of features in the hexamer and octamer data, we show a kinetic at the peak of the triplet region. Dashed lines show mono/bi exponential fits with constants in Appendix L and described in the Chapter 5 main text.

Appendix E - Summary of Kinetic fit parameters (OTV)

Kinetic parameters used to fit the kinetics throughout Chapter 5. In each case the range of possible values for the decay constant are given that return a reasonable fit to the data. For the longer oligomers we observe no emission or intersystem crossing suggesting we are able to approximate that non-radiative decay dominates. For the trimer and dimer, calculation of K_r, K_{nr} and K_{ISC} are shown in Appendix I.

Sample	[2]A_1 (%)	τ_1 (ps)	[2]A_2 (%)	τ_2 (ps)	[3]Zero Offset (%)
Octamer (600nm Exc)	100	1-1.4	--------	--------	0
Octamer (500nm Exc)	98.6	1.8-2.2	--------	--------	1.4
Octamer (400nm Exc)	92	1.8-2.2	8	16-33	0
Heptamer (600nm Exc)	100	1-1.4	--------	--------	0
Heptamer (500nm Exc)	98.3	2.2-2.7	--------	--------	1.7
Heptamer (400nm Exc)	91.6	2.2-2.7	8.3	18-41	0
Hexamer (500nm Exc)	98.3	3.8-4.5	--------	--------	1.7
Hexamer (400nm Exc)	86	3.8-4.5	14	50-172	0
Pentamer (500nm Exc)	96.2	11.2-13.1	--------	--------	3.7
Pentamer (400nm Exc)	61.4	11.2-13.1	38.5	33-100	0
Tetramer (500nm Exc)	100	50-62.5	--------	--------	0
Tetramer (400nm Exc)	80.3	50-62.5	19.7	100-526	0
Trimer (505nm rise)[1]	100	0.18-0.38	-------	-------	-------
Trimer (505nm decay)[1]	63	1.1-1.5ns	37	115-135ns	0
Trimer (1100nm decay)[1]	50	0.32-0.52	50	1.1-1.5ns	0
Trimer (FLUPS)	56	0.32-0.52	44	1.1-1.5ns	0
Dimer (420nm rise)[1]	100	101-111	--------	--------	--------
Dimer (625nm decay)[1]	99.9	95-130	0.1	0.5-2.5ns	0

[1] Fits of kinetics for the dimer and trimer are only presented after one excitation energy as we show there is no excitation energy dependence for these oligomers. The wavelengths listed in the table for the trimer and dimer are instead the wavelengths at which kinetics were taken.

[2] Kinetic fits were locked to start at time zero, however, convolution with the IRF causes the decay to begin after time zero (~0.5ps). As such amplitudes are given as percentages of the total intensity, as described in Ref[325]. This produces a source of error however the same procedure has been used to fit all oligomer kinetics.

[3] Zero offset is given as a percent of the maximum intensity

Appendix F - Octamer and Heptamer 600nm Excitation Kinetics
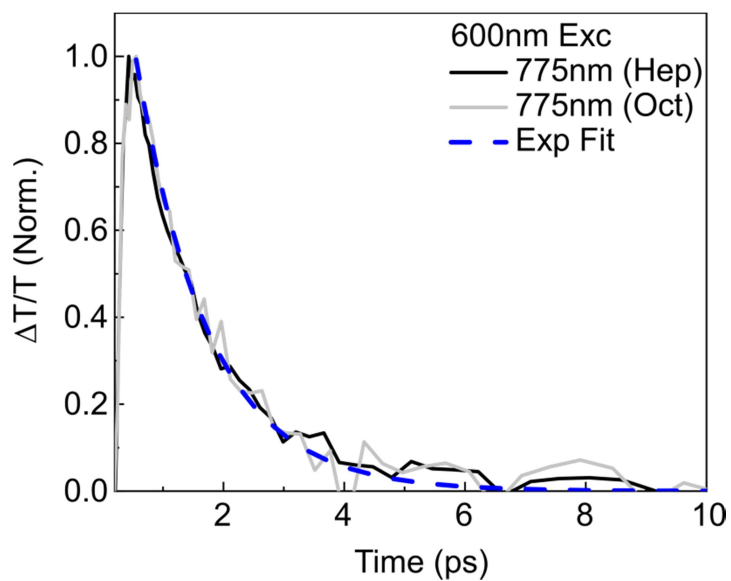
Figure 8.5: Kinetics following 600nm excitation of the octamer and heptamer: Transient absorption kinetics of the octamer and heptamer at the central wavelengths marked in the legend (10nm window). Due to a broadening of features in the heptamer and octamer data, we show a kinetic at the peak of the triplet region. Dashed lines show mono exponential fits with fir parameters in Appendix L.

Appendix G - Trimer Aggregation Check
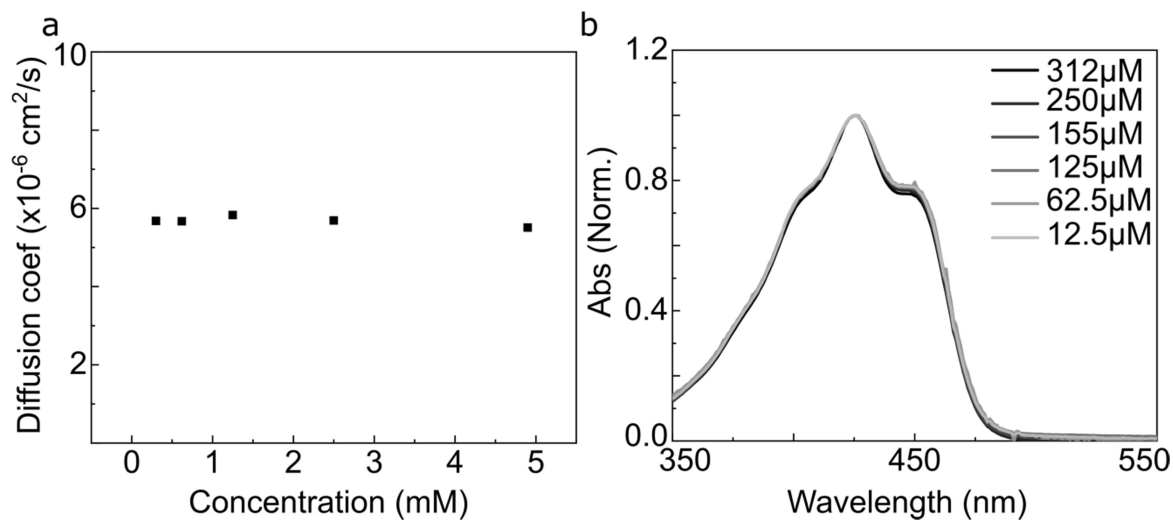
Figure 8.6: Ruling out aggregation in trimer samples with absorption and DOSY NMR. (a) Diffusion coefficient of trimer sampled over a large range of concentrations measured using DOSY NMR (by Iain Andrews, Imperial College London). The lack of change with concentrations rules out large scale aggregation. (b) Ground state absorption of trimer in the concentration range used for measurements (Abs saturation 0.5mM), showing no signs of aggregation.

Appendix H - Trimer Excitation Dependence
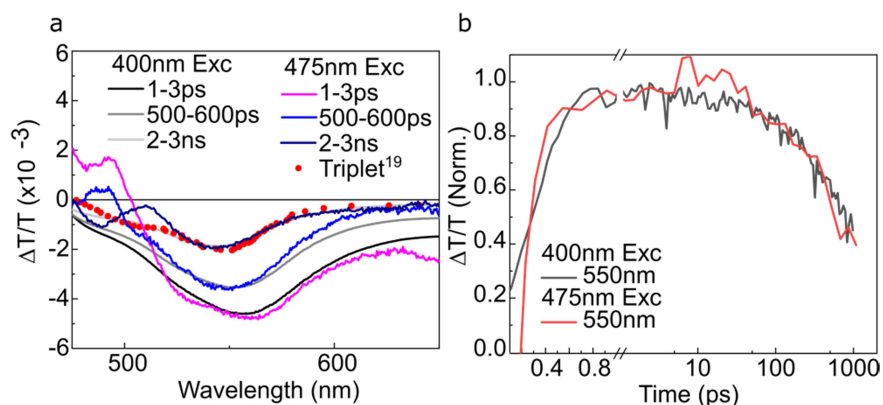
Figure 8.7: Excitation energy dependant transient absorption of the trimer: (a) Transient absorption spectra of the trimer excited at 475nm and 400nm (1mW power). Spectral slices are averaged over times marked in the legend. Included is the sensitised triplet spectra taken from Apperloo *et al.*[179]. The 500nm spectra have been scaled so that the 0-0 peak of the ground state bleach match the 400nm excitation data. (b) Transient absorption kinetics of the trimer at the central wavelengths marked in the legend (10nm window) excited at 475nm and 400nm (1mW power).

Appendix I - Calculation of Rate Constants

Parameter	Dimer	Trimer
Natural Lifetime (τ)[5]	106±5ps	1.1±0.2ns
Radiative rate (k_r)[1]	3±0.14ns^{-1}	13±2.4ns^{-1}
Non-radiative rate (k_{nr})[2]	1.2±0.45ns^{-1}	3±0.5ns^{-1}
Intersystem crossing rate (k_{isc})[3]	108±27ps^{-1}	2±0.5ns^{-1}
Emission quantum yield (ϕ_{PL})	3.6+±0.05%	10±.05%
Triplet yield $(\phi_{Triplet})$[4]	98±10%	53±10%

[1] Radiative rate was calculated using: $k_r = \dfrac{\phi_{PL}}{\tau}$

[2] Non-Radiative rate was calculated using: $k_{nr} = \dfrac{k_r - \phi_{PL}k_r - \phi_{PL}k_{isc}}{\phi_{PL}}$

[3] Intersystem crossing rate was calculated using: $k_{isc} = \dfrac{\phi_{Triplet}}{\tau}$

[4] We estimate the triplet yield using the equation shown below. Here we estimate the relative extinction coefficient of the triplet-triplet and ground state absorption transitions to be $\varepsilon_{S0-S2} = 1.1\,\varepsilon_{T-T*}$. We base this estimate in calculations carried out by William Barford (Oxford University), who found this relationship for a 18 site polyene chain (Chapter 6). This relationship is an estimate presuming no change with conjugation length, i.e. presuming both extinction coefficients change equally with conjugation length. We estimate a large error to account for possible limitations in this extinction coefficient relationship of 10%.

$$\frac{Pop_{S0-S2}}{Pop_{T-T*}} = \frac{Signal_{S0-S2}}{Signal_{T-T*}} \times \frac{\varepsilon_{S0-S2}}{\varepsilon_{T-T*}} => \frac{1}{Pop_{T-T*}} = \frac{Signal_{S0-S}}{Signal_{T-T*}} \times 0.9$$

[5] Error in the measured natural lifetime of the state is estimated by varying the fit parameters to assess the range of values that still give a reasonable fit to the data. This range then gives the error range in the fitting parameters. Errors in calculated parameters were calculated using standard error propagation equations.

Appendix J - Dimer Excitation Energy Dependence
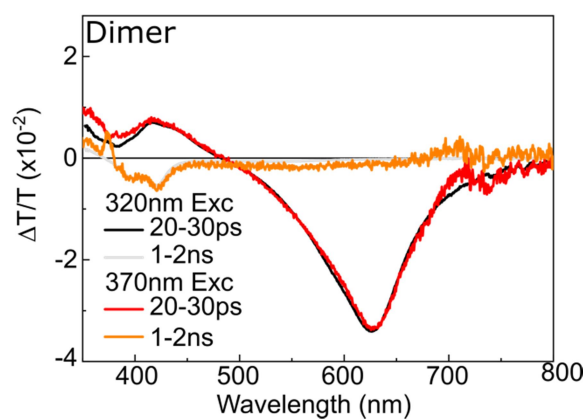
Figure 8.8: Transient absorption of the trimer. (a) Transient absorption spectra of the dimer excited at 320nm and 370nm averaged over time frames given in the legend (1mW power). We find no effect of excess energy excitation on the spectra of the dimer.

Appendix K - Assignment of S* impurity to *cis* isomers

We measured the transient absorption spectra of β-carotene and astaxanthin excited across their absorption band (400-520nm) (Figure 8.9). We compare the excitation energy dependence of the peak intensity of the transient absorption feature usually assigned as S* to the absorption of the isomers identified by Ostroumov *et al.* [150]. The impurity absorption spectrum (Figure 8.9, blue circles) was obtained by subtracting the all-*trans* absorption spectrum from the total sample spectrum from Ref [150], leaving only the collective absorption of the isomers [150]. For both β-carotene (Figure 8.9a) and astaxanthin (Figure 8.9b) we find a striking similarity between the two plots, with a complete loss of the impurity signal for excitation below 2.6eV (480nm). The lower-energy onset of S* absorption in astaxanthin is a result of a red-shift in absorption compared to β-carotene. We conclude that in both β-carotene and astaxanthin the long-lived feature assigned by others to S* is the impurity feature observed in Ref [150]. Interestingly, there is significantly less isomer population in astaxanthin ($\frac{\frac{\Delta T}{T} \text{ at 560nm and 1ps (S*)}}{\frac{\Delta T}{T} \text{ at 630nm and 1ps (S1)}} = 0.045$) as compared to β-carotene ($\frac{\frac{\Delta T}{T} \text{ at 540nm and 1ps (S*)}}{\frac{\Delta T}{T} \text{ at 590nm and 1ps (S1)}} = 0.25$) following 400nm excitation. A possible explanation for this is that astaxanthin has a much higher activation energy of isomer formation, found experimentally to be 101kJ/mol compared to 14kJ/mol for β-carotene [326,327].
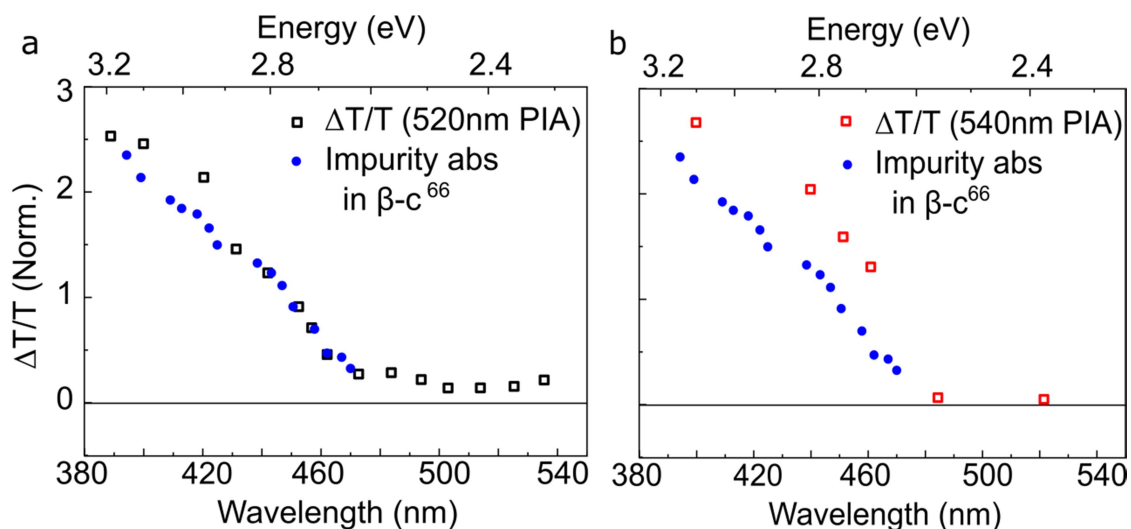
Figure 8.9: Excitation energy dependence of the so called S* feature. (a) and (b) show the peak intensity of the S* absorption feature in β-carotene (a) and astaxanthin (b) as a function of excitation energy (Open markers). For comparison we include the ground state absorption of the impurity identified by Ostroumov *et al.* [150] for β-carotene in both panels (closed markers). The absorption spectra were attained by subtracting the absorption spectrum of the purified (all-trans) β-carotene sample from the overall absorption of the sample.

Figure 8.10 presents high time resolution transient absorption data for β-carotene and astaxanthin excited with broadband ~10-fs pulses (490-570nm) versus narrowband (490-510nm) pulses. The broadband and narrowband pumps overlap with the carotenoid absorption spectrum without exciting above the 480nm threshold for isomer absorption (see Figure 8.9). Jailaubekov *et al.* demonstrated that narrowband (392-400nm) versus broadband excitation (389-416nm) has little effect on the proposed S* state in β-carotene [146]. As the hot ground state model (described in Chapter 2) requires population via impulsive raman scattering, this rules out a hot ground state population[146]. We likewise find no evidence of S* in the β-carotene and astaxanthin spectra, independent of pump pulse bandwidth (Figure 8.10), confirming that a hot ground state is not required to explain the transient absorption data. In fact, the dynamics in Figure 8.10 show an identical rise and decay at the wavelengths traditionally assigned to S* and S_1-S_n, suggesting that a single transition can fully explain the transient absorption spectra of β-carotene and astaxanthin. In Figure 8.10 we also show to result of a Franck-Condon analysis of the photo-induced absorption for both carotenoids. We presume equal FWHM for each peak and a single dominant vibrational mode.

In both cases the spectrum can be describe by the 0-0 and 0-1 of a Franck-Condon progression (details of Franck-Condon fit in Section 5.9.3). In agreement with this assignment, Balevicius *et al.*, have shown that the transient absorption spectrum is consistent with a vibronic progression from a single electronic state [153]. We assign this to S_1-S_n.
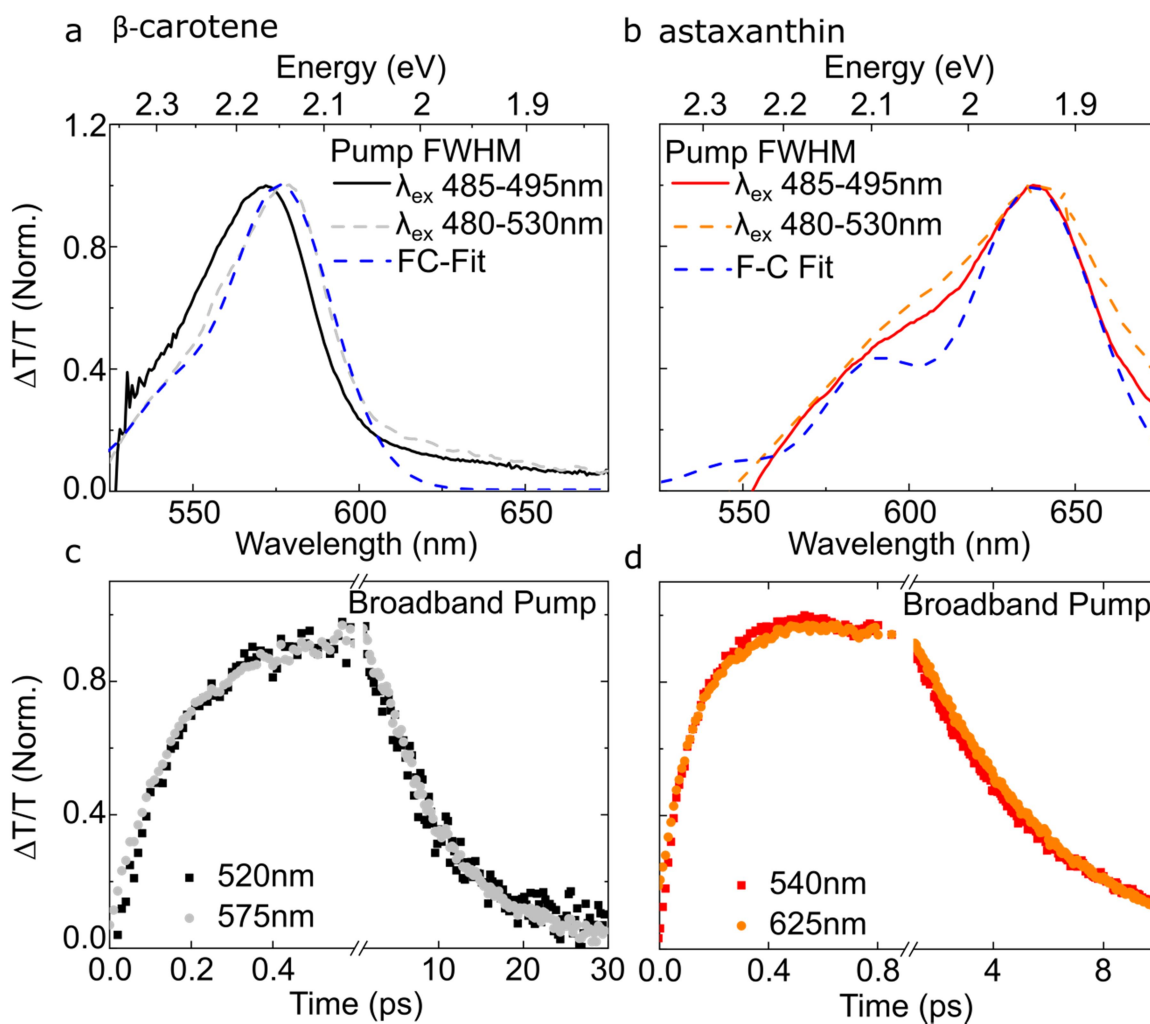
Figure 8.10: Narrowband versus broadband excitation transient absorption of carotenoids. (a, b) Transient absorption spectra of β-carotene (a), astaxanthin (b) averaged over 1-3ps after narrow and broadband excitation. The spectra have been normalised to the peak of the photo-induced absorption. Also included are Franck-Condon fits (blue dashed line) to the photo-induced absorption spectrum. Parameters of the fit are S = 0.32, 0-0 Energy = 2.145eV, Vibration = 130meV and σ = 55meV for β-carotene (a) and S = 0.342, 0-0 Energy = 1.945eV, Vibration = 160meV and σ = 55meV for astaxanthin (b). (c, d) Transient absorption kinetics of β-carotene (c), astaxanthin (d) taken after broadband excitation (480-530nm). Kinetics were taken in the S_1 and proposed S* PIA regions (10nm window around the peak averaged), and normalised for comparison.

Appendix L - Summary of Kinetic fit parameters (Carotenoids)

Kinetic parameters used to fit the kinetics throughout Chapter 6. In each case the range of possible values for the decay constant are given that return a reasonable fit to the data. We observe no emission or intersystem crossing suggesting we can approximate $K_{nr} \sim \tau$.

Sample	$^1A_1$ (%)	τ_1 (ps)	$^1A_2$ (%)	τ_2 (ps)	^{2}Zero Offset (%)
Monomer					
β-carotene (Band-Edge)	100	9.6±2	--------	--------	0
β-carotene (High-Energy)	52.8	9.6±2	47.2	95±25	0
Astaxanthin (Band-Edge)	100	5.3±1	--------	--------	0
Astaxanthin (High-Energy)	73.6	5.3±1	36.4	45±15	0
Echinenone (Band-Edge)	100	6.4±1	--------	--------	0
Echinenone (High-Energy)	83.5	6.4±1	16.5	41±10	0
Spheroidenone (Band-Edge)	100	7.2±0.4	--------	--------	0
Spheroidenone (High-Energy)	66.9	7.2±0.4	70.1	80±20	0
Protein-bound aggregates					
β-carotene	52.1	15±5	36.3	125±50	11.5
Astaxanthin	52.1	15±5	36.3	125±50	11.5
Echinenone	52.1	15±5	36.3	125±50	11.5
ns-TA					
Astaxanthin	28.5	1.7±0.7ns	71.4	1.4±0.2μs	0

[1] Kinetic fits were locked to start at peak intensity as convolution with the IRF causes the decay to begin after time zero (~0.5ps). As such Amplitude values are given as percentages of the total intensity, as described in Ref[325]. This produces a source of error however the same procedure has been used to fit all oligomer kinetics.

[2] Zero offset is given as a percent of the maximum intensity

Appendix M - Simulation of Aggregate Structures
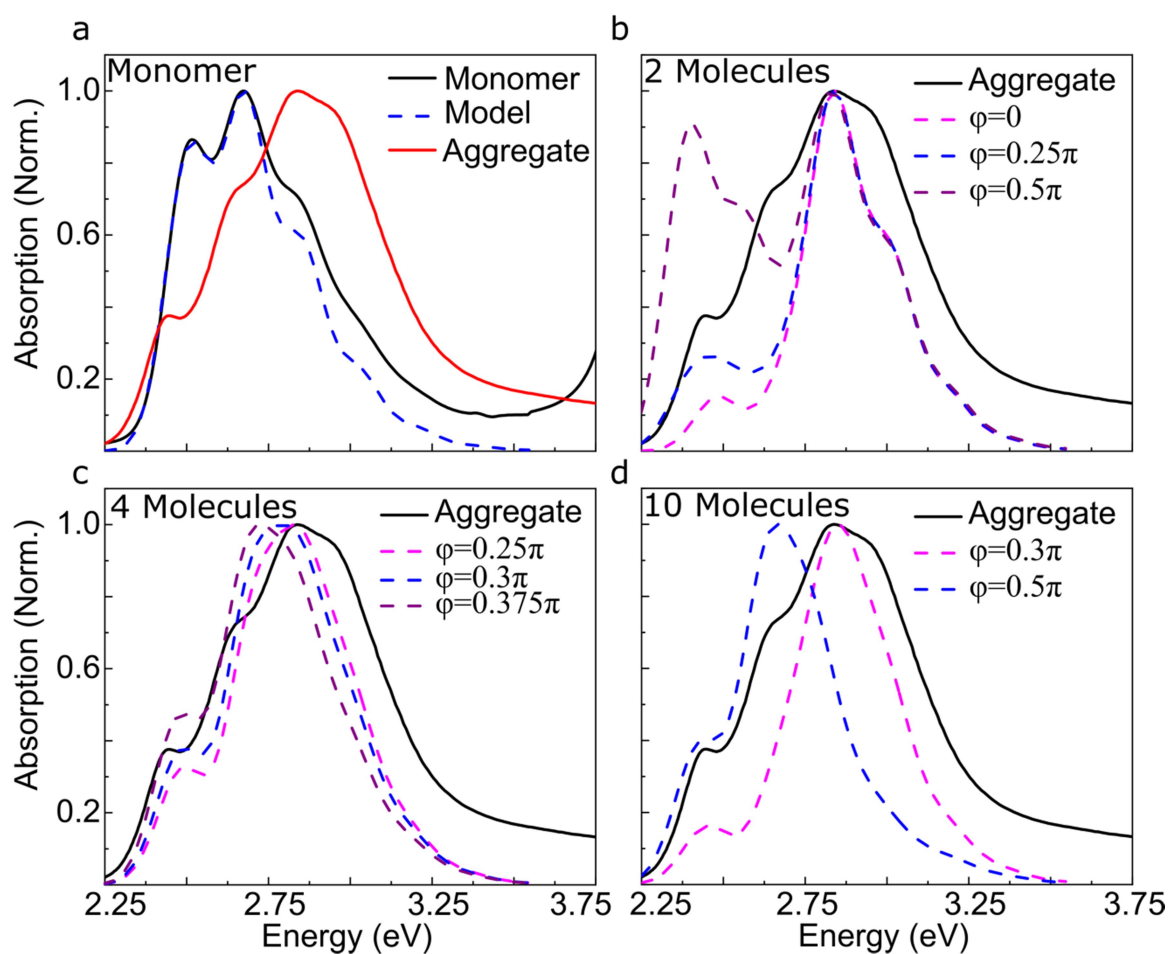
Figure 8.11: Simulation of β-carotene aggregate absorption spectrum. (a) Comparison between monomer and aggregate ground state absorption spectra. We include a Franck-Condon fit to the monomer absorption spectrum with the following parameters: ω_{0-0}=20,204cm^{-1}, Vibration spacing (Vib) = 1400cm^{-1}, Huang-Rhys = 1.09, Broadening = 0.57Vib. Details of the fit are given in Section 5.9.3. (b,c,d) Results of the model constructed by Frank Spano (Temple University, USA), compared to the ground state absorption spectrum of a protein-bound aggregate of β-carotene. Details of the model are given in Chapter 2 and Chapter 6. (b) Model considering a dimer of carotenoids molecules, with nearest neighbour coupling of 1200cm^{-1} and a varied relative angle of 0-0.5π. (c) Model considering a tetramer of carotenoid molecules, with nearest neighbour coupling of 900cm^{-1} and a varied relative angle of 0.25-0.375π. (d) Model considering 10 carotenoid molecules, with nearest neighbour coupling of 1400cm^{-1} and a varied relative angle of 0.3-0.5π.

9. References

1.   Ren21. *Renewables 2019 Global Status Report*. (Renewables Now, 2019).

2.   Allen, M. . *et al. Global Warming of 1.5°C. An IPCC Special Report on the impacts of global warming of 1.5°C above pre-industrial levels and related global greenhouse gas emission pathways, in the context of strengthening the global response to the threat of climate change,*. (2018).

3.   Mckay, D. J. C. *Sustainable energy - Without the hot air*. (Free Online, 2009).

4.   NREL. *NREL Efficiency Chart*. (U.S Department of Energy, 2019).

5.   Shockley, W. & Queisser, H. J. Detailed balance limit of efficiency of p-n junction solar cells. *J. Appl. Phys.* **32**, 510–519 (1960).

6.   Akshay, R. & Friend, H. R. Harnessing singlet exciton fission to break the Shockley–Queisser limit. *Nat. Rev. Mater.* **2**, 1–12 (2017).

7.   Ehrler, B., Wilson, M. W. B., Rao, A., Friend, R. H. & Greenham, N. C. Singlet exciton fission-sensitized infrared quantum dot solar cells. *Nano Lett.* **12**, 1053–1057 (2012).

8.   Congreve, D. N. N. *et al.* External quantum efficiency above 100% in a singlet-exciton-fission-based organic photovoltaic cell. .*Science* **340**, 334–337 (2013).

9.   Smith, M. B. & Michl, J. Recent Advances in Singlet Fission. *Annu. Rev. Phys. Chem.* **64**, 361–386 (2013).

10.   Smith, M. B. & Michl, J. Singlet fission. *Chem. Rev.* **110**, 6891–6936 (2010).

11.   Hanna, M. C. C. & Nozik, A. J. J. Solar conversion efficiency of photovoltaic and photoelectrolysis cells with carrier multiplication absorbers. *J. Appl. Phys.* **100**, (2006).

12.   Weiss, L. R. *et al.* Strongly exchange-coupled triplet pairs in an organic semiconductor. *Nat. Phys.* **13**, 176–181 (2017).

13.   Stern, H. L. *et al.* Vibronically coherent ultrafast triplet-pair formation and subsequent thermally activated dissociation control efficient endothermic singlet fission. *Nat. Chem.* **9**, 1205–1212 (2017).

14.   Stern, H. L. *et al.* Identification of a triplet pair intermediate in singlet exciton fission in solution. *Proc. Natl. Acad. Sci.* **112**, 7656–7661 (2015).

15.   Tayebjee, M. J. Y. *et al.* Quintet multiexciton dynamics in singlet fission. *Nat. Phys.* **13**, 182–188 (2017).

16.   Lukman, S. *et al.* Tuning the role of charge-transfer states in intramolecular singlet exciton fission through side-group engineering. *Nat. Commun.* **7**, 1–13 (2016).

17.   Wilson, M. W. B. *et al.* Ultrafast dynamics of exciton fission in polycrystalline pentacene. *J. Am. Chem. Soc.* **133**, 11830–11833 (2011).

18.   Korovina, N. V. *et al.* Singlet Fission in a Covalently Linked Cofacial Alkynyltetracene Dimer. *J. Am. Chem. Soc.* **138**, 617–627 (2016).

19.   Wilson, M. W. B. *et al.* Temperature-Independent Singlet Exciton Fission in Tetracene. *J. Am. Chem. Soc.* **135**, 16680–16688 (2013).

20.   Davis, N. J. L. K. *et al.* Singlet Fission and Triplet Transfer to PbS Quantum Dots in TIPS-Tetracene Carboxylic Acid Ligands. *J. Phys. Chem. Lett.* **9**, 1454–1460 (2018).

21.   Chan, W., Tritsch, J. R. & Zhu, X. Harvesting Singlet Fission for Solar Energy Conversion : One-versus Two-Electron Transfer from the Quantum Mechanical Superposition. *J. Am. Chem. Soc.* **134**, 18295–18302 (2012).

22.   Yost, S. R. *et al.* A transferable model for singlet-fission kinetics. *Nat. Chem.* **6**, 492–497 (2014).

23.   Wang, C. & Tauber, M. J. High-yield singlet fission in a zeaxanthin aggregate observed by picosecond resonance Raman spectroscopy. *J. Am. Chem. Soc.* **132**, 13988–13991 (2010).

24.   Wang, C., Angelella, M., Kuo, C.-H. & Tauber, M. J. Singlet fission in carotenoid aggregates: insights from transient absorption spectroscopy. *Phys. Chem. Interfaces Nanomater. XI* **8459**, 845905 (2012).

25.   Musser, A. J. *et al.* The nature of singlet exciton fission in carotenoid aggregates. *J. Am. Chem. Soc.* **137**, 5130–5139 (2015).

26.   Chang, H. T. *et al.* Singlet Fission Reaction of Light-Exposed β-Carotene Bound to Bovine Serum Albumin. A Novel Mechanism in Protection of Light-Exposed Tissue by Dietary Carotenoids. *J. Agric. Food Chem.* **65**, 6058–6062 (2017).

27.   Musser, A. J. *et al.* Activated singlet exciton fission in a semiconducting polymer. *J. Am. Chem. Soc.* **135**, 12747–12754 (2013).

28. Lanzani, G. *et al.* Triplet exciton generation and decay in a red polydiacetylene studied by femtosecond spectroscopy. *Chem. Phys. Lett.* **313**, 525–532 (1999).

29. Lanzani, G. *et al.* Triplet-exciton generation mechanism in a new soluble (red-phase) polydiacetylene. *Phys. Rev. Lett.* **87**, 1–4 (2001).

30. Kraabel, B., Hulin, D., Aslangul, C., Lapersonne-Meyer, C. & Schott, M. Triplet exciton generation, transport and relaxation in isolated polydiacetylene chains: Subpicosecond pump-probe experiments. *Chem. Phys.* **227**, 83–98 (1998).

31. Lukman, S. *et al.* Efficient Singlet Fission and Triplet-Pair Emission in a Family of Zethrene Diradicaloids. *J. Am. Chem. Soc.* **139**, 18376–18385 (2017).

32. Hashimoto, H., Uragami, C., Yukihira, N., Gardiner, A. T. & Cogdell, R. J. Understanding/unravelling carotenoid excited singlet states. *J. R. Soc. Interface* **15**, (2018).

33. Miyata, K., Conrad-burton, F. S., Geyer, F. L. & Zhu, X. Triplet Pair States in Singlet Fission. *Chem. Rev.* **119**, 4261–4292 (2019).

34. Musser, A. & Clark, J. Triplet Pair States in organic semiconductors. *Annu. Rev. Phys. Chem.* **70**, (2019).

35. Sanders, S. N. *et al.* Understanding the Bound Triplet-Pair State in Singlet Fission. *CHEM Rev.* 1–18 (2019) doi:10.1016/j.chempr.2019.05.012.

36. Fiedor, L., Dudkowiak, A. & Pilch, M. The origin of the dark S 1 state in carotenoids : a comprehensive model. *J. R. Soc. Interface* **16**, 20190191 (2019).

37. Datko, B. D. *et al.* Unravelling the enigma of ultrafast excited state relaxation in non-emissive aggregating conjugated polymers. *Phys. Chem. Chem. Phys.* **20**, 22159–22167 (2018).

38. Datko, B. D. *et al.* Large Excited-State Conformational Displacements Expedite Triplet Formation in a Small Conjugated Oligomer. *J. Phys. Chem. Lett.* **10**, 1259–1263 (2019).

39. Polívka, T. & Sundström, V. Dark excited states of carotenoids: Consensus and controversy. *Chem. Phys. Lett.* **477**, 1–11 (2009).

40. A. Kohler, H. B. *Electronic Processes in Organic Semiconductors: An Introduction*. (Wiley-VCH, 2015).

41. NJ. Turro, V.Ramamurthy, JC. Scaiano, D. *Modern Molecular Photohemistry Of Organic Molecules*. (University Science Books, 2010).

42.   W. Barford. *Electronic and Optical Properties of Conjugated Polymers*. (Oxford University Press, 2009).

43.   Barford, W., Bursill, R. J. & Lavrentiev, M. Y. Density-matrix renormalization-group calculations of excited states of linear polyenes. *Phys. Rev. B - Condens. Matter Mater. Phys.* **63**, 1–8 (2001).

44.   Lim, S.-H., Bjorklund, T. G., Spano, F. C. & Bardeen, C. J. Exciton Delocalization and Superradiance in Tetracene Thin Films and Nanoaggregates. *Phys. Rev. Lett.* **92**, 10–13 (2004).

45.   Scholes, G. D. & Rumbles, G. Excitons in nanoscale systems. *Nat. Mater.* **9**, 683–696 (2012).

46.   Laquai, F., Park, Y. S., Kim, J. J. & Basché, T. Excitation energy transfer in organic materials: From fundamentals to optoelectronic devices. *Macromol. Rapid Commun.* **30**, 1203–1231 (2009).

47.   M. Pope, CE. Swenberg. *Electronic Processes in Organic Crystals and Polymers*. (Oxford University Press, 1999).

48.   May, V. & Kuhn, O. *Charge and Energy Transfer Dynamics in Molecular Systems*. (Wiley-VCH, 2004).

49.   Tavan, P. & Schulten, K. Electronic excitations in finite and infinite polyenes. *Physical Review B* vol. 36 4337–4358 (1987).

50.   Farmany, A., Abbasi, S. & Naghipour, A. Probing the natural broadening of hydrogen atom spectrum based on the minimal length uncertainty. *Phys. Lett. Sect. B Nucl. Elem. Part. High-Energy Phys.* **650**, 33–35 (2007).

51.   Köhler, A. & Bässler, H. Triplet states in organic semiconductors. *Mater. Sci. Eng. R Reports* **66**, 71–109 (2009).

52.   Chynwat, V. & Frank, H. A. The application of the energy gap law to the S1 energies and dynamics of carotenoids. *Chem. Phys.* **194**, 237–244 (1995).

53.   Penfold, T. J., Gindensperger, E., Daniel, C. & Marian, C. M. Spin-Vibronic Mechanism for Intersystem Crossing. *Chem. Rev.* **118**, 6975–7025 (2018).

54.   Liebel, M., Schnedermann, C. & Kukura, P. Vibrationally coherent crossing and coupling of electronic states during internal conversion in β-carotene. *Phys. Rev. Lett.* **112**, 1–5 (2014).

55.   Oliver, T. A. A. & Fleming, G. R. Following Coupled Electronic-Nuclear Motion through Conical

Intersections in the Ultrafast Relaxation of β-Apo-8'-carotenal. *J. Phys. Chem. B* **119**, 11428–11441 (2015).

56. Olivucci, M., Ragazos, I. N., Bernadi, F. & Robb, M. A. A Conical Intersection Mechanism for the Photochemistry of Butadiene. A MC-SCF Study. *J. Am. Chem. Soc.* 3710–3721 (1993).

57. Schapiro, I., Melaccio, F., Laricheva, N. & Olivucci, M. Using the computer to understand the chemistry of conical intersections. *Photochem. Photobiol. Sci.* **10**, 867–886 (2011).

58. Xu, B. & Holdcroft, S. First observation of phosphorescence from pi-conjugated polymers. *J. Am. Chem. Soc.* **115**, 8447–8448 (1993).

59. McGlynn, S. P., Sltnseri, R. & Christodouleas, N. External heavy-atom spin-orbital coupling effect. I. The nature of the interaction. *J. Chem. Phys.* **37**, 1818–1824 (1962).

60. McGlynn, S. P., Daigre, J. & Smith, F. J. External heavy-atom spin-orbital coupling effect. IV. Intersystem crossing. *J. Chem. Phys.* **39**, 675–679 (1963).

61. Zobel, J. P., Nogueira, J. J. & González, L. Mechanism of Ultrafast Intersystem Crossing in 2-Nitronaphthalene. *Chem. - A Eur. J.* **24**, 5379–5387 (2018).

62. El-Sayed, M. A., Moomaw, W. R. & Chodak, J. B. The mechanism of the S1 ⤳ Tx intersystem crossing process in aromatic hydrocarbons from PMDR. *Chem. Phys. Lett.* **20**, 11–16 (1973).

63. El-Sayed, M. A. Spin-orbit coupling and the radiationless processes in nitrogen heterocyclics. *J. Chem. Phys.* **38**, 2834–2838 (1963).

64. Kölle, P., Schnappinger, T. & De Vivie-Riedle, R. Deactivation pathways of thiophene and oligothiophenes: Internal conversion versus intersystem crossing. *Phys. Chem. Chem. Phys.* **18**, 7903–7915 (2016).

65. KASHA, M. Energy Transfer Mechanisms and the Molecular Exciton Model for Molecular Aggregates. *Radiat. Res.* **20**, 55–70 (1963).

66. Kasha, M., Rawls, H. R. & Ashraf El-Bayoumi, M. The exciton model in molecular spectroscopy. *Pure Appl. Chem.* **11**, 371–392 (1965).

67. Forster, T. & Kasper, K. Ein Konzentrationsumschulag der Fluoreszenz. *Elektrochem* **59**, (1955).

68. Birks, J. B. & Christophorou, L. G. Excimer fluorescence spectra of pyrene derivatives. *Spectrochim. Acta* **19**, 401–410 (1963).

69. Hestand, N. J. & Spano, F. C. Expanded Theory of H- and J-Molecular Aggregates: The Effects of Vibronic Coupling and Intermolecular Charge Transfer. *Chem. Rev.* **118**, 7069–7163 (2018).

70. Spano, F. C. & Silva, C. H- and J-Aggregate Behavior in Polymeric Semiconductors. *Annu. Rev. Phys. Chem.* **65**, 477–500 (2014).

71. Spano, F. C. & Introduction, I. The Spectral Signatures of Frenkel Polarons in H and J Aggregates. *Acc. Chem. Res.* **43**, 429–439 (2010).

72. Spano, F. C. Modeling disorder in polymer aggregates: The optical spectroscopy of regioregular poly(3-hexylthiophene) thin films. *J. Chem. Phys.* **122**, (2005).

73. Köhler, A. & Bässler, H. Triplet states in organic semiconductors. *Mater. Sci. Eng. R Reports* **66**, 71–109 (2009).

74. R.C.Johnson, R.E.Merrifield & P.Avakian, and R. B. F. Effects of Magnetic Fields on the Mutual Annihilation of Triplet Excitons in Molecular Crystals. *Phys. Rev. Lett.* **19**, 285–288 (1967).

75. Johnson, R. C. & Merrifield, R. E. Effects of magnetic fields on the mutual annihilation of triplet excitons in anthracene crystals. *Phys. Rev. B* **1**, 896–902 (1970).

76. Casanova, D. Theoretical Modeling of Singlet Fission. *Chem. Rev.* **118**, 7164–7207 (2018).

77. Scholes, G. D. Correlated Pair States Formed by Singlet Fission and Exciton-Exciton Annihilation. *J. Phys. Chem. A* **119**, 12699–12705 (2015).

78. Burdett, J. J., Piland, G. B. & Bardeen, C. J. Magnetic field effects and the role of spin states in singlet fission. *Chem. Phys. Lett.* **585**, 1–10 (2013).

79. Kollmar, C. Electronic structure of diradical and dicarbene intermediates in short-chain polydiacetylene oligomers. *J. Chem. Phys.* **98**, 7210–7228 (1993).

80. Merrifield, R. E. E. Magnetic effects on triplet exciton interactions. *Pure Appl. Chem.* **27**, 481–498 (1971).

81. Merrifield, R. E. Theory of Magnetic Field Effects on the Mutual Annihilation of Triplet Excitons. *J. Chem. Phys.* **48**, 4318–4319 (1968).

82. Merrifield, R., Avakian, P. & Groff, R. . Fission of singlet excitons into pairs of triplet excitons in tetracene crystals. *Chem. Phys. Lett.* **3**, 5–7 (1969).

83. Geacintov, N., Pope, M. & Vogel, F. Effect of magnetic field on the fluorescence of tetracene crystals: exciton fission. *Phys. Rev. Lett.* **22**, 593–596 (1969).

84.	Paci, I. *et al.* Singlet Fission for Dye-Sensitized Solar Cells: Can a Suitable Sensitizer Be Found? *J. Am. Chem. Soc.* **128**, 16546–16553 (2006).

85.	Greyson, E. C., Vura-Weis, J., Michl, J. & Ratner, M. A. Maximizing Singlet Fission in Organic Dimers: Theoretical Investigation of Triplet Yield in the Regime of Localized Excitation and Fast Coherent Electron Transfer. *J. Phys. Chem. B* **114**, 14168–14177 (2010).

86.	Greyson, E. C. *et al.* Singlet exciton fission for solar cell applications: Energy aspects of interchromophore coupling. *J. Phys. Chem. B* **114**, 14223–14232 (2010).

87.	Reusswig, P. D., Congreve, D. N., Thompson, N. J. & Baldo, M. A. Enhanced external quantum efficiency in an organic photovoltaic cell via singlet fission exciton sensitizer. *Appl. Phys. Lett.* **101**, (2012).

88.	Lee, J. *et al.* Singlet exciton fission photovoltaics. *Acc. Chem. Res.* **46**, 1300–1311 (2013).

89.	Tabachnyk, M. *et al.* Resonant energy transfer of triplet excitons from pentacene to PbSe nanocrystals. *Nat. Mater.* **13**, 1033–1038 (2014).

90.	Ehrler, B., Musselman, K. P., Böhm, M. L., Friend, R. H. & Greenham, N. C. Hybrid pentacene/a-silicon solar cells utilizing multiple carrier generation via singlet exciton fission. *Appl. Phys. Lett.* **101**, 1–4 (2012).

91.	Ehrler, B. *et al.* In situ measurement of exciton energy in hybrid singlet-fission solar cells. *Nat. Commun.* **3**, 1019 (2012).

92.	Thompson, N. J. J. *et al.* Energy harvesting of non-emissive triplet excitons in tetracene by emissive PbS nanocrystals. *Interdiscip. Toxicol.* **11**, 1039–1043 (2014).

93.	Bayliss, S. L. *et al.* Tuning Spin Dynamics in Crystalline Tetracene. *J. Phys. Chem. Lett* **10**, 1908–1913 (2019).

94.	Yong, C. K. K. *et al.* The entangled triplet pair state in acene and heteroacene materials. *Nat. Commun.* **8**, 15953 (2017).

95.	Bayliss, S. L. *et al.* Spin signatures of exchange-coupled triplet pairs formed by singlet fission. *Phys. Rev. B* **94**, 1–7 (2016).

96.	Bayliss, S. L. *et al.* Geminate and nongeminate recombination of triplet excitons formed by singlet fission. *Phys. Rev. Lett.* **112**, 1–5 (2014).

97.	Zimmerman, P. M., Bell, F., Casanova, D. & Head-Gordon, M. Mechanism for singlet fission in

pentacene and tetracene: From single exciton to two triplets. *J. Am. Chem. Soc.* **133**, 19944–19952 (2011).

98. Zimmerman, P. M., Zhang, Z. & Musgrave, C. B. Singlet fission in pentacene through multi-exciton quantum states. *Nat. Chem.* **2**, 648–652 (2010).

99. Zimmerman, P. M., Musgrave, C. B. & Head-Gordon, M. A correlated electron view of singlet fission. *Acc. Chem. Res.* **46**, 1339–1347 (2013).

100. Renaud, N., Sherratt, P. A. & Ratner, M. A. Mapping the relation between stacking geometries and singlet fission yield in a class of organic crystals. *J. Phys. Chem. Lett.* **4**, 1065–1069 (2013).

101. Chan, W. *et al.* Observing the Multiexciton State in Singlet Fission and Ensuing Ultrafast Multielectron Transfer. .*Science* **334**, 1541–1545 (2011).

102. Berkelbach, T. C., Hybertsen, M. S. & Reichman, D. R. Microscopic theory of singlet exciton fission. II. Application to pentacene dimers and the role of superexchange. *J. Chem. Phys.* **138**, 114103 (2013).

103. Berkelbach, T. C., Hybertsen, M. S. & Reichman, D. R. Microscopic theory of singlet exciton fission. I. General formulation. *J. Chem. Phys.* **138**, (2013).

104. Chan, W. L. *et al.* The quantum coherent mechanism for singlet fission: Experiment and theory. *Acc. Chem. Res.* **46**, 1321–1329 (2013).

105. Ramanan, C., Smeigh, A. L., Anthony, J. E., Marks, T. J. & Wasielewski, M. R. Competition between Singlet Fission and Charge Separation in Solution-Processed Blend Films of 6,13-Bis(triisopropylsilylethynyl)- pentacene with Sterically-Encumbered Perylene-3,4:9,10-bis(dicarboximide)s. *J. Am. Chem. Soc.* **134**, 386–397 (2011).

106. Thorsmølle, V. K. *et al.* Morphology effectively controls singlet-triplet exciton relaxation and charge transport in organic semiconductors. *Phys. Rev. Lett.* **102**, 3–6 (2009).

107. Tomkiewicz, Y., Groff, R. P. & Avakian, P. Spectroscopic Approach to Energetics of Exciton Fission and Fusion in Tetracene Crystals. *J. Chem. Phys.* **54**, 4504 (1971).

108. Hu, W. & Chan, G. K. L. Excited-State Geometry Optimization with the Density Matrix Renormalization Group, as Applied to Polyenes. *J. Chem. Theory Comput.* **11**, 3000–3009 (2015).

109. Rademaker, H., Hoff, A., Grondelle, R. & Duysens, L. Carotenoid triplet yields in normal and deuterated rhodospirillum Rubrum. *Biochim. Biophys. Acta - Bioenerg.* **2**, 240–257 (1980).

110. Llansola-Portoles, M. J., Pascal, A. A. & Robert, B. Electronic and vibrational properties of carotenoids: From in vitro to in vivo. *J. R. Soc. Interface* **14**, 1–12 (2017).

111. Kohler, B. E. Experimental determination of conjugation lengths in long polyene chains. *J. Chem. Phys.* **103**, 6248–6252 (1995).

112. Polívka, T. & Sundström, V. Ultrafast dynamics of carotenoid excited states-from solution to natural and artificial systems. *Chem. Rev.* **104**, 2021–2071 (2004).

113. Cogdell, R. J. *et al.* How carotenoids protect bacterial photosynthesis. *Philos. Trans. R. Soc. B Biol. Sci.* **355**, 1345–1349 (2000).

114. Kloz, M. *et al.* Carotenoid photoprotection in artificial photosynthetic antennas. *J. Am. Chem. Soc.* **133**, 7007–7015 (2011).

115. Demmig-Adams, B. et al. Carotenoids and photoprotection in plants: A role for the xanthophyll zeaxanthin. *Biochim. Biophys. Acta - Bioenerg.* **1020**, 1–24 (1990).

116. Frank, H. A. & Cogdeip, R. J. Carotenoids in Photosynthesis. *Photochem. Photobiol.* **63**, 257–264 (1996).

117. Niyogi, K. K., Björkman, O., Grossman, R., Bjorkman, O. & Grossman, A. R. The roles of specific xanthophylls in photoprotection. *Proc. Natl. Acad. Sci.* **94**, 14162–14167 (2002).

118. Johnson, G. N., Young, A. J., Scholes, J. D. & Horton, P. The dissipation of excess excitation energy in British plant species. *Plant. Cell Environ.* **16**, 673–679 (1993).

119. Cazzonelli, C. I. Carotenoids in nature: insights from plants and beyond. *Funct. Plant Biol.* **38**, 833 (2011).

120. A. Jeffrey. Whitehead, Julie. A. Mares, R. P. D. Macular Pigment. *Arch Ophthalmol* **124**, 1038–1045 (2006).

121. Schmidt, M. & Tavan, P. Electronic excitations in long polyenes revisited. *J. Chem. Phys.* **136**, (2012).

122. Larsen, D. S. *et al.* Excited state dynamics of β-carotene explored with dispersed multi-pulse transient absorption. *Chem. Phys. Lett.* **381**, 733–742 (2003).

123. Kosumi, D., Yanagi, K., Fujii, R., Hashimoto, H. & Yoshizawa, M. Conjugation length dependence of relaxation kinetics in β-carotene homologs probed by femtosecond Kerr-gate fluorescence spectroscopy. *Chem. Phys. Lett.* **425**, 66–70 (2006).

124. Polli, D. *et al.* Conjugation Length Dependence of Internal Conversion in Carotenoids: Role of the Intermediate State. *Phys. Rev. Lett.* **93**, 1–4 (2004).

125. Wohlleben, W. *et al.* Pump-deplete-probe spectroscopy and the puzzle of carotenoid dark states. *j. Phys. Chem. B* **108**, 3320–3325 (2004).

126. Papagiannakis, E., Kennis, J. T. M., van Stokkum, I. H. M., Cogdell, R. J. & van Grondelle, R. An alternative carotenoid-to-bacteriochlorophyll energy transfer pathway in photosynthetic light harvesting. *Proc. Natl. Acad. Sci. U. S. A.* **99**, 6017–6022 (2002).

127. Papagiannakis, E. *et al.* Light harvesting by carotenoids incorporated into the B850 light-harvesting complex from Rhodobacter sphaeroides R-26.1: Excited-state relaxation, ultrafast triplet formation, and energy transfer to bacteriochlorophyll. *J. Phys. Chem. B* **107**, 5642–5649 (2003).

128. Beck, W. F., Bishop, M. M., Roscioli, J. D., Ghosh, S. & Frank, H. A. Excited state conformational dynamics in carotenoids: Dark intermediates and excitation energy transfer. *Arch. Biochem. Biophys.* **572**, 175–183 (2015).

129. Andersson, P. O., Bachilo, S. M., Chen, R. L. & Gillbro, T. Solvent and temperature effects on dual fluorescence in a series of carotenes. Energy gap dependence of the internal conversion rate. *J. Phys. Chem.* **99**, 16199–16209 (1995).

130. Fujii, R., Onaka, K., Kuki, M., Koyama, Y. & Watanabe, Y. The 2Ag-energies of all-trans-neurosporene and spheroidene as determined by fluorescence spectroscopy. *Chem. Phys. Lett.* **288**, 847–853 (1998).

131. Fujii, R. *et al.* Fluorescence spectroscopy of all-trans-anhydrorhodovibrin and spirilloxanthin: Detection of the 1Bu- fluorescence. *J. Phys. Chem. A* **105**, 5348–5355 (2001).

132. Mimuro, M. *et al.* Molecular structure and optical properties of carotenoids for the in vivo energy transfer function in the algal photosynthetic pigment system. *BBA - Bioenerg.* **1098**, 271–274 (1992).

133. Zigmantas, D., Polfvka, T., Killer, R. G., Yartsev, A. & Sundstrom, V. Spectroscopic and dynamic properties of the peridinin lowest singlet excited states. *J. Phys. Chem. A* **105**, 10296–10306 (2001).

134. Frank, H. A., Bautista, J. A., Josue, J. S. & Young, A. J. Mechanism of nonphotochemical quenching in green plants: Energies of the lowest excited singlet states of violaxanthin and zeaxanthin. *Biochemistry* **39**, 2831–2837 (2000).

135. Frank, H. A. *et al.* Spectroscopic and photochemical properties of open-chain carotenoids. *J. Phys. Chem. B* **106**, 2083–2092 (2002).

136. Chadwick, R. R., Zgierski, M. Z. & Hudson, B. S. Resonance Raman scattering of butadiene: Vibronic activity of a Bu mode demonstrates the presence of a 1Ag symmetry excited electronic state at low energy. *J. Chem. Phys.* **95**, 7204–7211 (1991).

137. Buma, W. J., Kohler, B. E. & Song, K. Lowest energy excited singlet state of isolated cis-hexatriene. *J. Chem. Phys.* **94**, 6367–6376 (1991).

138. Gavin, R. M., Weisman, C., McVey, J. K. & Rice, S. A. Spectroscopic properties of polyenes. III. 1,3,5,7-Octatetraene. *J. Chem. Phys.* **68**, 522–529 (1978).

139. Christensen, R. L. *et al.* Energies of Low-Lying Excited States of Linear Polyenes. *J. Phys. Chem.* **112**, 12629–12636 (2008).

140. Bachilo, S. M. M. & Gilibro, T. β-carotene S1 fluorescence. *Spie* **2370**, 719–723 (1994).

141. Gillbro, T. & Cogdell, R. J. Carotenoid Fluorescence. *Chem. Phys. Lett.* **158**, 312–316 (1989).

142. Frank, H. A. A. *et al.* Spectroscopic properties of spheroidene analogs having different extents of π-electron conjugation. *J. Phys. Chem. A* **101**, 149–157 (1997).

143. Gradinaru, C. C. C. *et al.* An unusual pathway of excitation energy deactivation in carotenoids: Singlet-to-triplet conversion on an ultrafast timescale in a photosynthetic antenna. *Proc. Natl. Acad. Sci.* **98**, 2364–2369 (2002).

144. Papagiannakis, E. *et al.* Excited-state dynamics of carotenoids in light-harvesting complexes. 1. Exploring the relationship between the S1 and S* states. *J. Phys. Chem. B* **110**, 5727–5736 (2006).

145. Niedzwiedzki, D. M. & Blankenship, R. E. Nature of the S* excited electronic state of carotenoids in light harvesting complexes from purple photosynthetic bacteria. *J. Phys. Chem. B* **120**, 11123–11131 (2016).

146. Jailaubekov, A. E., Song, S. H., Vengris, M., Cogdell, R. J. & Larsen, D. S. Using narrowband excitation to confirm that the S* state in carotenoids is not a vibrationally-excited ground state species. *Chem. Phys. Lett.* **487**, 101–107 (2010).

147. Billsten, H. H. *et al.* Excited-state processes in the carotenoid zeaxanthin after excess energy excitation. *J. Phys. Chem. A* **109**, 6852–6859 (2005).

148. Cong, H. *et al.* Ultrafast time-resolved carotenoid to-bacteriochlorophyll energy transfer in LH2 complexes from photosynthetic bacteria. *J. Phys. Chem. B* **112**, 10689–10703 (2008).

149. Niedzwiedzki, D. M., Sullivan, J. O., Polívka, T., Birge, R. R. & Frank, H. A. Femtosecond time-resolved transient absorption spectroscopy of xanthophylls. *J. Phys. Chem. B* **110**, 22872–22885 (2006).

150. Ostroumov, E. E., Müller, M. G., Reus, M. & Holzwarth, A. R. On the nature of the 'dark S*' excited state of β-carotene. *J. Phys. Chem. A* **115**, 3698–3712 (2011).

151. Zechmeister, L. Cis-trans isomerization and stereochemistry of carotenoids and diphenyl-polyenes. *Chem. Rev.* **34**, 267–344 (1944).

152. Pesek, C. A., Warthesen, J. J. & Taoukis, P. S. A Kinetic Model for Equilibration of Isomeric β-Carotenes. *J. Agric. Food Chem.* **38**, 41–45 (1990).

153. Balevicius Jr., V. *et al.* Vibronic energy relaxation approach highlighting deactivation pathways in carotenoids. *Phys. Chem. Chem. Phys.* **4**, 1166–1169 (2015).

154. Hofling, S. *et al.* An electrically pumped polariton laser. *Nature* **497**, 348–352 (2013).

155. Deng, H., Weihs, G., Snoke, D., Bloch, J. & Yamamoto, Y. Polariton lasing vs. photon lasing in a semiconductor microcavity. **100**, 1603–1606 (2003).

156. Langoudakis, K. *The Physics of Exciton Polariton Condensates*. (EPFL Press, 2013).

157. Kavokin, A., Baumberg, J., Malpuech, G. & Laussy, F. *Microcavities*. (Oxford Science Publications, 2007).

158. Grant, R. T. *et al.* Efficient Radiative Pumping of Polaritons in a Strongly Coupled Microcavity by a Fluorescent Molecular Dye. *Adv. Opt. Mater.* **4**, 1615–1623 (2016).

159. Anand, N. & Mohapatra, A. Simulation of two-level quantum system using classical coupled oscillators. *Natl. Inst. Sci.* 1–11.

160. Coles, D. M. *et al.* Vibrationally assisted polariton-relaxation processes in strongly coupled organic-semiconductor microcavities. *Adv. Funct. Mater.* **21**, 3691–3696 (2011).

161. Hutchison, J. A., Schwartz, T., Genet, C., Devaux, E. & Ebbesen, T. W. Modifying chemical landscapes by coupling to vacuum fields. *Angew. Chemie - Int. Ed.* **51**, 1592–1596 (2012).

162. George, J. *et al.* Ultra-strong coupling of molecular materials: Spectroscopy and dynamics. *Faraday Discuss.* **178**, 281–294 (2015).

163. Michetti, P. & La Rocca, G. C. Exciton-phonon scattering and photoexcitation dynamics in J-aggregate microcavities. *Phys. Rev. B - Condens. Matter Mater. Phys.* **79**, 1–6 (2009).

164. Michetti, P. & La Rocca, G. C. Simulation of J-aggregate microcavity photoluminescence. *Phys. Rev. B - Condens. Matter Mater. Phys.* **77**, 1–11 (2008).

165. Litinskaya, M. & Reineker, P. Loss of coherence of exciton polaritons in inhomogeneous organic microcavities. *Phys. Rev. B - Condens. Matter Mater. Phys.* **74**, 1–11 (2006).

166. Agranovich, V. M., Litinskaia, M. & Lidzey, D. G. Cavity polaritons in microcavities containing disordered organic semiconductors. *Phys. Rev. B - Condens. Matter Mater. Phys.* **67**, 1–10 (2003).

167. Agranovich, V. M. & Gartstein, Y. N. Nature and dynamics of low-energy exciton polaritons in semiconductor microcavities. *Phys. Rev. B - Condens. Matter Mater. Phys.* **75**, 1–7 (2007).

168. Virgili, T. *et al.* Ultra-fast polariton dynamics in an organic microcavity. *EPJ Web Conf.* **41**, 04015 (2013).

169. Grant, R. T. R. T. *et al.* Strong coupling in a microcavity containing β-carotene. *Opt. Express* **26**, 3320 (2018).

170. Cookson, T. *et al.* A Yellow Polariton Condensate in a Dye Filled Microcavity. *Adv. Opt. Mater.* **5**, 1700203 (2017).

171. Coles, D. M., Michetti, P., Clark, C., Adawi, A. M. & Lidzey, D. G. Temperature dependence of the upper-branch polariton population in an organic semiconductor microcavity. *Phys. Rev. B* **84**, 205214 (2011).

172. Lidzey, D. G. *et al.* Experimental study of light emission from strongly coupled organic semiconductor microcavities following nonresonant laser excitation. *Phys. Rev. B - Condens. Matter Mater. Phys.* **65**, 1953121–19531210 (2002).

173. Tassone, F., Piermarocchi, C., Savona, V., Quattropani, A. & Schwendimann, P. Photoluminescence decay times in strong-coupling semiconductor microcavities. *Phys. Rev. B - Condens. Matter Mater. Phys.* **53**, R7642–R7645 (1996).

174. Schwartz, T. *et al.* Polariton dynamics under strong light-molecule coupling. *ChemPhysChem* **14**, 125–131 (2013).

175. Tassone, F., Piermarocchi, C., Savona, V. & Quattropani, A. Bottleneck effects in the relaxation and photoluminescence of microcavity polaritons. *Phys. Rev. B - Condens. Matter*

Mater. Phys. **56**, 7554–7563 (1997).

176.   Ebbesen, T. W. Hybrid Light–Matter States in a Molecular and Material Science Perspective. *Acc. Chem. Res.* **49**, 2403–2412 (2016).

177.   Ballarini, D. *et al.* Polariton-Induced Enhanced Emission from an Organic Dye under the Strong Coupling Regime. *Adv. Opt. Mater.* **2**, 1076–1081 (2014).

178.   Chi, S. C. *et al.* Assembly of functional photosystem complexes in Rhodobacter sphaeroides incorporating carotenoids from the spirilloxanthin pathway. *Biochim. Biophys. Acta - Bioenerg.* **1847**, 189–201 (2015).

179.   Apperloo, J. J., Martineau, C., Van Hal, P. A., Roncali, J. & Janssen, R. A. J. Intra- and intermolecular photoinduced energy and electron transfer between oligothienylenevinylenes and N-methylfulleropyrrolidine. *J. Phys. Chem. A* **106**, 21–31 (2002).

180.   Ono, N., Okumura, H. & Murashima, T. Synthesis of Oligo(thienylenevinylenes) substituted with Alkoxy groups. *Heteroat. Chem.* **12**, 414–417 (2001).

181.   Elandaloussi, E. H. *et al.* Effect of chain extension on the electrochemical and electronic properties of π-conjugated soluble thienylenevinylene oligomers. *J. Am. Chem. Soc.* **119**, 10774–10784 (1997).

182.   Jestin, I. *et al.* Synthesis and characterization of the electronic and electrochemical properties of thienylenevinylene oligomers with multinanometer dimensions. *J. Am. Chem. Soc.* **120**, 8150–8158 (1998).

183.   Roncali, J. Oligothienylenevinylenes as a new class of multinanometer linear π- conjugated systems for micro- and nanoelectronics. *Acc. Chem. Res.* **33**, 147–156 (2000).

184.   Karpicz, R. *et al.* Exciton dynamics in an energy up-converting solid state system based on diphenylanthracene doped with platinum octaethylporphyrin. *Chem. Phys.* **429**, 57–62 (2014).

185.   Islangulov, R. R., Lott, J., Weder, C. & Castellano, F. N. Noncoherent low-power upconversion in solid polymer films. *J. Am. Chem. Soc.* **129**, 12652–12653 (2007).

186.   Polak, D. *et al.* Manipulating matter with strong coupling harvesting triplet excitons in organic exciton microcavities. *arXiv* (2019).

187.   Odom, S. A., Parkin, S. R. & Anthony, J. E. Tetracene Derivatives as Potential Red Emitters for Organic LEDs. *Org. Lett.* **5**, 4245–4248 (2003).

188. Lu, L., Wu, J., Wei, L. & Fang, W. Temperature dependence of aggregated structure of β-carotene by absorption spectral experiment and simulation. *Spectrochim. Acta - Part A Mol. Biomol. Spectrosc.* **169**, 116–121 (2016).

189. Buchwald, M. & Jencks, W. P. Optical Properties of Astaxanthin Solutions and Aggregates. *Biochemistry* **7**, 834–843 (1968).

190. Robertson, D. E. *et al.* Design and synthesis of multi-haem proteins. *Nature* **368**, 425–432 (1994).

191. Koder, R. L. *et al.* Design and engineering of an O2 transport protein. *Nature* **458**, 305–309 (2009).

192. Watkins, D. W. *et al.* Construction and in vivo assembly of a catalytically proficient and hyperthermostable de novo enzyme. *Nat. Commun.* **8**, 1–9 (2017).

193. Farid, T. A. *et al.* Elementary tetrahelical protein design for diverse oxidoreductase functions. *Nat. Chem. Biol.* **9**, 826–833 (2013).

194. Sutherland, G. *et al.* Design and engineering of water-soluble carotenoid proteins for singlet exciton fission. *Submiss.* (2019).

195. Block, H. *et al.* Immobilized-Metal Affinity Chromatography (IMAC): A Review. *Methods Enzymol.* **463**, 439–473 (2009).

196. Pace, C. N., Grimsley, G. R. & Scholtz, J. M. Protein Ionizable Groups : pK Values and Their Contribution. *J. Biol. Chem.* **284**, 13285–13289 (2010).

197. Levison, P. R. Large-scale ion-exchange column chromatography of proteins comparison of different formats. *J. Chromatogr. B* **790**, 17–33 (2003).

198. Birks, J. & Dyson, D. The Relations Between the Fluorescence and Absorption Properties of Organic Molecules. *Commun. (B.H. Flowers, F.R.S)* (1963).

199. Maciejewski, A. *et al.* Transient absorption experimental set-up with femtosecond time resolution. Femto- and picosecond study of DCM molecule in cyclohexane and methanol solution. *J. Mol. Struct.* **555**, 1–13 (2000).

200. Berera, R., van Grondelle, R. & Kennis, J. T. M. Ultrafast transient absorption spectroscopy: Principles and application to photosynthetic systems. *Photosynth. Res.* **101**, 105–118 (2009).

201. Albert-Seifried, S. & Friend, R. H. Measurement of thermal modulation of optical absorption

in pump-probe spectroscopy of semiconducting polymers. *Appl. Phys. Lett.* **98**, 98–101 (2011).

202. Rao, A., Wilson, M. W. B., Albert-Seifried, S., Di Pietro, R. & Friend, R. H. Photophysics of pentacene thin films: The role of exciton fission and heating effects. *Phys. Rev. B - Condens. Matter Mater. Phys.* **84**, 1–8 (2011).

203. Ekvall, K. *et al.* Cross phase modulation artifact in liquid phase transient absorption spectroscopy. *J. Appl. Phys.* **87**, 2340–2352 (2000).

204. Agrawal, G., Baldeck, P. & Alfano, R. Temporal and spectral effects of cross-phase modulation on copropagating ultrashort pulses in optical fibers. *Phys. Rev. A* **40**, 5063–5073 (1989).

205. Schott, S., Steinbacher, A., Buback, J., Nuernberger, P. & Brixner, T. Generalized magic angle for time-resolved spectroscopy with laser pulses of arbitrary ellipticity. *J. Phys. B At. Mol. Opt. Phys.* **47**, (2014).

206. Shen, Y. & Yang, G. *The supercontinuum Laser Source: Theory of Self-Phase Modulation and Spectral Broadening*. (Springer, 1989).

207. Coles, D. M. *et al.* Polariton-mediated energy transfer between organic dyes in a strongly coupled optical microcavity. *Nat. Mater.* **13**, 712–719 (2014).

208. Orgiu, E. *et al.* Conductivity in organic semiconductors hybridized with the vacuum field. *Nat. Mater.* **14**, 1123–9 (2015).

209. Herrera, F. & Spano, F. C. Cavity-Controlled Chemistry in Molecular Ensembles. *Phys. Rev. Lett.* **116**, 1–6 (2016).

210. Martínez-Martínez, L. A., Du, M., Ribeiro, R. F., Kéna-Cohen, S. & Yuen-Zhou, J. Polariton-Assisted Singlet Fission in Acene Aggregates. *J. Phys. Chem. Lett.* **9**, 1951–1957 (2018).

211. Flick, J., Ruggenthaler, M., Appel, H. & Rubio, A. Atoms and molecules in cavities, from weak to strong coupling in quantum-electrodynamics (QED) chemistry. *Proc. Natl. Acad. Sci.* **114**, 3026–3034 (2017).

212. Feist, J., Galego, J. & Garcia-Vidal, F. J. Polaritonic Chemistry with Organic Molecules. *ACS Photonics* **5**, 205–216 (2018).

213. Kasprzak, J. *et al.* Bose–Einstein condensation of exciton polaritons. *Nature* **443**, 409–414 (2006).

214. Amo, A. *et al.* Collective fluid dynamics of a polariton condensate in a semiconductor microcavity. *Nature* **457**, 291–295 (2009).

215. Daskalakis, K. S., Maier, S. A., Murray, R. & Kéna-Cohen, S. Nonlinear interactions in an organic polariton condensate. *Nat. Mater.* **13**, 271–278 (2014).

216. Lerario, G. *et al.* Room-temperature superfluidity in a polariton condensate. *Nat. Phys.* **13**, 837–841 (2017).

217. Berloff, N. G. *et al.* Realizing the classical XY Hamiltonian in polariton simulators. *Nat. Mater.* **16**, 1120–1126 (2017).

218. Sanvitto, D. & Kéna-Cohen, S. The road towards polaritonic devices. *Nat. Mater.* **15**, 1061–1073 (2016).

219. Graf, A. *et al.* Electrical pumping and tuning of exciton-polaritons in carbon nanotube microcavities. *Nat. Mater.* **16**, 911–917 (2017).

220. Held, M. *et al.* Ultrastrong Coupling of Electrically Pumped Near-Infrared Exciton-Polaritons in High Mobility Polymers. *Adv. Opt. Mater.* **6**, 1700962 (2018).

221. Eizner, E. *et al.* Organic Photodiodes with an Extended Responsivity Using Ultrastrong Light-Matter Coupling. *ACS Photonics* **5**, 2921–2927 (2018).

222. Lidzey, D. G. *et al.* Strong exciton-photon coupling in an organic semiconductor microcavity. *Nature* **395**, 53–55 (1998).

223. Barachati, F. *et al.* Tunable Third-Harmonic Generation from Polaritons in the Ultrastrong Coupling Regime. *ACS Photonics* **5**, 119–125 (2018).

224. Holmes, R. J. & Forrest, S. R. Exciton-photon coupling in organic materials with large intersystem crossing rates and strong excited-state molecular relaxation. *Phys. Rev. B* **71**, 235203 (2005).

225. Plumhof, J. D., Stoeferle, T., Mai, L., Scherf, U. & Mahrt, R. F. Room-temperature Bose-Einstein condensation of cavity exciton-polaritons in a polymer. *Nat. Mater.* **13**, 247–252 (2014).

226. Bardeen, C. J. Excitonic processes in molecular crystalline materials. *MRS Bull.* **38**, 65–71 (2013).

227. Baldo, M. A. *et al.* Highly efficient phosphorescent emission from organic electroluminescent

devices. *Nature* **395**, 151–154 (1998).

228. Rao, A. *et al.* The role of spin in the kinetic control of recombination in organic photovoltaics. *Nature* **500**, 435–439 (2013).

229. Singh-Rachford, T. N. & Castellano, F. N. Photon upconversion based on sensitized triplet-triplet annihilation. *Coord. Chem. Rev.* **254**, 2560–2573 (2010).

230. Goudarzi, H. & Keivanidis, P. E. Triplet-triplet annihilation-induced up-converted delayed luminescence in solid-state organic composites: Monitoring low-energy photon up-conversion at low temperatures. *J. Phys. Chem. C* **118**, 14256–14265 (2014).

231. Salvadori, E. *et al.* Ultra-fast spin-mixing in a diketopyrrolopyrrole monomer/fullerene blend charge transfer state. *J. Mater. Chem. A* **5**, 24335–24343 (2017).

232. Musser, A. J. *et al.* Intermolecular states in organic dye dispersions: Excimers: vs. aggregates. *J. Mater. Chem. C* **5**, 8380 (2017).

233. Schweitzer, C. & Schmidt, R. Physical mechanisms of generation and deactivation of singlet oxygen. *Chem. Rev.* **103**, 1685–757 (2003).

234. Mauck, C. M. *et al.* Singlet Fission via an Excimer-Like Intermediate in 3,6-Bis(thiophen-2-yl)diketopyrrolopyrrole Derivatives. *J. Am. Chem. Soc.* **138**, 11749–11761 (2016).

235. Dzebo, D., Börjesson, K., Gray, V., Moth-Poulsen, K. & Albinsson, B. Intramolecular Triplet-Triplet Annihilation Upconversion in 9,10-Diphenylanthracene Oligomers and Dendrimers. *J. Phys. Chem. C* **120**, 23397–23406 (2016).

236. Cheng, Y. Y. *et al.* Kinetic analysis of photochemical upconversion by triplet-triplet annihilation: Beyond any spin statistical limit. *J. Phys. Chem. Lett.* **1**, 1795–1799 (2010).

237. Basel, B. S. *et al.* Unified model for singlet fission within a non-conjugated covalent pentacene dimer. *Nat. Commun.* **8**, 1–8 (2017).

238. Lubert-Perquel, D. *et al.* Identifying triplet pathways in dilute pentacene films. *Nat. Commun.* **9**, 4222 (2018).

239. Bayliss, S. L. *et al.* Site-selective measurement of coupled spin pairs in an organic semiconductor. *Proc. Natl. Acad. Sci.* **115**, 5077–5082 (2018).

240. Yamagata, H. *et al.* The nature of singlet excitons in oligoacene molecular crystals. *J. Chem. Phys.* **134**, (2011).

241. Feng, X., Luzanov, A. V. & Krylov, A. I. Fission of entangled Spins: An electronic structure perspective. *J. Phys. Chem. Lett.* **4**, 3845–3852 (2013).

242. Aryanpour, K., Shukla, A. & Mazumdar, S. Theory of Singlet Fission in Polyenes, Acene Crystals, and Covalently Linked Acene Dimers. *J. Phys. Chem. C* **119**, 6966–6979 (2015).

243. Beljonne, D., Yamagata, H., Brédas, J. L., Spano, F. C. & Olivier, Y. Charge-transfer excitations steer the davydov splitting and mediate singlet exciton fission in pentacene. *Phys. Rev. Lett.* **110**, 1–5 (2013).

244. Bakulin, A. A. *et al.* Real-time observation of multiexcitonic states in ultrafast singlet fission using coherent 2D electronic spectroscopy. *Nat. Chem.* **8**, 16–23 (2016).

245. Aragó, J. & Troisi, A. Dynamics of the Excitonic Coupling in Organic Crystals. *Phys. Rev. Lett.* **114**, 026402 (2015).

246. Nijegorodov, N., Ramachandran, V. & Winkoun, D. P. The dependence of the absorption and fluorescence parameters, the intersystem crossing and internal conversion rate constants on the number of rings in polyacene molecules. *Spectrochim. Acta Part A Mol. Biomol. Spectrosc.* **53**, 1813–1824 (1997).

247. Freeman, D. M. E. *et al.* Synthesis and Exciton Dynamics of Donor-Orthogonal Acceptor Conjugated Polymers: Reducing the Singlet-Triplet Energy Gap. *J. Am. Chem. Soc.* **139**, 11073–11080 (2017).

248. Wallikewitz, B. H., Kabra, D., Gélinas, S. & Friend, R. H. Triplet dynamics in fluorescent polymer light-emitting diodes. *Phys. Rev. B* **85**, 1–15 (2012).

249. Antognazza, M. R. *et al.* Ultrafast excited state relaxation in long-chain polyenes. *Chem. Phys.* **373**, 115–121 (2010).

250. Okada, S., Peng, S., Spevak, W. & Charych, D. Color and Chromism of Polydiacetylene Vesicles. *Acc. Chem. Res.* **31**, 229–239 (1998).

251. Winter, M., Grupp, A., Mehring, M. & Sixl, H. Transient esr observation of triplet-soliton pairs in a conjugated polymer single crystal. *Chem. Phys. Lett.* **133**, 482–484 (1987).

252. IV. Zozulenko. Charge Carrier Geminate Recombination In One-Dimentional Polymer Strcuture With Traps. *Solid State Commun.* **36**, 357 (1999).

253. Zhang, C. *et al.* Poly(3-dodedyl-2,5-thienylenevinylene)s from the Stille coupling and the Horner-Emmons reaction. *Polym. Chem.* **1**, 663–669 (2010).

254. Xie, H. Q., Liu, C. M. & Guo, J. S. Further study of the preparation and properties of poly(thienylene vinylene) via an organic-soluble precursor polymer. *Eur. Polym. J.* **32**, 1131–1137 (1996).

255. Lafalce, E., Jiang, X. & Zhang, C. Generation and recombination kinetics of optical excitations in poly(3-dodecylthienylenevinylene) with controlled regioregularity. *J. Phys. Chem. B* **115**, 13139–13148 (2011).

256. Lafalce, E., Toglia, P., Zhang, C. & Jiang, X. Photophysics and morphology of poly (3-dodecylthienylenevinylene)-[6,6]- phenyl-C 61-butyric acid methyl ester composite. *Appl. Phys. Lett.* **100**, 213306 (2012).

257. Mello, J. de, Wittmann, H. & Friend, R. An Improved Experimental Determination of External Photoluminescence Quantum Efficiency. *Adv. Mater.* **9**, 73–83 (1997).

258. Cardozo, T. M., Aquino, A. J. A., Barbatti, M., Borges, I. & Lischka, H. Absorption and fluorescence spectra of poly(p -phenylenevinylene) (PPV) oligomers: An ab initio simulation. *J. Phys. Chem. A* **119**, 1787–1795 (2015).

259. Olejnik, E. *et al.* Ultrafast optical studies of ordered poly(3-thienylene-vinylene) films. *Phys. Rev. B - Condens. Matter Mater. Phys.* **85**, 2–7 (2012).

260. Hu, Z. *et al.* Effect of the side-chain-distribution density on the single-conjugated- polymer-chain conformation. *ChemPhysChem* **14**, 4143–4148 (2013).

261. Brey, L. A., Schuster, G. B. & Drickamer, H. G. High pressure fluorescence studies of radiative and nonradiative processes in diphenyl hexatriene, diphenyl octatetraene, and retinyl acetate. *J. Chem. Phys.* **71**, 2765–2772 (1979).

262. Saidani, M. A. *et al.* Franck-Condon analysis of the photoluminescence spectra of a triple-bond containing polymer as a solution and as a thin film. *Synth. Met.* **184**, 83–85 (2013).

263. Vezie, M. S. *et al.* Exploring the origin of high optical absorption in conjugated polymers. *Nat. Mater.* **15**, 746–753 (2016).

264. Schumacher, S. *et al.* Effect of exciton self-trapping and molecular conformation on photophysical properties of oligofluorenes. *J. Chem. Phys.* **131**, (2009).

265. Itoh, T. & Kohler, B. E. Dual fluorescence of diphenylpolyenes. *J. Phys. Chem.* **91**, 1760–1764 (1987).

266. Clark, J., Nelson, T., Tretiak, S., Cirmi, G. & Lanzani, G. Femtosecond torsional relaxation. *Nat.*

Phys. **8**, 225–231 (2012).

267. Kawski, A., Kubick, A., Kuklinski, B. & Piszczek, G. Isomerization of Diphenyl Polyenes. Part V. The Origin of Fluorescence of l, 6-Diphenyl-l, 3, 5-hexatriene in Poly (vinyl alcohol) Films. *Zeitschrift fur Naturforsch. - Sect. A J. Phys. Sci.* **48**, 861–867 (1993).

268. Anger, F. *et al.* Photoluminescence spectroscopy of pure pentacene, perfluoropentacene, and mixed thin films. *J. Chem. Phys.* **136**, (2012).

269. Greco, J. A. *et al.* Spectroscopic Investigation of the Carotenoid Deoxyperidinin: Direct Observation of the Forbidden S0 → S1 Transition. *J. Phys. Chem. B* **120**, 2731–2744 (2016).

270. Petek, H. *et al.* The 2 1 A g state of trans,trans-1,3,5,7-octatetraene in free jet expansions. *J. Chem. Phys.* **98**, 3777–3794 (1993).

271. Dillon, R. J., Piland, G. B. & Bardeen, C. J. Different rates of singlet fission in monoclinic versus orthorhombic crystal forms of diphenylhexatriene. *J. Am. Chem. Soc.* **135**, 17278–17281 (2013).

272. Fang, H., Thrash, R. & Leroi, G. E. Observation Of The Low-Energy Ag State Of DiphenylhexatieneBy two-photon excitation spectroscopy. *Chem. Phys. Lett.* **57**, 59–63 (1978).

273. Kohler, B. E. & Spiglanin, T. A. Vibrationally resolved optical spectra of cis , trans-1,3,5,7-octatetraene. *J. Chem. Phys.* **80**, 3091–3096 (1984).

274. Granville, M. F., Holtom, G. R., Kohler, B. E., Christensen, R. L. & D'Amico, K. L. Experimental confirmation of the dipole forbidden character of the lowest excited singlet state in 1,3,5,7-octatetraene. *J. Chem. Phys.* **70**, 593–594 (1979).

275. Christensen, R. L. & Kohler, B. E. Vibronic coupling in polyenes: High resolution optical spectroscopy of 2,10-dimethylundecapentaene. *J. Chem. Phys.* **63**, 1837–1846 (1975).

276. Noguchi, T., Hayashi, H., Tasumi, M. & Atkinson, G. H. Solvent effects on the ag carbon-carbon double bond stretching mode in the 21Ag- excited state of .beta.-carotene and two derivatives: picosecond time-resolved resonance Raman spectroscopy. *J. Phys. Chem.* **95**, 3167–3172 (2005).

277. Andrews, J. R. & Hudson, B. S. Environmental effects on radiative rate constants with applications to linear polyenes. *J. Chem. Phys.* **68**, 4587–4594 (1978).

278. Khan, S. & Mazumdar, S. Linker Dependent Excited State Absorptions from the Free Triplets

versus Correlated Triplet-Triplet State in Pentacene Dimers. *arXiv* 1–19 (2019).

279. Khan, S. & Mazumdar, S. Theory of Transient Excited State Absorptions in Pentacene and Derivatives: Triplet-Triplet Biexciton versus Free Triplets. *J. Phys. Chem. Lett.* **8**, 5943–5948 (2017).

280. Y, K., Akiyama, K. & Tero-Kubota, S. Anisotropic intersystem crossing from the upper excited triplet states of anthracenes: Two-laser time-resolved EPR study. *J. Phys. Chem. A* **103**, 1714–1718 (1999).

281. Bennati, M., Grupp, A., Mehring, M. & Bäuerle, P. Pulsed EPR spectroscopy of the photoexcited triplet states of thiophene oligomers in frozen solution. *J. Phys. Chem.* **100**, 2849–2853 (1996).

282. Kamata, Y., Akiyama, K., Tero-Kubota, S. & Tabata, M. Two-laser two-color time-resolved EPR study on higher-excited-state triplet-singlet intersystem crossing of porphyrins and phthalocyanines. *Appl. Magn. Reson.* **23**, 409–420 (2002).

283. Akiyama, K., Tero-Kubota, S. & Ikegami, Y. Time-resolved EPR observation of the short-lived excited triplet states of diamagnetic metallophthalocyanines in a rigid glassy matrix. *Chem. Phys. Lett.* **185**, 65–67 (1991).

284. Küpper, B., Kleinschmidt, M., Schaper, K. & Marian, C. M. On the photophysics of 1,6-diphenyl-1,3,5-hexatriene isomers and rotamers. *ChemPhysChem* **12**, 1872–1879 (2011).

285. Kohler, B. E. The polyene 2 1Ag state in polyacetylene photoinduced absorption and thermal isomerization. *J. Chem. Phys.* **88**, 2788–2792 (1988).

286. Rissler, J. Effective conjugation length of π-conjugated systems. *Chem. Phys. Lett.* **395**, 92–96 (2004).

287. Meier, H., Stalmach, U. & Kolshorn, H. Effective conjugation length and UV/vis spectra of oligomers. *Acta Polym.* **48**, 379–384 (1997).

288. Aryanpour, K., Shukla, A. & Mazumdar, S. Electron correlations and two-photon states in polycyclic aromatic hydrocarbon molecules: A peculiar role of geometry. *J. Chem. Phys.* **140**, 104301 (2014).

289. Chandross, M., Shimoi, Y. & Mazumdar, S. Diagrammatic exciton-basis valence-bond theory of linear polyenes. *Phys. Rev. B* **59**, 4822–4838 (1999).

290. Zhang, X. X. *et al.* Femtosecond broadband fluorescence upconversion spectroscopy:

Improved setup and photometric correction. *Rev. Sci. Instrum.* **82**, 2–10 (2011).

291. Hudson, B. S. & Kohler, B. E. A low-lying weak transition in the polyene α,ω-diphenyloctatetraene. *Chem. Phys. Lett.* **14**, 299–304 (1972).

292. Kuznetsova, V., Southall, J., Cogdell, R. J. J., Fuciman, M. & Polívka, T. Spectroscopic properties of the S1 state of linear carotenoids after excess energy excitation. *Chem. Phys. Lett.* **683**, 448–453 (2017).

293. Schulten, K. & Karplus, M. On the origin of a low-lying forbidden transition in polyenes and related molecules. *Chem. Phys. Lett.* **14**, 305–309 (1972).

294. Lustres, J. L. P., Dobryakov, A. L., Holzwarth, A. & Veiga, M. S2→S1 internal conversion in β-carotene: Strong vibronic coupling from amplitude oscillations of transient absorption bands. *Angew. Chemie - Int. Ed.* **46**, 3758–3761 (2007).

295. MacPherson, A. N. & Gillbro, T. Solvent dependence of the ultrafast S2-S1 internal conversion rate of β-carotene. *J. Phys. Chem. A* **102**, 5049–5058 (1998).

296. McCamant, D. W., Kukura, P. & Mathies, R. A. Femtosecond time-resolved stimulated Raman spectroscopy: Application to the ultrafast internal conversion in β-carotene. *J. Phys. Chem. A* **107**, 8208–8214 (2003).

297. Shreve, A. P., Trautman, J. K., Owens, T. G. & Albrecht, A. C. Determination of the S2 lifetime of β-carotene. *Chem. Phys. Lett.* **178**, 89–96 (1991).

298. Kim, H. & Zimmerman, P. M. Coupled double triplet state in singlet fission. *Phys. Chem. Chem. Phys.* **20**, 30083–30094 (2018).

299. H. Kingma. RV. Grondelle, L. D. Magnetic-field effects in photosynthetic bacteria. II. Formation of triplet states in the reaction center and the antenna of Rhodospirillum rubrum and Rhodopseudomonas sphaeroides. Magnetic-field effects. *Biochim. Biophys. Acta - Bioenerg.* **808**, 383–399 (1985).

300. Kingma, H., van Grondelle, R. & Duysens, L. N. M. Magnetic-field effects in photosynthetic bacteria. I. Formation of triplet states in the reaction center and the antenna of Rhodospirillum rubrum and Rhodopseudomonas sphaeroides. Magnetic-field effects. *BBA - Bioenerg.* **808**, 383–399 (1985).

301. Klein, G., Voltz, R. & Schott, M. Magnetic field effect on prompt fluorescence in anthracene: evidence for singlet exciton fission. *Chem. Phys. Lett.* **16**, 340–344 (1972).

302. Klenina, I. B. *et al.* Singlet-triplet fission of carotenoid excitation in light-harvesting LH2 complexes of purple phototrophic bacteria. *Biochem.* **79**, 235–241 (2014).

303. Klenina, I. B., Makhneva, Z. K., Moskalenko, A. A., Kuzmin, A. N. & Proskuryakov, I. I. Singlet-triplet excitation fission in light-harvesting complexes of photosynthetic bacteria and in isolated carotenoids. *Biophysics (Oxf).* **58**, 43–50 (2013).

304. Scholes, G. D., Harcourt, R. D. & Fleming, G. R. Electronic Interactions in Photosynthetic Light-Harvesting Complexes: The Role of Carotenoids. *j. Phys. Chem. B* **101**, 7302–7312 (1997).

305. Yu, J. *et al.* Carotenoid Singlet Fission Reactions in Bacterial Light Harvesting Complexes As Revealed by Triplet Excitation Profiles. *J. Am. Chem. Soc.* **139**, 15984–15993 (2017).

306. Niedzwiedzki, D. M., Swainsbury, D. J. K., Martin, E. C., Hunter, C. N. & Blankenship, R. E. Origin of the S* excited state feature of carotenoids in light-harvesting complex 1 from purple photosynthetic bacteria. *J. Phys. Chem. B* **121**, 7571–7585 (2017).

307. Niedzwiedzki, D. M. *et al.* New insights into the photochemistry of carotenoid spheroidenone in light-harvesting complex 2 from the purple bacterium Rhodobacter sphaeroides. *Photosynth. Res.* **131**, 291–304 (2016).

308. Zigmantas, D. *et al.* Effect of a conjugated carbonyl group on the photophysical properties of carotenoids. *Phys. Chem. Chem. Phys.* **6**, 3009–3016 (2004).

309. Bachilo, S. M. β-carotene triplet state absorption in the near-IR range. *J. Photochem. Photobiol. A Chem.* **91**, 111–115 (1995).

310. Golibrzuch, K. *et al.* Ultrafast excited state dynamics and spectroscopy of 13,13'-diphenyl-β-carotene. *Phys. Chem. Chem. Phys.* **13**, 6340–51 (2011).

311. De Weerd, F. L., Van Stokkum, I. H. M. & Van Grondelle, R. Subpicosecond dynamics in the excited state absorption of all-trans-β-carotene. *Chem. Phys. Lett.* **354**, 38–43 (2002).

312. Chábera, P., Fuciman, M., Híbek, P. & Polívka, T. Effect of carotenoid structure on excited-state dynamics of carbonyl carotenoids. *Phys. Chem. Chem. Phys.* **11**, 8795–8803 (2009).

313. Herkstroeter, W. G. Triplet energies of azulene, β-carotene, and ferrocene. *J. Am. Chem. Soc.* **97**, 4161–4167 (1975).

314. Burke, M., Land, E. J., McGarvey, D. J. & Truscott, T. G. Carotenoid triplet state lifetimes. *J. Photochem. Photobiol. B Biol.* **59**, 132–138 (2000).

315. Rodgers, M. A. J. & Bates, A. L. Kinetic and Spectroscopic Features of Some Carotenoid Triplet States: Sensitization By Singlet Oxygen. *Photochem. Photobiol.* **31**, 533–537 (1980).

316. Wang, C., Schlamadinger, D. E., Desai, V. & Tauber, M. J. Triplet excitons of carotenoids formed by singlet fission in a membrane. *ChemPhysChem* **12**, 2891–2894 (2011).

317. Manzoni, C. & Cerullo, G. Design criteria for ultrafast optical parametric amplifiers. *J. Opt.* **18**, 1–33 (2016).

318. Hashimoto, H., Koyama, Y., Hirata, Y. & Mataga, N. S1 and T1 species of .beta.-carotene generated by direct photoexcitation from the all-trans, 9-cis, 13-cis, and 15-cis isomers as revealed by picosecond transient absorption and transient Raman spectroscopies. *J. Phys. Chem.* **95**, 3072–3076 (1991).

319. Mancini, J. A. *et al.* De novo synthetic biliprotein design, assembly and excitation energy transfer. *J. R. Soc. Interface* **15**, (2018).

320. Grieco, C. *et al.* Harnessing Molecular Vibrations to Probe Triplet Dynamics during Singlet Fission. *J. Phys. Chem. Lett.* **8**, 5700–5706 (2017).

321. Pensack, R. D. *et al.* Observation of Two Triplet-Pair Intermediates in Singlet Exciton Fission. *J. Phys. Chem. Lett.* **7**, 2370–2375 (2016).

322. Grieco, C. *et al.* Direct Observation of Correlated Triplet Pair Dynamics during Singlet Fission Using Ultrafast Mid-IR Spectroscopy. *J. Phys. Chem. C* **122**, 2012–2022 (2018).

323. Chen, M. *et al.* Singlet Fission in Covalent Terrylenediimide Dimers: Probing the Nature of the Multiexciton State Using Femtosecond Mid-Infrared Spectroscopy. *J. Am. Chem. Soc.* **140**, 9184–9192 (2018).

324. Deng, G.-H. *et al.* Vibronic fingerprint of singlet fission in hexacene. *J. Chem. Phys.* **151**, 054703 (2019).

325. Kovrigin, E. L. Integrative Data Analysis Platform : 1 . Data Processing , Fitting , and Model Selection. *BioRxiv* 1–12 (2017).

326. Yuan, J. P. & Chen, F. Kinetics for the reversible isomerization reaction of trans-astaxanthin. *Food Chem.* **73**, 131–137 (2001).

327. Lemmens, L. *et al.* β-Carotene isomerization kinetics during thermal treatments of carrot puree. *J. Agric. Food Chem.* **58**, 6816–6824 (2010).